School of Mathematics and Physical Sciences

Department of Mathematics

Mathematical modelling in cellular biology through compartmentalisation and conservation laws

Davide Cusseddu

Supervisors:

Anotida Madzvamuse

Stéphanie Portet

March 2019

A thesis submitted for the degree of Doctor of Philosophy in Mathematics

Declaration

I hereby declare that this thesis has not been and will not be submitted in whole or in part to another University for the award of any other degree. I also declare that this thesis was composed by myself, under the supervision of Professor Anotida Madzvamuse and Dr Stéphanie Portet, and that the work contained therein is my own, except where stated otherwise, such as citations.

.....

(Davide Cusseddu)

Brighton, 11th July 2019

UNIVERSITY OF SUSSEX

DAVIDE CUSSEDDU

PHD IN MATHEMATICS

MATHEMATICAL MODELLING IN CELLULAR BIOLOGY THROUGH COMPARTMENTALISATION AND CONSERVATION LAWS

SUMMARY

The aim of this thesis focuses on addressing several open questions in cell biology by using different mathematical approaches and numerical analysis methods to study the evolution of distinct protein families in various cellular phenomena, such as cell polarisation and cytoskeleton remodelling. Our approaches are based on conservation laws and compartmentalisation of proteins within appropriate geometrical subdomains representing different cellular structures, such as the cell membrane and cytosol.

The Rho GTPase are proteins responsible of coordinating the cell polarisation response, which is a biological process involving a huge number of different proteins and intricate networks of biochemical reactions. Rho GTPases localise their activity in specific cell regions where they interact with the cell cytoskeleton. Reducing the biological assumptions to a minimal level of complexity, we will present a simple qualitative model for cell polarisation in which proteins cycle between cell membrane and cytosol in an active and inactive form. This is described through a bulk-surface system of two reaction-diffusion equations coupled by the boundary condition. The model supports pattern formation and we will confirm

this claim by using both mathematical analysis and simulations. The bulk-surface finite element method is presented and used to solve the model on different geometries.

Secondly, we will present a mathematical model for keratin intermediate filament dynamics in resting cells. This model, characterised by a quantitative approach, is a data-driven extension of a pre-existing model, initially introduced by Portet et al. (*PlosONE*, 2015). We will discuss the new assumptions and modelling ideas, and compare the solution of our model to the experimental data. Part of the biological impact of our model relies in its ability to estimate the amount of assembled and disassembled keratin material as a function of space and time, consistent with the biological model proposed by Windoffer et al. (*Journal of Cell Biology*, 2011).

In the last part we will introduce a second mathematical model for keratin spatio-temporal dynamics in non-resting cells. In this case, the model is derived on two- and three-dimensional geometries and accounts for a more detailed description of the processes involved in the keratin cytoskeleton remodelling process. The evolution of three different forms of keratin is modelled by a system composed of one reaction-diffusion equation and two reaction-advection-diffusion equations. Keratin kinetics are also described by the boundary conditions, which are posed both at the cell membrane and at the nuclear envelope. In solving the model, we will use the Streamline Upwind Petrov Galerkin method, as described in the text. In conclusion, in view of a future estimation of biologically relevant parameters, a simulation is presented, showing consistency of our mathematical model with the biological model proposed by Windoffer et al. (*Journal of Cell Biology*, 2011).

In summary, this thesis presents methods and techniques for data-driven modelling supported by rigorous mathematical analysis and novel numerical methods and simulations. Our approach involving the use of quantitative methods serves as a blue-print for how to study the synergy interplay between mathematics and its applications to experimental sciences.

This project has received funding from the European Union's Horizon 2020 research and innovation programme under the Marie Skłodowska-Curie grant agreement no 642866.

Acknowledgements

Looking back to the start of my PhD, I really feel that this has been an incredible journey, in all senses: scientifically, personally and... literally. And like all journeys, I had the pleasure of meeting so many people who played a fundamental part in my work, that this section could not be any shorter.

Undoubtedly the first people I would like to thank profoundly are my supervisors, Anotida Madzvamuse and Stéphanie Portet. They introduced me into the scientific world and guided me through it with inspiring enthusiasm, helping and supporting me during these years. In addition, they constantly offered me appropriate opportunities to travel around the world, broadening my knowledge and widening my horizons. Thanks to them, I had so many fulfilling experiences, which made these years a wonderful period of my life.

I started my PhD programme as an early stage researcher within *InCeM*, which was a Marie Skłodowska-Curie Innovative Training Network, focused on studying cell migration. Therefore, I am extremely grateful to the European Community and its research and innovation programme Horizon 2020, which funded my studies entirely. I also would like to thank all the InCeM members for the useful discussions, suggestions and for the constructive criticism. In particular, many thanks to the amazing ESRs group: Lea, Nikos, Anne, Nadieh, Kritika, Galia, Laura, Tina, Rutuja, Katerina, Roman, Victor, Shore and Dmytro, for the fun and the lovely time we always had during our meetings.

Besides the InCeM meetings, a lot of my biological knowledge comes from visiting biology labs and interacting with experimental researchers. Hence, I particularly would like to thank Nadieh Kuijpers, Anne Pora, Reinhard Windoffer and Rudolf Leube, who on many occasions, including my visit to the RWTH Aachen University, were very kind and helpful in explaining to me the known and unknown properties of the keratin cytoskeletal network. Our discussions were crucial for the work presented in Chapters 3 and 4. I am extremely grateful also to Alexander Bershadsky and all his research group, in particular to Naila Alieva, Nisha Rafiq and Salma Jalal, for the beautiful time and the many things I learned during my visit to the Mechanobiology Institute in Singapore. Also many thanks

to Sandrine Etienne-Manneville and her group, who I had the pleasure of visiting at the Pasteur Institute in Paris. In particular, many thanks to Bertille Bance for the discussions about the focal adhesions, which helped in the development of the FA model presented in Appendix C. Furthermore, I benefited greatly from visiting my supervisor Stéphanie Portet at the University of Manitoba and John Mackenzie at the University of Strathclyde, who I sincerely acknowledge, together with Christopher Rowlatt. Many thanks as well to the Isaac Newton Institute, which I had the pleasure of visiting at different times in 2015 during the 6-month research programme *Coupling Geometric PDEs with Physics for Cell Morphology, Motility and Pattern Formation* and the MASAMU programme, which I attended in 2016 and 2017.

I would really like to thank Jane White for her support and the motivating conversations we had. Many thanks also to Leah Edelstein-Keshet for her ideas and invaluable suggestions regarding the work in Chapter 2 and, in the final stages, to Fred Vermolen and Istvan Kiss for their critical reading and their valuable suggestions, which improved the overall quality of this thesis.

While this thesis is definitely the result of many trips, workshops and research visits, most of it comes from my time in Brighton, which has been really enjoyable. This has been possible thanks to the lovely people I have met. Many thanks to my friend and housemate David Macdonald for these wonderful years and to *The Gang*: Silvio Fanzon, Victor Juma, Matteo Perugini, Farzad Fatehi Chenar. Many thanks also to Stelios Katsarakis, Wakil Sarfaraz and all the other PhD friends and colleagues I spent most of my time with. *Muchas gracias* also to Manuel and the Boulder Brighton friends. Furthermore, I would like to thank Pietro, Sandra, Eli, Mireia and the rest of the group for the great time I had in Cambridge, and Megah, Marisa, Febrina for making my Singaporean time a wonderful experience. As always, many thanks to my friends in Sardinia and Rome, who, every time, made going home a great pleasure.

To conclude, my heartfelt thanks to the people which have always supported me, which compose my family: Enrico, Maurizia, Valeria, Claudia, Tonino, Giulio and, lastly, Roberta.

Grazie.

Contents

Chapter 1

Introduction

Mathematics has often been a powerful tool in addressing answers to complex biological questions. Historically, there are excellent examples of this, for instance Michaelis and Menten (1913) proposed a fundamental mathematical model for enzymatic reactions, Hodgkin and Huxley (1952) were awarded with the Nobel prize for their mathematical model describing the action potential in function of the ion channels at the cellular membrane, Turing (1952) published *"The Chemical Basis of Morphogenesis"*, a pioneering work on pattern formation based on a system of two reaction-diffusion equations, Luria and Delbrück (1943) revealed important insights about bacteria resistance from viruses by coupling experiments to mathematical models (see also Möbius and Laan (2015)) and crucial advances in evolutionary biology have been made thanks to mathematical support (see for example Shou et al. (2015); Servedio et al. (2014)). Currently, one evergreen field for applied mathematicians (and modellers in general) is cell biology, which is the study of the cell and its structures, essential subject for the understanding of higher scale components such as tissues and organs. From the modellers' point of view, cell biology is a very heterogeneous field and an immense source of open questions, in which an interdisciplinary approach is often fundamental (regarding this, see for example the editorial by Madzvamuse and Lubkin (2016) about an international 6-months research programme joined by both modellers and experimentalists).

This thesis proposes different mathematical modelling approaches to open questions in cell biology, resulting from three years of research within the *InCeM* network, which was a *Marie Skłodowska-Curie Innovative Training Network* funded by the EU's framework programme HORIZON 2020. The main goal of our network was to study and understand mechanisms related to single cell migration through an interdisciplinary approach, with a combination of different projects involving both theoretical and experimental methods.

Hence this thesis comes out as one part of a bigger project and it is the conclusion of a scientific work in which the support and the many discussions with experimentalists, internal and external to InCeM, played a fundamental role. As we will discuss in this introduction, cell migration is a very complex process, which involves a huge number of biological players. Despite the fact that great advances in science have been made in this field, many questions are still open, especially on the role and behaviour of all the biological entities involved. Thus, the thesis is focused in getting better insights into the biology of the cell, discussing on different, and apparently distant, intracellular phenomena. Even though cell migration is never explicitly considered throughout this thesis, in a certain sense, our work can be thought as the result of a *divide et impera* strategy, in which sub-problems are tackled with the aim of getting some more biological knowledge, inspired by the complexity of the bigger picture in the context of cell migration.

Besides the intrinsic complexity of cell biology processes, often modellers have to face with a second type of complexity, which arises from the mathematical description of the biological phenomena. Indeed, when many variables are considered to be fundamental, the resulting mathematical model might be very hard to analyse and understand. In particular, this discussion motivates the work presented in Chapter 2, in which a conceptual model with minimal assumptions is able to show cell polarisation response, which is a biological process involving a huge number of molecules and proteins. Another form of complexity involved in the modelling process might emerge when dealing with experimental data. In Chapter 3 we will present a data-driven model for keratin network dynamics. In that case, a fundamental step is the understanding of the technical difficulties involved in the data collection, which might compromise the data quality. As we will see, mathematical modelling is not only a tool to propose and validate biological assumptions but it can be also a suitable approach to fill the gaps in the available data.

Before proceeding further in the modelling aspects, we now give a description of the biological processes and structures we have studied in the thesis.

1.1 A biological background

The purpose of this section is to guide the reader into the general picture in which the modelled biological structures are placed and interact. Since the three main chapters of this thesis (Chapters 2, 3 and 4) are always accompanied by an exhaustive biological introduction, here we will not go too much into the details. Instead, we propose a general description which also highlights the role of each biological player in the cell migration

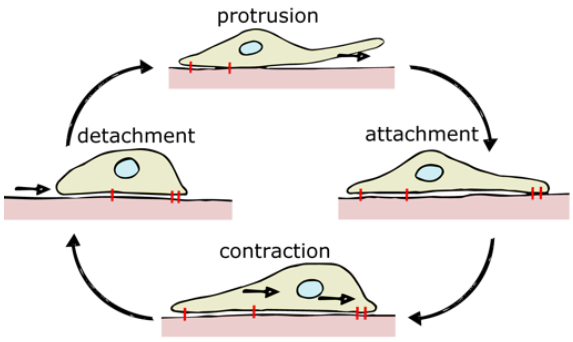

Figure 1.1: A schematic representation of the different cyclic phases of cell migration. The migrating cell needs to achieve a very complex coordination between biochemical signalling pathways and mechanical forces. Fundamental coordinators of the biochemical processes are the Rho GTPase proteins (see Section 1.1.5), which direct the remodelling of the cell cytoskeleton (see Section 1.1.2), responsible of the mechanics behind the migration.

process. In particular, we start by giving a brief introduction to cell migration, followed by a description of the cytoskeleton with particular emphasis on keratin intermediate filaments. Brief references to cell adhesions and Rho GTPase proteins will also be given.

1.1.1 Cell migration

Cell migration is a fundamental aspect of all living organisms, which accompanies them since their initial formation. Indeed, during embryonic development, morphogenesis, which is the process driving the shape of growing tissues and organs, is highly dependent on cell migration (Davies, 2013). As well, this phenomenon characterises natural processes such as renewal of tissues, wound healing, immunoresponse, but also pathological processes such as cancer, vascular diseases, osteoporosis (Ridley et al., 2003; Ridley, 2015; De Pascalis and Etienne-Manneville, 2017). Hence, a more complete understanding of cell migration can lead to fundamental scientific and medical discoveries. Different modes of migrations have been identified, depending on the cell type, tissues and environment (Vicente-Manzanares, 2005; DeSimone and Horwitz, 2014). Without going too much into details, the classical model of a single cell migration in two-dimensions is generally described with four different steps: 1) the cell forms protrusions in the direction of migration, a necessary process for sensing the environment and apply traction forces; 2) the protrusions are stabilised through attachment to the substrate; 3) the cell contracts forward and 4) the adhesions at the tail of the migrating cell are finally disassembled (Mitchison and Cramer, 1996; Ridley, 2001). These four steps are repeated cyclically during migration, see Figure 1.1. Each one of them involves a huge number of proteins and cellular structures, such as the three cytoskeleton components (actin filaments, microtubules, intermediate filaments), cell adhesions, myosin

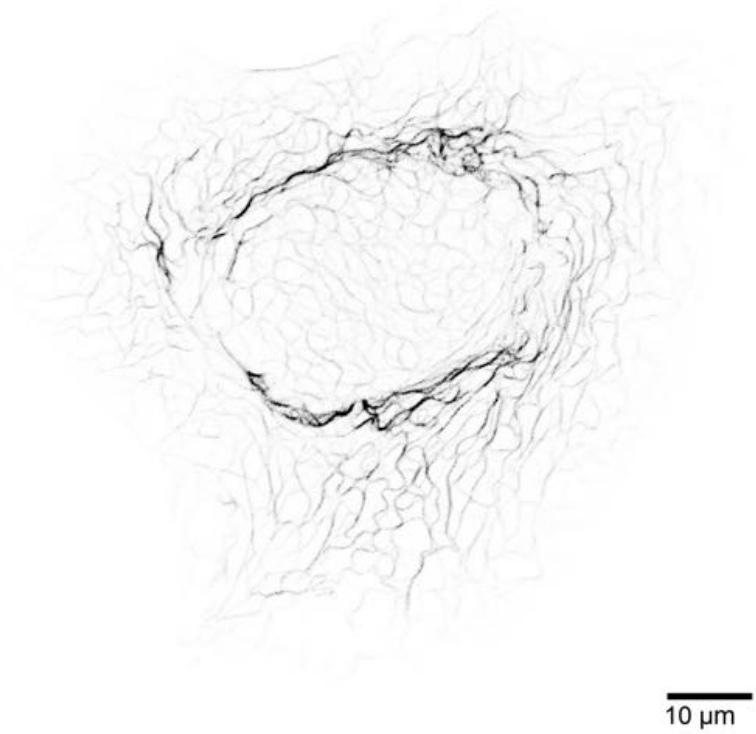

Figure 1.2: The keratin cytoskeleton in a single hepatocellular carcinoma-derived PLC cell. Image adapted from Portet et al. (2015).

proteins and proteins of the Rho-GTPase family. Since all these components are strictly interlinked, the cell needs to coordinate an impressive amount of biochemical reactions and mechanical forces which permit the movement (Trepat et al., 2012).

1.1.2 The cytoskeleton

The cytoskeleton is a structure responsible of the internal organisation of the cell and provides the fundamental mechanical support to carry out essential cellular functions, such as cell division and cell migration (Fletcher and Mullins, 2010). It is composed of complex filament networks of three major classes: *microfilaments* or *actin filaments*, *microtubules* and *intermediate filaments*. During cell migration the cytoskeleton is continuously remodelled to permit protrusion formation and application of traction forces. In this process actin filaments are continuously assembled at the leading edge and these push the membrane forward. Actin filaments form stress fibres, which are anchored to the cell-substrate adhesions and aligned in the direction of the migration (Pollard and Borisy, 2003). Contraction forces are generated by the association of actin with another protein called *myosin* (Mitchison and Cramer, 1996; Pollard and Cooper, 2009). The microtubules are filaments composed of *tubulin* and are main players in cell division (Iwasa and Marshall, 2016) and

fundamental regulators of cell migration, in which they take part with intracellular protein transport and regulation of cell adhesions (Watanabe et al., 2005; Etienne-Manneville, 2013). Both actin filaments and microtubules are polarised structures, which is a necessary property for intracellular transport and directed cell migration. On the other hand, intermediate filaments are the non polar components of the cytoskeleton and the proteins composing their structure differ depending on the cell type. In epithelial cells, intermediate filaments are composed of *keratins*. A brief description on their role in migration, and more generally in cells, is given in the following section.

1.1.3 Keratin intermediate filaments

Intermediate filaments (IFs) constitute a network of filaments and bundles which extends all over the cell cytoplasm, enveloping the nucleus in a protective cage. A major role recognised to the IFs is the reinforcement of the cell structure and organisation of the cell into tissues (Etienne-Manneville, 2018). In epithelial cells, keratin IFs cover an essential role in regulating the cell stiffness and the integrity of the epithelial tissue. Indeed, mutations of keratins have been reported to cause more than 60 different pathological disorders and diseases, characterised by cell and tissue fragility (Irvine and McLean, 1999; Toivola et al., 2015). A classical example of this is a group of genetic diseases called *epidermolysis bullosa*, which causes easy blistering and erosion of the skin after minor mechanical traumas such as rubbing (Omary et al., 2004; Coulombe et al., 2009). Another important medical aspect of keratins is that they are excellent biomarkers in neoplastic diseases (Omary et al., 2004; Pan et al., 2013).

Keratin filaments and bundles form a highly dynamic viscoelastic network subject to continuously renewal and reorganisation (Windoffer et al., 2011; Etienne-Manneville, 2018). Apart from its viscoelastic properties, the network is characterised by a remarkable ability to resist to mechanical stress and deformation (Ramms et al., 2013; Jacob et al., 2018). A picture of the keratin cytoskeleton is proposed in Figure 1.2.

Unlike actin filaments and microtubules, whose role in cell migration is well recognised, the role of intermediate filaments still needs a more complete understanding. In particular, it varies remarkably depending on the intermediate filament protein types, but also on the cell type and the mode of migration (Leduc and Etienne-Manneville, 2015). Hence, the relationship between IFs and migration might appear contradictory if one wants to find a general answer. Restricting the discussion to solely keratins does not help in identifying a unique response. Indeed, keratins are a very large family composed of 54 functional keratin

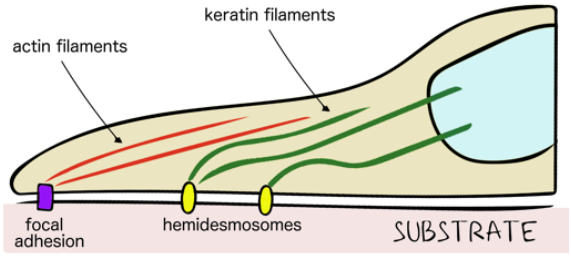

Figure 1.3: A schematic diagram illustrating cell-substrate adhesions: focal adhesions are anchoring sites for actin bundles, while keratin cytoskeleton attaches to the cell membrane through the hemidesmosomes.

genes and their effect on migration strongly differs for specific keratins and type of cells. For instance, keratinocytes lacking keratin IFs show increased invasive properties (Seltmann et al., 2013), while keratin K19 has been shown to promote invasion of hepatocellular carcinomas (Etienne-Manneville, 2018).

For more biological details, we refer to Chapter 3 and 4, where we will present two different mathematical models for keratin spatio-temporal dynamics.

1.1.4 Cell adhesions

Cell adhesions to the extracellular matrix (ECM) are mainly mediated by *integrin* receptors, which are transmembrane proteins responsible of creating a physical link between the cell cytoskeleton to the ECM, as well as sensing the extracellular environment. They have a mechanical role in regulating the force transmission across the cell membrane and they also have a biochemical role in transmitting inside-out and outside-in signals describing the location and the environment, which is a necessary aspect for cell migration (Harburger and Calderwood, 2009; Tsuruta et al., 2011). *Focal adhesions* are complexes composed of a huge number of proteins, for example *paxillin, vinculin, talin*, known for binding actin filaments (Geiger et al., 2009). They are essential in cell migration, being robust mechanical-dependent anchoring points for the actin-myosin system. Moreover focal adhesions control the migration, possibly refraining it (Zaidel-Bar et al., 2003, 2004). A second type of adhesion structures in keratinocyte cells are the *hemidesmosomes*, which are known for binding the keratin filament network (Tsuruta et al., 2011; Seltmann et al., 2013; Nahidiazar et al., 2015). They also play an essential role in maintaining the integrity of the tissues (Tsuruta et al., 2011). See also Figure 1.3.

1.1.5 Cell polarisation and Rho GTPases

While stationary cells are characterised by a radially symmetrical organisation of the internal processes and distribution of molecules and proteins, migrating cells are generally characterised by strong asymmetries. This is observed for instance in keratinocytes, which are epithelial cells (Yam et al., 2007). Directed cell migration is an activity in which the cell has defined its own front and rear. In these regions the local processes are very different, in order to permit the cell to move in a specific direction. This cellular asymmetry is a particular *cell polarisation* response and is the result of complex networks of biochemical reactions, which are also responsible of the cytoskeleton remodelling (Iden and Collard, 2008; Hanna and El-Sibai, 2013; Ladoux et al., 2016).

Main protagonists of the cell polarisation process are proteins of the *Rho GTPase family* (GTP stands for *guanosine triphosphate*), which activate different cellular responses depending on the stimulus. In cell migration, for example, Rho GTPases are fundamental regulators of the actin network and cell adhesions (Ridley, 2001; Ridley et al., 2003; Ridley, 2015). Among this family, *Cdc42*, *Rac* and *Rho* are the most representative components. During migration the first two are mainly active at the leading edge, while Rho mediates the cellular processes also at the rear of the cell (Sadok and Marshall, 2014; Fritz and Pertz, 2016), see also Figure 1.4.

Rho GTPase proteins are molecular switches that cycle between an active (GTP-bound) and an inactive (GDP-bound) state. This cycling is regulated by specific biological factors. Activation is governed by the activity of *GEFs*, which are guanine nucleotide exchange factors that convert GDP into GTP. In turn, *GAPs* stimulate the reverse transformation of GTP in GDP, thus regulating the GTPase inactivation (Ridley et al., 2003; Fritz and Pertz, 2016). Interestingly, a switching occurs also in the cellular space, because of the activity of Rho-specific guanine nucleotide dissociation inhibitors called *GDIs*, which prevent Rho GTPases to bind to the cell membrane. In particular, they bind to inactive GTPases, sequestering them in the cytosol and preventing their activation by GEFs (DerMardirossian and Bokoch, 2005; Boulter and Garcia-Mata, 2010; Garcia-Mata et al., 2011; Hodge and Ridley, 2016). Hence, inactive GTPases are found both on the membrane and in the cytosol, while active GTPases are generally present only at the cell membrane. A graphical summary is proposed in Figure 1.4(c). These biological features will be the starting point for the derivation of a mathematical model which will be presented in Chapter 2.

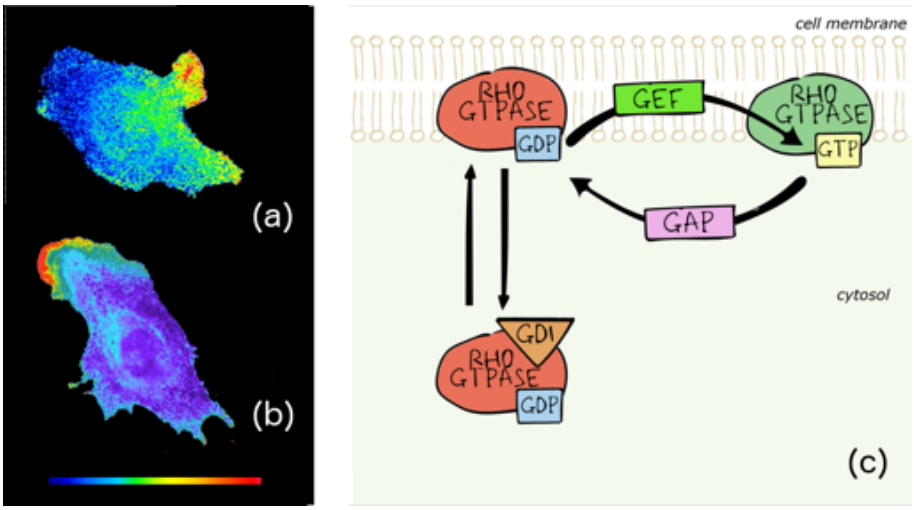

Figure 1.4: Rho GTPase activity localises in specific regions of the cell, as depicted and described in these images. (a) RhoA activity in a migrating HeLa cell from Nalbant et al. (2009); (b) A screenshot of Cdc42 activity in a MEF cell from a supplementary video attached to the paper by Machacek et al. (2009). In both these images, red colour indicates the highest activity level, blue colour the lowest level; (c) A schematic diagram: Rho GTPases cycle between an active (GTP-bound) and inactive (GDP-bound) form. Spatial movement between cell membrane and cytosol is regulated by the GDI action. *Figure (a) is republished with permission of American Society for Cell Biology, Copyright (2009); permission conveyed through Copyright Clearance Center, Inc. Figure (b) is adapted by permission from Springer Nature Customer Service Centre GmbH: Springer Nature, Copyright (2009).*

1.2 Mathematical modelling

When modelling interactions and reactions between proteins, one is often interested in studying the evolution of their corresponding concentrations. A typical approach relies on the derivation of a system of differential equations. If the interest is focused purely on the temporal evolution of a substance, ordinary differential equations are often used. This is well described in a useful (and very successful) review of different common scenarios of regulatory and signalling pathways in cells, published by Tyson et al. (2003). Classical kinetic reaction models are also briefly described in Appendix A.3 of this thesis.

On the other hand, when one is interested in studying concentrations in a broader environment, such as the cell, which is a spatially heterogeneous environment, systems of partial differential equations are often adopted (classical examples can be found in the textbooks by Murray (2003) and Edelstein-Keshet (2005)). These equations are often derived by physical laws as discussed in the following section.

1.2.1 Conservation laws

Conservation laws are broadly employed in modelling the spatio-temporal evolution of some biological quantities. Given a certain substance U, whose concentration in a domain

$\Omega \subset \mathbb{R}^d$ is described by a smooth function $u : \Omega \to \mathbb{R}$, the equation

$$\frac{\partial u}{\partial t}(\mathbf{x}, t) = -\nabla \cdot \mathbf{J}(\mathbf{x}, t, u) + f(\mathbf{x}, t, u), \qquad \mathbf{x} \in \Omega,\ t > 0, \tag{1.1}$$

follows from conservation laws. In words, if the substance U is subject to a flow $\mathbf{J}(\mathbf{x}, t, u)$ and the function $f(\mathbf{x}, t, u)$ describes its production (or depletion), then the temporal variation of u at a given point $\mathbf{x} \in \Omega$ is the sum of both spatial effects (in terms of the divergence of its flow $\mathbf{J}$) and local effects (described by the function f). Hence, if a model can be stated in this form, the main efforts are then directed in the identification of a proper expression for the flow $\mathbf{J}$ and the reaction function f. A common choice for purely diffusive substances, for example cytoplasmic proteins, is the use of the *Fick's law*:

$$\mathbf{J}(\mathbf{x}, t, u) = -D_u(\mathbf{x}, t, u)\nabla u(\mathbf{x}, t), \qquad \text{with } D_u > 0, \tag{1.2}$$

whose principle states that if the substance is heterogeneously distributed, i.e. if there is a nonzero gradient of u, then a flow is generated, and the substance U starts moving from regions with higher concentrations to regions with lower concentrations, proportionally to the gradient (Okubo and Levin, 2001). D_u is generally called the *diffusion coefficient* and in many biological situations, depending on the environment and substance properties, is assumed to be a positive constant (Milo and Phillips, 2015). If this is the case, then equation (1.1) takes the form

$$\frac{\partial u}{\partial t}(\mathbf{x}, t) = D_u \Delta u + f(\mathbf{x}, t, u), \qquad \mathbf{x} \in \Omega,\ t > 0, \tag{1.3}$$

which is the well-known reaction-diffusion equation. However one can consider also the following expression for the flow

$$\mathbf{J}(\mathbf{x}, t, u) = -D_u \nabla u(\mathbf{x}, t) + u(\mathbf{x}, t)\mathbf{v}(\mathbf{x}, t), \tag{1.4}$$

where D_u is a positive constant and $\mathbf{v} : \Omega \times [0, \infty) \to \mathbb{R}^2$ is a vector field describing a flow in which the substance is moving. This new expression adds the term $u\mathbf{v}$ to the Fick's part $-D_u \nabla u$, and it can be understood by thinking about some certain substance thrown into a river, which is both diffusing and subject to the river current. The equation (1.1) takes the form

$$\frac{\partial u}{\partial t}(\mathbf{x}, t) = D_u \Delta u - \nabla \cdot (u\mathbf{v}) + f(\mathbf{x}, t, u), \qquad \mathbf{x} \in \Omega, t > 0, \tag{1.5}$$

which is known as reaction-advection-diffusion equation.

As we will see, conservation laws constitute the starting point for the derivation of the mathematical models presented in this thesis. In the next section we will introduce another modelling idea which will be adopted in the discrimination between proteins confined in different cellular structures, such as the cell membrane and cytosol.

1.2.2 Protein compartmentalisation and the bulk-surface models

The plasma membrane of a cell does not only constitute its external boundary, but it is a very dynamic and crowded environment. It hosts a huge number of molecular activities and is responsible of many cellular processes such as signal and energy transduction, intercellular interactions, cell adhesions, regulation of intra- and extra-cellular transport. In many cases, some form of proteins live only on the membrane, for example receptor transmembrane proteins (Iwasa and Marshall, 2016). Therefore, when modelling biological processes involving membrane-bound proteins it could be necessary to consider this aspect by compartmentalising cytosolic and membrane-bound proteins. An elegant mathematical approach relies on the fact that the ratio between membrane thickness and cell diameter is around 1:500 (Milo and Phillips, 2015). This allows, with a reasonable good level of approximation, to describe the cell membrane with a two-dimensional closed surface Γ, which envelops a three-dimensional volume Ω, representing the cell interior. In this way, the concentration of membrane-bound proteins can be represented by a function $v : \Gamma \to \mathbb{R}$, whose spatial transport is restricted to solely tangential movements. On the other hand, cytosolic proteins are defined over the three-dimensional space $\overline{\Omega}$ and their concentration can be described as a function $u : \overline{\Omega} \to \mathbb{R}$. Since membrane-bound proteins are spatially confined over the cell membrane, interactions between the two forms u and v can only occur over the surface Γ (see also Figure 1.4). These can be included into the model through the boundary condition for the bulk component u and in a reaction function of the equation for v.

Coupled bulk-surface models are generally described by systems of differential equations representing bulk and surface interacting variables. Nowadays, this modelling approach is receiving an increasing attention by the mathematicians and modellers in general, as it easily finds applications in many different scientific areas. Cell biology is only one of the many (and several examples are given in Chapter 2) but, for example, coupled bulk-surface models have been used in modelling crystal growth (Kwon and Derby, 2001), surfactant dynamics (Fernández et al., 2016) and monument degradation due to marble sulphation

(Bonetti et al., 2019).

1.3 Research questions and thesis outline

Besides this introduction, the thesis is composed of three main and self-contained chapters, adequately supported by three appendixes, and a conclusive discussion. In this section we will introduce the research questions underpinning this thesis and the modelling ideas used during our investigation.

1.3.1 A coupled bulk-surface model for cell polarisation

As previously briefly introduced, when dealing with networks of biochemical reactions, one might end up with very complex mathematical models. In particular, this is surely the risk if one wants to model cell polarisation driven by Rho GTPase activity, since interactions between different GTPase types, which involve activations, inactivations, inhibitions, positive and negative feedbacks and spatial movements are many and intricate (Guilluy et al., 2011). Thus, a reasonable question is whether it is possible to model cell polarisation with manageable mathematical tools, which allow the analysis and understanding of the model. In order to answer this question, a necessary thinking path requires the identification of a minimal number of fundamental features shared by the GTPase proteins, with a consequent reduction of the number of mathematical variables and functions appearing in the equations. However, would this be helpful for a biologist? The identification of all the interactions between different GTPase forms is clearly a necessary step in the understanding of the signalling network pathways leading to cell polarisation. However are all these interactions equally important? Is there a predominant one? In a certain sense, potentially this modelling approach could provide a reading key of this complex network, which would help the biologists in the understanding of the main paths in the biochemical network.

Following these questions, in Chapter 2, a three-dimensional mathematical model describing cell polarisation is presented. The model generalises to a bulk-surface setting the well-known *wave pinning* model, which was initially proposed by Mori et al. (2008) as one of the simplest possible models for cell polarisation. Its derivation follows from the application of conservation laws and includes the spatial compartmentalisation, between cell membrane and cytosol, of two different forms of Rho GTPase protein. The result is a system composed of one surface reaction-diffusion equation and one bulk diffusion equation, coupled by the boundary condition for the bulk component. Two types of mathematical analysis are applied in order to describe the general behaviour of the model, and simula-

tions will be presented in order to show the polarisation process on different geometries. We remark that the main part of this chapter was published recently in Cusseddu et al. (2018).

1.3.2 Spatio-temporal dynamics of the keratin network in one dimension

The work introduced in the above section represents an example of qualitative mathematical model. However, the understanding of biological processes has always also required measurements, which express substances and observations in terms of real numbers. This is the aim of the paper by Moch et al. (2013), in which the authors measured the dynamics of the keratin cytoskeleton in resting cells, through experimental work and the support of image analysis and mathematical tools. However, a mathematical model was needed for completing the work on the assembly/disassembly cycle of the keratin network. Indeed, the benefits coming from a mathematical model relies in its ability to predict the dynamics of interest continuously in time, while experimental data represent a description at some given time points (which are often not so many). Hence, based on the same experimental measurements by Moch et al. (2013), Portet et al. (2015) proposed a mathematical model in the form of two reaction-diffusion equations with an advective term, resulting from a selection of different plausible scenarios. In this work, keratin material is considered in two forms (soluble and insoluble) and, since circular symmetry is a reasonable assumption in resting cells, the model is posed on a spatial interval. Curiously, the two approaches (the experimental one by Moch et al. (2013) and mathematical by Portet et al. (2015)) showed discrepancies in their results. Indeed, among 36 different scenarios proposed by Portet et al. (2015), the ones in which the data were used the most did not classify between the first positions of the model selection. How can this be explained?

This question will be addressed in Chapter 3. Indeed, following the discussions from Portet et al. (2015), we investigate the reasons of such discrepancy, by extending their mathematical model, but keeping the model in its original form (a system of two reaction-diffusion equations with an advective term). In our work we propose new modelling ideas and new biological assumptions on the experimental data in order to overcome the technical limitations affecting the measurements. As we will show, part of the biological relevance of our model relies in its ability to estimate the keratin spatio-temporal turnover dynamics during the network remodelling process. As well, our results support the biological model which was proposed by Windoffer et al. (2011).

This work is the direct result of a collaboration within the InCeM network. In par-

ticular, the biological assumptions on the experimental data are the result of different discussions with Reinhard Windoffer, Rudolf Leube and Nadieh Kuijpers from RWTH Aachen University.

1.3.3 A multidimensional model for the spatio-temporal dynamics of the keratin network

The assembly of the keratin network passes through different steps. Among these steps are nucleation of keratin particles from elementary subunits, integration of keratin filaments into the network and lateral association of keratin subunits into pre-existing filaments (Windoffer et al., 2011). In describing the assembly of the keratin filaments, the model proposed in Chapter 3 does not keep track of these different processes. In a sense, that approach is supported by the fact that separate experimental measurements for each single process are hard to obtain. Thus, one of the motivations for developing the work presented in Chapter 4 was the understanding of each one of the assembly steps. How can we identify the different phases characterising the network remodelling? In order to address this question, we categorise keratin material into three different forms (soluble, precursors, network) and introduce new kinetic functions. In this sense, Chapter 4 can be seen as a refinement of the work presented in Chapter 3.

A second fundamental question to be answered regards how polarisation and different cell shapes affect the keratin network remodelling and vice versa. As described in Section 1.1, this is particularly of interest in the context of cell migration, where the cell changes its shape and it is characterised by strong asymmetries (Kirfel and Herzog, 2004), like the polarisation response described in Chapter 2. In this case, the model proposed in Chapter 3 can not provide an answer, as it is only valid for resting cells. Hence, since circular symmetry assumption can no longer be applied, an extension to two- or three-dimensional spatial geometries is needed.

Finally, in Chapter 4 we present a second model for keratin spatio-temporal dynamics, which is characterised by a detailed description of the keratin processes and it is applicable in the case of different cell shapes. The presence of the nucleus is taken into account, constituting a hole inside the two- or three-dimensional domain. Boundary conditions are applied at the cell membrane and nucleus surface, and describe kinetic processes of the network remodelling. Lastly, we will present the numerical method used to solve the model which is based on the Streamline Upwind Petrov Galerkin method (Brooks and Hughes, 1982).

Also this work results from a collaboration within the InCeM network. In particular the biological assumptions of the model were discussed with Anne Pora, Nadieh Kuijpers, Reinhard Windoffer and Rudolf Leube from RWTH Aachen University.

In conclusion, in this section we have outlined the biological processes considered and analysed in the thesis. Recent studies prove evidence of existing connections between these processes and the next section is devoted to presenting these results.

1.4 The biological connections: keratins, GTPases and focal adhesions

The work of this thesis is devoted to the modelling of different cellular mechanisms involved in cell migration. Besides the ones outlined in Section 1.3, in Appendix C we include a modelling hint describing the evolution of the focal adhesions shape. From the biological point of view, the involvement of Rho GTPases, keratin dynamics and cell adhesions in cell migration was described throughout Section 1.1.

However legitimate questions might be on how cell polarisation and keratin filaments link together, what role have cell adhesions in the keratin dynamics or, more generally, which kind of links exist between the biological processes and structures considered in this thesis. These questions are currently a research subject for the biologists and, in particular, the role of keratin filaments in polarisation and cell migration is still not clear (see Section 1.1.3). Biological answers to these questions are then far from being exhaustive. However, as we will see, several studies have focused on the identification of the relationships between Rho GTPases, keratin network and cell adhesions. Therefore, this section is aimed at presenting these works, which highlight links between the different biological entities considered in this thesis.

It is known that cytoskeleton, GTPases and focal adhesions are strictly connected. In particular, Cdc42 and Rac are known to regulate actin polymerisation at the leading edge of the migrating cells. Rac and Rho are also involved in the regulation of the focal adhesions (Ridley et al., 2003; Sadok and Marshall, 2014). Activation of Rho is regulated by microtubules, that release GEF factors (Chang et al., 2008). Microtubules have also been shown to grow towards focal adhesions and establish a contact with them (Rafiq et al., 2018).

The role of intermediate filaments is, however, not so clear and this could possibly

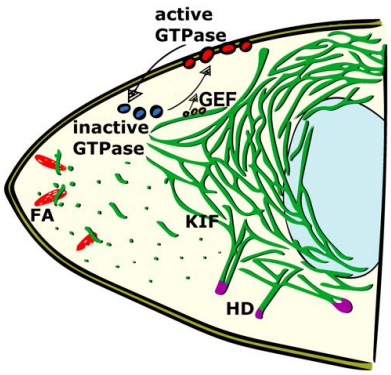

Figure 1.5: A sketched summary of biological connections (see Section 1.4): activation of Rho-GTPase is possible thanks to GEF factors. Solo is a GEF known to bind to keratin intermediate filaments (KIF) (Fujiwara et al., 2016). Focal adhesions (FAs) might be involved in the formation of keratin particles (Windoffer et al., 2006; Moch et al., 2016), which are filament precursors. The hemidesmosomes (HD) are anchoring points for the keratin cytoskeleton.

be due also to the differences between the IF type-specific properties. Keratin network remodelling is mediated by the actin system, which is believed to be the main player, responsible for the transport of these intermediate filaments (Kölsch et al., 2009; Moch et al., 2016), even though the biological mechanism is still poorly understood. Also a microtubule-mediated transport has been studied, but this accounts for a very small and negligible percentage of keratin particles (Liovic et al., 2003; Wöll et al., 2005). Despite the fact that *in vivo* experiments on epithelial cells show that the interaction between focal adhesions and keratin filaments is a transient and rare event (Leube et al., 2015), in the literature a spatial correlation between focal adhesions and nucleation of keratin filaments has been repeatedly noted and proposed (Windoffer et al., 2006, 2011; Moch et al., 2016).

Bordeleau et al. (2012) studied the effects of keratin filaments (constituted of K8/K18 keratins) on Rho GTPase activity and actin cytoskeleton. They show that, in hepatic epithelial cells, Rho GTPase activity is strongly influenced by the presence of keratin IFs. In particular, by comparing cells with an intact keratin cytoskeleton with keratin-lacking cells, it resulted that the expression of the protein Rho is much higher in the second case. However it also resulted that the Rho GTPase activity is much diminished in absence of keratin cytoskeleton, hence lack of keratin is suggested to damage Rho activation. Furthermore they analysed the actin cytoskeleton which, consistently with the results regarding Rho activity, it resulted altered in keratin-lacking cells.

Interestingly, on other cell lines, Fujiwara et al. (2016) identify a relationship between the same keratin filaments as in Bordeleau et al. (2012) (i.e. constituted of K8/K18 keratins) and *Solo*, which is a GEF targeting a Rho protein called RhoA. They suggest that Solo binds to keratin filaments through at least three binding sites and it is required for

the formation of a well organised keratin network. They also confirm that Rho activity is noticeably decreased in cells lacking keratin filaments. In particular, keratin suppression leads to a significant reduction of the number of force-induced actin stress fibres. In their study, Fujiwara et al. (2016) focused their attention in highlighting the interplay between Solo, RhoA, keratin cytoskeleton and actin fibres and its importance in the biomechanical cell response, which is fundamental for cell migration. On the other side, Jiu et al. (2017) studied interactions between intermediate filament and actin cytoskeletons in fibroblasts, where the IFs are constituted of *vimentin*, revealing how vimentin cytoskeleton mediates the assembly of actin stress fibres. In particular, the depletion of vimentin promotes the activity of RhoA through microtubule-associated GEFs, with the consequent increasing of the cell contractility.

In conclusion, in this section we have presented some results which are fundamental in describing the biological interconnections between the chapters of this thesis and give a bigger picture of these biological processes, which are also summarised in Figure 1.5. In the following sections we will introduce the notation and some standard results which will be used throughout the thesis.

1.5 Mathematical notation and background

For a better clarity in reading this thesis, in this section we first introduce the mathematical notation and definitions which will be used in the following chapters. Secondly, we present a summary of differential geometry elements, which are employed for the description of the spatio-temporal evolution of proteins at the cell membrane in Chapter 2.

1.5.1 Notation and definitions

We now briefly define some analysis concepts which will be used in this thesis. For more details we refer to the classical textbooks by Evans (2010) and Brezis (2010).

Definition 1.5.1 (Locally Lipschitz)**.** A function $\mathbf{f} : \mathbb{R}^d \to \mathbb{R}^n$ is said to be *locally Lipschitz* if it is Lipschitz for all compact subsets in $\mathbb{R}^d$, i.e. if $\forall\, K \subset \mathbb{R}^d$, K compact, there exists a constant $L = L(K)$ such that

$$\|\mathbf{f}(\mathbf{x}) - \mathbf{f}(\mathbf{y})\|_{\mathbb{R}^n} \leq L \|\mathbf{x} - \mathbf{y}\|_{\mathbb{R}^d}$$

for all $\mathbf{x}, \mathbf{y} \in K$.

Definition 1.5.2 (Locally integrable)**.** Let Ω be an open subset of $\mathbb{R}^d$ and $u : \Omega \to \mathbb{R}$ a Lebesgue measurable function. Hence, if for all compact subsets K of Ω

$$\int_K |u| \, \mathrm{d}\mathbf{x} < \infty,$$

then u is said to be *locally integrable*. The set of all locally integrable functions on Ω is defined:

$$L^1_{loc}(\Omega) := \big\{ u : \Omega \to \mathbb{R} \text{ such that } u \in L^1(K),\ \forall K \subseteq \Omega,\ K \text{ compact} \big\}.$$

Definition 1.5.3 (Weak derivative)**.** Let Ω be an open subset of $\mathbb{R}^d$, $u, v \in L^1_{loc}(\Omega)$ and $\boldsymbol{\alpha} = (\alpha_1, \ldots, \alpha_d)$ a multi index in $\mathbb{N}^d$ with $|\boldsymbol{\alpha}| = \sum_{j=1}^d \alpha_j$. If

$$\int_\Omega u D^{\boldsymbol{\alpha}} \varphi \, \mathrm{d}\mathbf{x} = (-1)^{|\boldsymbol{\alpha}|} \int_\Omega v\varphi \, \mathrm{d}\mathbf{x}, \qquad \forall \varphi \in C_0^\infty(\Omega),$$

then v is called $\boldsymbol{\alpha}$*-th weak derivative* of u and is written $D^{\boldsymbol{\alpha}} u = v$.

Definition 1.5.4 (Sobolev space)**.** For $1 \leq p \leq \infty$ and $k \in \mathbb{N}$, the space

$$W^k_p(\Omega) := \Big\{ u \in L^p(\Omega) \text{ such that } D^{\boldsymbol{\alpha}} u \in L^p(\Omega),\ \forall \boldsymbol{\alpha} \in \mathbb{N}^d,\ |\boldsymbol{\alpha}| \leq k \Big\}$$

is called *Sobolev space*. For $p = 2$ and $k = 1$ the Sobolev space is denoted by $H^1(\Omega)$.

Definition 1.5.5. Let X be a Banach space with norm $||\cdot||_X$. We will often consider the following space

$$L^2([0,T]; X) := \left\{ u : [0,T] \to X \text{ s.t. } \int_0^T ||u||_X^2 \, dt < \infty \right\},$$

which is known as the *Bochner space* (Roubíček, 2013).

1.5.2 Some elements of differential geometry

In this section we briefly introduce some elements of differential geometry which will be used in Chapter 2. For more details we refer to the work by Dziuk and Elliott (2013) or the textbook by Do Carmo (1976).

Definition 1.5.6. $\Gamma \subset \mathbb{R}^{d+1}$ is a C^k*-hypersurface* for $k \in \mathbb{N} \cup \{\infty\}$ if $\forall \mathbf{x_0} \in \Gamma$ there exists an open set $U \subset \mathbb{R}^{d+1}$ and a function $\phi : U \to \mathbb{R}$ such that:

- $\mathbf{x_0} \in U$,

- $\phi \in C^k(U)$ and $\nabla\phi(\mathbf{x}) \neq \mathbf{0}$ for $\mathbf{x} \in \Gamma \cap U$,
- $\Gamma \cap U = \{\mathbf{x} \in U \mid \phi(\mathbf{x}) = 0\}$.

Definition 1.5.7. The *tangent space* to a hypersurface Γ at a point $\mathbf{x} \in \Gamma$ is so defined:

$$T_{\mathbf{x}}\Gamma = \{\boldsymbol{\tau} \in \mathbb{R}^{d+1} \text{ such that } \exists \boldsymbol{\gamma} : (-\varepsilon, \varepsilon) \to \mathbb{R}^{d+1} \text{ differentiable, } \boldsymbol{\gamma}((-\varepsilon, \varepsilon)) \subset \Gamma, \\ \boldsymbol{\gamma}(0) = \mathbf{x} \text{ and } \boldsymbol{\gamma}'(0) = \boldsymbol{\tau}\}.$$

Remark 1.5.1. Since for $\boldsymbol{\tau} \in T_{\mathbf{x}}\Gamma$ the following holds

$$\nabla\phi(\mathbf{x}) \cdot \boldsymbol{\tau} = \nabla\phi(\boldsymbol{\gamma}(0)) \cdot \boldsymbol{\gamma}'(0) = \frac{\partial}{\partial\xi}\bigg|_{\xi=0} \phi(\boldsymbol{\gamma}(\xi)) = 0,$$

as $\phi(\mathbf{x}) = 0$, $\forall \mathbf{x} \in \Gamma$ and $\gamma(\xi) \in \Gamma$, $\forall \xi \in (-\varepsilon, \varepsilon)$, the tangent space to Γ at $\mathbf{x}$ is orthogonal to $\nabla\phi(\mathbf{x})$, so it can also been written as:

$$T_{\mathbf{x}}\Gamma = \{\boldsymbol{\tau} \in \mathbb{R}^{d+1} \mid \nabla\phi(\mathbf{x}) \cdot \boldsymbol{\tau} = 0\}.$$

For this reason we can write the orthogonal unit vectors $\boldsymbol{\nu}$ at $\mathbf{x} \in \Gamma$ as:

$$\boldsymbol{\nu}(\mathbf{x}) = \frac{\nabla\phi(\mathbf{x})}{|\nabla\phi(\mathbf{x})|} \quad \text{or} \quad \boldsymbol{\nu}(\mathbf{x}) = -\frac{\nabla\phi(\mathbf{x})}{|\nabla\phi(\mathbf{x})|}, \tag{1.6}$$

depending on the direction (outgoing or ingoing) with respect to the surface.

Definition 1.5.8. Consider $\mathbf{x} \in \Gamma$, where Γ is a C^1-hypersurface in $\mathbb{R}^{d+1}$ and let $f : \Gamma \to \mathbb{R}$ be a differentiable function at $\mathbf{x}$. The *tangential gradient* of f at $\mathbf{x}$ is defined as:

$$\nabla_\Gamma f(\mathbf{x}) := \nabla\bar{f}(\mathbf{x}) - \big(\nabla\bar{f}(\mathbf{x}) \cdot \boldsymbol{\nu}(\mathbf{x})\big)\boldsymbol{\nu}(\mathbf{x}), \tag{1.7}$$

where ∇ is the classical gradient and $\bar{f}$ a smooth extension of f to an $(d+1)$-dimensional neighbourhood U of Γ such that $\bar{f}(\mathbf{x}) = f(\mathbf{x})$ for every $\mathbf{x} \in \Gamma$.

Remark 1.5.2. From (1.7) with (1.6) it follows that $\nabla_\Gamma f(\mathbf{x}) \in T_{\mathbf{x}}\Gamma$.

For a better understanding of the following definition it is useful to write the i-th component of the tangential gradient:

$$\underline{D}_i f(\mathbf{x}) = D_i\bar{f}(\mathbf{x}) - \big(\nabla\bar{f}(\mathbf{x}) \cdot \boldsymbol{\nu}(\mathbf{x})\big)\nu_i(\mathbf{x}), \qquad i = 1, ..., d+1.$$

Definition 1.5.9. The *Laplace-Beltrami operator* is defined as the tangential divergence

of the tangential gradient, that is:

$$\Delta_\Gamma f(\mathbf{x}) := \nabla_\Gamma \cdot \nabla_\Gamma f(\mathbf{x}) = \sum_{i=1}^{d+1} \underline{D}_i \underline{D}_i f(\mathbf{x}). \tag{1.8}$$

We are now ready to present some useful results.

Theorem 1.5.1 (*Integration by parts*)**.** Let Γ be a hypersurface in $\mathbb{R}^{d+1}$ with smooth boundary $\partial\Gamma$. Let $\boldsymbol{\mu}$ be an orthogonal vector to $\partial\Gamma$ and tangent to Γ and f a function $C^1(\bar{\Gamma})$. Then

$$\int_\Gamma \nabla_\Gamma f \, \mathrm{d}s = \int_\Gamma f H \boldsymbol{\nu} \, \mathrm{d}s + \int_{\partial\Gamma} f \boldsymbol{\mu} \, \mathrm{d}S$$

where $H(\mathbf{x}) = \nabla_\Gamma \cdot \boldsymbol{\nu}(\mathbf{x})$ is the *mean curvature* of Γ in $\mathbf{x}$.

Theorem 1.5.2 (*Divergence theorem*)**.** Under the same hypothesis of Theorem 1.5.1, for every vector valued function $\boldsymbol{\xi} : \mathbb{R}^{d+1} \to \mathbb{R}^{d+1}$ the following holds:

$$\int_\Gamma \nabla_\Gamma \cdot \boldsymbol{\xi} \, \mathrm{d}s = \int_\Gamma \boldsymbol{\xi} \cdot \boldsymbol{\nu} H \, \mathrm{d}s + \int_{\partial\Gamma} \boldsymbol{\xi} \cdot \boldsymbol{\mu} \, \mathrm{d}S.$$

Using this last theorem, one can easily prove:

Theorem 1.5.3 (*Green's formula*)**.** Under the same hypothesis of Theorem (1.5.1), for every function $g \in C^2(\bar{\Gamma})$ the following result holds:

$$\int_\Gamma \nabla_\Gamma f \cdot \nabla_\Gamma g \;\; \mathrm{d}s = -\int_\Gamma f \Delta_\Gamma g \, \mathrm{d}s + \int_{\partial\Gamma} f \nabla_\Gamma g \cdot \boldsymbol{\mu} \, \mathrm{d}S. \tag{1.9}$$

In particular, it is immediate to prove the following.

Corollary 1.5.1. If $\partial\Gamma = \emptyset$, from (1.9) it follows that

$$\int_\Gamma \Delta_\Gamma g \, \mathrm{d}s = 0$$

for every function $g \in C^2(\Gamma)$.

Proof. Consider $f = 1$ in Theorem 1.5.3. □

1.5.3 Numerical methods and simulations

The mathematical models presented in Chapter 2 and 4 are numerically solved by using finite element methods, which are explained in detail in each chapter. We have implemented these methods by developing a code in Python 2.7, with the support of FEniCS, which is an

open source finite element software package for solving partial differential equations (Alnæs et al., 2015). In the thesis, the models are tested on different geometries. The simplest ones, with the corresponding meshes, were created using the FEniCS mesh generator *mshr* (Alnæs et al., 2015), while the software Gmsh (Geuzaine and Remacle, 2009) has been used for more complex geometries.

Chapter 2

A coupled bulk-surface model for cell polarisation

2.1 Introduction

Cell polarity is a complex process by which cells lose symmetry. However, its precise definition is still not clear (Frankel, 2018). Polarity appears in single-cell organisms and multi-cell tissues. Many common basic polarisation mechanisms are shared and adapted by many different kinds of cells (Nelson, 2003). Roughly speaking, by breaking symmetry, cells define their front and rear and this process is characterised and driven by molecular chemical processes. Cell polarity is mediated and coordinated by a huge number of molecules and proteins and their interactions (Drubin and Nelson, 1996; Guilluy et al., 2011). The polarisation process, which can be caused by some external stimuli or can be spontaneous (Andrew and Insall, 2007; Graessl et al., 2017), is necessary for many cellular activities, such as morphogenesis, and directed cell migration (Ladoux et al., 2016; St Johnston and Ahringer, 2010). Studies have identified the main drivers of this phenomenon in the Rho family small guanosine triphosphate (GTP)-binding proteins (Rho GTPases). They behave like molecular switches, cycling between active (GTP-bound) and inactive forms (GDP-bound). Activation and inactivation are regulated by guanine nucleotide exchange factors (GEFs) and GTPase-activating proteins (GAPs). Moreover, the inactive Rho GTPases are sequestered in the cytosol by guanine nucleotide dissociation inhibitors (GDIs), that prevent the association of Rho GTPases with the plasma membrane (DerMardirossian and Bokoch, 2005; Hodge and Ridley, 2016). Among the Rho GTPase family, RhoA, Rac and Cdc42 are the most well known representatives in initiating the polarisation of migrating cells (Etienne-Manneville, 2008; Ridley et al., 2003; Sadok and

Marshall, 2014). During cell migration, Rac and Cdc42 tend to concentrate their activities at the front, controlling the protrusive actin network, while RhoA is mostly active at the rear and regulates large focal adhesions and stress fibres (Mayor and Carmona-Fontaine, 2010; Ohashi et al., 2017). Microtubules and intermediate filaments are also involved in the process, for example binding the RhoA-effectors GEF-H1 and Solo (Chang et al., 2008; Fujiwara et al., 2016).

In recent years, Rho GTPases and cell polarisation have attracted the attention of many modellers (Goryachev and Leda, 2017; Rappel and Edelstein-Keshet, 2017). Marée et al. (2006) were able to simulate polarisation on a two-dimensional domain, in which the crosstalk between RhoA, Rac and Cdc42 in their active and inactive forms could generate the expected patterns. However, despite the fact that good computational results were obtained, a rigorous mathematical analysis of the biochemical system comprising six partial differential equations (PDEs), remained out of reach (Edelstein-Keshet et al., 2013), until two years later, when Mori et al. (2008) proposed a significant mathematical simplification of this modelling framework for cell polarisation, which became very popular and can be considered as the starting point of our study. The work in Mori et al. (2008) focused on a conceptual minimal model of a single Rho GTPase and its switch between active and inactive forms, in which activation was supported by a positive feedback of the active GTPase in its own activation (see Figure 2.1 for a schematic representation). Their model consisted of the following pair of reaction-diffusion equations posed on a one

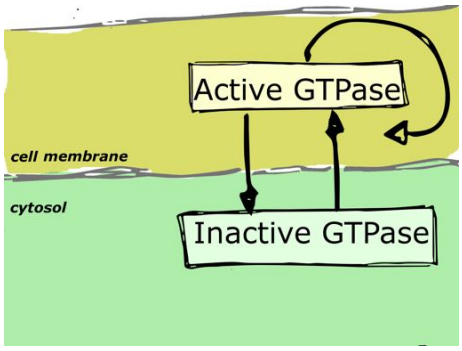

Figure 2.1: The minimal GTPase circuit with positive feedback for the activation (Mori et al., 2008; Altschuler et al., 2008). Active GTPase is bounded to the membrane, while inactive GTPase has also a cytosolic form.

dimensional domain

$$\frac{\partial a}{\partial t} = D_a \frac{\partial^2 a}{\partial^2 x} + f(a,b), \qquad x \in (0,L),\ t > 0, \tag{2.1}$$

$$\frac{\partial b}{\partial t} = D_b \frac{\partial^2 b}{\partial^2 x} - f(a,b), \qquad x \in (0,L),\ t > 0, \tag{2.2}$$

with

$$f(a,b) = \Big(k_0 + \frac{\gamma a^2}{K^2 + a^2}\Big)b - \beta a, \tag{2.3}$$

and boundary conditions

$$\frac{\partial a}{\partial x} = \frac{\partial b}{\partial x} = 0, \qquad\qquad x = 0, L,\ t > 0, \tag{2.4}$$

where $a(x,t)$ and $b(x,t)$ denote the active and inactive forms, respectively. Here, k_0 represents the basal rate of activation and β is the rate of inactivation. The maximal rate for the positive feedback is indicated by γ and K is the parameter representing the quantity of a needed to achieve a feedback-induced activation rate of $\gamma/2$ in the reaction.

The mathematical model was based on three key properties: (1) a large difference in diffusivities between active and inactive forms ($D_a/D_b \ll 1$); (2) conservation in time of the total mass $\int_0^L (a+b)dx$; and (3) bistability in the reaction term $f(a,b)$ with respect to a. Bistable reaction-diffusion equations are known to produce travelling waves for certain initial conditions (Fife and McLeod, 1977). In this work (Mori et al., 2008), a local narrow peak of active GTPase was able to generate a travelling wave of active GTPase which is eventually stopped due to the interplay with the inactive GTPase, where conservation of total mass and fast cytosolic diffusion were key ingredients. An asymptotic analysis of the model, known as wave pinning (WP) phenomena, was later carried out in Mori et al. (2011).

Over the years, the need for a mathematical understanding of cell polarity led to the reduction of different mathematical models of polarisation to minimal conceptual models, revealing different underlying mechanisms, not necessarily based on wave pinning. Some of them, however, share common features, for example positive feedback is still the key to achieve cell polarity in the work by Altschuler et al. (2008), in which a system composed of one ordinary and one partial differential equation (ODE-PDE system) and one stochastic model are proposed for the interactions between an active and inactive GTPase component. Reaction-diffusion systems have also been used by Otsuji et al. (2007). They derive conceptual models of two components based on mass conservation and difference in diffusivity, which they show to be fundamental properties to achieve polarisation. In addition, Goryachev and Pokhilko (2008) proposed a reaction-diffusion model for Cdc42 clustering in budding yeast, which was based on the Turing pattern formation mechanism. In Jilkine and Edelstein-Keshet (2011) and Edelstein-Keshet et al. (2013) some of these models are described and compared.

An important biological aspect of cell polarisation is the compartmentalisation of the membrane-bound and cytosolic proteins, which has inspired several works: Novak et al. (2007) presented a computational approach for three-dimensional modelling of Rac proteins cycling between cell membrane and cytosol, using reaction-diffusion equations. In a more recent paper, (Xu and Jilkine, 2018), a one-dimensional model for Cdc42 and its GEFs in budding yeast is proposed. The cytosolic components purely diffuse over the line domain while slow membrane diffusion motivates the use of ordinary differential equations (ODEs) to model the membrane-bound species at the two ends. Interactions between the two occur through the flux conditions of the cytosolic components and the ODE reactions. A three-dimensional bulk-surface model showing Turing pattern formation is proposed in Rätz and Röger (2014). The GDI-bound inactive GTPase diffuses freely in the cell interior (the bulk) and, through an appropriate coupling boundary condition, it binds to the cell membrane (surface of the domain), on which its membrane-bound counterpart interacts with the active form. These latter two species were both modelled by reaction-diffusion equations. Another three-dimensional bulk-surface model is also proposed by Spill et al. (2016). This model is more detailed as all the three GTPases Cdc42, Rac, RhoA (in the cytosolic, membrane-bound active and membrane-bound inactive forms) and phosphatidylinositols (PIPs) are taken into account. The model results in a system of twelve reaction-diffusion equations.

The wave pinning model has seen its bulk-surface extension in two works (Ramirez et al., 2015; Giese et al., 2015) and more recently in Diegmiller et al. (2018). The first one by Ramirez et al. (2015) adapts the WP model to GTPases in dendritic spines in neurons. The cytosolic GTPase is assumed spatially homogeneous, while the membrane-bound active form is subject to a surface reaction-diffusion equation. The interesting result is that the pinning mechanism can be induced only by the geometry of the domain: the smaller the neck of the spine, the easier is the confinement of the active GTPase. Confinement is also facilitated by higher diffusion, which however is in contrast with other models for cell polarisation based on slow membrane diffusivity. The second work, by Giese et al. (2015), presents a natural extension of the wave pinning model in the bulk-surface setting (see the following equations (2.15)-(2.17)), where the molecular interactions between the bulk and surface chemical components are mediated through an appropriate coupling boundary condition on the surface. In their work they investigate the role of shape, internal organelles and inhomogeneities in polarisation processes. Diegmiller et al. (2018) have recently presented a three-dimensional analysis of the steady state of the wave

pinning model in the bulk-surface setting on a sphere. They were able to show pattern formation in the surface component, after having shown analytically that spatial variation of the bulk component is negligible.

Inspired by these previous works, we study the extension of the wave pinning model in more general three-dimensional stationary convex and non-convex domains. Indeed in the work by Ramirez et al. (2015) the geometry naturally reduces the model to a single one-dimensional reaction-diffusion equation and the cytosolic component is assumed constant, while in Giese et al. (2015) the results are entirely two-dimensional. Finally the work by Diegmiller et al. (2018) reveals very important insights, however it is restricted to a sphere and indeed spherical symmetry is very conveniently used. The novelty of our work lies in that we mathematically quantify the role of the three-dimensional geometry in the wave pinning process, yielding new insights into this minimal model for wave pinning. For simplicity throughout the paper, we will refer to the reformulated WP model as the bulk-surface wave pinning (BSWP) model. Our work was recently published by the Journal of Theoretical Biology (Cusseddu et al., 2018). In this chapter we report it with a higher level of details and new results obtained post-publication are also included.

We present new three-dimensional results on regular and irregular geometries, exhibiting the wave pinning process on complex domains. A key part of our study involves the numerical simulation of the BSWP model in three-dimensional geometries using a recently developed bulk-surface finite element method (BS-FEM) (Dziuk and Elliott, 2013; Elliott and Ranner, 2013; MacDonald et al., 2016a; Madzvamuse and Chung, 2016a,b; Madzvamuse et al., 2015). This numerical framework allows to compute the solutions of the BSWP model on complex convex and non-convex geometries.

To put into context our computational framework with respect to the current-state-of-the-art, throughout this paper we confirm previous works based on the wave pinning model (2.1)-(2.3) and show analogies with our results. For example, we show the evolution of the solutions of the model at very large times which display interesting spatial effects. Our results reveal that certain geometries induce a metastable behaviour of the model, in which the apparently stable active patch undergoes a very slow shifting on the surface towards more rounded areas of the domain. This was also shown in previous published results for the two-dimensional wave pinning model presented by Vanderlei et al. (2011). In addition, the BSWP model shows competition between active regions, as recently shown in the classical WP model (Chiou et al., 2018). We also show how the geometry of the domain plays a crucial role in the pattern formation for the special case of spatial homogeneous initial

conditions. This was interestingly reported in the two-dimensional case by Giese et al. (2015). Hence, our work through mathematical and numerical analysis, aims to extend the current knowledge of the wave pinning model to realistic three-dimensional settings and to provide some understanding of the influence of the geometry on the polarisation mechanism.

The structure of this chapter is therefore as follows: In Section 2.2 the model is derived and presented in its complete form together with the parameters. Existence and uniqueness of the solution is proved in Section 2.3, whereas its fundamental properties are shown and discussed in Section 2.4. A nondimensional version of the BSWP model is obtained in Section 2.6, which is later used to explain the polarisation mechanism in Section 2.7 by applying an asymptotic analysis on a simple geometry. In Section 2.8 we present the parameter regions for bistability and polarisation. Analysis of the steady states for the well-mixed system provide a bistability region, whereas spatial effects were studied using the local perturbation analysis (LPA) (Holmes, 2014; Holmes et al., 2015). This latter tool is able to identify parameter spaces in which a local and narrow perturbation of the spatially homogeneous slow-diffusing component can generate spatial effects on the system. In our work we present a novel application of the LPA in a bulk-surface setting, which provides a natural way to investigate the effect of the ratio between surface area and bulk volume on the system. In Section 2.9 we present the bulk-surface finite element method (BS-FEM) (MacDonald et al., 2016a; Madzvamuse and Chung, 2016b), used to simulate the model on various geometries. Numerical results are then presented in Section 2.10 to confirm and validate theoretical findings. These also highlight the importance of the geometry on the model evolution, which suggested a new series of simulations on more complex domains presented in the following section 2.11.

A summary of the main results and a discussion follow in Section 2.13, with suggestions on future extensions and applications of the BSWP model.

2.2 Derivation of the bulk-surface wave pinning model

The model is derived for a single stationary cell (studies on migrating cells are deferred to future work) whose shape is described by a smooth closed surface $\Gamma \subset \mathbb{R}^3$, hence with no boundary, which encloses a bulk geometry $\Omega \subset \mathbb{R}^3$ such that $\Gamma = \partial\Omega$. In biological terms, Γ represents the cell membrane and Ω the cell interior. The considered time interval is $[0, T]$ for a given constant $T > 0$. In the next sections we will derive the model equations for the two forms of proteins and discuss the kinetics coupling them.

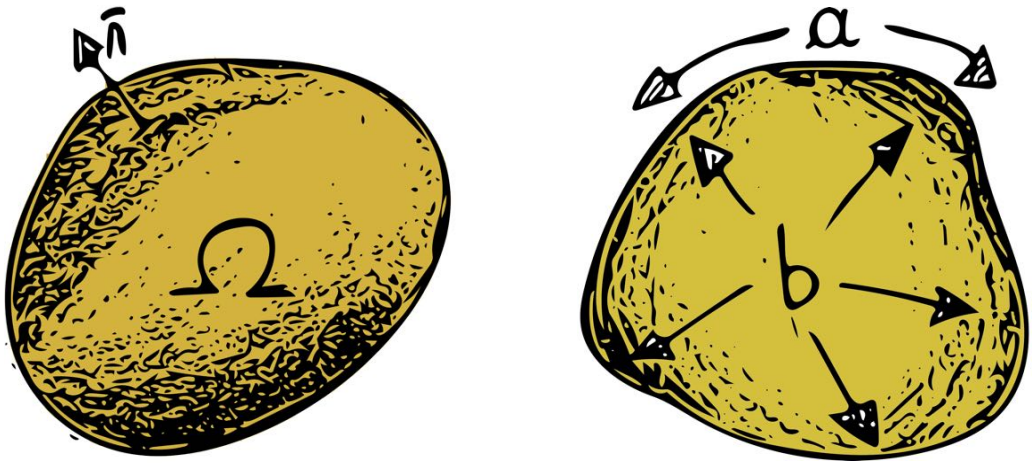

(a) **(b)**

Figure 2.2: (a) A three-dimensional domain Ω representing the cell. (b) Activation of the bulk species occurs through the boundary conditions and propagates over the surface Γ of the domain.

We recall that even if GTPases tend to stay on the cell membrane, it is possible to observe them in the cytosol, binded to GDI proteins. In particular, GDIs bind predominantly inactive GTPases, sequestering them in the cytosol (Hodge and Ridley, 2016). In turn, active GTPases are very rare in the cytosol, therefore in the cell interior we will only consider the presence of inactive species.

2.2.1 Bulk component

Let us first focus only on protein distribution in the cell interior and let

$$b : \bar{\Omega} \times [0,T] \to \mathbb{R} \tag{2.5}$$

represent the concentration of the inactive GTPase, measured in mol μm^{-3}. In the following we will always suppose $b \in C(\overline{\Omega} \times [0,T]) \cap C^{2,1}(\Omega \times (0,T]) \cap C^{1,0}(\overline{\Omega} \times (0,T])$, where $C^{k,h}$ indicates the set of functions k times continuously differentiable in space and h times in time. Let us now consider V as an arbitrary subset of Ω. If we assume there is no intracellular production of GTPase, by the conservation law the variation of b in the region V is equal to the net flow rate crossing the boundary ∂V, represented by the flux $\mathbf{j}_b : \Omega \times [0,T] \to \mathbb{R}^3$. This can be expressed in mathematical terms as follows:

$$\frac{d}{dt}\int_V b \, \mathrm{d}\mathbf{x} = -\int_{\partial V} \mathbf{j}_b \cdot \mathbf{n}_V \, \mathrm{d}s, \tag{2.6}$$

where $\mathbf{n}_V : \partial V \to \mathbb{R}^3$ is the outgoing orthogonal unit vector to ∂V at each point. Taking the temporal derivative inside the integral and using the divergence theorem on the right

hand side term we obtain:

$$\int_V \frac{\partial b}{\partial t}\, \mathrm{d}\mathbf{x} = -\int_V \nabla \cdot \mathbf{j}_b \, \mathrm{d}\mathbf{x}. \tag{2.7}$$

Given the arbitrarity of the domain V, from the previous equation we deduce

$$\frac{\partial b}{\partial t} = -\nabla \cdot \mathbf{j}_b, \qquad \forall \mathbf{x} \in \Omega. \tag{2.8}$$

As a final step, we use the *Fick's law* to describe the flow $\mathbf{j}_b$ (see Section 1.2.1), so that

$$\mathbf{j}_b = -D_b \nabla b. \tag{2.9}$$

If we then assume the coefficient D_b to be constant in time over Ω, we finally obtain:

$$\frac{\partial b}{\partial t} = D_b \Delta b, \qquad \mathbf{x} \in \Omega, \tag{2.10}$$

where the constant D_b represents the diffusion coefficient and has unit dimension $\mu\mathrm{m}^2\ \mathrm{s}^{-1}$.

We then impose a flux boundary condition:

$$-D_b \mathbf{n} \cdot \nabla b = q, \qquad \text{on } \Gamma, \tag{2.11}$$

where $\mathbf{n}$ is now the outgoing orthogonal unit vector to Γ and $q : \Gamma \to \mathbb{R}$ is the net outgoing flux of b at the cell membrane. We will model q in the next sections, taking into account the basic activation/inactivation mechanism for GTPase proteins.

2.2.2 Surface component

In the previous section we have derived the equation for spatio-temporal distribution of the inactive GTPase in the interior of the cell. Here we want to do the same for the active form on the closed surface Γ, whose concentration, in mol $\mu\mathrm{m}^{-2}$, is defined by the function

$$a : \Gamma \times [0, T] \to \mathbb{R}, \tag{2.12}$$

assumed to belong to $C(\Gamma \times [0, T]) \cap C^{2,1}(\Gamma \times (0, T])$. As in the previous section we will start from a conservation law and use some general concepts from differential geometry of curves and surfaces, summarised in Section 1.5.2 of the introduction of this thesis. Let us consider an arbitrary portion S of the surface Γ. Then the variation of the concentration in S is given by the difference between the amount of internal production of a, represented

by a function f, that we assume to depend on both a and b, and the amount of outgoing proteins, subject to a flux $\mathbf{j}_a : \Gamma \times [0,T] \to \mathbb{R}^3$. In mathematical terms this is written as

$$\frac{d}{dt}\int_S a \, \mathrm{d}s = -\int_{\partial S} \mathbf{j}_a \cdot \boldsymbol{\mu}_S \, \mathrm{d}S + \int_S f(a,b) \, \mathrm{d}s, \tag{2.13}$$

where $\boldsymbol{\mu}_S : \partial S \to \mathbb{R}^3$ is the outgoing orthogonal unit vector to ∂S tangent to S. As the normal component of the flux to Γ is cancelled by the dot product, we can consider the flux $\mathbf{j}_a$ to be just a tangent vector to Γ. The divergence theorem on surfaces (Theorem 1.5.2, Section 1.5.2) applied to the first term of the right hand side of (2.13) states:

$$-\int_{\partial S} \mathbf{j}_a \cdot \boldsymbol{\mu}_S \, \mathrm{d}s = -\int_S \nabla_\Gamma \cdot \mathbf{j}_a \, \mathrm{d}s - \int_S \mathbf{j}_a \cdot \boldsymbol{\nu}_S H \, \mathrm{d}s,$$

where ∇_Γ is the tangential gradient (see (1.7) in Section 1.5.2), $\boldsymbol{\nu}_S : S \to \mathbb{R}^3$ is the outgoing orthogonal unit vector to S and $H = \nabla_\Gamma \cdot \nu$ is the mean curvature of Γ. As we are considering only tangential fluxes to Γ, $\mathbf{j}_a \cdot \boldsymbol{\nu}_S = 0$, and from (2.13), taking the derivative inside the integral, we have

$$\int_S \frac{\partial a}{\partial t} \, \mathrm{d}s = -\int_S \Big(\nabla_\Gamma \cdot \mathbf{j}_a - f(a,b) \Big) \, \mathrm{d}s.$$

Given that S is an arbitrary domain, the above yields:

$$\frac{\partial a}{\partial t} = -\nabla_\Gamma \cdot \mathbf{j}_a + f(a,b), \qquad \mathbf{x} \in \Gamma.$$

We use Fick's law to model the flow as described in Section 1.2.1. In this case, however, as we are considering the flow to be tangent to Γ, we need to take the tangential component of the gradient of a, which means

$$\mathbf{j}_a = -D_a \nabla_\Gamma a.$$

We assume the diffusivity parameter D_a to be constant with unit dimension of $\mu\mathrm{m}^2 \ \mathrm{s}^{-1}$. We finally obtain the following reaction-diffusion equation for a on Γ:

$$\frac{\partial a}{\partial t} = D_a \Delta_\Gamma a + f(a,b), \qquad \mathbf{x} \in \Gamma. \tag{2.14}$$

The Laplace-Beltrami operator Δ_Γ is defined in (1.8), Section 1.5.2. Lastly, it is clear that since the curve Γ has no boundary, as itself is the boundary of a domain, no boundary conditions for a are required.

2.2.3 Kinetics: the GTPase cycle

We first simplify the interconversion between a and b (protein activation and inactivation) on the cell membrane with a very simple chemical reaction represented by the following scheme:

$$B \underset{k_{ab}}{\overset{k_{ba}}{\rightleftarrows}} A,$$

where k_{ab} and k_{ba} are kinetic parameters associated to the velocity of the reaction. In order to derive some kinetic equations we make use of the *Law of mass action*, which states that the rate of a reaction is directly proportional to the concentration of its reagents, see also Appendix A.3. Hence, the kinetic evolution of a is described by the following ordinary differential equation:

$$\frac{\partial a}{\partial t} = k_{ba} b - k_{ab} a.$$

Furthermore, as we explained in the introduction of this chapter, the active GTPase induces an increasing of GEF activity. Recalling that GEFs are factors that enhance the activation of proteins, this reaction is so described:

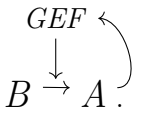

In a sense, the positive feedback can be simplified stating that the active form of the protein promotes its own production. Therefore, it follows the complete kinetic diagram

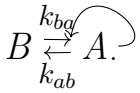

The GTPase "self-activation" can be seen as a type of *cooperative kinetic reaction*, reactions generally described by the Hill function, see Appendix A.3 for more details. In short, still referring to the Appendix A.3, a can be seen as the active substrate in the production of other a. Defining $k_{ba} = \omega k_0$ and $k_{ab} = \beta$, with k_0 and β having unit dimension s^{-1} and ω unit dimension μm, this new reaction is incorporated into the previous ODE as follows:

$$\frac{da}{dt} = \omega \left(k_0 + \frac{\gamma a^n}{K^n + a^n} \right) b - \beta a,$$

where $\frac{\gamma a^n}{K^n + a^n}$ is the Hill function of exponent $n > 1$. Following Rätz and Röger (2012) we have introduced the parameter $\omega := |\Omega|/|\Gamma|$ which is the ratio between bulk volume and

surface area; it characterises the geometric effects in the reaction function and can be seen as a parameter describing the protein *binding* to the cell membrane. The unit dimension of ω is needed to reduce the dimensionality of the bulk protein to the two-dimensional surface, where activation occurs. For a fixed volume, ω is maximal when Ω is spherical, so activation is enhanced in resting cells which generally have, at least in two-dimensions, a rounded shape (Kozlov and Mogilner, 2007). Hence, we define the kinetic function $f(a,b)$ of eq. (2.14) as

$$f(a,b) := \omega\left(k_0 + \frac{\gamma a^n}{K^n + a^n}\right) b - \beta a.$$

As in Mori et al. (2008) we set the Hill coefficient $n = 2$. It must be noted that other choices for $n > 1$ have been studied (Holmes and Edelstein-Keshet, 2016; Diegmiller et al., 2018).

On the other side, since no kinetics occur in the interior of the cell, where the only bulk component b is present, one key property of the model is that the reactions for the bulk species are directly incorporated into the boundary condition (2.11). Indeed, we describe the outgoing flux $q = q(a,b)$ of b at the cell membrane as the variation of the bulk component due to activation and inactivation of the GTPase at the cell membrane, i.e.

$$-D_b \mathbf{n} \cdot \nabla b = f(a,b).$$

We are now ready to present the complete spatio-temporal model in the next section. We will later show in Section 2.4 that with the GTPase kinetics incorporated in the boundary condition for b, the spatio-temporal model still preserves the total amount of a and b.

2.2.4 The bulk-surface wave pinning (BSWP) model

As a result of the previous sections, the bulk-surface wave pinning model reads

$$\frac{\partial b}{\partial t} = D_b \Delta b, \qquad \mathbf{x} \in \Omega,\ t \in (0,T], \tag{2.15}$$

$$-D_b(\mathbf{n} \cdot \nabla b) = f(a,b), \qquad \mathbf{x} \in \Gamma,\ t \in (0,T], \tag{2.16}$$

$$\frac{\partial a}{\partial t} = D_a \Delta_\Gamma a + f(a,b), \qquad \mathbf{x} \in \Gamma,\ t \in (0,T], \tag{2.17}$$

with reaction function

$$f(a,b) = \omega\Big(k_0 + \frac{\gamma a^2}{K^2 + a^2}\Big) b - \beta a, \tag{2.18}$$

Param.	Value/Unit	Description
a	mol μm^{-2}	concentration of active GTPase
b	mol μm^{-3}	concentration of inactive GTPase
D_a	0.1 μm^2 s^{-1}	diffusion coefficient of a
D_b	10 μm^2 s^{-1}	diffusion coefficient of b
k_0	0.067 s^{-1}	basal activation rate
β	1 s^{-1}	deactivation rate
γ	1 s^{-1}	feedback activation rate
K	1 mol μm^{-2}	saturation parameter
n	2	Hill coefficient
ω	μm	volume to surface ratio membrane binding parameter

Table 2.1: Parameters used in the bulk-surface model; the diffusion coefficients are taken as in Postma et al. (2004), and the kinetic parameter values as in Mori et al. (2008).

coupled with initial conditions

$$b(\mathbf{x},0) = b_{in}(\mathbf{x}), \qquad \mathbf{x} \in \Omega, \tag{2.19}$$

$$a(\mathbf{x},0) = a_{in}(\mathbf{x}), \qquad \mathbf{x} \in \Gamma, \tag{2.20}$$

where $b \in C(\overline{\Omega}\times[0,T]) \cap C^{2,1}(\Omega\times(0,T]) \cap C^{1,0}(\overline{\Omega}\times(0,T])$ and $a \in C(\Gamma\times[0,T]) \cap C^{2,1}(\Gamma\times(0,T])$. All the parameters are listed in Table 2.1.

2.3 Existence and uniqueness of the solution to the BSWP model

The existence and uniqueness of classical solutions to general bulk-surface systems of arbitrary number of reaction-diffusion equations was proved by Sharma and Morgan (2016). For convenience the two components version of their result (one on the surface and one in the bulk) is stated in the following.

Theorem 2.3.1. (Sharma and Morgan, 2016) Let $\Omega \subset \mathbb{R}^d$ $(d \geq 2)$ be a bounded domain with a smooth boundary $\partial\Omega = \Gamma$ of class $C^{2+\lambda}$ with $\lambda > 0$. We consider the system

$$\frac{\partial u}{\partial t} = D_\Omega \Delta u + H(u), \qquad \mathbf{x} \in \Omega, t \in (0,T), \tag{2.21}$$

$$\frac{\partial v}{\partial t} = D_\Gamma \Delta_\Gamma v + F(u,v), \qquad \mathbf{x} \in \Gamma, t \in (0,T), \tag{2.22}$$

$$D_\Omega \nabla u \cdot \mathbf{n} = G(u,v), \qquad \mathbf{x} \in \Gamma, t \in (0,T), \tag{2.23}$$

$$u = u_0 \geq 0, \qquad \mathbf{x} \in \Omega, t = 0, \tag{2.24}$$

$$v = v_0 \geq 0, \qquad \mathbf{x} \in \Gamma, t = 0, \tag{2.25}$$

with $D_\Omega, D_\Gamma > 0$, the functions $H : \mathbb{R} \to \mathbb{R}$, $F, G : \mathbb{R} \times \mathbb{R} \to \mathbb{R}$ are locally Lipschitz (Definition 1.5.1) and satisfy the *quasi-positivity condition*:

$$H(0) \geq 0, \tag{2.26}$$

$$F(x, 0) \geq 0, \qquad \forall x > 0, \tag{2.27}$$

$$G(0, y) \geq 0, \qquad \forall y > 0. \tag{2.28}$$

Let the initial conditions (2.24)-(2.25) satisfy

$$u_0 \in W_p^2(\Omega), \qquad v_0 \in W_p^2(\Gamma), \qquad p > d, \tag{2.29}$$

$$D_\Omega \nabla u_0 \cdot \mathbf{n} = G(u_0, v_0), \qquad \mathbf{x} \in \Gamma \qquad (\textit{compatibility condition}). \tag{2.30}$$

Furthermore, if the following conditions hold: $\forall x, y \geq 0$

$$\exists \alpha, \beta, \gamma > 0 \ : \ \gamma F(x, y) + G(x, y) \leq \alpha(x + y + 1) \text{ and } H(x) \leq \beta(x + 1), \tag{2.31}$$

$$\exists K_G > 0 \ : \ G(x, y) \leq K_g(x + y + 1), \tag{2.32}$$

$$\exists l \in \mathbb{N} \text{ and } K_F > 0 \ : \ F(x, y) \leq K_F(x + y + 1)^l, \tag{2.33}$$

then the system admits a unique non negative global solution (u, v).

Proof. See (Sharma and Morgan, 2016). □

We recall (u, v) is said to be a solution of (2.21)-(2.25) if and only if $u \in C(\overline{\Omega} \times [0, T)]) \cap C^{1,0}(\overline{\Omega} \times (0, T)) \cap C^{2,1}(\Omega \times (0, T))$ and $v \in C(\Gamma \times [0, T)]) \cap C^{2,1}(\Gamma \times (0, T))$ satisfy the equations of the system. $C^{k,h}$ is the notation used to indicate the set constituted of all the functions which are k times differentiable in $\mathbf{x}$ and h times in t and W_p^k is the Sobolev space (see Definition 1.5.4, Section 1.5.1).

Using this result, we are able to prove the following theorem regarding the bulk-surface wave pinning model (2.15)-(2.18).

Theorem 2.3.2. The BSWP model (2.15)-(2.18) admits a unique and non-negative classical solution (b, a) at any time $t > 0$, for any non-negative initial condition satisfying (2.29)-(2.30)

Proof. It is enough to show that the bulk-surface wave pinning model (2.15)-(2.18) satisfies the assumptions of Theorem 2.3.1, where in our case $H(b) = 0$ and $F(a, b) = -G(a, b) =$

$f(a,b)$. We first note that, since

$$\nabla f(a,b) = \begin{pmatrix} \frac{\partial f}{\partial a} \\ \frac{\partial f}{\partial b} \end{pmatrix} = \begin{pmatrix} 2\omega\gamma K^2 \frac{ab}{(K^2+a^2)^4} - \beta \\ \omega\left(k_0 + \gamma \frac{a^2}{K^2+a^2}\right) \end{pmatrix},$$

both $\frac{\partial f}{\partial a}(a,b)$ and $\frac{\partial f}{\partial b}(a,b)$ exist and are bounded in any compact set $\mathcal{K} \subset \mathbb{R}^2$. This guarantees f to be locally Lipschitz. The quasi-positivity conditions (2.26)-(2.28) are then satisfied as

$$G(a,0) = -f(a,0) = \beta a > 0, \qquad \text{for } a > 0$$

and

$$F(0,b) = f(0,b) = \omega k_0 b > 0, \qquad \text{for } b > 0.$$

The condition (2.31) is satisfied as $\forall a, b \geq 0$

$$\gamma F(a,b) + G(a,b) = (\gamma - 1) f(a,b) \leq \alpha(a+b+1)$$

is true for $\gamma = 1$ and $\forall \alpha > 0$. Condition (2.32) can be verified by taking $K_G = \beta$, indeed

$$G(a,b) = \beta a - \omega\left(k_0 + \frac{\gamma a^2}{K^2+a^2}\right) b < \beta a < \beta(a+b+1)$$

$\forall a, b \geq 0$. Condition (2.33) is also satisfied as $\forall a, b \geq 0$.

$$F(a,b) = \omega\left(k_0 + \frac{\gamma a^2}{K^2+a^2}\right) b - \beta a \leq \omega\,(k_0+\gamma)\, b < K_F (a+b+1)^l,$$

just by taking $K_F = \omega\,(k_0+\gamma)$ and $l = 1$. Therefore by Theorem 2.3.1, the BSWP model (2.15)-(2.18) admits a unique solution (b,a) for any non negative initial conditions satisfying (2.29)-(2.30). □

2.4 Fundamental properties of the BSWP model

As it will be clear from Section 2.7, the polarisation behaviour of the BSWP model (2.15)-(2.18) is mainly based on the following three main properties.

1. *Conservation of total species.* The total amount of proteins cycling between cell membrane and cytosol is maintained constant at all times by the bulk-surface wave pinning model, i.e.

Proposition 2.4.1. Let a and b be solutions of (2.15)-(2.17). Then

$$M(t) := \int_\Omega b(\mathbf{x},t)\ \mathrm{d}\mathbf{x} + \int_\Gamma a(\mathbf{x},t)\ \mathrm{d}s = M_0, \quad \forall t \geq 0, \tag{2.34}$$

where $M_0 \in \mathbb{R}$ represents the initial total amount of active and inactive GTPase, defined by the initial conditions (2.19)-(2.20):

$$M_0 := \int_\Omega b_{in}(\mathbf{x})\ \mathrm{d}\mathbf{x} + \int_\Gamma a_{in}(\mathbf{x})\ \mathrm{d}s. \tag{2.35}$$

Proof. We show that $M'(t) = 0$. Differentiating (2.34) we get

$$M'(t) = \int_\Omega \frac{\partial b}{\partial t}(\mathbf{x},t)\ \mathrm{d}\mathbf{x} + \int_\Gamma \frac{\partial a}{\partial t}(\mathbf{x},t)\ \mathrm{d}s,$$

which, from (2.15) and (2.17), results in

$$M'(t) = \int_\Omega D_b \Delta b\ \mathrm{d}\mathbf{x} + \int_\Gamma \left(D_a \Delta_\Gamma a + f(a,b)\right)\ \mathrm{d}s.$$

Using the divergence theorem and the zero-integral property of the Laplace-Beltrami operator on surfaces with no boundary (see Corollary 1.5.1 in Section 1.5.2, we obtain

$$M'(t) = \int_\Gamma D_b \left(\mathbf{n}\cdot\nabla b\right)\ \mathrm{d}s + \int_\Gamma f(a,b)\ \mathrm{d}s.$$

The conclusion follows by using the boundary condition (2.16). □

We remark that in the proof we never make use of the explicit expression of $f(a,b)$. Indeed, Proposition 2.4.1 can be seen as a corollary to the following (more general) result.

Theorem 2.4.1. Let us consider the following bulk-surface reaction-diffusion system composed of $n_\Omega \geq 1$ bulk equation and $n_\Gamma \geq 1$ surface equations

$$\frac{\partial u_i}{\partial t} = D_i \Delta u_i + h_i(u_1,\dots,u_{n_\Omega}), \qquad \mathbf{x}\in\Omega, t\in(0,T], \tag{2.36}$$

$$\frac{\partial v_j}{\partial t} = d_j \Delta_\Gamma v_i + f_j(u_1,\dots,u_{n_\Omega},v_1,\dots,v_{n_\Gamma}), \qquad \mathbf{x}\in\Gamma, t\in(0,T], \tag{2.37}$$

$$D_i\nabla u_i\cdot\mathbf{n} = g_i(u_1,\dots,u_{n_\Omega},v_1,\dots,v_{n_\Gamma}), \qquad \mathbf{x}\in\Gamma, t\in(0,T], \tag{2.38}$$

$$u_i = u_i^0, \qquad \mathbf{x}\in\Omega, t=0, \tag{2.39}$$

$$v_j = v_j^0, \qquad \mathbf{x}\in\Gamma, t=0, \tag{2.40}$$

for $i = 1, \dots, n_\Omega$ and $j = 1, \dots, n_\Gamma$, with $u_i^0 \in L^1(\Omega)$, $v_j^0 \in L^1(\Gamma)$ given. If the following conditions are satisfied

$$\int_\Omega \sum_{i=1}^{n_\Omega} h_i \, \mathrm{d}\mathbf{x} = 0, \tag{2.41}$$

$$\int_\Gamma \left(\sum_{j=1}^{n_\Gamma} f_j + \sum_{i=1}^{n_\Omega} g_i \right) \, \mathrm{d}s = 0, \tag{2.42}$$

then the solution $(u_1, \dots, u_{n_\Omega}, v_1, \dots, v_{n_\Gamma})$ of the above system satisfies

$$M(t) := \sum_{i=1}^{n_\Omega} \int_\Omega u_i \, \mathrm{d}\mathbf{x} + \sum_{j=1}^{n_\Gamma} \int_\Gamma v_j \, \mathrm{d}s = M_0, \quad \forall t \geq 0, \tag{2.43}$$

where

$$M_0 := \sum_{i=1}^{n_\Omega} \int_\Omega u_i^0 \, \mathrm{d}\mathbf{x} + \sum_{j=1}^{n_\Gamma} \int_\Gamma v_j^0 \, \mathrm{d}s \tag{2.44}$$

is defined by the initial conditions (2.39)-(2.40).

Proof. In order to prove the theorem, we extend the steps of the proof of Proposition 2.4.1. We start by differentiating $M(t)$ from (2.43):

$$M'(t) = \sum_{i=1}^{n_\Omega} \int_\Omega \frac{\partial u_i}{\partial t} \, \mathrm{d}\mathbf{x} + \sum_{j=1}^{n_\Gamma} \int_\Gamma \frac{\partial v_j}{\partial t} \, \mathrm{d}s,$$

which, applying (2.36)-(2.37), is equivalent to

$$M'(t) = \sum_{i=1}^{n_\Omega} \int_\Omega (D_i \Delta u_i + h_i) \, \mathrm{d}\mathbf{x} + \sum_{j=1}^{n_\Gamma} \int_\Gamma (d_j \Delta_\Gamma v_i + f_j) \, \mathrm{d}s.$$

Using the divergence theorem and the zero-integral property of the Laplace-Beltrami operator on surfaces with no boundary (Corollary 1.5.1, Section 1.5.2), we obtain

$$M'(t) = \sum_{i=1}^{n_\Omega} \int_\Gamma D_i \nabla u_i \cdot \mathbf{n} \, \mathrm{d}s + \sum_{j=1}^{n_\Gamma} \int_\Gamma f_j \, \mathrm{d}s,$$

where the integrals in Ω of the bulk reactions h_i disappear, due to (2.41). Applying the boundary conditions (2.38) and bringing the sum inside the integrals, we have

$$M'(t) = \int_\Gamma \sum_{i=1}^{n_\Omega} g_i \, \mathrm{d}s + \int_\Gamma \sum_{j=1}^{n_\Gamma} f_j \, \mathrm{d}s,$$

which is zero due to condition (2.42). The theorem is then proved. □

2. *Difference in diffusivities.* As protein diffusion over the membrane is known to occur much slower than in the cytosol, we consider $D_a \ll D_b$ (Postma et al., 2004; Milo and Phillips, 2015).

3. *Bistability.* The following proposition holds

Proposition 2.4.2. (Mori et al., 2011) Let f be defined by (2.18). Then for every positive fixed value $\bar{b} > 0$, the equation $f(a, \bar{b}) = 0$ always admits at least one solution $a = a_*(\bar{b}) > 0$. Moreover, if

$$8k_0 < \gamma, \tag{2.45}$$

there exist two positive values b_1 and b_2 such that if $\bar{b} \in (b_1, b_2)$, the function $f(a, \bar{b})$ has three zeros $0 < a_1(\bar{b}) < a_2(\bar{b}) < a_3(\bar{b})$ and

$$\frac{\partial f}{\partial a}(a_1(\bar{b}), \bar{b}) < 0, \ \frac{\partial f}{\partial a}(a_2(\bar{b}), \bar{b}) > 0, \ \frac{\partial f}{\partial a}(a_3(\bar{b}), \bar{b}) < 0. \tag{2.46}$$

Proof. From (2.18) we have

$$\begin{aligned} f(a,b) &= \omega\left(k_0 + \frac{\gamma a^2}{K^2+a^2}\right) b - \beta a = \omega k_0 b + \omega\gamma b \frac{a^2}{K^2+a^2} - \beta a \\ &= \frac{1}{K^2+a^2}\left(\omega k_0 b\left(K^2+a^2\right) + \omega\gamma b a^2 - \beta a\left(K^2+a^2\right)\right) \\ &= \frac{\beta}{K^2+a^2}\left(-a^3 + \frac{\omega(k_0+\gamma)}{\beta} b a^2 - K^2 a + \frac{\omega k_0 K^2}{\beta} b\right) \\ &= \frac{\beta K^3}{K^2+a^2}\left(-\left(\frac{a}{K}\right)^3 + \frac{\omega(k_0+\gamma)}{\beta K} b\left(\frac{a}{K}\right)^2 - \left(\frac{a}{K}\right) + \frac{\omega k_0}{\beta K} b\right), \end{aligned}$$

where the last step is done in order to simplify the calculations. Since $\frac{\beta K^3}{K^2+a^2} > 0$, defining

$$d_1 := d_1(b) = D_1 b > 0, \qquad D_1 := \omega(k_0+\gamma)/(\beta K) > 0, \tag{2.47}$$

$$d_2 := d_2(b) = D_2 b > 0, \qquad D_2 := \omega k_0/(\beta K) > 0, \tag{2.48}$$

we just have to study the roots of the cubic polynomial:

$$p_b(a/K) := -\left(\frac{a}{K}\right)^3 + d_1\left(\frac{a}{K}\right)^2 - \left(\frac{a}{K}\right) + d_2.$$

However since division by K is just a scaling which does not change the qualitative

nature of p_b it is enough to study the function

$$p_b(a) := -a^3 + d_1 a^2 - a + d_2. \tag{2.49}$$

For the moment we consider b as a real positive parameter and we search for solutions $a = a(b)$. In particular we are interested in positive real roots. It is important to remark that for every $b > 0$ the newly defined constants d_1 and d_2 are real and positive. By a simple observation of the function p_b, which is a cubic polynomial, we find out that at least one real root exists. The first statement of the proposition is then proved by observing that $p_b(0) > 0$ and $\lim_{a\to+\infty} p_b(a) < 0$.

The Descartes' rule of signs tells us more: $p_b(a)$ has either only one positive real root or three positive real roots. Using the Descartes criterion as well on $p_b(-a)$, we notice that no negative real roots are possible. Then the possibilities are restricted just to two different cases: either p_b admits three positive real roots or it has only one positive real root and two complex. For a general cubic polynomial of the form: $p(x) = x^3 + a_2x^2 + a_1x + a_0$ we can define the quantity $\Delta_3^p := 18a_2a_1a_0 - 4a_2^3a_0 + a_2^2a_1^2 - 4a_1^3 - 27a_0^2$, for which we have three different cases:

- $\Delta_3^p > 0$: $p(x)$ has three distinct real roots;
- $\Delta_3^p = 0$: $p(x)$ has two real roots, one with multiplicity 2;
- $\Delta_3^p < 0$: $p(x)$ has only one real root.

For more details see for example Irving (2004). We can then apply this method to the polynomial $q_b(a) := -p_b(a) = a^3 - d_1a^2 + a - d_2$, as it has the same roots of p_b and study the sign of $\Delta_3 = 18d_1d_2 - 4d_1^3d_2 + d_1^2 - 4 - 27d_2^2$, finding conditions on b for which we have $\Delta_3 > 0$ (or $= 0$, or < 0). The function Δ_3 depends on b and, using (2.47)-(2.48), it can be written as:

$$\begin{aligned}\Delta_3(b) &= 18D_1D_2b^2 - 4D_1^3D_2b^4 + D_1^2b^2 - 4 - 27D_2^2b^2 \\ &= -4D_1^3D_2b^4 + (18D_1D_2 + D_1^2 - 27D_2^2)b^2 - 4.\end{aligned} \tag{2.50}$$

Before proceeding, let us notice some facts:

- $\Delta_3(b)$ is a continuous function well defined for any $b \in (-\infty, \infty)$. In particular it is a forth degree polynomial and an even function (see Figure 2.3).

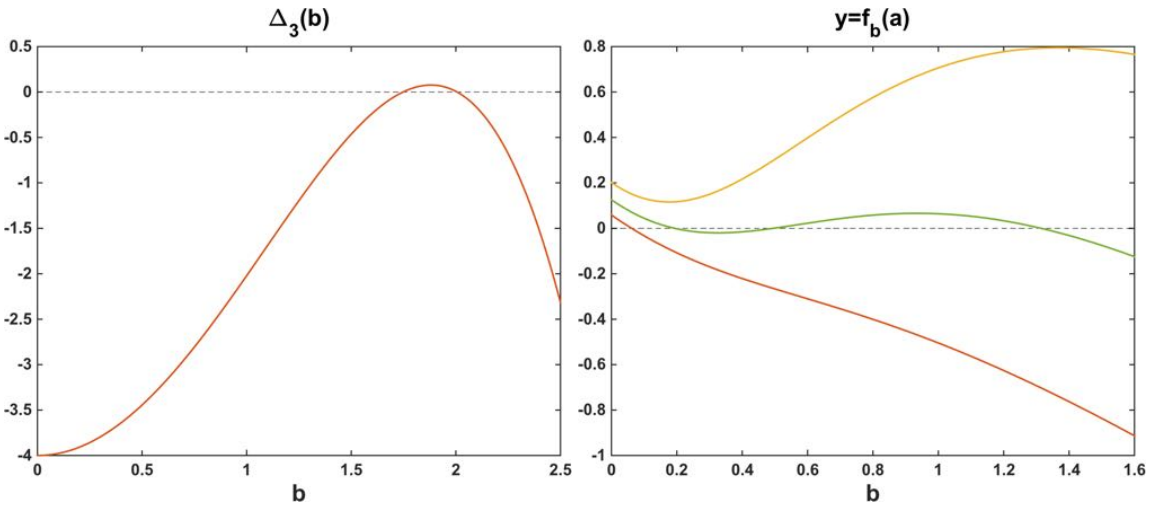

(a) (b)

Figure 2.3: (a) The function $\Delta_3(b)$ for the parameter values in Table 2.1 and $\omega = 1$. (b) Plots of the function $f_b(a) = f(a, \bar{b})$ for three different fixed values for $\bar{b}$ and parameters given in Table 2.1 with $\omega = 1$: the orange line for $\bar{b} < b_1$; the green line for $\bar{b} = \frac{b_1+b_2}{2}$; the yellow line for $\bar{b} > b_2$. The values b_1, b_2 define the range of b for which $f(a, b)$ admits three different zeros $(a(b), b)$.

- $\Delta_3(0) = -4 < 0$. Then, if $\Delta_3(b)$ does not have any real roots, $\Delta_3(b) < 0$, $\forall b \in \mathbb{R}$ and the function $p_b(a)$ has only one real root, which is positive.

- as $\Delta_3(b)$ is a symmetric function, if a positive real root b_* exists, also $-b_*$ is a root. However, we must recall that we are interested only in positive values of b.

- By the Fundamental Theorem of Algebra, $\Delta_3(b)$ admits up to 4 real roots counted with multiplicity. As a consequence of this and of the previous considerations, we have that no more than two positive real roots $b_1 < b_2$ are possible. If this is the case, we will have:

  – If $0 \leq b < b_1$ or $b > b_2$, $\Delta_3(b) < 0$ and the function $p_b(a)$ has only one real (and positive) root and two complex.

  – If $b = b_1$ or $b = b_2$, $\Delta_3(b) = 0$ and the function $p_b(a)$ has two real roots, both positive, but one has multiplicity 2.

  – If $b_1 < b < b_2$, $\Delta_3(b) > 0$ and the function $p_b(a)$ has three real roots, all positive.

In the new variable $t := b^2$, the function $\Delta_3(t) = -4D_1^3D_2t^2 + (18D_1D_2 + D_1^2 -$

$27D_2^2)t - 4$ describes a parabola, with zeros given by:

$$t_{1,2} = \frac{-(18D_1D_2 + D_1^2 - 27D_2^2) \pm \sqrt{(18D_1D_2 + D_1^2 - 27D_2^2)^2 - 64D_1^3D_2}}{-8D_1^3D_2}$$
$$= \frac{(18D_1D_2 + D_1^2 - 27D_2^2) \mp \sqrt{(18D_1D_2 + D_1^2 - 27D_2^2)^2 - 64D_1^3D_2}}{8D_1^3D_2}. \quad (2.51)$$

Depending on the sign of $(18D_1D_2 + D_1^2 - 27D_2^2)^2 - 64D_1^3D_2$, the zeros of $\Delta_3(t)$ *(i)* can be real and distincts ($t_1 < t_2$), or *(ii)* real but equals ($t_1 = t_2$) or *(iii)* complex. With respect to b the values we are interested in, if t_1, t_2 exist in $\mathbb{R}^+$, are

$$b_1 = \sqrt{t_1} \text{ and } b_2 = \sqrt{t_2}. \quad (2.52)$$

Let us consider the three cases with their respective subcases:

(i) If $(18D_1D_2 + D_1^2 - 27D_2^2)^2 - 64D_1^3D_2 > 0$ we can have two diffent situations:

(a) If $18D_1D_2 + D_1^2 - 27D_2^2 < 0$ then $t_1 < t_2 < 0$ (as $-64D_1^3D_2 < 0$) and from (2.52) we deduce that b_1, b_2 are complex numbers. This implies that $\Delta_3(b)$ has no real roots and $\Delta_3(b) < 0,\ \forall b \in \mathbb{R}$. So, $\forall b \in \mathbb{R}^+$, $p_b(a) = 0$ admits only one real solution $a_* = a_*(b)$ (which is positive).

(b) If $18D_1D_2 + D_1^2 - 27D_2^2 > 0$ then $0 < t_1 < t_2$ and we deduce that $b_1 < b_2 \in \mathbb{R}^+$. Moreover, as previously discussed:

(b_1) If $t \in (t_1, t_2),\ \Delta_3(t) > 0$. It implies $\Delta_3(b) > 0, \forall b \in (b_1, b_2)$: for these values of b, $p_b(a) = 0$ admits three different real (and positive) solutions $a_1 = a_1(b),\ a_2 = a_2(b),\ a_3 = a_3(b)$.

(b_2) If $t = t_1$ (or $t = t_2$), $\Delta_3(t) = 0$. It implies $\Delta_3(b) = 0$, for $b = b_1$ (or $b = b_2$): it is a limit case and for these values of b, $p_b(a) = 0$ admits two different real (and positive) solutions $a_1 = a_1(b),\ a_2 = a_2(b)$, one with multiplicity 2.

(b_3) If $t < t_1$ (or $t > t_2$), $\Delta_3(t) < 0$. It implies $\Delta_3(b) < 0$, for $b < b_1$ (or $b > b_2$): for these values of b, $p_b(a) = 0$ admits only one real (and positive) solution $a_* = a_*(b)$.

(ii) If $(18D_1D_2 + D_1^2 - 27D_2^2)^2 - 64D_1^3D_2 = 0$ then $t_1 = t_2$ with two different possibilities:

(a) If $18D_1D_2 + D_1^2 - 27D_2^2 < 0$ then $t_1 = t_2 < 0$ and we deduce that b_1, b_2 are complex numbers. This implies that $\Delta_3(b) < 0,\ \forall b \in \mathbb{R}$ and $p_b(a) = 0$

admits just one real (and positive) solution $a_* = a_*(b),\ \forall b \in \mathbb{R}^+$.

(b) If $18D_1D_2 + D_1^2 - 27D_2^2 > 0$ then $0 < t_1 = t_2$ and we deduce that $b_1 = b_2 \in \mathbb{R}^+$. This implies that $\Delta_3(b) < 0$, for $\forall b \neq b_1$ then $p_b(a) = 0$ admits only one real (and positive) solution $a_* = a_*(b)$. However, for $b = b_1 = b_2$ then $\Delta_3(b) = 0$: only for this value of b, $p_b(a)$ admits two different (positive) real roots $a_1 = a_1(b_1), a_2 = a_2(b_1)$, one with multiplicity 2.

(iii) If $(18D_1D_2 + D_1^2 - 27D_2^2)^2 - 64D_1^3D_2 < 0$ then $\Delta_3(t)$ has two complex roots t_1, t_2, and we deduce that the roots b_1, b_2 of $\Delta_3(b)$ are also complex numbers. This implies that $\Delta_3(b) < 0\ \forall b \in \mathbb{R}^+$: $p_b(a) = 0$ admits just one real (positive) solution $a_* = a_*(b), \forall b \in \mathbb{R}^+$.

Therefore, under the conditions:

$$(18D_1D_2 + D_1^2 - 27D_2^2)^2 - 64D_1^3D_2 > 0, \tag{2.53}$$

$$18D_1D_2 + D_1^2 - 27D_2^2, > 0, \tag{2.54}$$

three different solutions $(a_1(b), b)$, $(a_2(b), b)$, $(a_3(b), b)$ exist in $\mathbb{R}^+ \times \mathbb{R}^+$ for every $b \in (\sqrt{t_1}, \sqrt{t_2})$, with D_1, D_2, t_1 and t_2 defined in (2.47), (2.48) and (2.51),

Condition (2.54) can be written more explicitly:

$$\begin{aligned}
&18D_1D_2 + D_1^2 - 27D_2^2 \\
&= \left(\frac{\omega}{\beta K}\right)^2 \left(18(k_0+\gamma)k_0 + (k_0+\gamma)^2 - 27k_0^2\right) \\
&= \left(\frac{\omega}{\beta K}\right)^2 \left(18k_0^2 + 18\gamma k_0 + k_0^2 + \gamma^2 + 2\gamma k_0 - 27k_0^2\right) \\
&= \left(\frac{\omega}{\beta K}\right)^2 \left(\gamma^2 + 20\gamma k_0 - 8k_0^2\right) > 0,
\end{aligned}$$

that is satisfied for $\left(\frac{\gamma}{k_0}\right)^2 + 20\left(\frac{\gamma}{k_0}\right) - 8 > 0$, i.e. if $\gamma > (6\sqrt{3} - 10)k_0$.

Also condition (2.53) can be simplified, indeed with some algebraic calculations it can be proven

$$(18D_1D_2 + D_1^2 - 27D_2^2)^2 - 64D_1^3D_2 = (D_1 - 9D_2)^3(D_1 - D_2),$$

so (2.53) is equivalent to

$$(D_1 - 9D_2)(D_1 - D_2) > 0,$$

and due to the fact that $D_1 - D_2 = \omega(k_0+\gamma)/(\beta K) - \omega k_0/(\beta K) = \omega\gamma/(\beta K) > 0$, this condition reduces to

$$(D_1 - 9D_2) = \frac{\omega(k_0+\gamma)}{\beta K} - 9\frac{\omega k_0}{\beta K} = \frac{\omega}{\beta K}(\gamma - 8k_0) > 0,$$

which is satisfied if and only if $\gamma > 8k_0$. In particular this condition implies $\gamma > (6\sqrt{3}-10)k_0$, therefore the second step of the proposition is satisfied.

For completeness, some limit cases can occur: two solutions can merge together on the same one if $\gamma \geq 8k_0$ and $b = \sqrt{t_1}$ or $b = \sqrt{t_2}$.

It now remains to prove (2.46). But this follows by observing that $f(0,b) > 0$ and $\lim_{a\to\infty} f(a,b) = -\infty$ and applying continuity arguments.

□

Condition (2.45) represents and highlights the important role of the feedback-induced activation rate in the model, while we will refer to (2.46) as the *bistability condition*. A representation of the level set of $f(a,b)$ will be shown in Figure 2.4 in Section 2.7.

2.5 Convergence towards a steady state for a limit case

If we impose $\omega = 0$ (or equivalently $k_0 = \gamma = 0$), then system (2.15)-(2.16) reads

$$\frac{\partial b}{\partial t} = D_b \Delta b, \qquad \mathbf{x} \in \Omega,\ t \in (0,T], \tag{2.55}$$

$$-D_b(\mathbf{n}\cdot\nabla b) = -\beta a, \qquad \mathbf{x} \in \Gamma,\ t \in (0,T], \tag{2.56}$$

$$\frac{\partial a}{\partial t} = D_a \Delta_\Gamma a - \beta a, \qquad \mathbf{x} \in \Gamma,\ t \in (0,T]. \tag{2.57}$$

This represents the limit case in which the system is not able to activate the bulk component and shows only inactivation of the membrane-bound protein. In this case, it is easy to describe the long-time behaviour of the system. Therefore, in the following, we will show the convergence of the solution (a,b) to a steady state $(\overline{a},\overline{b})$. We first note that since (2.57) does not depend on b, we can analyse this equation independent of the bulk variable. Let us first multiply both sides of (2.57) by a and integrate in Γ. We get

$$\int_\Gamma a\frac{\partial a}{\partial t}\,\mathrm{d}s = D_a\int_\Gamma a\Delta_\Gamma a\,\mathrm{d}s - \int_\Gamma \beta a^2\,\mathrm{d}s, \tag{2.58}$$

where the first term can be rewritten as

$$\int_\Gamma a\frac{\partial a}{\partial t}\,\mathrm{d}s = \frac{1}{2}\int_\Gamma \frac{\partial a^2}{\partial t}\,\mathrm{d}s = \frac{1}{2}\frac{\mathrm{d}}{\mathrm{d}t}\int_\Gamma a^2\,\mathrm{d}s = \frac{1}{2}\frac{\mathrm{d}}{\mathrm{d}t}\|a\|^2_{L^2(\Gamma)}\,,$$

and the second term, by using Theorem 1.5.3, is

$$D_a\int_\Gamma a\Delta_\Gamma a\,\mathrm{d}s = -D_a\int_\Gamma \nabla_\Gamma a\cdot\nabla_\Gamma a\,\mathrm{d}s = -D_a\|\nabla_\Gamma a\|^2_{L^2(\Gamma)}\,.$$

Hence (2.58) is equivalent to

$$\frac{1}{2}\frac{\mathrm{d}}{\mathrm{d}t}\|a\|^2_{L^2(\Gamma)} = -D_a\|\nabla_\Gamma a\|^2_{L^2(\Gamma)} - \beta\|a\|^2_{L^2(\Gamma)}\,.$$

Thus, it must be

$$\frac{\mathrm{d}}{\mathrm{d}t}\|a\|^2_{L^2(\Gamma)} + 2\beta\|a\|^2_{L^2(\Gamma)} \le 0,$$

i.e.

$$\frac{\mathrm{d}}{\mathrm{d}t}\left(e^{2\beta t}\|a\|^2_{L^2(\Gamma)}\right) \le 0,$$

from which we get

$$e^{2\beta t}\|a(\mathbf{x},t)\|^2_{L^2(\Gamma)} \le \|a(\mathbf{x},0)\|^2_{L^2(\Gamma)}\,.$$

This finally leads to the convergence estimate

$$0 \le \|a(\mathbf{x},t)\|_{L^2(\Gamma)} \le \|a(\mathbf{x},0)\|_{L^2(\Gamma)}\,e^{-\beta t}. \tag{2.59}$$

Therefore the $L^2(\Gamma)-$norm of the solution a tends exponentially to zero, which implies that a tends to zero almost everywhere on Γ, i.e.

$$\overline{a} = 0 \text{ a.e. in } \Gamma. \tag{2.60}$$

Regarding the bulk component b, since we want to consider the large-time behaviour, we introduce the new time variable $\tau = \varepsilon t$ for an arbitrary small parameter $\varepsilon > 0$. Therefore (2.55) can be written as

$$\varepsilon\frac{\partial b}{\partial \tau} = D_b\Delta b, \qquad\qquad \mathbf{x}\in\Omega,\ t\in(0,T].$$

Sending ε to zero, a tends to the steady state (2.60) and the evolution of the bulk component

tends to be described by the system

$$\begin{aligned} \Delta b &= 0, && \mathbf{x} \in \Omega,\ t \in (0,T], \\ -\mathbf{n}\cdot\nabla b &= 0, && \text{a.e. } \mathbf{x} \in \Gamma,\ t \in (0,T], \end{aligned}$$

which is the Laplace equation coupled with homogeneous Neumann condition, i.e b tends to a spatial uniform profile. Finally, using the conservation of total mass (2.34) we get

$$\overline{b} = \frac{1}{|\Omega|} M_0,$$

since $\overline{a} = 0$ almost everywhere.

2.6 Non-dimensionalisation

Let A and B be some dimensional concentration quantities with $[A]$ =mol $\mu\text{m}^{-(d-1)}$, and $[B]$ =mol μm^{-d} where d is the dimension of the domain. Let L be a typical length in the cell ($[L] = \mu$m), representing for example its radius, and T a temporal quantity ($[T]$ =s). Then we can define the nondimensional variables

$$\hat{a} = a/A, \quad \hat{b} = b/B, \quad \hat{t} = t/T, \quad \hat{\mathbf{x}} = \mathbf{x}/L.$$

Using the chain rule in the derivation we have

$$\frac{\partial}{\partial t} = \frac{1}{T}\frac{\partial}{\partial \hat{t}}, \quad \nabla = \frac{1}{L}\hat{\nabla}, \quad \Delta = \frac{1}{L^2}\hat{\Delta}.$$

Therefore, from (2.15)-(2.18), we obtain

$$\begin{aligned} \frac{B}{T}\frac{\partial \hat{b}}{\partial \hat{t}} &= D_b \frac{B}{L^2}\hat{\Delta}\hat{b}, && \mathbf{x} \in \hat{\Omega}, \\ \frac{A}{T}\frac{\partial \hat{a}}{\partial \hat{t}} &= D_a \frac{A}{L^2}\hat{\Delta}_\Gamma \hat{a} + f(A\hat{a}, B\hat{b}), && \mathbf{x} \in \partial\hat{\Omega}, \\ -D_b \frac{B}{L}(\mathbf{n}\cdot\nabla\hat{b}) &= f(A\hat{a}, B\hat{b}), && \mathbf{x} \in \partial\hat{\Omega}, \\ f(A\hat{a}, B\hat{b}) &= \Big(k_0 + \frac{\gamma\hat{a}^2}{\left(\frac{K}{A}\right)^2 + \hat{a}^2}\Big)\omega B\hat{b} - \beta A\hat{a}. \end{aligned}$$

We now set $\hat{K} = K/A$ so we can write

$$f(A\hat{a}, B\hat{b}) = \beta A\left[\frac{\omega B}{\beta A}\left(k_0 + \frac{\gamma\hat{a}^2}{\hat{K}^2 + \hat{a}^2}\right)\hat{b} - \hat{a}\right].$$

In the system we get

$$\begin{aligned}
\frac{\partial \hat{b}}{\partial \hat{t}} &= \frac{D_b T}{L^2}\hat{\Delta}\hat{b}, && \mathbf{x} \in \hat{\Omega}, \\
\frac{1}{T}\frac{\partial \hat{a}}{\partial \hat{t}} &= \frac{D_a}{L^2}\hat{\Delta_\Gamma}\hat{a} + \beta\left[\frac{\omega B}{\beta A}\left(k_0 + \frac{\gamma \hat{a}^2}{\hat{K}^2 + \hat{a}^2}\right)\hat{b} - \hat{a}\right], && \mathbf{x} \in \partial\hat{\Omega}, \\
-(\mathbf{n}\cdot\hat{\nabla}\hat{b}) &= \frac{AL}{D_b B}\beta\left[\frac{\omega B}{\beta A}\left(k_0 + \frac{\gamma \hat{a}^2}{\hat{K}^2 + \hat{a}^2}\right)\hat{b} - \hat{a}\right], && \mathbf{x} \in \partial\hat{\Omega},
\end{aligned}$$

As in Mori et al. (2011), we consider

$$L = \sqrt{\frac{D_b}{\beta}}$$

i.e. L is approximately the length that the diffusing protein b covers in its biochemical activation time scale. With this choice, using the parameters in Table 2.1 we have $L = 10\mu$m. We also define $A = K$ and $B = K/L$, so A and B are related to the quantity K, which represents the concentration of active component needed to reach half of the maximal activation rate induced by the positive feedback. For the time scaling we use

$$T = \frac{1}{\beta}\sqrt{\frac{D_b}{D_a}} = \frac{L}{\sqrt{\beta D_a}}.$$

This choice is particularly convenient for the analysis of the model at different time scales in Section 2.7. For comparison with the previous works, we remark that the same expressions for L and T were used in Mori et al. (2011). Finally we get

$$\begin{aligned}
\frac{\partial \hat{b}}{\partial \hat{t}} &= \sqrt{\frac{D_b}{D_a}}\hat{\Delta}\hat{b}, && \mathbf{x} \in \hat{\Omega}, \\
\cancel{\beta}\sqrt{\frac{D_a}{D_b}}\frac{\partial \hat{a}}{\partial \hat{t}} &= \cancel{\beta}\frac{D_a}{D_b}\hat{\Delta_\Gamma}\hat{a} + \cancel{\beta}\left[\left(\hat{k_0} + \frac{\hat{\gamma}\hat{a}^2}{1 + \hat{a}^2}\right)\hat{b} - \hat{a}\right], && \mathbf{x} \in \partial\hat{\Omega}, \\
-(\mathbf{n}\cdot\hat{\nabla}\hat{b}) &= \left(\hat{k_0} + \frac{\hat{\gamma}\hat{a}^2}{1 + \hat{a}^2}\right)\hat{b} - \hat{a}, && \mathbf{x} \in \partial\hat{\Omega},
\end{aligned}$$

where

$$\hat{k_0} = \frac{\omega B}{\beta A}k_0 = \frac{\omega}{\sqrt{\beta D_b}}k_0 \quad \text{and} \quad \hat{\gamma} = \frac{\omega B}{\beta A}\gamma = \frac{\omega}{\sqrt{\beta D_b}}\gamma.$$

Since one of the main assumption of the model is that a diffuses much slower than b, we set

$$\varepsilon^2 = \frac{D_a}{D_b} \ll 1.$$

Finally, dropping all the hats, the nondimensional BSWP model is described by the following system

$$\varepsilon \frac{\partial b}{\partial t} = \Delta b, \qquad \mathbf{x} \in \Omega, \tag{2.61}$$

$$-(\mathbf{n} \cdot \nabla b) = f\ (a, b), \qquad \mathbf{x} \in \Gamma, \tag{2.62}$$

$$\varepsilon \frac{\partial a}{\partial t} = \varepsilon^2 \Delta_\Gamma a + \ f(a, b), \qquad \mathbf{x} \in \Gamma, \tag{2.63}$$

with

$$f(a, b) := \left(k_0 + \frac{\gamma a^2}{1 + a^2} \right) b - a, \tag{2.64}$$

2.7 Asymptotic analysis on a disk

The basic mechanisms of the BSWP model (2.15)-(2.18) can be understood through an asymptotic analysis which is here presented in order to highlight the main steps of the spatio-temporal evolution of certain classes of initial conditions. Since the core of the analysis is based on the crucial difference of protein diffusivity between cell membrane and cytosol, a convenient setting to stress this relationship is the use of the nondimensional version of the BSWP model, given in (2.61)-(2.64).

Provided condition (2.45) is satisfied, for b within a certain range (b_1, b_2), the function $f(a, b)$ has three distinct and positive roots $a_1(b) < a_2(b) < a_3(b)$ and (2.46) is satisfied, i.e. $a_1(b)$ and $a_3(b)$ are stable steady states for the ordinary differential equation corresponding to (2.63) considered with zero diffusion. Bistable reaction-diffusion equations are known to produce travelling wave solutions (Fife and McLeod, 1977) and this is a crucial aspect of the wave pinning mechanism. Figure 2.4 shows the zero level set of $z = f(a, b)$, which represents the nullcline of the ordinary differential equation (2.63) with zero diffusion.

We consider initial conditions of the following type

$$b_{in}(\mathbf{x}) = \overline{b_0} \in (b_1, b_2), \qquad \mathbf{x} \in \Omega, \tag{2.65}$$

$$a_{in}(\mathbf{x}) = a_g + a_p(\mathbf{x}), \qquad \mathbf{x} \in \Gamma, \tag{2.66}$$

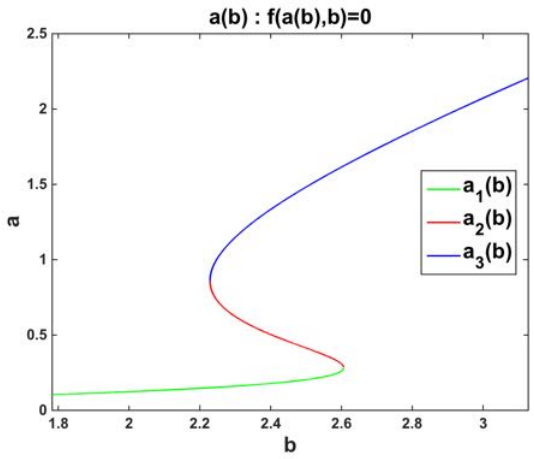

Figure 2.4: The solutions (a, b) solving $f(a, b) = 0$ as defined in (2.64) with parameters $k_0 = 0.05$ and $\gamma = 0.79$ (these values are obtained using the parameters from Table 2.1 in the nondimensionalisation process).

where $a_g \in \left[0, a_2(\overline{b_0})\right)$ and a_p is a continuous function over Γ such that, given

$$\Gamma_p := \left\{\mathbf{x} \in \Gamma \ : \ a_p(\mathbf{x}) + a_g > a_2(\overline{b_0})\right\},$$

$0 < |\Gamma_p| \ll |\Gamma|$ and

$$\int_{\Gamma_p} a_p \, \mathrm{d}\mathbf{x} \ll \int_{\Gamma} a_{in} \, \mathrm{d}\mathbf{x}.$$

In biological terms, the above relations describe that initially the inactive cytosolic protein is spatially uniform, while the initial concentration of active protein is less than the value $a_2(\overline{b_0})$ in most of its domain except for tiny regions in which the mass exceeding $a_2(\overline{b_0})$ is negligible. In the simulations we have represented a_p with very narrow Gaussian functions.

We consider a flat cell $\Omega = \{(x, y) \ : \ x^2 + y^2 < r^2, \ r > 0\}$ which, being a simple circular domain, makes the exposition clearer. We are also interested in a single peak for a, which means Γ_p is connected, in other words, $a_{in}(\mathbf{x}) = a_2(\overline{b_0})$ has two solutions $\mathbf{x}$. In our exposition we next show that the evolution of a is strongly characterised by different time scales with the development of well defined spatial patterns and formation of boundary layers in which the solution drastically passes from one "stable" state to the other (the inverted commas are used because these states actually depend on b, which is also subject to evolution). This corresponds to a sudden large variation of the gradient of a in very small regions, which is otherwise negligible elsewhere. Therefore our analysis will make use of a spatial rescaling around these more critical areas. A typical strategy for studying this class of equations is presented in Rubinstein and Sternberg (1992), where a

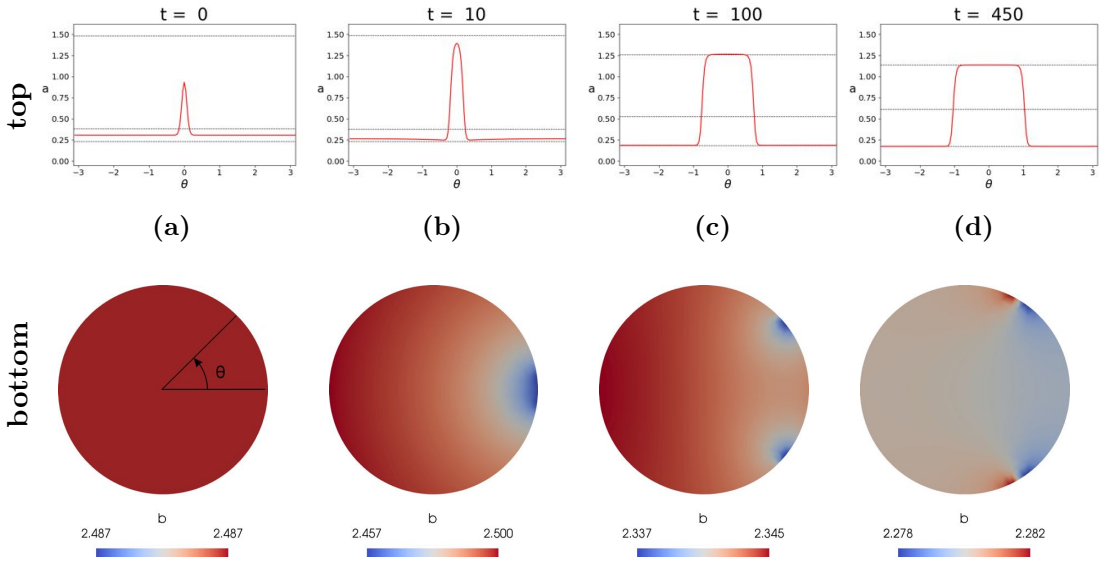

Figure 2.5: Numerical solutions of the BSWP model (2.61)-(2.64) with $\varepsilon^2 = 0.001$ on a disc at different time steps. The parameter ε plays a crucial role in sharpening the fronts of the solution a, see Mori et al. (2011). Smaller values of ε result in a clearer effect of the BSWP mechanism. On the top row we plot the solution a (red line) over the circle at different time steps, whereas the horizontal dashed lines indicate the three solutions a_1, a_2, a_3 of $f\left(a, \overline{b}\right) = 0$, where $\overline{b} = \frac{1}{|\Omega|}\int_\Omega b \, \mathrm{d}\mathbf{x}$ and $a_1 < a_2 < a_3$. On the bottom row we plot the solution b inside the disk. It is important to note the scale values for b: at every time step, b is approximately spatially constant. (a) (top) A narrow Gaussian function is summed over a spatially homogeneous initial condition. In most of its domain a is initially smaller than a_2, except for the Gaussian peak. We use the centre of the peak as reference for the polar coordinate system. (bottom) The initial condition for b is spatially homogeneous. (b) (top) Attraction of a towards the values a_1 and a_3 is well visible: the peak grows towards a_3, while the rest of the solution tends to the lower value a_1. (bottom) Depletion of b starts from the boundary of the disc at around $\theta = 0$. (c) (top) At time $t = 100$ a overlaps a_1 and a_3 in most of the domain except in the two very small areas where the transition between the two states occurs very sharply. In addition, the peak of a has visibly increased its width, as propagation has started. (bottom) b is depleted in correspondence of the sharp moving fronts of active GTPase. (d) The steady states for a and b. b has reached its critical value and there is no more source of GTPase available for a, which therefore is pinned in an almost piece-wise constant shape. Details of the numerical methods and tools used for the simulation will be given in Section 2.9.

mass conserved reaction-diffusion equation with a double-well potential is studied through multiple temporal rescaling and matched asymptotic analysis. Our analysis is described in four steps (see also Figure 2.5) as outlined below, and it follows the asymptotic analysis done by Mori et al. (2011) for the unidimensional model (2.1)-(2.3), which we have re-adapted to the BSWP model (2.15)-(2.18) thanks to the circular geometry.

(a) At the initial time, a evolves into a well defined profile with two fronts: over Γ_p it is attracted by $a_3(b)$, while on the rest of the domain it is attracted by $a_1(b)$. On the other hand, b is approximately spatially homogeneous. We study this evolution over the zoomed time scale $\tau = t/\varepsilon$.

(b) In the intermediate time scale t we observe the movement of the fronts in the a profile,

in particular we are interested in the expansion of the high concentration peak. In order to achieve this, we need to show that

- The speed of the propagating fronts is strictly related to the sign of the function defined by
$$I(b) := \int_{a_1(b)}^{a_3(b)} f(\xi, b)\mathrm{d}\xi, \quad b \in (b_1, b_2). \tag{2.67}$$
- $I(b)$ is an increasing function in (b_1, b_2) and there exists $b_c \in (b_1, b_2)$ such that $I(b_c) = 0$.

(c) The propagation of a coincides with the depletion of b, which is always approximately spatially homogeneous (note the color scale in Fig 2.5 bottom).

(d) Under particular conditions on the initial concentrations, the propagation stops before the whole boundary is activated. This occurs when b has decreased to its critical value b_c.

We are now in a position to discuss the steps (a)-(d) in more detail.

Step a) We first study the initial evolution of the system (2.61)-(2.64) by introducing the fast time scale $\tau = t/\varepsilon$. Temporal rescaling results in the following coupled bulk-surface system

$$\begin{aligned} \frac{\partial b}{\partial \tau} &= \Delta b, && \mathbf{x} \in \Omega, \\ \frac{\partial a}{\partial \tau} &= \varepsilon^2 \Delta_\Gamma a + \ f(a, b), && \mathbf{x} \in \Gamma, \\ -(\mathbf{n} \cdot \nabla b) &= f\ (a, b) && \mathbf{x} \in \Gamma. \end{aligned}$$

Looking for solutions of the form $a = a_0 + a_1\varepsilon + a_2\varepsilon^2 + \cdots$ and $b = b_0 + b_1\varepsilon + a_2\varepsilon^2 + \cdots$ we find, at the leading order

$$\begin{aligned} \frac{\partial b_0}{\partial \tau} &= \Delta b_0, && \mathbf{x} \in \Omega, \\ \frac{\partial a_0}{\partial \tau} &= f(a_0, b_0), && \mathbf{x} \in \Gamma, \\ -\mathbf{n} \cdot \nabla b_0 &= f(a_0, b_0), && \mathbf{x} \in \Gamma. \end{aligned}$$

The equation for a_0 is an ordinary differential equation and, at each $\mathbf{x}$, the solution will tend to the stable stationary point $a_3(b)$ for $\mathbf{x} \in \Gamma_p$ or $a_1(b)$ elsewhere: at the end of this time scale we will have $\frac{\partial a_0}{\partial \tau} \approx 0$. This means that over Γ, $f(a_0, b_0) \approx 0$.

The equation for b_0 is the heat equation with Neumann boundary conditions that will become approximately homogeneous at the end of the time scale. Then $b_0(\mathbf{x}, \tau)$ will tend to reach a spatially homogeneous profile over the domain Ω.

Step b) In the intermediate time scale t, we again look for solutions of the form $a = a_0 + a_1\varepsilon + a_2\varepsilon^2 + \cdots$ and $b = b_0 + b_1\varepsilon + a_2\varepsilon^2 + \cdots$. At the leading order we have

$$\begin{aligned} \Delta b_0 &= 0, && \mathbf{x} \in \Omega, \\ f(a_0, b_0) &= 0, && \mathbf{x} \in \Gamma, \\ -\mathbf{n} \cdot \nabla b_0 &= f(a_0, b_0), && \mathbf{x} \in \Gamma. \end{aligned}$$

We see that the flux condition is actually $-\mathbf{n} \cdot \nabla b_0 = 0$, consistently with the Laplace equation in Ω. $b_0(\mathbf{x}, t)$ is now at equilibrium all over the domain. On the other hand, $a_0(\mathbf{x}, t)$ remains at its low and high values, either $a_1(b)$ or $a_3(b)$. This is valid far from the two front layers where the solution passes from a_1 to a_3 and vice versa. Our goal is to see if these front layers move in time over the boundary Γ. We take advantage of the circular geometry of the domain and re-write the model (2.61)-(2.64) in polar coordinates

$$\begin{aligned} \varepsilon \frac{\partial b}{\partial t} &= \frac{\partial^2 b}{\partial \rho^2} + \frac{1}{\rho}\frac{\partial b}{\partial \rho} + \frac{1}{\rho^2}\frac{\partial^2 b}{\partial \theta^2}, && \rho \in (0, r), \theta \in (-\pi, \pi], \\ \varepsilon \frac{\partial a}{\partial t} &= \frac{\varepsilon^2}{r^2}\frac{\partial^2 a}{\partial \theta^2} + f(a, b), && \rho = r, \theta \in (-\pi, \pi], \\ -\frac{\partial b}{\partial \rho} &= f(a, b), && \rho = r, \theta \in (-\pi, \pi], \end{aligned}$$

where r is the radius of the disk. In this coordinate system it becomes easier to define the positions of the front layers. Indeed, an angle θ is enough to uniquely identify a point on Γ. Let us set $\theta = 0$ at the centre of the boundary subset Γ_p, so that there exist a value $\theta_1 < \pi$ such that $\Gamma_p = (-\theta_1, \theta_1)$, see also Figure 2.5a (top and bottom).

The positions of the two fronts of a are therefore initially defined by $-\theta_1$ and θ_1 and our goal is to show that these positions can change in time subject to (2.61)-(2.64). We will consider $\theta_1(t)$, which is initially small. We define the variable

$$\varphi_1(t) := \frac{\theta - \theta_1(t)}{\varepsilon},$$

such that

$$\lim_{\varepsilon \to 0} \varphi_1 = \begin{cases} +\infty & \text{if } \theta > \theta_1 \\ -\infty & \text{if } \theta < \theta_1 \end{cases}$$

and

$$\lim_{\varphi_1\to-\infty} a(\varphi_1) = a_3(b), \quad \lim_{\varphi_1\to+\infty} a(\varphi_1) = a_1(b),$$

i.e. the wave front connects the high and low plateau values of a. We remark that for $\theta < 0$ the situation reverses: the solution is close to $a_1(b)$ for values of $\theta < -\theta_1$ and to $a_3(b)$ for $\theta > -\theta_1$. More generally, the periodicity of the two-dimensional domain requires an even number of fronts in $(-\pi, \pi]$, which was not necessary in previous works on the wave pinning mechanism. The equation for a in the new coordinate $\hat{a}(\varphi_1(t), t) = a\left(\frac{\theta-\theta_1(t)}{\varepsilon}, t\right)$ is

$$\varepsilon\frac{d\hat{a}}{dt} - \theta_1'(t)\frac{\partial\hat{a}}{\partial\varphi_1} = \frac{1}{r^2}\frac{\partial^2\hat{a}}{\partial\varphi_1^2} + f(\hat{a}, b), \quad \varphi_1 \in (-\infty, +\infty).$$

The term $\theta_1'(t)$ in the left hand side of the above equation describes the speed of the front, which we want now to investigate. Using again asymptotic expansion $\hat{a} = \sum \hat{a}_i\varepsilon^i$ we get, at the leading order

$$\frac{1}{r^2}\frac{\partial^2\hat{a}_0}{\partial\varphi_1^2} + \theta_1'(t)\frac{\partial\hat{a}_0}{\partial\varphi_1} + f(\hat{a}_0, b) = 0, \quad \varphi_1 \in (-\infty, +\infty).$$

Multiplying the above by $\frac{\partial\hat{a}_0}{\partial\varphi_1}$ and integrating in $\varphi_1 \in (-\infty, \infty)$ leads to

$$\frac{1}{2r^2}\int_{-\infty}^{+\infty}\frac{\partial}{\partial\varphi_1}\left(\frac{\partial\hat{a}_0}{\partial\varphi_1}\right)^2 \mathrm{d}\varphi_1 + \theta_1'(t)\int_{-\infty}^{+\infty}\left(\frac{\partial\hat{a}_0}{\partial\varphi_1}\right)^2 \mathrm{d}\varphi_1 + \int_{-\infty}^{+\infty} f(\hat{a}_0, b_0)\frac{\partial\hat{a}_0}{\partial\varphi_1}\,\mathrm{d}\varphi_1 = 0.$$

The first integral is zero

$$\frac{1}{2r^2}\int_{-\infty}^{+\infty}\frac{\partial}{\partial\varphi_1}\left(\frac{\partial\hat{a}_0}{\partial\varphi_1}\right)^2 \mathrm{d}\varphi_1 = \frac{1}{2r^2}\left(\frac{\partial\hat{a}_0}{\partial\varphi_1}\right)^2\Big|_{\varphi_1=-\infty}^{\varphi_1=+\infty} = 0,$$

since $\hat{a}_0$ is constant at the limits of φ_1. Applying a change of variable $s = \hat{a}_0(\varphi_1, t)$ the last integral can be written as

$$\int_{-\infty}^{+\infty} f(\hat{a}_0, \bar{b}_0)\frac{\partial\hat{a}_0}{\partial\varphi_1}\,\mathrm{d}\varphi_1 = -\int_{a_1(\bar{b}_0)}^{a_3(\bar{b}_0)} f(\xi, \bar{b}_0)\,\mathrm{d}\xi.$$

Hence, finally the following equality holds

$$\theta_1'(t) = \frac{\int_{a_1(\bar{b}_0)}^{a_3(\bar{b}_0)} f(\xi, \bar{b}_0)\,\mathrm{d}\xi}{\int_{-\infty}^{+\infty}\left(\frac{\partial\hat{a}_0}{\partial\varphi_1}\right)^2 \mathrm{d}\varphi_1}. \tag{2.68}$$

As $\int_{-\infty}^{+\infty}\left(\frac{\partial\hat{a}_0}{\partial\varphi_1}\right)^2 d\varphi_1 > 0$, the previous equality gives us an important information about

the speed of the front, which moves with the same sign of the function

$$I(b) = \int_{a_1(b)}^{a_3(b)} f(s,b)\ \mathrm{d}s, \tag{2.69}$$

which is represented in Figure 2.6.

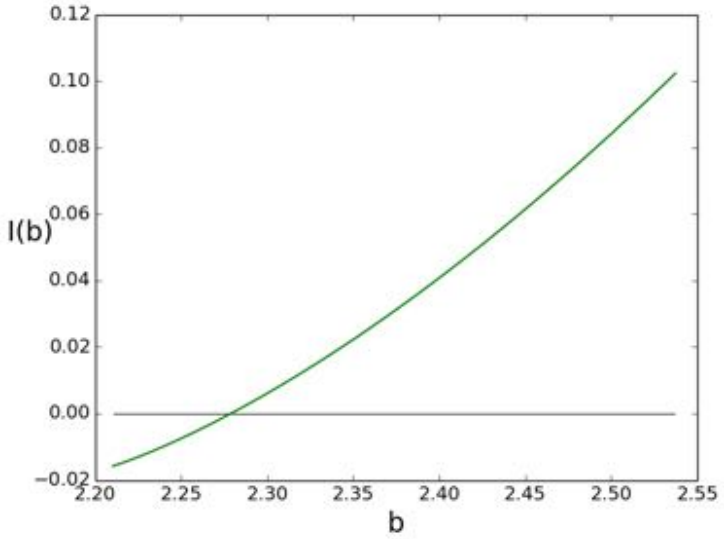

Figure 2.6: The integral $I(b) = \int_{a_1(b)}^{a_3(b)} f(s,b)\mathrm{d}s$ with f defined in (2.64) and parameter values in Table 2.1. $I(b)$ increases in $[b_1, b_2]$ and has one zero $b_c \approx 2.28$, obtained by numerical estimation. The speed of the propagation of a is related to a decreasing of the bulk component and stops when b reaches the critical value b_c.

We remark that $I(b)$ is an increasing function, since

$$\begin{aligned} I'(b) &= f(a_3(b),b)a_3'(b) - f(a_1(b),b)a_1'(b) + \int_{a_1(b)}^{a_3(b)} \frac{\partial f(a,b)}{\partial b}\ \mathrm{d}a \\ &= \int_{a_1(b)}^{a_3(b)} \left(k_0 + \frac{\gamma a^2}{1+a^2}\right)\ \mathrm{d}a > 0 \end{aligned}$$

given that $a_1(b) < a_3(b)$ and the parameters k_0 and γ are positive. The existence of a critical value b_c such that $I(b_c) = 0$ can be proven by showing that, for some $\varepsilon > 0$, $I(b_1+\varepsilon) < 0$ and $I(b_2-\varepsilon) > 0$, where b_1 and b_2 are the extremal values for the existence of three zeros $a(b)$ of $f(a,b)$. In fact when $b = b_1$ or $b = b_2$ the function $f(a,b)$ has only two roots, i.e. between the roots it is either entirely negative or entirely positive. If $b = b_1 - \varepsilon$ or $b = b_2 + \varepsilon$ then the integral is infinite. However as $I(b)$ is an increasing function, by continuity it follows that $I(b_1+\varepsilon) < 0$ and $I(b_2-\varepsilon) > 0$. This shows the existence of the critical value b_c and, by (2.68), follows that a increases its high concentration region for $b > b_c$.

Step c) We now prove that if θ_1 increases, i.e. the high concentration peak for a

expands its width, then the quantity b decreases all over the domain. Since a_1 and a_3 are not constant, in principle propagation of a does not necessarily imply an increment of its overall amount (which, by conservation of total mass (2.34) would have implied depletion of b). Therefore, we start rewriting (2.34) in terms of the asymptotic expansion as

$$M_0 = \int_\Omega b_0 \, \mathrm{d}\mathbf{x} + \int_\Gamma a_0 \, \mathrm{d}s + O(\varepsilon).$$

At the previous step we have seen that b_0 is spatially homogeneously distributed and a_0 is approximately $a_3(b_0)$ if $|\theta| < \theta_1$ or $a_1(b_0)$ otherwise. Therefore we can rewrite the previous equation as

$$\pi r^2 b_0(t) + 2\theta_1(t) r \, a_3(b_0) + 2r \left(\pi - \theta_1(t)\right) a_1(b_0) + O(\varepsilon) = M_0. \tag{2.70}$$

Discarding terms $O(\varepsilon)$ and differentiating (2.70) with respect to t results in

$$\pi r^2 b_0'(t) + 2r\theta_1'(t) a_3(b_0) + 2r\theta_1(t) a_3'(b_0) b_0'(t) + 2r(\pi - \theta_1(t)) a_1'(b_0) b_0'(t) - 2r\theta_1'(t) a_1(b_0) = 0,$$

from which, rearranging the terms, leads to

$$b_0'(t) = -2 \frac{a_3(b_0) - a_1(b_0)}{\pi r^2 + 2\theta_1(t) r \, a_3'(b_0) + 2r \left(\pi - \theta_1(t)\right) a_1'(b_0)} \theta_1'(t) r. \tag{2.71}$$

We now prove that the denominator in (2.71) is positive. Let us differentiate with respect to b the equation $f(a_i(b), b) = 0$ for $i = 1$ and 3

$$0 = \frac{d}{db} f(a_i(b), b) = a_i'(b) \frac{\partial f}{\partial a}\Big|_{(a,b)=(a_i(b),b)} + \frac{\partial f}{\partial b}\Big|_{(a,b)=(a_i(b),b)}. \tag{2.72}$$

From which we get

$$a_i'(b) = -\left(\frac{\partial f}{\partial a}\Big|_{(a,b)=(a_i(b),b)} \right)^{-1} \frac{\partial f}{\partial b}\Big|_{(a,b)=(a_i(b),b)}. \tag{2.73}$$

We recall that the bistability condition (2.46) requires $\frac{\partial f}{\partial a}\Big|_{(a,b)=(a_i(b),b)} \neq 0$ and this is also clear from (2.72), since $\frac{\partial f}{\partial b} > 0, \forall a$. Hence, using (2.46) in (2.73), we conclude that

$$a_1'(b) > 0, \quad \text{and} \quad a_3'(b) > 0. \tag{2.74}$$

From (2.74), it is now clear the positiveness of the denominator in (2.71), while the sign of the numerator of (2.71) is the opposite of the sign of $\theta_1'(t)$: if $\theta_1'(t) > 0$ then $b_0'(t) < 0$ and

vice versa. This finally proves that the propagation of active GTPase a over the boundary is related to a decreasing of the bulk component b.

Step d) In order to achieve polarisation, the propagation of a needs to stop, i.e. at a certain time $\bar{t}$, $\theta_1'(\bar{t}) = 0$ and this happens when $b(t)$ reaches the critical value b_c. Therefore, ignoring terms of order $O(\varepsilon)$ we have

$$M_0 = \pi r^2 b_c + 2\theta_1(\bar{t}) r \; a_3(b_c) + 2r(\pi - \theta_1(\bar{t}))a_1(b_c).$$

We rewrite it in the form

$$M_0 = \pi r^2 b_c + 2r\theta_1(\bar{t})\big(a_3(b_c) - a_1(b_c)\big) + 2\pi r \; a_1(b_c).$$

Since we require $0 < \theta_1 < \pi$ then

$$M_0 < \pi r^2 b_c + 2\pi r\big(a_3(b_c) - a_1(b_c)\big) + 2\pi r \; a_1(b_c) = \pi r^2 b_c + 2\pi r \; a_3(b_c)$$

and

$$M_0 > \pi r^2 b_c + 2\pi r \; a_1(b_c).$$

We therefore have found a condition on M_0 equivalent to the classical wave pinning model (Mori et al., 2011). To have pinning we need to take an initial value $b_0 > b_c$ and a_0 such that

$$m_1 < M_0 < m_2, \tag{2.75}$$

where the quantity $m_1 := \pi r^2 b_c + 2\pi r \; a_1(b_c)$ represents the total mass at the equilibrium with the lowest active GTPase, while the quantity $m_3 := \pi r^2 b_c + 2\pi r \; a_3(b_c)$ represents the total mass at the equilibrium where the whole membrane has been activated, with no pinning taking place. In order to have a heterogeneous steady state for a, *i.e.* obtain a pinned active GTPase propagation state, the total amount M_0 of GTPase should not be neither too low nor too high.

2.8 Bistability and polarisation

In this section we are interested in mapping parameter regions for all possible different behaviours of the two- and three-dimensional BSWP model (2.15)-(2.18) in order to get some insights on the role of geometry. Indeed, depending on the parameters, the model is able to generate different responses, for example it supports spatial homogeneous solu-

tions. We will start from this point, analysing the role of the reactions in the system. In a second step, we will use an approximated nonlinear analysis in order to identify the spatial responses of the BSWP model with respect to small perturbations of the boundary component from the spatially homogeneous state. We remark that the following analysis is basically independent of the spatial dimension.

2.8.1 Well mixed model

Integrating equation (2.15) in Ω and applying the divergence theorem with (2.16), we get

$$\int_\Omega \frac{\partial b}{\partial t}\, \mathrm{d}\mathbf{x} = -\int_\Gamma f(a,b)\, \mathrm{d}s.$$

Since we want to consider spatial homogeneous solutions (b_g, a_g), this corresponds to

$$\frac{\partial b_g}{\partial t}\int_\Omega 1\, \mathrm{d}\mathbf{x} = -f(a_g,b_g)\int_\Gamma 1\, \mathrm{d}s,$$

from which, dividing by $\int_\Gamma 1\, \mathrm{d}s$, we obtain

$$\omega\frac{\mathrm{d}b_g}{\mathrm{d}t} = -f(a_g,b_g). \tag{2.76}$$

Here $\omega = |\Omega|/|\Gamma|$ appears as a consequence of the difference in dimensionality between bulk and surface, while in Section 2.2.3 it was introduced in the function $f(a,b)$ as a binding parameter for the Rho GTPase proteins. We also recall that ω, having unit length, makes the above equation dimensionally consistent (see also Table 2.1).

Equation (2.76) coupled to

$$\frac{\mathrm{d}a_g}{\mathrm{d}t} = f(a_g,b_g), \tag{2.77}$$

constitutes the so-called *well mixed system*, which we aim to study in this section. We note that in (2.76)-(2.77) the following quantity is conserved

$$\frac{a_g(t)}{\omega} + b_g(t) = \frac{a_g(0)}{\omega} + b_g(0),$$

which can be interpreted as a scaled total concentration. Indeed, it follows from (2.34) that

$$M_0 = \int_\Gamma a(\mathbf{x},t)\, \mathrm{d}s + \int_\Omega b(\mathbf{x},t)\, \mathrm{d}\mathbf{x} = |\Gamma|a_g(t) + |\Omega|b_g(t) = |\Omega|\left(\frac{a_g(t)}{\omega} + b_g(t)\right)$$

and the analysis of (2.76)-(2.77) reduces to the single equation

$$\frac{\mathrm{d}a_g}{\mathrm{d}t} = f\left(a_g, m_0 - \frac{a_g}{\omega}\right), \tag{2.78}$$

where $m_0 := \frac{M_0}{|\Omega|}$. From the study of the steady states, $f\left(a_g, m_0 - \frac{a_g}{\omega}\right) = 0$ is a third degree polynomial in a_g and, by the Descartes' rule of signs, it can be shown that it has either one or three positive real roots. Therefore, from the negativity of the leading order coefficient, it follows that there exists either a single stable steady state or 3 steady states where the outer two are stable. Bistability corresponds to the co-existence of high and low GTPase activities at the cell membrane. When only a single steady state is possible, then the well mixed model admits only one response between low and high activities.

The responses of the model for different values of the parameters m_0 and γ are shown in Figure 2.7, where the bistability region is indicated by the blue color, while the remaining region (white and red areas) indicates existence of a unique steady state for (2.78).

2.8.2 Local perturbation analysis

Local perturbation analysis (LPA) is a convenient tool that can be very useful in understanding how a local perturbation might affect some classes of reaction-diffusion systems with fast and slow components. We refer to (Holmes, 2014; Holmes et al., 2015; Holmes and Edelstein-Keshet, 2016) for more details and the LPA. The basic idea is the following: let system (2.15)-(2.18) possess a spatially homogeneous profile $(b_g(t), a_g(t))$ and apply a narrow and well localised perturbation to the slow-diffusive component a, such as the one defined by equation (2.66). Based on the fact that we have a fast and a slow variable $(D_b >> D_a)$ we consider the limits $D_b \to \infty$ and $D_a \to 0$. In this case, (2.15)-(2.16) tend to

$$\begin{aligned} \Delta b &= 0, \qquad \mathbf{x} \in \Omega, \\ \mathbf{n} \cdot \nabla b &= 0, \qquad \mathbf{x} \in \Gamma, \end{aligned}$$

and b maintains a global spatial uniform profile $b_g(t)$. On the other hand $a(\mathbf{x}, t)$ initially has a global spatial uniform profile a_g in most of the cell membrane, except in the narrow area where the perturbation a_p is applied. Considering the limit $D_a \to 0$, the equation for a (2.17) reduces to an ODE. The perturbation a_p does not influence through diffusion the baseline level a_g and, given its small mass, it does neither substantially influence b. In these terms it is possible to consider $a_p(t)$ and $a_g(t)$ as different entities to obtain the

following ODE system

$$\frac{\mathrm{d}a_p}{\mathrm{d}t} = f\left(a_p, b_g\right), \tag{2.79}$$
$$\frac{\mathrm{d}a_g}{\mathrm{d}t} = f\left(a_g, b_g\right), \tag{2.80}$$
$$\omega\frac{\mathrm{d}b_g}{\mathrm{d}t} = -f\left(a_g, b_g\right). \tag{2.81}$$

It can be easily shown using conservation that the above system can be reduced to the following system

$$\frac{\mathrm{d}a_p}{\mathrm{d}t} = f\left(a_p, m_0 - \frac{a_g}{\omega}\right), \tag{2.82}$$
$$\frac{\mathrm{d}a_g}{\mathrm{d}t} = f\left(a_g, m_0 - \frac{a_g}{\omega}\right). \tag{2.83}$$

The above ODE system indicates that steady states for a_p might differ from the steady states for a_g. Indeed, we interpret this case as the polarisation response: the perturbation has affected the system and two states on the boundary are simultaneously present, with a localised high activity and low activity elsewhere. Using this analysis and numerical calculations, we obtain the polarisation region in the parameter plane $m_0\gamma$, which is shown by the coloured areas (red and blue regions) in Figure 2.7.

We have calculated the bistability and the polarisation regions for different values of ω, obtaining qualitatively identical results. However, the regions increase their sizes with decreasing ω. For the three-dimensional case, for a given volume $|\Omega|$, $\max_\Gamma \omega = r/3$ where r is the radius of the sphere enclosing that volume. Therefore, having a fixed volume, the more the surface increases, the smaller ω becomes. This is an interesting result which suggests that changes in shapes and increases in the cell surface relative to its volume enhance the possibility of achieving polarisation. Indeed a key feature of cell migration is the change in cell shape (Reig et al., 2014).

In Holmes and Edelstein-Keshet (2016) the same analysis was done for the model (2.1)-(2.3) where a and b are defined on the same unidimensional spatial domain. They derive a well mixed and LPA system which is a special case of our models (2.76)-(2.77) and (2.79)-(2.81) when $\omega = 1$. They initially use a sharp switch approximation for the reaction (2.18) (passing to the limit as $n \to \infty$) in order to be able to calculate the steady states analytically. Then they numerically calculate the bistability and polarisation regions for (2.18) with $n = 4$. Our results, when $n = 2$, are totally in line with their work and suggests that the bulk-surface framework maintains and extends the features of the original wave

pinning model (2.1)-(2.2).

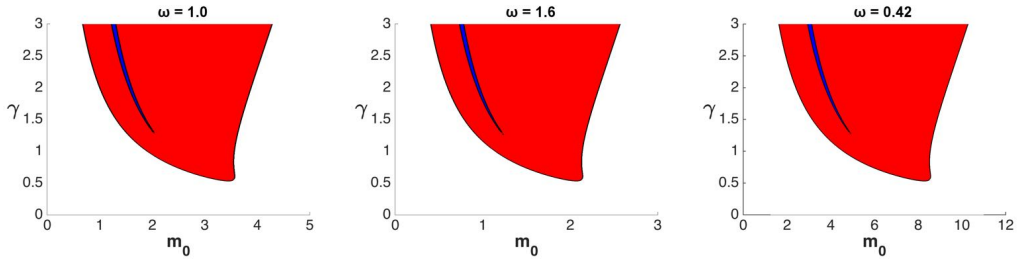

Figure 2.7: Bistability (blue) and polarity (red and blue) regions for different values of the parameter $\omega = |\Omega|/|\Gamma|$. On the x-axis we vary the total mass per unit volume $m_0 = M_0/|\Omega|$. On the y-axis the activation rate γ of Rho-GTPase positive feedback is varied. The blue region defines the parameter region in which all the possible responses (uniform high activity, uniform low activity or polarisation) can take place. Note that for small values of the positive-feedback rate γ no polarisation is possible and the stronger the feedback, the bigger can be the total initial concentration. From left to right: $\omega = 1$ μm, which can be generated taking Ω as a sphere of radius 3 μm; $\omega = 1.6$ μm which correspond to the choice of a sphere of radius of 5 μm, as in Mori et al. (2008); $\omega = 0.42$ μm which corresponds to a non-spherical domain having a surface 4 times bigger than the one of a sphere of radius 5 μm but with same volume. While we show qualitatively similar results, we also highlight the role of ω: it represents the ratio between volume and surface area of the cell and, on domains of the same volume, ω is smaller in the ones having larger surfaces. The figure shows that decrements of ω cause enlargements in the bistability and polarisation areas. Although the three figures look almost the same, note the differences in the horizontal scales representing the amount of m_0.

2.9 The bulk-surface finite element method

Next, we present the bulk-surface finite element method (BS-FEM) (see for example Madzvamuse and Chung (2016b)) which we adopt to solve the BSWP model (2.15)-(2.18). The basic idea is to describe the model numerically by systems of linear equations, which are easy to solve. In order to do this, we first restate the BSWP model in a weaker formulation, then in a second step we discretise the spatial and temporal domains. This allows us to finally derive the systems of linear equations.

2.9.1 Weak formulation

The weak formulation of the BSWP model (2.15)-(2.18) is obtained by testing equations (2.17) and (2.15) respectively by any function $w \in H^1(\Gamma)$ and $v \in H^1(\Omega)$, as follows:

$$\int_\Gamma \dot{a} w \, \mathrm{d}s = D_a \int_\Gamma \Delta_\Gamma a \, w \, \mathrm{d}s + \int_\Gamma f(a,b) w \, \mathrm{d}s,$$
$$\int_\Omega \dot{b} v \, \mathrm{d}\mathbf{x} = D_b \int_\Omega \Delta b \, v \, \mathrm{d}\mathbf{x},$$

where we have used the dot notation to indicate the temporal derivative. Applying the divergence theorem (see also Theorem 1.5.3 in Section 1.5.2) to the above equations we

obtain:

$$\int_\Gamma \dot{a}w \, \mathrm{d}s + D_a \int_\Gamma \nabla_\Gamma a \cdot \nabla_\Gamma w \, \mathrm{d}s = \int_\Gamma f(a,b)w \, \mathrm{d}s,$$
$$\int_\Omega \dot{b}v \, \mathrm{d}\mathbf{x} + D_b \int_\Omega \nabla b \cdot \nabla v \, \mathrm{d}\mathbf{x} = D_b \int_\Gamma \mathbf{n} \cdot \nabla b v \, \mathrm{d}s.$$

Lastly, using the boundary condition (2.16) in the equation for b, we obtain the weak formulation of the BSWP model (2.15)-(2.18), which reads: find

$$a \in L^2([0,T]; H^1(\Gamma)) \cap L^\infty([0,T] \times \Gamma)$$

with $\dot{a} \in L^2([0,T]; H^{-1}(\Gamma))$ and

$$b \in L^2([0,T]; H^1(\Omega)) \cap L^\infty([0,T] \times \overline{\Omega})$$

with $\dot{b} \in L^2([0,T]; H^{-1}(\Omega))$ such that

$$\int_\Gamma \dot{a}w \, \mathrm{d}s + D_a \int_\Gamma \nabla_\Gamma a \cdot \nabla_\Gamma w \, \mathrm{d}s = \int_\Gamma f(a,b)w \, \mathrm{d}s, \tag{2.84}$$
$$\int_\Omega \dot{b}v \, \mathrm{d}\mathbf{x} + D_b \int_\Omega \nabla b \cdot \nabla v \ \ \mathrm{d}\mathbf{x} = -\int_\Gamma g(a) b \, v \, \mathrm{d}s + \int_\Gamma \beta a \, v \, \mathrm{d}s, \tag{2.85}$$

$\forall w \in H^1(\Gamma)$ and $\forall v \in H^1(\Omega)$ and such that (2.19)-(2.20) are satisfied. For future convenience, in equation (2.85) we have introduced the function $g(a) := \omega\Big(k_0 + \frac{\gamma a^2}{K^2+a^2}\Big)$. We remind that the spaces H^1 and $L^2(0,T;H^1)$ are defined in Section 1.5.1, while H^{-1} is the dual space of H^1 (for definition and theory see for example the textbook Evans (2010)).

2.9.2 Spatial discretisation

We consider a closed polyhedral approximation Ω_h of Ω and define a mesh over it, i.e. we find a suitable set $\mathcal{T}_h = \{T_1, ..., T_{N_\mathcal{T}}\}$ such that $\overline{\Omega_h} = \bigcup_{i=1}^{N_\mathcal{T}} T_i$, where each T_i is a tetrahedron, such that for any $i \neq j$ we have $\overset{\circ}{T}_i \cap \overset{\circ}{T}_j = \emptyset$ and if $T_i \cap T_j \neq \emptyset$ then the intersection is either a common face, side or vertex of the two elements. As well, we approximate Γ with $\Gamma_h := \partial\Omega_h$. A natural mesh $\mathcal{S}_h$ for Γ_h can be easily deduced from the bulk mesh $\mathcal{T}_h$. Indeed, the boundary of Ω_h is discretised by the external faces of some tetrahedra of $\mathcal{T}_h$. These faces, which are triangles, compose $\mathcal{S}_h$. We indicate with N_h the number of vertices in the mesh $\mathcal{T}_h$ and with $\hat{N}_h$ the number of vertices in $\mathcal{S}_h$. The definition of the two meshes $\mathcal{T}_h$ and $\mathcal{S}_h$ and their compatibility is a crucial point for the bulk-surface finite element method.

Let now $\mathbb{P}_1(D)$ be the space of first degree polynomials over a set $D \subset \mathbb{R}^d$ and we define the following function spaces

$$V_h(\Omega_h) := \left\{ v : \Omega_h \to \mathbb{R} \ : \ v \in C^0(\Omega_h), v|_T \in \mathbb{P}_1(T), \ \forall T \in \mathcal{T}_h \right\},$$
$$W_h(\Gamma_h) := \left\{ w : \Gamma_h \to \mathbb{R} \ : \ w \in C^0(\Gamma_h), w|_S \in \mathbb{P}_1(S), \ \forall S \in \mathcal{S}_h \right\},$$

which are subsets, respectively, of $H^1(\Omega_h)$ and $H^1(\Gamma_h)$. A semi-discrete finite element formulation can be obtained by restricting the search space of the solutions from $H^1(\Omega_h)$ and $H^1(\Gamma_h)$ to their representatives in the subsets $V_h(\Omega_h)$ and $W_h(\Gamma_h)$. For the FEM theory we refer to the textbooks by Thomée (1997) and Quarteroni and Valli (2008).

Hence, the semi-discrete weak formulation reads: find $a_h \in L^2([0,T]; W_h(\Gamma_h))$ with $\dot{a_h} \in L^2([0,T]; W_h(\Gamma_h))$ and $b_h \in L^2([0,T]; V_h(\Omega_h))$ with $\dot{b} \in L^2([0,T]; V_h(\Omega_h))$ such that

$$\int_{\Gamma_h} \dot{a_h} w_h \, \mathrm{d}s + D_a \int_{\Gamma_h} \nabla_\Gamma a_h \cdot \nabla_\Gamma w_h \, \mathrm{d}s = \int_{\Gamma_h} f(a_h, b_h) w_h \, \mathrm{d}s, \tag{2.86}$$
$$\int_{\Omega_h} \dot{b_h} v_h \, \mathrm{d}\mathbf{x} + D_b \int_{\Omega_h} \nabla b_h \cdot \nabla v_h \, \mathrm{d}\mathbf{x} = -\int_{\Gamma_h} g(a_h) b_h \, v_h \, \mathrm{d}s + \int_{\Gamma_h} \beta a_h \, v_h \, \mathrm{d}s, \tag{2.87}$$

$\forall w_h \in W_h(\Gamma_h)$ and $\forall v_h \in V_h(\Omega_h)$ and such that a_h, b_h satisfy

$$a_h(\mathbf{x}, 0) = a_{in,h}(\mathbf{x}), \qquad \mathbf{x} \in \Gamma_h, \tag{2.88}$$
$$b_h(\mathbf{x}, 0) = b_{in,h}(\mathbf{x}), \qquad \mathbf{x} \in \Omega_h, \tag{2.89}$$

where $a_{in,h}(\mathbf{x}) \in W_h(\Gamma_h)$ and $b_{in,h}(\mathbf{x}) \in V_h(\Omega_h)$ are approximations respectively of $a_{in}(\mathbf{x}) \in H^1(\Gamma)$ and $b_{in}(\mathbf{x}) \in H^1(\Omega)$, as given in (2.19)-(2.20). A remark on how to approximate the initial conditions is given at the end of the section.

A basis for $W_h(\Gamma_h)$ is the set of the hat functions $\psi_i \in W_h(\Gamma_h)$ with the property that $\psi_i(\mathbf{x}_j) = \delta_{i,j}$ for any vertex $\mathbf{x}_j$ of $\mathcal{S}_h$ and $\forall i, j = 1, \ldots, \hat{N}_h$, where $\delta_{i,j}$ indicates the Kronecker delta ($\delta_{i,j} = 1$ if $i = j$, zero otherwise). As well, we denote with $\varphi_1, \ldots, \varphi_{N_h}$ the hat functions on $\mathcal{T}_h$, which generate a basis of $V_h(\Omega_h)$. Therefore we seek solutions of the form

$$a_h(\mathbf{x}, t) = \sum_{j=1}^{\hat{N}_h} a_j(t) \psi_j(\mathbf{x}), \quad \text{with } a_j(t) := a_h(\mathbf{x}_j, t), \quad j = 1, \ldots, \hat{N}_h, \tag{2.90}$$
$$b_h(\mathbf{x}, t) = \sum_{j=1}^{N_h} b_j(t) \varphi_j(\mathbf{x}), \quad \text{with } b_j(t) := b_h(\mathbf{x}_j, t), \quad j = 1, \ldots, N_h. \tag{2.91}$$

In terms of the basis functions, (2.86)-(2.87) are equivalent to the following two ODE

systems

$$\sum_{j=1}^{\hat{N}_h} \dot{a_j} \int_{\Gamma_h} \psi_j \psi_i \, \mathrm{d}s + D_a \sum_{j=1}^{\hat{N}_h} a_j \int_{\Gamma_h} \nabla_\Gamma \psi_j \cdot \nabla_\Gamma \psi_i \, \mathrm{d}s = \int_{\Gamma_h} f(a_h, b_h) \psi_i \, \mathrm{d}s, \qquad i = 1, \ldots, \hat{N}_h \tag{2.92}$$

$$\begin{aligned} \sum_{j=1}^{N_h} \dot{b_j} \int_{\Omega_h} \varphi_j \varphi_i \, \mathrm{d}\mathbf{x} + D_b \sum_{j=1}^{N_h} b_j \int_{\Omega_h} \nabla \varphi_j \cdot \nabla \varphi_i \, \mathrm{d}\mathbf{x} &= -\sum_{j=1}^{N_h} b_j \int_{\Gamma_h} g(a_h) \varphi_j \varphi_i \, \mathrm{d}s \\ &+ \sum_{j=1}^{\hat{N}_h} a_j \int_{\Gamma_h} \beta \psi_j \varphi_i \, \mathrm{d}s, \qquad i = 1, \ldots, N_h \end{aligned} \tag{2.93}$$

which we write in compact form as follows:

$$\mathrm{M}_{\Gamma_h} \dot{\boldsymbol{a}} + D_a \mathrm{K}_{\Gamma_h} \boldsymbol{a} = F(\boldsymbol{a}, \boldsymbol{b}), \tag{2.94}$$

$$\mathrm{M}_{\Omega_h} \dot{\boldsymbol{b}} + D_b \mathrm{K}_{\Omega_h} \boldsymbol{b} + G(\boldsymbol{a}) \boldsymbol{b} = \beta H \boldsymbol{a}, \tag{2.95}$$

where

$$\begin{aligned} &\boldsymbol{a} = (a_j(t))_{j=1,\ldots,\hat{N}_h}, \ \boldsymbol{b} = (b_j(t))_{j=1,\ldots,N_h}, \ \mathrm{M}_{\Gamma_h} = \left(\int_{\Gamma_h} \psi_j \psi_i \, \mathrm{d}s \right)_{i,j=1,\ldots,\hat{N}_h}, \\ &\mathrm{K}_{\Gamma_h} = \left(\int_{\Gamma_h} \nabla_\Gamma \psi_j \cdot \nabla_\Gamma \psi_i \, \mathrm{d}s \right)_{i,j=1,\ldots,\hat{N}_h}, \ F(\boldsymbol{a}, \boldsymbol{b}) = \left(\int_{\Gamma_h} f(a_h, b_h) \psi_i \, \mathrm{d}s \right)_{i=1,\ldots,\hat{N}_h}, \\ &\mathrm{M}_{\Omega_h} = \left(\int_{\Omega_h} \varphi_j \varphi_i \, \mathrm{d}\mathbf{x} \right)_{i,j=1,\ldots,N_h}, \ \mathrm{K}_{\Omega_h} = \left(\int_{\Omega_h} \nabla \varphi_j \cdot \nabla \varphi_i \, \mathrm{d}\mathbf{x} \right)_{i,j=1,\ldots,N_h}, \\ &G(\boldsymbol{a}) = \left(\int_{\Gamma_h} g(a_h) \varphi_j \varphi_i \ \mathrm{d}s \right)_{i,j=1,\ldots,\hat{N}_h} \text{ and } H = \left(\int_{\Gamma_h} \psi_j \varphi_i \ \mathrm{d}s \right)_{\substack{i=1,\ldots,N_h \\ j=1,\ldots,\hat{N}_h}}. \end{aligned}$$

The approximation of the initial conditions in the discrete spaces $W_h(\Gamma_h)$ and $V_h(\Omega_h)$ requires the definition of the coefficients of $a_{in,h}(\mathbf{x})$ and $b_{in,h}(\mathbf{x})$ over all the vertices of the mesh. One possible way of solving this problem is by linear interpolation over the mesh of the continuous initial conditions (2.19)-(2.20), i.e. the coefficients a_i^0, b_i^0 of the linear combinations

$$a_{in,h}(\mathbf{x}) = \sum_{i=1}^{\hat{N}_h} a_i^0 \psi_i(\mathbf{x}) \text{ and } b_{in,h}(\mathbf{x}) = \sum_{i=1}^{N_h} b_i^0 \varphi_i(\mathbf{x}).$$

are given by

$$a_i^0 = a_{in}(\mathbf{x}_i), \qquad i = 1, \ldots, \hat{N}_h, \tag{2.96}$$

$$b_i^0 = b_{in}(\mathbf{x}_i), \qquad i = 1, \ldots, N_h. \tag{2.97}$$

Before proceeding further in the numerical approximation of the BSWP model, we show the following conservation property of the semi-discrete system (2.94)-(2.95).

Theorem 2.9.1. The semi-discrete system (2.94)-(2.95) conserves the initial total mass, i.e.

$$\int_{\Omega_h} b_h(\mathbf{x},t)\,\mathrm{d}\mathbf{x}+\int_{\Gamma_h} a_h(\mathbf{x},t)\,\mathrm{d}s=\int_{\Omega_h} b_{in,h}(\mathbf{x})\,\mathrm{d}\mathbf{x}+\int_{\Gamma_h} a_{in,h}(\mathbf{x})\,\mathrm{d}s,\qquad \forall t\in(0,T]. \tag{2.98}$$

Proof. The proof takes advantage of the following basis functions property

$$\sum_{i=1}^{\hat{N}_h}\psi_i(\mathbf{x})=1 \text{ and } \sum_{i=1}^{N_h}\varphi_i(\mathbf{x})=1, \tag{2.99}$$

from which, by summing equation (2.92) over the index $i=1,\dots,\hat{N}_h$, we get

$$\sum_{j=1}^{\hat{N}_h}\int_{\Gamma_h}\dot{a_j}\psi_j\,\mathrm{d}s=\int_{\Gamma_h} f(a_h,b_h)\,\mathrm{d}s.$$

We observe that the integral relative to the diffusion term has disappeared since $\sum_i \nabla_\Gamma\psi_i=\nabla_\Gamma\left(\sum_i\psi_i\right)=\nabla 1=\mathbf{0}$. In the same way, summing (2.93) over $i=1,\dots,N_h$ we obtain

$$\sum_{j=1}^{N_h}\int_{\Omega_h}\dot{b_j}\varphi_j\,\mathrm{d}\mathbf{x}=-\sum_{j=1}^{N_h}b_j\int_{\Gamma_h} g(a_h)\varphi_j\,\mathrm{d}s+\sum_{j=1}^{\hat{N}_h}a_j\int_{\Gamma_h}\beta\psi_j\,\mathrm{d}s.$$

Taking the time derivatives outside the integrals and using (2.90)-(2.91), the above equations can be written as

$$\begin{aligned}\frac{\mathrm{d}}{\mathrm{d}t}\int_{\Gamma_h} a_h\,\mathrm{d}s&=\int_{\Gamma_h} f(a_h,b_h)\,\mathrm{d}s,\\ \frac{\mathrm{d}}{\mathrm{d}t}\int_{\Omega_h} b_h\,\mathrm{d}\mathbf{x}&=-\int_{\Gamma_h} f(a_h,b_h)\,\mathrm{d}s.\end{aligned}$$

And summing these last two, we get

$$\frac{\mathrm{d}}{\mathrm{d}t}\left(\int_{\Gamma_h} a_h(\mathbf{x},t)\,\mathrm{d}s+\int_{\Omega_h} b_h(\mathbf{x},t)\,\mathrm{d}\mathbf{x}\right)=0,$$

which implies (2.98), concluding the proof. □

Remark 2.9.1. Theorem 2.9.1 holds for any function $f(a,b)$ in $L^1(\Gamma_h)$.

2.9.3 Temporal discretisation

We discretise the time interval $[0, T]$ uniformly with $N_t \in \mathbb{N}$ time points, corresponding to choosing a time step $\tau_h = \frac{T}{N_t}$. We define

$$t^n = t^{n-1} + \tau_h, \text{ or equivalently } t^n = n\tau_h, \quad n = 1, \cdots, N_t,$$

with $t^0 = 0$. We will indicate the solutions at discrete time t^n with a_h^n and b_h^n and the corresponding coefficient vectors with $\boldsymbol{a}^n$ and $\boldsymbol{b}^n$. These are initialised by setting $\boldsymbol{a}^0 = \left(a_1^0, \ldots, a_{\hat{N}_h}^0\right)$ and $\boldsymbol{b}^0 = \left(b_1^0, \ldots, b_{N_h}^0\right)$, whose elements are defined by (2.96)-(2.97). We use a predictor-corrector finite difference method to approximate the time-derivatives (see for example MacDonald et al. (2016a)). To calculate the solution of (2.94)-(2.95) at each time point, we follow the steps outlined below.

1. We predict a solution $\tilde{\boldsymbol{a}}^n$ for the surface component using the IMEX method (IMplicit diffusion, EXplicit reaction), solving the following system of linear equations:

$$\left(M_\Gamma + \tau_h D_a K_\Gamma\right) \tilde{\boldsymbol{a}}^n = M_\Gamma \boldsymbol{a}^{n-1} + \tau_h F(\boldsymbol{a}^{n-1}, \boldsymbol{b}^{n-1}). \tag{2.100}$$

2. We calculate the solution $\boldsymbol{b}^n$ using Crank-Nicolson time discretisation and the predicted solution $\tilde{\boldsymbol{a}}^n$

$$\begin{aligned}&\left(M_\Omega + \frac{1}{2}\tau_h D_b K_\Omega + \frac{1}{2}\tau_h G(\tilde{\boldsymbol{a}}^n)\right) \boldsymbol{b}^n \\ &= \left(M_\Omega - \frac{1}{2}\tau_h D_b K_\Omega - \frac{1}{2}\tau_h G(\boldsymbol{a}^{n-1})\right) \boldsymbol{b}^{n-1} + \frac{1}{2}\tau_h \beta H \tilde{\boldsymbol{a}}^n + \frac{1}{2}\tau_h \beta H \boldsymbol{a}^{n-1}.\end{aligned} \tag{2.101}$$

3. Using the predicted $\tilde{\boldsymbol{a}}^n$ and $\boldsymbol{b}^n$, we correct the predicted solution for $\tilde{\boldsymbol{a}}^n$ using the Crank-Nicolson scheme

$$\left(M_\Gamma + \frac{1}{2}\tau_h D_a K_\Gamma\right) \boldsymbol{a}^n = M_\Gamma \boldsymbol{a}^{n-1} - \frac{1}{2}\tau_h D_a K_\Gamma \tilde{\boldsymbol{a}}^n + \frac{1}{2}\tau_h F(\tilde{\boldsymbol{a}}^n, \boldsymbol{b}^n) + \frac{1}{2}\tau_h F(\boldsymbol{a}^{n-1}, \boldsymbol{b}^{n-1}). \tag{2.102}$$

This method is based on the resolution, at each time step, of three different systems of linear equations, obtained from the finite element discretisation in space and finite difference discretisation in time. It is worth to mention that the method is second order accurate in time (Quarteroni et al., 2010; MacDonald et al., 2016a), and moreover the following property holds.

Proposition 2.9.1. The numerical method (2.100)-(2.102) is conservative, i.e.

$$\int_{\Omega_h} b_h(\mathbf{x},t^n)\,\mathrm{d}\mathbf{x}+\int_{\Gamma_h} a_h(\mathbf{x},t^n)\,\mathrm{d}s=\int_{\Omega_h} b_h(\mathbf{x},0)\,\mathrm{d}\mathbf{x}+\int_{\Gamma_h} a_h(\mathbf{x},0)\,\mathrm{d}s,$$

for all $n=1,...,N_t$.

Proof. Similarly to the proof of Theorem 2.9.1, we take advantage of the basis functions property (2.99). Let us now consider the system (2.101) in its extended form

$$\begin{aligned}
\sum_{j=1}^{N_h} b_j^n\int_{\Omega_h}\varphi_j\varphi_i\,\mathrm{d}\mathbf{x}+\frac{1}{2}\tau_h D_b\sum_{j=1}^{N_h} b_j^n\int_{\Omega_h}\nabla\varphi_j\cdot\nabla\varphi_i\,\mathrm{d}\mathbf{x}\\
+\frac{1}{2}\tau_h\sum_{j=1}^{N_h} b_j^n\int_{\Gamma_h} g(\tilde{a}_h^n)\varphi_j\,\varphi_i\,\mathrm{d}s=\sum_{j=1}^{N_h} b_j^{n-1}\int_{\Omega_h}\varphi_j\varphi_i\,\mathrm{d}\mathbf{x}\\
-\frac{1}{2}\tau_h D_b\sum_{j=1}^{N_h} b_j^{n-1}\int_{\Omega_h}\nabla\varphi_j\cdot\nabla\varphi_i\,\mathrm{d}\mathbf{x}-\frac{1}{2}\tau_h\sum_{j=1}^{N_h} b_j^{n-1}\int_{\Gamma_h} g(a_h^{n-1})\varphi_j\,\varphi_i\,\mathrm{d}s\\
+\frac{1}{2}\tau_h\beta\sum_{j=1}^{\hat{N}_h}\tilde{a}_j^n\int_{\Gamma_h}\psi_j\,\varphi_i\,\mathrm{d}s+\frac{1}{2}\tau_h\beta\sum_{j=1}^{\hat{N}_h} a_j^{n-1}\int_{\Gamma_h}\psi_j\,\varphi_i\,\mathrm{d}s,\quad i=1,\dots,N_h.
\end{aligned}$$

Summing this expression over the index i we get

$$\begin{aligned}
\sum_{j=1}^{N_h} b_j^n\int_{\Omega_h}\varphi_j\,\mathrm{d}\mathbf{x}+\frac{1}{2}\tau_h\sum_{j=1}^{N_h} b_j^n\int_{\Gamma_h} g(\tilde{a}_h^n)\varphi_j\,\mathrm{d}s=\sum_{j=1}^{N_h} b_j^{n-1}\int_{\Omega_h}\varphi_j\,\mathrm{d}\mathbf{x}\\
-\frac{1}{2}\tau_h\sum_{j=1}^{N_h} b_j^{n-1}\int_{\Gamma_h} g(a_h^{n-1})\varphi_j\,\mathrm{d}s+\frac{1}{2}\tau_h\beta\sum_{j=1}^{\hat{N}_h}\tilde{a}_j^n\int_{\Gamma_h}\psi_j\,\mathrm{d}s+\frac{1}{2}\tau_h\beta\sum_{j=1}^{\hat{N}_h} a_j^{n-1}\int_{\Gamma_h}\psi_j\,\mathrm{d}s.
\end{aligned}$$

For convenience the above equation can be written as follows

$$\int_{\Omega_h} b_h^n\,\mathrm{d}\mathbf{x}=\int_{\Omega_h} b_h^{n-1}\,\mathrm{d}\mathbf{x}-\frac{1}{2}\tau_h\int_{\Gamma_h} f(\tilde{a}_h^n,b_h^n)\,\mathrm{d}s-\frac{1}{2}\tau_h\int_{\Gamma_h} f(a_h^{n-1},b_h^{n-1})\,\mathrm{d}s.\qquad(2.103)$$

The system (2.102) in its extended form is

$$\begin{aligned}
\sum_{j=1}^{\hat{N}_h} a_j^n\int_{\Gamma_h}\psi_j\psi_i\,\mathrm{d}s+\frac{1}{2}\tau_h D_a\sum_{j=1}^{\hat{N}_h} a_j^n\int_{\Gamma_h}\nabla_\Gamma\psi_j\cdot\nabla_\Gamma\psi_i\,\mathrm{d}s=\sum_{j=1}^{\hat{N}_h}\tilde{a}_j^{n-1}\int_{\Gamma_h}\psi_j\psi_i\,\mathrm{d}s\\
-\frac{1}{2}\tau_h D_a\sum_{j=1}^{\hat{N}_h}\tilde{a}_j^n\int_{\Gamma_h}\nabla_\Gamma\psi_j\cdot\nabla_\Gamma\psi_i\,\mathrm{d}s+\frac{1}{2}\tau_h\int_{\Gamma_h} f(\tilde{a}_h^n,b_h^n)\psi_i\,\mathrm{d}s\\
+\frac{1}{2}\tau_h\int_{\Gamma_h} f(a_h^{n-1},b_h^{n-1})\psi_i\,\mathrm{d}s,\quad i=1,\dots,\hat{N}_h.
\end{aligned}$$

Summing over $i = 1, \dots, \hat{N}_h$ we get

$$\sum_{j=1}^{\hat{N}_h} a_j^n \int_{\Gamma_h} \psi_j \, \mathrm{d}s = \sum_{j=1}^{\hat{N}_h} \tilde{a}_j^{n-1} \int_{\Gamma_h} \psi_j \, \mathrm{d}s + \frac{1}{2}\tau_h \int_{\Gamma_h} f(\tilde{a}_h^n, b_h^n) \, \mathrm{d}s + \frac{1}{2}\tau_h \int_{\Gamma_h} f(a_h^{n-1}, b_h^{n-1}) \, \mathrm{d}s$$

or, equivalently,

$$\int_{\Gamma_h} a_h^n \, \mathrm{d}s = \int_{\Gamma_h} \tilde{a}_h^{n-1} \, \mathrm{d}s + \frac{1}{2}\tau_h \int_{\Gamma_h} f(\tilde{a}_h^n, b_h^n) \, \mathrm{d}s + \frac{1}{2}\tau_h \int_{\Gamma_h} f(a_h^{n-1}, b_h^{n-1}) \, \mathrm{d}s. \tag{2.104}$$

We want to show that $\int_{\Omega_h} b_h^n \, \mathrm{d}\mathbf{x} + \int_{\Gamma_h} a_h^n \, \mathrm{d}s$ is constant for every n. From (2.103) and (2.104) follows that

$$\int_{\Omega_h} b_h^n \, \mathrm{d}\mathbf{x} + \int_{\Gamma_h} a_h^n \, \mathrm{d}s = \int_{\Omega_h} b_h^{n-1} \, \mathrm{d}\mathbf{x} + \int_{\Gamma_h} a_h^{n-1} \, \mathrm{d}s,$$

from which, iterating, we finally obtain

$$\int_{\Omega_h} b_h^n \, \mathrm{d}\mathbf{x} + \int_{\Gamma_h} a_h^n \, \mathrm{d}s = \int_{\Omega_h} b_h^0 \, \mathrm{d}\mathbf{x} + \int_{\Gamma_h} a_h^0 \, \mathrm{d}s,$$

which concludes the proof. □

We remark that, following the above steps, one could prove conservation of total mass also for other temporal approximations, for example the same holds if Euler backward method is used for approximating equations (2.94)-(2.95).

2.10 Results

In this section we present some simulations on three different domains: a sphere, a capsule and a complex domain, caricature of a polarised fibroblast cell. In all the simulations except for the last one, we set the initial conditions as follows: referring to Proposition 2.4.2, the bulk component is spatially homogeneous with value

$$\overline{b_0} = b_2 - \varepsilon_b(b_2 - b_1), \tag{2.105}$$

with $\varepsilon_b < 1$ such that $\overline{b_0} > b_c$, where b_c is the only zero of $I(b)$ in (2.67). For the surface component, we superimpose a narrow Gaussian function with magnitude $a_p = (a_2 + a_3)/2$ on a spatially homogeneous profile $a_g = (a_1 + a_2)/2$, where a_1, a_2, a_3 are the solutions of

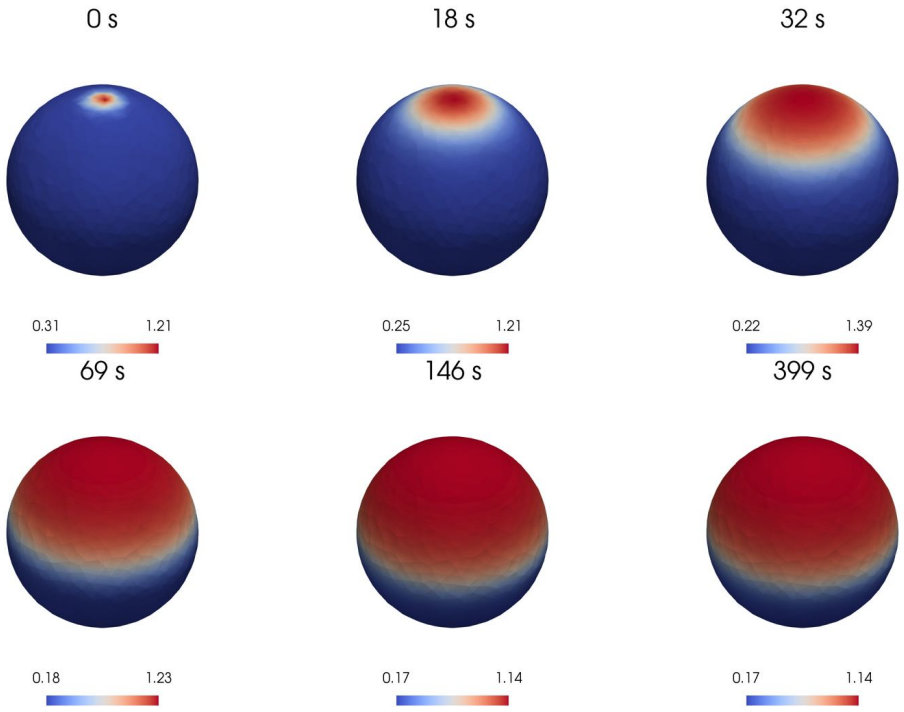

Figure 2.8: Numerical simulations of the BSWP model (2.15)-(2.18) on a sphere: The active form of Rho GTPase a propagating from a "stimulating" initial condition (2.66) over a sphere. The numerical solution reaches a stable configuration after about 100 seconds. See text for further details.

$f(a, \overline{b_0}) = 0$, i.e.

$$a_{in} = a_g + a_p \exp\left(-\frac{(x-x_0)^2 + (y-y_0)^2 + (z-z_0)^2}{\sigma^2}\right) \tag{2.106}$$

where (x_0, y_0, z_0) is the centre of the perturbation. In case of two perturbation peaks with centres (x_0, y_0, z_0) and (x_1, y_1, z_1), we impose the following initial condition

$$\begin{aligned} a_{in} = a_g &+ a_p \exp\left(-\frac{(x-x_0)^2 + (y-y_0)^2 + (z-z_0)^2}{\sigma^2}\right) \\ &+ a_p \exp\left(-\frac{(x-x_1)^2 + (y-y_1)^2 + (z-z_1)^2}{\sigma^2}\right). \end{aligned} \tag{2.107}$$

The following simulations present a variety of choices for the parameters ε_b, σ^2 as well as for the centre of the perturbations. Despite the fact that these parameters clearly play a role in the localisation and extension of the active patch, the behaviour of the model is generally characterised by propagation, pinning and stabilisation for a biologically relevant time. Here we show a selection of our most significant results, which are later extended in next section 2.11 for long times in other geometries.

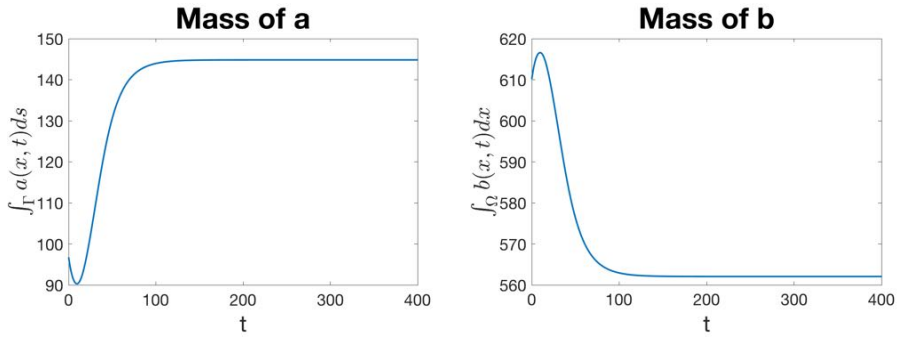

Figure 2.9: Variation in time of the total mass of active (left) and inactive (right) GTPases of the numerical solution shown in Figure 2.8. The initial decrease in the mass of a is due to the attraction of the solution towards the smaller value $a_1(b)$ in most of its domain. Consequently we observe an initial increase of the mass of b. The mass of a starts increasing with the spreading of its activity over the surface, which reduces the mass of b. After about 100 seconds the two components approach the equilibrium in mass.

2.10.1 Sphere

Our first three-dimensional geometry on which we solve the BSWP model (2.15)-(2.18) is the sphere which is the simplest possible three-dimensional shape. We consider a radius of 5μm, which is the radius used in the simulations of the WP model (Mori et al., 2008). We set $\varepsilon_b = 0.154$ in (2.105) and $\sigma^2 = 0.5\mu\text{m}^2$ in (2.106). The perturbation of the homogeneous state is strong enough to trigger polarisation: from this small region, a propagative activation is started in all directions. This will be finally pinned in about 100 seconds, resulting in a stable active area. In Figure 2.8 we show the evolution of a and in Figure 2.9 the temporal evolution of the masses of a and b which become constants when the propagation gets pinned.

2.10.2 Capsule

As a second example, we compute numerical solutions of the BSWP model (2.15)-(2.18) on a capsule composed of a cylinder of radius 5 μm and height 4 μm and two spherical caps at its extremities. The results shown in Figure 2.10 are obtained for the parameter $\varepsilon_b = 0.006$ in (2.105) and $\sigma^2 = 0.2\mu\text{m}^2$ in (2.106). A very small value of ε_b is chosen in order to have an initial total quantity of b very close to its possible maximal value b_2, which corresponds to a higher amount of the available source for the activation. The small value for σ^2 narrows the initial activated area, but it is still big enough to maintain the ability to propagate. As expected, the initial condition triggers the activation process, which apparently reaches the steady state in about 120 seconds, see Figure 2.10. Eventually, we compute and observe the behaviour of the numerical solutions for very long times and notice that the activated region is moving very slowly from its “apparent" steady state, towards one of the caps of

the capsule, which is finally covered in more than 3 hours. Vanderlei et al. (2011) showed the same property for the classical wave pinning model (2.1)-(2.3): on two-dimensional geometries the active concentration at its “steady state" has the tendency to move very slowly towards more rounded regions of the domain. It is interesting to note that in our case, the slow motion requires a much bigger time, which in Vanderlei et al was of only around 200 seconds. This behaviour is also observed influencing the mechanics of cell migration in a model based on the wave pinning mechanisms proposed by Camley et al. (2017).

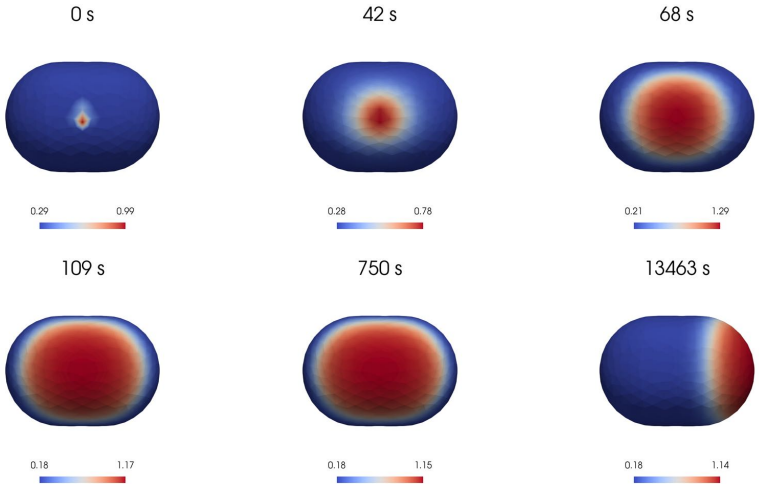

Figure 2.10: Numerical simulations of the BSWP model (2.15)-(2.18) on a capsule. The solution a is here reported at several time steps: a small area in the lateral side of the capsule is activated, causing the activation of the entire lateral section which reaches its maximal size after around 120 seconds. Eventually, after a very long time, the activated area moves towards one of the spherical caps of the domain.

2.10.3 Polarised cell shape

Next, we consider a more complex geometry whose shape mimics that of a polarised cell *in vitro*, see Figure 2.11. The domain has a volume of 538 μm^3 and surface area of 911 μm^2, almost three times more than the surface area of a sphere with the same volume. The front of the domain presents some protrusions with five tips. We set $\varepsilon_b = 0.154$ in (2.105) and $\sigma^2 = 0.5$ in (2.107). In Figure 2.12 we activate one external tip and one internal tip, while in Figure 2.13 activation starts from the external tips. Both perturbations are strong enough to trigger the polarisation process, which starts with the enlargement of the polarity patches. In the first simulation shown in Figure 2.12, in about four minutes the two activated spots merge together into a unique stable active region which enlarges over the whole front of the domain and gets pinned in about 10 minutes.

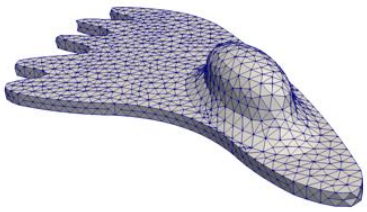

Figure 2.11: The surface of a polarised cell shaped domain. The domain has been discretised with 5362 tetrahedrons which induced a surface discretisation with 3044 triangles.

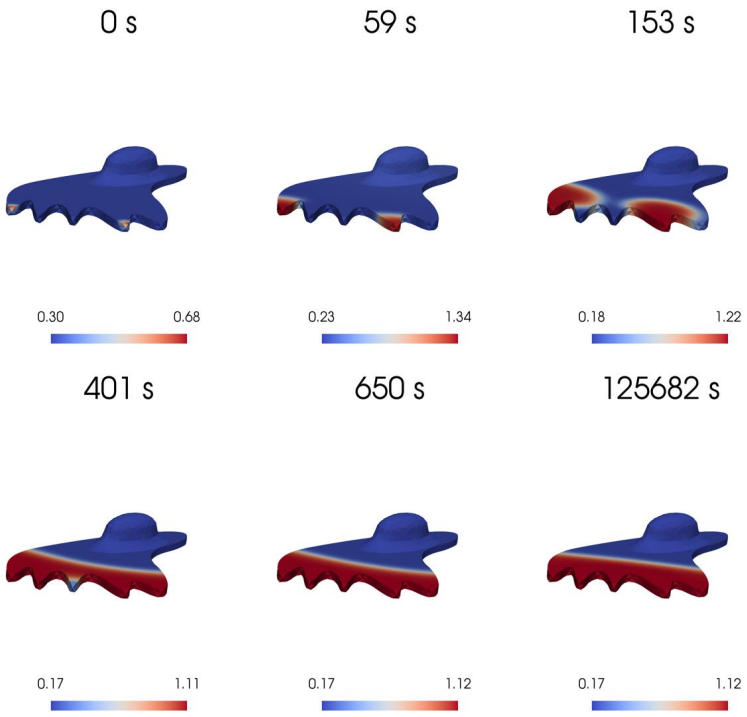

Figure 2.12: Numerical simulation of the BSWP model (2.15)-(2.18) on a more complex domain, caricature of a polarised cell. The numerical results show the solution a at different stages of the polarisation process: a small area in two of the five tips of the domain is activated and this generates two propagating fronts which merge together in about 4 minutes. The activated area stabilises covering the whole front of the domain in about 10 minutes. A video illustrating the wave pinning process is provided in the supplementary material of Cusseddu et al. (2018)

In the second simulation shown in Figure 2.13, the cell needs a much longer time to stabilise as it has to deal with two polarity patches, for which a competitive behaviour is observed. Initially, propagation occurs normally with two different enlarging areas. After about five minutes one active region inverts its behaviour and starts disappearing. This leads to a winning tip, which continues enlarging on its side, until final stabilisation. The competitive behaviour was shown and investigated by Chiou et al. (2018) for the classical wave pinning model and Figure 2.13 confirms this feature also for the bulk-surface extension (2.15)-(2.18). Further investigations are left for future work.

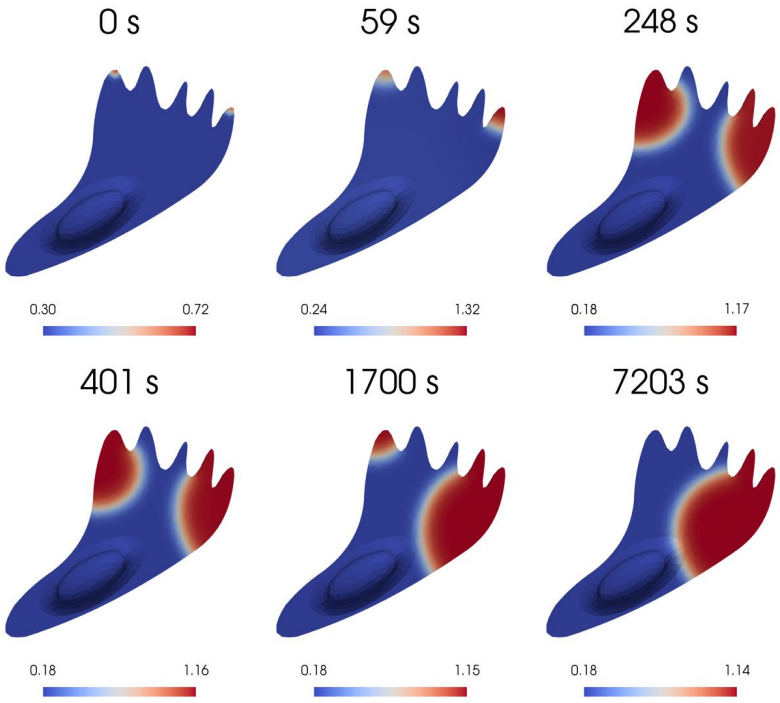

Figure 2.13: Numerical simulation of the BSWP model (2.15)-(2.18) on a domain mimicking a polarised cell. In this simulation the external tips are activated. Two active waves are generated and start propagating on the surface. After about 5 minutes the competition effects between the two active patches start being visible, and one active region (left tip) starts reducing its size, until it disappears completely. Disappearing and stabilisation of the remaining active area occur after more than 30 minutes. Competition in two-dimensional wave pinning model was very recently investigated in Chiou et al. (2018).

In all previous simulations, we have used suitable initial conditions in the form of perturbations of the spatially homogeneous profile of a. This has been shown to be enough to give rise to polarisation, in the numerical results, as well as for the asymptotic and local perturbation analysis. However, similar perturbations can be induced by perturbing the reaction (2.18). Indeed, in most of the papers simulating the WP model, polarisation was initiated from a stimulus included in the reaction function, rather than a stimulus in the initial conditions, which were, in turn, spatially homogeneous. Following this latter approach, the BSWP model is given by equations (2.15)-(2.18) with reaction

$$f(a,b) = \omega\Big(k_0 + \frac{\gamma a^2}{K^2 + a^2}\Big)b - \beta a + \omega k^s b, \qquad \mathbf{x} \in \Gamma. \tag{2.108}$$

where $k^s = k^s(\mathbf{x}, t)$ is an arbitrary function, generally non-negative until a certain time t_s and zero afterwards (Mori et al., 2008). Appropriate choices of k^s can lead to the formation of local peaks in the solutions, which trigger the propagation of a over the surface. An interesting result of the two-dimensional BSWP model (2.15)-(2.18) was its ability to self polarise from homogeneous initial conditions in asymmetric geometries when a spatially

homogeneous stimulus was applied in an initial time interval $[0, t_s]$ (Giese et al., 2015). In Figure 2.14 we present the same experiment on our three-dimensional domain in which we apply a homogeneous stimulus of 0.03 s^{-1} for 20 seconds. This induces a rapid local activation of the ellipsoidal volume on the top of the cell, with noticiable effects within the first 5 seconds. The high a concentration starts increasing and sharpening the fronts, and successively it spreads towards the rear of the domain. Our simulation confirms the interesting geometry-induced self-polarisation ability also for the three-dimensional case.

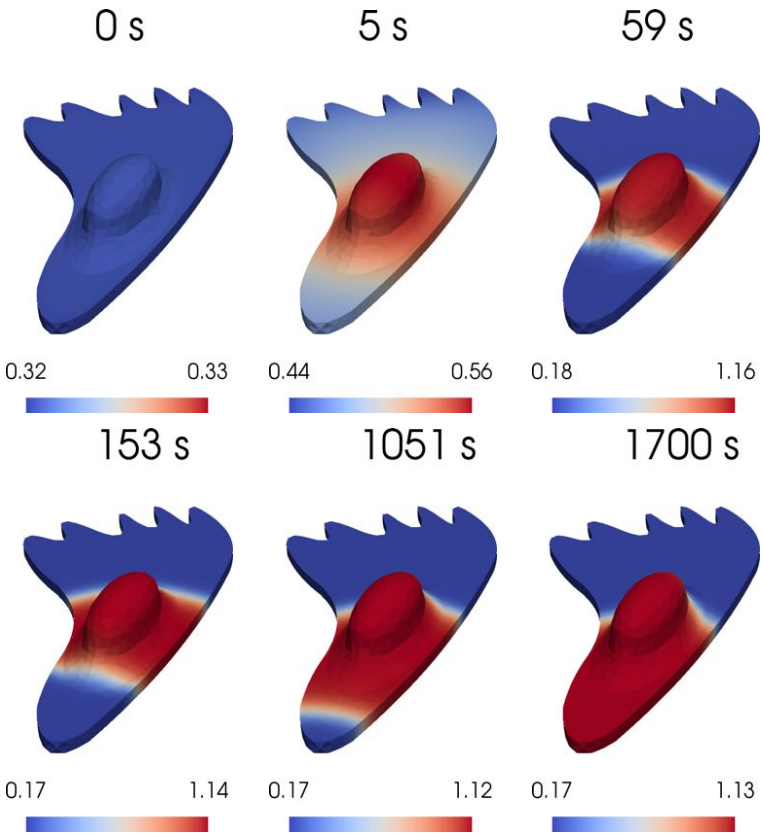

Figure 2.14: Numerical simulation of the BSWP model (2.15)-(2.16) and (2.17) with reaction kinetics (2.108) on a domain mimicking a polarised cell. We apply a constant stimulus $k^s(\mathbf{x}, t) = 0.03\ s^{-1}$ until time t_S=20 s which induces an activation at the level of the nucleus-shaped volume. From here, a wave starts, covering the whole rear. In about 20 minutes the BSWP model has reached its steady state, with the rear having high levels of active GTPase.

In the next section we present a second series of numerical results on different geometries, which were not previously included in our article (Cusseddu et al., 2018). These are part of an ongoing project focused on the understanding of the long-time behaviour of the surface solution a of (2.15)-(2.18) and, in particular, of the slow-motion of the active patch in function of the domain geometry.

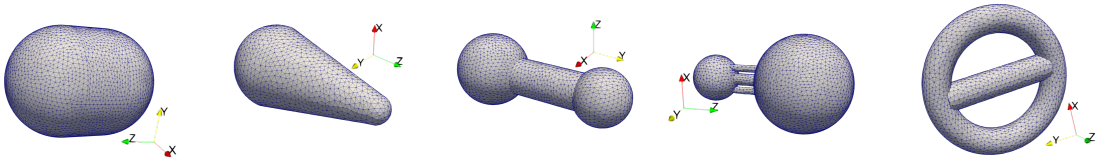

(a) (b) (c) (d) (e)

Figure 2.15: The computational meshes over the domains Ω considered in this section. (a) a capsule composed of a cylinder of radius $R = 5$ and bases centered, respectively in $(0, 0, 0)$ and $(0, 0, 4)$. At the ends of the cylinder are placed two half spheres of same radius $R = 5$; (b) a club-shaped domain composed of a truncated cone with bases centred in (0, 0, 0) and (0, 0, 8) and basal radii, respectively, $R_1 = 3$ and $R_2 = 1$. This geometry is completed by two half spheres of same radii R_1, R_2 at its ends; (c) a uneven dumbbell-shaped domain composed of the union of a cylinder of radius $R_c = 2$ and bases centered in $(0, 0, 0)$ and $(0, 10, 0)$ and two sphere at its ends, centered in $(0, -2, 0)$ and $(0, 11, 0)$ and radius, respectively $R_S = 4$ and $R_s = 3$; (d) this domain is composed of the union of three cylinders connecting two spheres: the main cylinder, of radius $R_1 = 0.5$ has bases centered in $(0, 0, 0)$ and $(0, 0, 8)$, while the other two have both radius $R_2 = R_3 = 0.3$ and the two bases are respectively centered in $(1, 0, 0)$, $(1, 0, 8)$ and in $(-1, 0, 0)$, $(-1, 0, 8)$. The smallest sphere has radius $R_s = 2$ and center $(0, 0, 0)$, the biggest one has radius $R_S = 4$ and center in $(0, 0, 8)$; (e) a steering wheel-shaped domain, composed of a torus and a cylinder. The torus is centered in $(0, 0, 0)$, its tube has radius $r = 1$ and the distance between the center of the torus and the center of the tube is $R = 4.5$. The cylinder has radius $r = 1$ and bases centered in $(0, -4, 0)$ and $(0, 8, 0)$. All the quantities reported in this caption have unit dimension μm.

2.11 The effects of the domain shape on the BSWP model

The simulations reported in the previous section highlight the fact that the geometry of the domain has a strong impact on the evolution of the BSWP model (2.15)-(2.18). This is particularly evident in the domain mimicking a polarised cell (in particular see figures 2.13 and 2.14). As well, the simulation reported in Figure 2.10 shows an interesting long-time behaviour. The active patch, which appears to be stable for a substantially long time, at least for all the biologically relevant time (in the figure for at least 750 seconds), undergoes towards a slow transition, attracted by one of the capsule caps.

A deeper investigation on the effects of the geometry on the patterning of the BSWP model is definitely an attractive future goal of this work. Currently this constitutes a work in progress and, without claiming completeness, in the following we present some interesting preliminary results of the model on different geometries, which are shown, together with the corresponding spatial meshes, in Figure 2.15. The BSWP model (2.15)-(2.18) is tested for different initial conditions of the surface component a, while for the bulk component b we keep considering the homogeneous profile (2.105) with $\varepsilon_b = 0.001$.

2.11.1 Capsule

In Section 2.10.2 the BSWP model (2.15)-(2.18) was tested on the capsule (Figure 2.15a) with initial conditions (2.105)-(2.106), where activation started from a small peak localised on the lateral surface of the domain. Keeping the same homogeneous initial condition for b we have simulated the model for three different initial spatial profile of the surface component a.

A circular high activity over the lateral surface is imposed through the initial condition

$$a_{in}(\mathbf{x}) = \begin{cases} a_g + a_p \exp\left(-\frac{\left(\sqrt{(z-z_0)^2+y^2}-R\right)^2}{\sigma^2}\right), & \text{if } x > 0, \\ a_g, & \text{otherwise.} \end{cases} \tag{2.109}$$

The result of the simulation is shown in Figure 2.16. The impact of the geometry is evident from the images: the propagation is mainly directed towards the internal area of the initial circle, which gets very quickly activated, but the propagation outside the circle occurs much slower. Indeed the boundary of the final configuration appears as a small expansion, mainly towards the two caps, of the initial ring. Interestingly the final configuration shown in Figure 2.16 is very similar to the solution at 750 seconds shown in Figure 2.10.

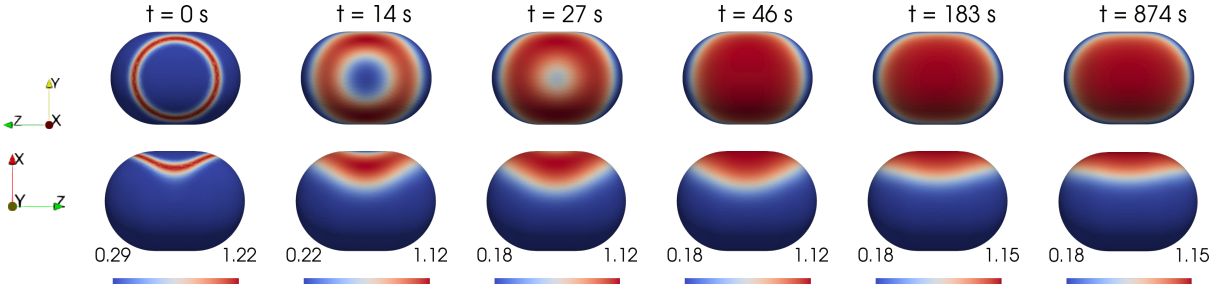

Figure 2.16: Numerical simulation of the BSWP model (2.15)-(2.18) on a capsule with initial condition given in (2.109) with $z_0 = 2\mu$m, $R = 4\mu$m, $\sigma^2 = 0.21\mu\text{m}^2$. The solution is shown from two different point of view: the first line offers a view from the top of the x axis, while in the second line the view is from the top of the y axis (see Cartesian axes on the left side of the image).

Figure 2.17 shows the evolution of the BSWP model (2.15)-(2.18) subject to the following initial condition for a:

$$a_{in}(\mathbf{x}) = a_g + a_p \exp\left(-\frac{(z-z_0)^2}{\sigma^2}\right). \tag{2.110}$$

This is visualised as a ring across the capsule length. The model shows a very interesting behaviour as the ring quickly expands its width, reaching an apparently stable profile which lasts for a reasonable long time (compare solution at time 35 and 304 seconds). However the apparent stability is eventually lost at around 550 seconds: the ring breaks and the

active region moves towards the lateral surface, reaching a very similar configuration as in the previous case (Figure 2.16).

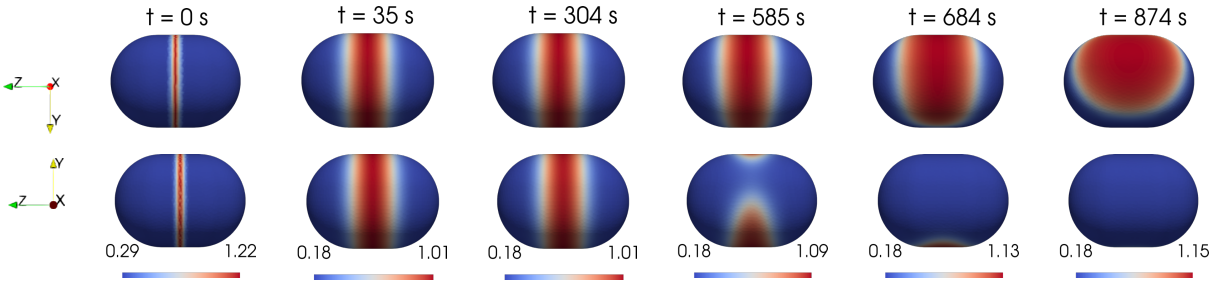

Figure 2.17: Numerical simulation of the BSWP model (2.15)-(2.18) on a capsule with initial condition given in (2.110) with $z_0 = 2\mu$m, $R = 4\mu$m, $\sigma^2 = 0.15\mu\text{m}^2$. The solution is shown from two different point of view: the first line offers a view from the bottom of the x axis, while in the second line the view is from the top of the x axis (see Cartesian axes on the left side of the image).

The last simulation of the BSWP model (2.15)-(2.18) on the capsule is shown in Figure 2.18 and describes the evolution of the model subject to the following initial condition:

$$a_{in}(\mathbf{x}) = a_g + a_p \exp\left(-\frac{\left(\sqrt{(z-z_0)^2+y^2}-R\right)^2}{\sigma^2}\right) \tag{2.111}$$

This function is the symmetrical version of (2.109) with respect to the plane $x = 0$. For R large enough the two circles intersect, creating two X-shaped crosses. In this way, the initial condition (2.111) can be seen as a high-activity curve enveloping the capsule. It is interesting to observe how the two circles break (first line of Figure 2.18), while the two X-shaped crosses are able to propagate, eventually stabilising over two opposite active patches at the capsule lateral surface (second line of Figure 2.18). Also in this case, at the final time the configuration is the very similar to the one in the previous simulations (Figures 2.16-2.17), with the only difference that for this last initial condition two different patches, symmetrical with respect to the plane $y = 0$, are formed.

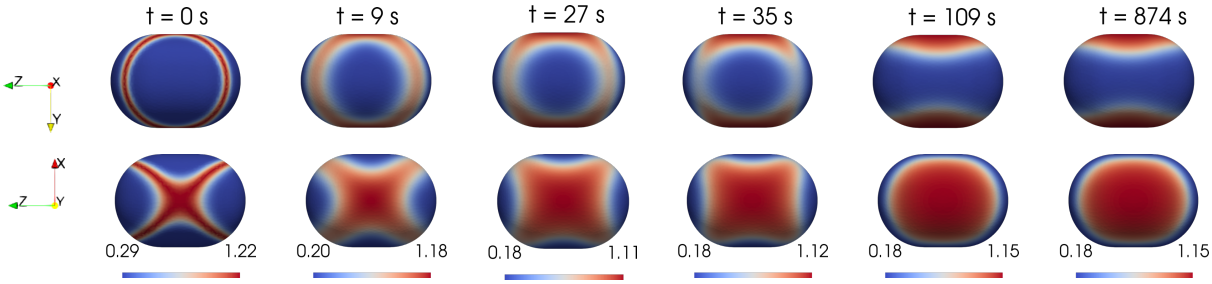

Figure 2.18: Numerical simulation of the BSWP model (2.15)-(2.18) on a capsule with initial condition given in (2.111) with $z_0 = 2\mu$m, $R = 5\mu$m, $\sigma^2 = 0.21\mu\text{m}^2$. The solution is shown from two different point of view: the first line offers a view from the bottom of the x axis, while in the second line the view is from the bottom of the y axis (see Cartesian axes on the left side of the image).

2.11.2 Dumbbell-shaped domain

The BSWP model (2.15)-(2.18) is tested on the dumbbell-shaped domain shown in Figure 2.15c for three different initial conditions. Since in the capsule simulation of Figure 2.10 the active path moves towards one of the caps, a natural question regards under which criterium one cap is preferred to the other one. Given the symmetry of the problem, this could be related to the mesh used by the bulk-surface finite element method. Hence, in order to get better insights about attractive regions, we use an asymmetrical dumbbell-shaped domain having one sphere bigger than the other one.

First we propose to use the following initial condition

$$a_{in}(\mathbf{x}) = a_g + a_p \exp\left(-\frac{(x-x_0)^2 + (y-y_0)^2 + (z-z_0)^2}{\sigma^2}\right), \tag{2.112}$$

and playing with the perturbation center (x_0, y_0, z_0) we activate either the small sphere (Figure 2.19, top row) or the big sphere (Figure 2.19, bottom row). As shown in the figures, both spheres appear to be stable regions for the active patch, which in the final configuration is localised over the initially perturbed sphere. Therefore in order to see

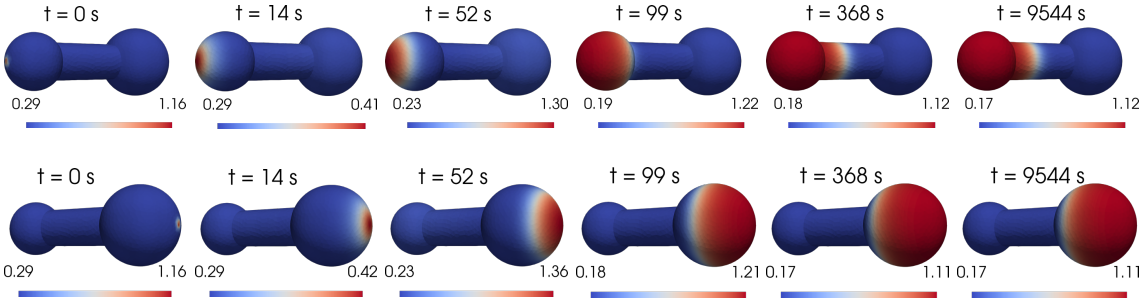

Figure 2.19: Two different numerical simulations of the BSWP model (2.15)-(2.18) on a dumbbell-shaped domain with initial conditions given in (2.112) with $\sigma^2 = 0.2\mu\text{m}^2$. On the first row the homogeneous profile for a is perturbed over the small sphere ($(x_0, y_0, z_0) = (0, 14, 0)$, while on the second row the perturbation is imposed over the biggest sphere ($(x_0, y_0, z_0) = (0, -6, 0)$).

which one of the two spheres is more "attractive", we initially impose a perturbation over the cylinder, equidistant from the two spheres, with the function

$$a_{in}(\mathbf{x}) = a_g + a_p \exp\left(-\frac{(y-y_0)^2}{\sigma^2}\right). \tag{2.113}$$

The corresponding simulation is shown in Figure 2.20: the active ring imposed by (2.113) quickly expands propagating over the entire cylinder surface. After around 50 seconds the solution a appears to be stable. However this configuration does not hold for all the time. Slowly the active patch starts moving towards the small sphere, which is completely activated by the end of the simulation. The final configuration is very similar to the one

presented in Figure 2.21 (top).

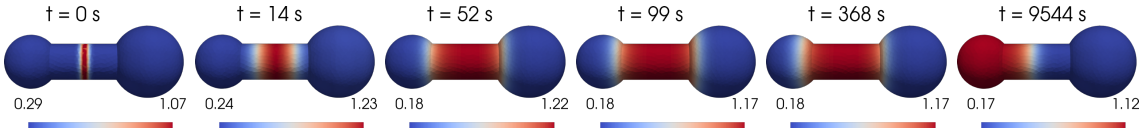

Figure 2.20: Numerical simulation of the BSWP model (2.15)-(2.18) on a dumbbell-shaped domain with initial condition given in (2.112) with $y_0 = 5.0\mu$m and $\sigma^2 = 0.2\mu\text{m}^2$. The homogeneous profile is perturbed locally in the cylinder, equidistantly from the two spheres.

2.11.3 Club-shaped domain

In this section the simulations over the dumbbell are replicated over a club-shaped domain in order to further test our findings. The initial perturbation is localised at one end of the domain. The two different cases are considered and shown over the two rows of Figure 2.21. As expected, consistently with the simulations in Figure 2.19, in both cases the initial condition triggers a propagation which stabilises at the perturbed ends.

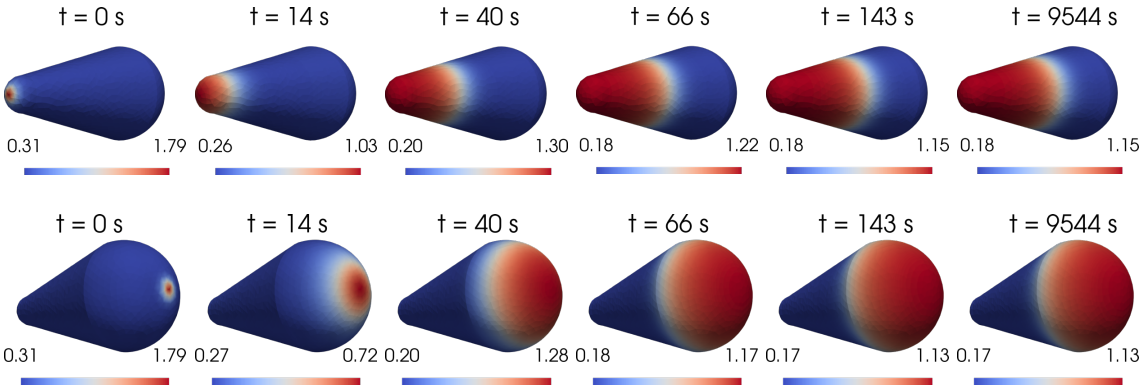

Figure 2.21: Two numerical simulations of the BSWP model (2.15)-(2.18) on a club-shaped domain. On the first row the homogeneous profile for a is perturbed at the smaller tip of the domain, while on the second row the perturbation is applied at the top of the big half sphere. The initial condition imposed in the first simulation (first row) is $a_{in}(\mathbf{x}) = a_g + a_p \exp\left(-\frac{x^2+y^2}{\sigma^2}\right)\mathbf{1}(\mathbf{x})_{\{z>h/2\}}$, while on the second simulation (second row) the initial condition is $a_{in}(\mathbf{x}) = a_g + a_p \exp\left(-\frac{x^2+y^2}{\sigma^2}\right)\mathbf{1}(\mathbf{x})_{\{z<h/2\}}$. In both cases we set $\sigma^2 = 0.21\mu\text{m}^2$ and $h = 8\mu$m.

Again, to evaluate if the spherical ends of the domain are more attractive, we perturb the central region using initial conditions of the following form:

$$a_{in}(\mathbf{x}) = a_g + a_p \exp\left(-\frac{(z-z_0)^2}{\sigma^2}\right), \tag{2.114}$$

which is visualised as a ring over the cone. Figure 2.22 describe the model evolution for two different positions of the ring. Interestingly the qualitative aspect of the evolution is the same in both cases. Even when the ring is much closer to the biggest half sphere, the active patch is attracted by the smallest sphere.

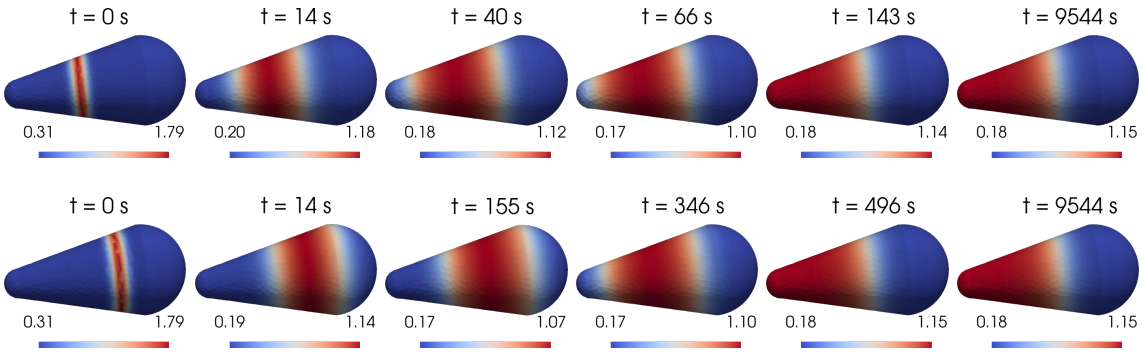

Figure 2.22: Two different numerical simulations of the BSWP model (2.15)-(2.18) on a club -shaped domain. On the first row the initial condition is (2.114) with $z_0 = 4\mu$m and $\sigma^2 = 0.2\mu\text{m}^2$, i.e. the ring is placed at the half-length of the cone.

Nevertheless, the smallest tip of the domain is not always the most attractive one, as the simulation in Figure 2.23 shows. In this case the initial condition was (2.112) with $(x_0, y_0, z_0) = (0, 2, 4)$ and $\sigma^2 = 0.2$, which corresponds to a small activity peak localised on the lateral surface of the cone. In this case the perturbation evolves into a lateral patch apparently stable for more than 300 seconds. At 650 seconds the movement of patch is noticeable and at the last time the biggest end of the domain is finally covered.

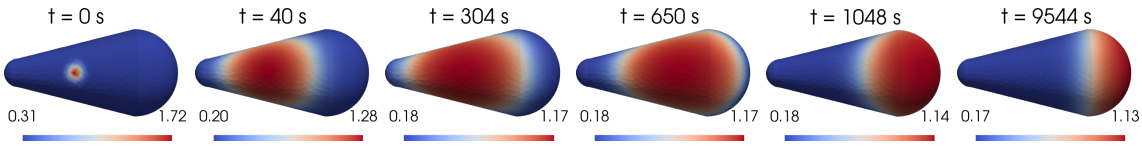

Figure 2.23: Numerical simulation of the BSWP model (2.15)-(2.18) on a club-shaped domain with initial condition (2.114) and $(x_0, y_0, z_0) = (0, 2, 4)$ and $\sigma^2 = 0.2\mu\text{m}^2$.

2.11.4 Three cylinders connecting two spheres

The same behaviour is also observed when solving the model in the more complex domain of Figure 2.15d. For a small initial activity peak localised on the tip of a spherical end of the domain, a propagates over the perturbed sphere and finally stabilises covering it. When the perturbation is applied at the small sphere the high-activity region reaches also the three cylinders, covering them. For a perturbation over the big sphere, this extends for around half of the sphere surface. The numerical results are shown in Figure 2.24.

We now apply the ring-type initial condition (2.114) with $z_0 = 3$ μm, and $\sigma^2 = 0.3$ μm^2, which localises the perturbation transversally over the three cylinders. The formed active patch is again attracted by the small sphere at the end of the domain, and this is covered in a relatively short time (in about 600 seconds). See Figure 2.25 for the results.

Figure 2.26 shows another interesting evolution of the BSWP model (2.15)-(2.18) from a different initial condition. This is given in form of (2.113) with $y_0 = 0$ and $\sigma^2 = 0.3$ μm^2.

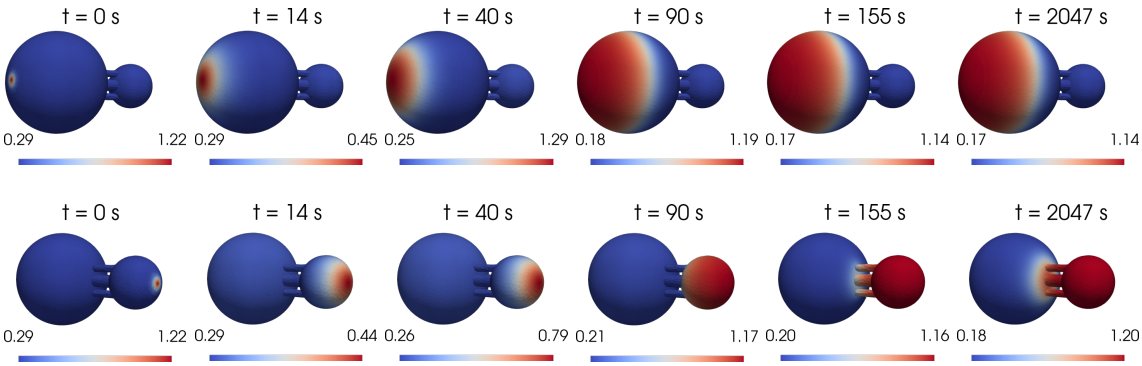

Figure 2.24: Two numerical simulations of the BSWP model (2.15)-(2.18) on a complex domain evolving from initial conditions (2.112) with $(x_0, y_0, z_0) = (0, 0, 12)$ (first row) or $(x_0, y_0, z_0) = (0, 0, -2)$ (second row), and $\sigma^2 = 0.2\mu\text{m}^2$.

The perturbation crosses the whole domain in a longitudinal ring fashion. This triggers a propagation resulting in a total coverage of the small sphere and a successive breakage of the ring in the biggest sphere, as was observed also in Figure 2.18. The solution at the final time shows a clearly asymmetrical profile.

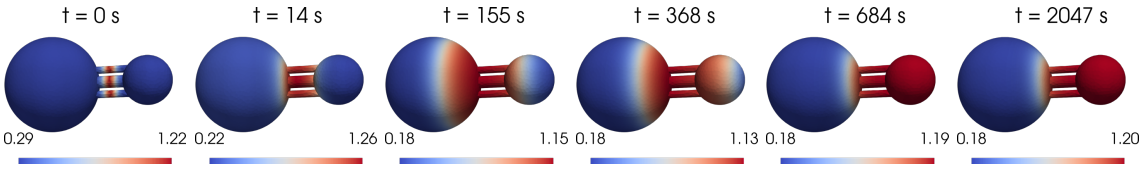

Figure 2.25: Numerical simulation of the BSWP model (2.15)-(2.18) on a complex domain with initial condition given in (2.114) with $z_0 = 3\ \mu$, and $\sigma^2 = 0.3\ \mu\text{m}^2$.

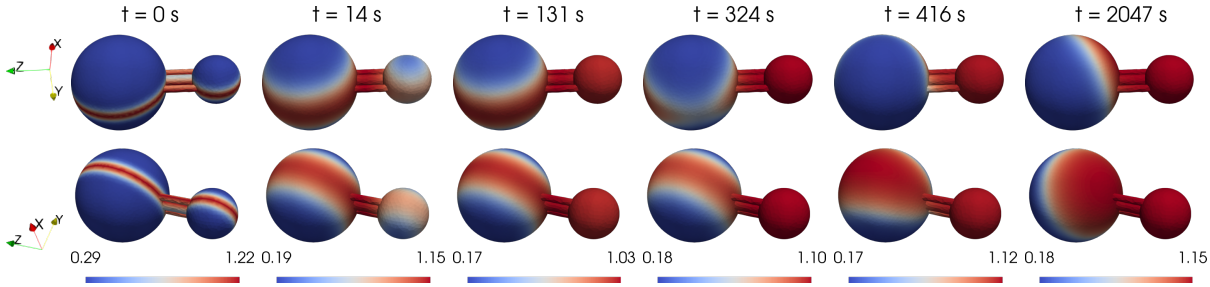

Figure 2.26: Numerical simulation of the BSWP model (2.15)-(2.18) on a complex domain with initial condition given (2.113) with $y_0 = 0$ and $\sigma^2 = 0.3\ \mu\text{m}^2$. The solution is visualised from two different point of view, as indicated in both rows by the Cartesian axes.

2.11.5 Steering wheel

Finally, the last investigation is made on the torus-cylinder domain of Figure 2.15e. In one case, shown in Figure 2.27, a competitive behaviour is again observed. The initial condition, given by (2.113) with $y_0 = 0\ \mu\text{m}$ and $\sigma^2 = 0.3\ \mu\text{m}^2$, visually reminds three rings over the tubes. As expected they all expand and very quickly reach a more stable configuration. However, eventually a is depleted from the central cylinder, with a consequent expansion

of the other two active surfaces on the torus. A similar behaviour was already observed in the simulation of Figure 2.13.

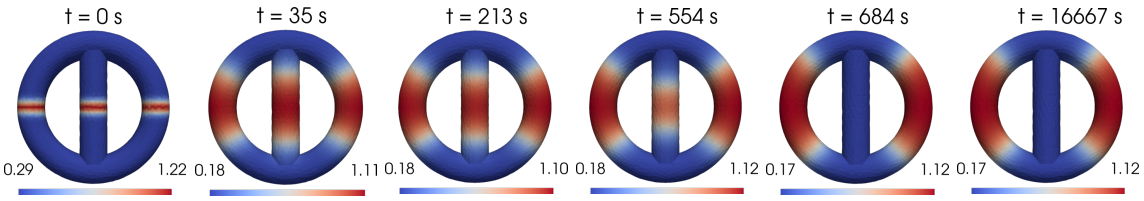

Figure 2.27: Numerical simulation of the BSWP model (2.15)-(2.18) on the geometry of Figure 2.15e with initial condition given by (2.113) with $y_0 = 0$ μm and $\sigma^2 = 0.3$ μm^2.

In the last two simulations we present the evolution of the BSWP model (2.15)-(2.18) where the initial conditions are perturbations of the homogeneous spatial profile localised only on the central cylinder. In one case, shown in Figure 2.28, the initial condition is given by

$$a_{in}(\mathbf{x}) = a_g + a_p \exp\left(-\frac{x^2+y^2}{\sigma^2}\right), \tag{2.115}$$

with $\sigma^2 = 0.2$ μm^2. This can be described as a circular peak localised at the centre of the cylinder, on both faces of the domain. In the second case, shown in Figure 2.29, the initial condition is given by

$$a_{in}(\mathbf{x}) = \begin{cases} a_g + a_p \exp\left(-\frac{y^2}{\sigma^2}\right), & \text{if } |x| < 1.5 \ \mu\text{m}, \\ a_g, & \text{otherwise}, \end{cases} \tag{2.116}$$

with $\sigma^2 = 0.2$ μm^2, which describes a single ring across the cylinder. These simulations are interesting because despite the fact that a reaches a similar apparently stable configuration in both cases, in which the whole cylinder is activated, in the second case the active patch finally breaks out of the cylinder and starts propagating over the torus.

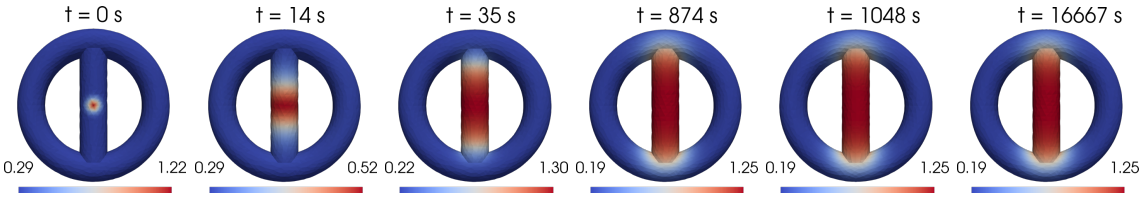

Figure 2.28: Numerical simulation of the BSWP model (2.15)-(2.18) with initial condition given by (2.115) with $\sigma^2 = 0.2$ μm^2.

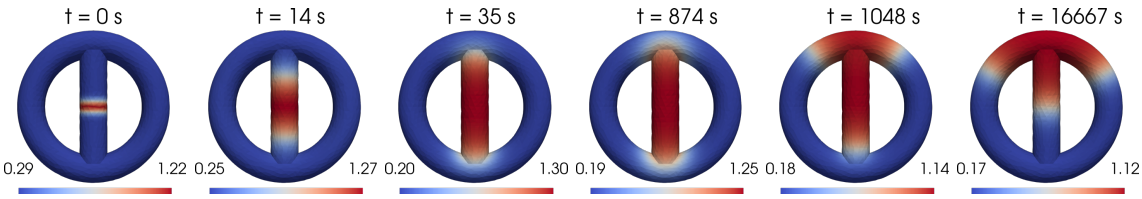

Figure 2.29: Numerical simulation of the BSWP model (2.15)-(2.18) with initial condition given by (2.116) with $\sigma^2 = 0.2\ \mu\text{m}^2$.

2.12 Some preliminary results for the BSWP model in evolving domains

A future extension of the work presented in this Chapter regards the study of the model (2.15)-(2.20) in a migrating cell. In this case, the cell membrane needs to be represented by an evolving surface $\Gamma(t) \subset \mathbb{R}^3$ and the cell interior by an evolving volume $\Omega(t) \subset \mathbb{R}^3$, for $t \in [0, T]$. Hence, the position $\mathbf{x}$ of a point on $\Gamma(t)$ or in $\Omega(t)$ is defined by

$$\begin{aligned} \frac{\mathrm{d}\mathbf{x}}{\mathrm{d}t} &= \mathbf{v}(\mathbf{x}, t), \qquad t \in (0, T], \\ \mathbf{x}(0) &= \mathbf{x}_0 \in \{\Gamma_0, \Omega_0\}, \end{aligned}$$

where $\Omega(0) = \Omega_0$ and $\Gamma(0) = \Gamma_0$ represent the initial shape of the cell and $\mathbf{v} \in C^1(V \times [0, T])$ is the velocity of the cell. Furthermore we assume the existence of a bounded open set $V \subset \mathbb{R}^3$ such that $\Omega(t) \subset V$ for all $t \in [0, T]$.

In this case, the derivation of the biochemical model (2.15)-(2.20) presented in Section 2.2 needs to be modified in order to take into account the non-stationarity of the domain. In particular we make use of the following theorems.

Theorem 2.12.1 (Reynold's transport theorem)**.** Let $\Omega(t)$ be an open set in $\mathbb{R}^3$ with boundary $\Gamma(t) \in C^1([0, T])$. Hence, if $f \in C^1(\Omega(t) \times [0, T])$, it holds

$$\frac{\mathrm{d}}{\mathrm{d}t} \int_{\Omega(t)} f \, \mathrm{d}\mathbf{x} = \int_{\Omega(t)} \left(\frac{\partial f}{\partial t} + \nabla \cdot (f\mathbf{v}) \right) \mathrm{d}\mathbf{x}. \tag{2.117}$$

A similar result holds for surfaces, as follows:

Theorem 2.12.2. If $g \in C^1(\Gamma(t) \times [0, T])$, it holds

$$\frac{\mathrm{d}}{\mathrm{d}t} \int_{\Gamma(t)} g \, \mathrm{d}s = \int_{\Gamma(t)} \left(\frac{\partial g}{\partial t} + \mathbf{v} \cdot \nabla g + g \nabla_\Gamma \cdot \mathbf{v} \right) \mathrm{d}s. \tag{2.118}$$

For more details about Theorem 2.12.1 we refer to the textbook by DiBenedetto (2010) or Temam et al. (2003), while for Theorem 2.12.2 we refer to Dziuk and Elliott (2007,

2013). Hence, using the above theorems, the adaptation of the steps followed in Section 2.2 to the new context is straightforward and the new model reads:

$$\frac{\partial b}{\partial t} + \nabla \cdot (b\mathbf{v}) = D_b \Delta b, \qquad \mathbf{x} \in \Omega(t),\ t \in (0,T], \tag{2.119}$$

$$-D_b(\mathbf{n} \cdot \nabla b) = f(a,b), \qquad \mathbf{x} \in \Gamma(t),\ t \in (0,T], \tag{2.120}$$

$$\frac{\partial a}{\partial t} + \mathbf{v} \cdot \nabla a + a\nabla_\Gamma \cdot \mathbf{v} = D_a \Delta_\Gamma a + f(a,b), \qquad \mathbf{x} \in \Gamma(t),\ t \in (0,T], \tag{2.121}$$

coupled with initial conditions

$$b(\mathbf{x},0) = b_{in}(\mathbf{x}), \qquad \mathbf{x} \in \Omega_0, \tag{2.122}$$

$$a(\mathbf{x},0) = a_{in}(\mathbf{x}), \qquad \mathbf{x} \in \Gamma_0, \tag{2.123}$$

and f defined in (2.18).

As in Section 2.4, we can find an equivalent of Proposition 2.4.1 regarding the conservation of the initial total mass, as follows.

Proposition 2.12.1. Let a and b be solutions of (2.119)-(2.123). Then

$$M(t) := \int_{\Omega(t)} b(\mathbf{x},t)\ \mathrm{d}\mathbf{x} + \int_{\Gamma(t)} a(\mathbf{x},t)\ \mathrm{d}s = M_0, \quad \forall t \geq 0, \tag{2.124}$$

where

$$M_0 := \int_{\Omega(0)} b_{in}(\mathbf{x})\ \mathrm{d}\mathbf{x} + \int_{\Gamma(0)} a_{in}(\mathbf{x})\ \mathrm{d}s. \tag{2.125}$$

Proof. We follow the same steps as in Proposition (2.4.1). Differentiating (2.124) and using Theorem 2.12.1 and 2.12.2, we get

$$M'(t) = \int_{\Omega(t)} \left(\frac{\partial b}{\partial t}(\mathbf{x},t) + \nabla \cdot (b\mathbf{v}) \right)\ \mathrm{d}\mathbf{x} + \int_{\Gamma(t)} \left(\frac{\partial a}{\partial t}(\mathbf{x},t) + a\nabla_\Gamma \cdot \mathbf{v} + \mathbf{v} \cdot \nabla a \right)\ \mathrm{d}s,$$

which, from (2.119) and (2.121), results in

$$M'(t) = \int_{\Omega(t)} D_b \Delta b\ \mathrm{d}\mathbf{x} + \int_{\Gamma(t)} \left(D_a \Delta_\Gamma a + f(a,b) \right)\ \mathrm{d}s.$$

Now applying the divergence theorem to the bulk integral and the boundary condition (2.120), together with Corollary 1.5.1 for the Laplace-Beltrami term for the surface integral, we get $M'(t) = 0$, which proves the proposition. □

In view of future extensions, since Rho GTPase proteins are key players in cell polarisation and cell motility (see Section 1.1.5), we expect to model the cell velocity $\mathbf{v}$ as a function

of the active GTPase a, as done for example by Vanderlei et al. (2011) and Camley et al. (2017). This should be accompanied by the extension of the bulk-surface finite element method of Section 2.9 to evolving domains. Many works have been already devoted to numerical methods for these kinds of problems (see, for example Elliott et al. (2012), MacDonald et al. (2016b), MacKenzie et al. (2016), Madzvamuse and Chung (2016b), Tuncer and Madzvamuse (2017)).

2.13 Conclusion

In this chapter, we have presented a three-dimensional extension of the wave pinning model in a bulk-surface setting, in which membrane-bound GTPase and cytosolic GTPase are spatially localised and their interactions occur on the cell surface. The model describes cell polarisation through a minimal circuit of GTPase switching between active and inactive forms as well as between the membrane and the cytosol. In our work, we were able to show many analogies to the classical wave pinning model (Mori et al., 2008, 2011; Vanderlei et al., 2011) not previously shown in three-dimensional domains.

In this framework, the bulk-surface wave pinning (BSWP) model (2.15)-(2.18) maintains the three key properties (conservation of total mass, different diffusivities and bistability of the reaction) which are necessary to achieve polarisation. This phenomenon is achieved by patterning in the distribution of the active GTPase, characterised by the presence of high and low concentration regions over the surface of the domain. Different techniques and methods have been used to get a good understanding of the behaviour of the model. By employing asymptotic analysis, in Section 2.7 we show how a local perturbation of homogeneous initial conditions for a can trigger a propagation of the high level of active GTPase over the cell membrane. Effects of the geometry and parameters mapping have been investigated in Section 2.8, where we have highlighted how polarisation behaviour is more probable in complex domains. This has been done by using local perturbation analysis which allows a reduction of the bulk-surface PDE system to a system composed of three ordinary differential equations. Finally, using the bulk-surface finite element method, presented in Section 2.9 and 2.11, we computed numerical solutions of the BSWP model on different domains. An interesting result has been obtained over a capsule-shaped domain, where the long time behaviour of the model shows another common property of the classical wave pinning model (Vanderlei et al., 2011): the high active concentration region moves very slowly from its apparent stable steady state towards more rounded areas, until it covers one of the spherical caps of the capsule. This behaviour was also confirmed by a

series of simulations on different geometries, shown in Section 2.11.

Simulations have been done also on a more complex geometry mimicking a polarised cell-like shape. We showed competition between different highly active areas, as previously reported for the classical wave pinning mechanism (Chiou et al., 2018). In addition, we show how geometry plays a crucial role on the spontaneous polarisation in our three-dimensional BSWP model, as reported in the two-dimensional case by Giese et al. (2015). In the latter case, the asymmetric geometry of the domain plays a crucial role in enhancing GTPase activation. Indeed, activation was induced by a spatial homogeneous stimulus, but its effects appear well localised in specific areas of the surface.

Positive feedback, known to be a biological feature of Rho GTPases (Graessl et al., 2017), has been confirmed as a key player in the new formulation of the model. It is represented by the Hill function in (2.18), but studies involving other nonlinear choices would be of great interest. Identification of Rho GTPase feedback is an extremely interesting task and hopefully coordinated efforts between biologists and mathematicians can lead the way to a more complete understanding of cell polarisation and migration.

We expect the BSWP model (2.15)-(2.18) to be a starting point for a more complete work, in which the biochemical mechanisms shown above are coupled with mechanical properties of the cell, such as membrane tension and migration. Indeed, in real cells, GTPase concentration would lead to shape changes, through cytoskeleton interactions. In light of this, an extension of the model on evolving domains was introduced in Section 2.12. The classical wave pinning model has been already coupled to mechanistic models for membrane tension (Wang et al., 2017) and cell migration (Vanderlei et al., 2011; Camley et al., 2017). In these latter works the migrating cell, instead of keeping a straight direction, was turning over one side. This corresponds to the slow motion of the polarised area, as discussed in the Section 2.10.2. In view of this and taking into account the influence of the geometry of the domain, it can be of interest to extend these results and investigate how the bulk-surface approach influences the mechanical properties. Indeed, as reported in Figure 2.10, the slow motion appears to be slower with respect to the one reported in the literature (Vanderlei et al., 2011) and, in a reasonable amount of time, the turning effect might not affect too much the model. As well, the effects of the geometry shown by the local perturbation analysis (Section 2.8) might play an important role on evolving domains describing more accurately migrating cells, in which the parameter $\omega = |\Omega|/|\Gamma|$ is subject to changes in time. However, efforts should also be concentrated on the investigation of the effects of the surface curvature over the BSWP model (2.15)-(2.18). This is well motivated

by the simulations presented in Section 2.11. One could start this investigation from the reduced model proposed by Diegmiller et al. (2018), in which, given the high diffusivity of the bulk component, the inactive component b is assumed spatially uniform. In this way, the BSWP model is reduced to the single surface equation for the active component a and the analysis can be substantially simplified.

Lastly, another interesting extension of this study is whether it is possible to achieve similar mechanisms in a bulk-surface model with three species, when membrane recruitment of cytosolic GTPase is taken into account. This idea of GTPase model has been presented by Rätz and Röger (2014), but the polarisation mechanisms were Turing-type. In our case surface components would have same diffusivity, hence it is crucial to define a suitable membrane-binding function able to overcome this issue.

Chapter 3

Spatio-temporal dynamics of the keratin network in one dimension

3.1 Introduction

The aim of this chapter is to derive, analyse and simulate an experimentally-driven predictive mathematical model describing the spatio-temporal dynamics of the keratin network in epithelial cells. This network spans the whole cell interior, providing mechanical support to the cell, and protects the nucleus through a dense filamentous cage. Its dynamical behaviour shows a very interesting balance between assembly and disassembly phenomena and a continuous inward flow of proteins towards the nucleus of the cell.

Our model substantially extends the ideas of a simpler model previously proposed by Portet et al. (2015). A research visit at the Institute of Molecular and Cellular Anatomy of the RWTH Aachen University has been a fundamental step towards the development of the new model, since we had the opportunity to reinterpret the biological data previously used in the work by Portet et al. With new data-based modelling assumptions, plus some relaxation of the hypothesis, our new approach is able to describe the experimental measurements more accurately, predicting the spatio-temporal assembly and disassembly rates as well as regions of sources and sinks of keratin material, supporting the biological model proposed by Windoffer et al. (2011).

The chapter is then organised as follows: first, a brief introduction regarding the biological process of the keratin network remodelling in cells is presented, followed by a quick overview of the related mathematical modelling approaches proposed in the last 15 years; still within the introduction, we describe the work done by Portet et al. (2015) and their model, since this is necessary for a complete understanding of our extensions, which are

later presented in Section 3.2; our work permits us to obtain a new model, dependent on multiple parameters, which are finally estimated by an optimisation algorithm in Section 3.3; in the numerical results, shown in Section 3.4, we compare our solution to the experimental data and to the previous solution by Portet et al. As well we focus our attention on the optimal kinetics for keratin turnover. A discussion of the results and possible future directions follows in the conclusive section.

3.1.1 Biology of the spatio-temporal dynamics of the keratin network

The cytoskeleton is a structure responsible of the internal organisation of the cell and provides the fundamental support to carry out essential cellular functions, such as cell division or cell movement (Fletcher and Mullins, 2010). It is composed of complex filament networks of three major classes: microtubules, microfilaments and intermediate filaments (IFs). The latter is the most diverse, as it is constituted by several different proteins, whose expression depends on the cell type. Indeed, based on their amino-acid sequence, IF proteins are grouped in different types (Herrmann et al., 2007; Leduc and Etienne-Manneville, 2015):

- *Type I*: acidic keratins;
- *Type II*: basic keratins;
- *Type III*: vimentin, desmin, glial fibrillary acidic protein (GFAP) *and others*;
- *Type IV*: neurofilaments, α-internexin;
- *Type V*: nuclear lamins;
- *Type VI*: synemin, nestin *and others*.

In epithelial cells IFs are typically composed of keratin polypeptides (Windoffer et al., 2004), i.e. intermediate filaments of type I and type II. At the molecular level, all IF proteins share a similar structure that is composed of a central α-helical rod domain flaked by non-α-helical N- and C- terminal ends (head and tail of the protein) (Herrmann et al., 2007). *In vitro* experiments have described the formation of keratin filaments, see for example (Lichtenstern et al., 2012).

In cells, keratins are generally observed in the form of filaments or bundles constituting a network, which spans the whole cytoplasm and takes particular care of protecting the nucleus through a nuclear cage (Windoffer et al., 2011; Moch et al., 2013) (see Figure 3.1) This network is highly dynamic (Strnad et al., 2002; Leube et al., 2011; Windoffer

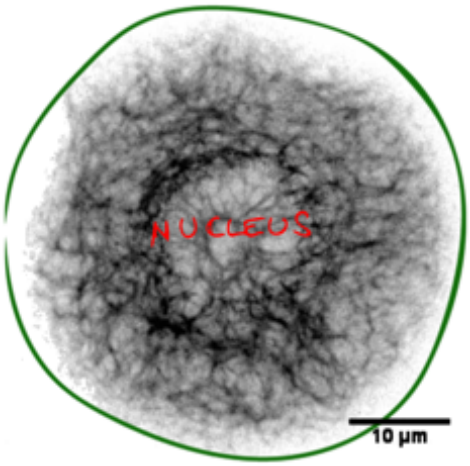

Figure 3.1: The keratin network organisation in a resting cell. The green curve approximately indicates the cell boundary. Human HaCaT B10 keratinocyte grown on a circular fibronectin island. HaCaT B10 cells producing fluorescent human keratin 5 were described in (Moch et al., 2013). They were seeded on fibronectin islands (1800 μm^2) and imaged after one day with a spinning disc confocal microscope as described (Tee et al., 2015). Picture taken by Nadieh Kuijpers at the Mechanobiology Institute of the National University of Singapore.

et al., 2011; Snider and Omary, 2014) and is constantly subject to a readaptation process to support the viscoelastic nature of epithelial cells, facilitating several cellular activities, such as cell migration (Leduc and Etienne-Manneville, 2015; Leube et al., 2015) (see Figure 4.1 in the next Chapter).

Remodelling of the network is made possible by the existence of a rapid diffusive *soluble pool* of keratins which is the source for the formation of new filaments and thickening of the existing ones (Windoffer et al., 2004). On the other side, the amount of overall filamentous keratin constitutes the *insoluble pool*, whose partial disassembly replenishes the soluble pool, in a way that the total amount of keratin is conserved over time. The complete keratin cycle was biologically described by Windoffer et al. (2011) and it is illustrated in Figure 3.2. At the cell periphery, apparently in proximity of focal adhesions which are protein complexes responsible of the cell-substrate adhesion, keratin is nucleated from the soluble. This assembly process creates precursors which are transported towards the keratin network while they elongate to form filaments. Once they reach the network they get integrated, either by becoming a new filament of the meshwork, or bundling with other filaments. This process is nicely highlighted in the videos included in the supplementary material of the paper by Windoffer et al. (2004). Around the nuclear cage, disassembly of the existing filaments is observed. This is a fundamental part of the keratin cycle, as it balances the assembly of new filaments.

We will come back to the biology behind of the keratin cycle in the next chapter,

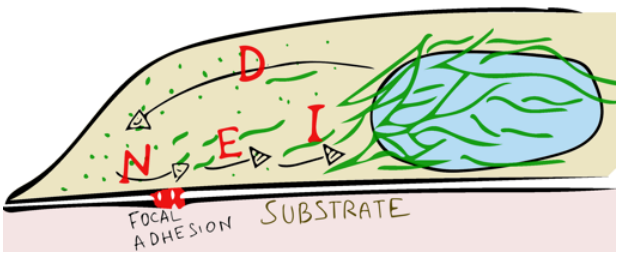

Figure 3.2: An adaptation of the keratin cycle as presented in Windoffer et al. (2011). *N* indicates *nucleation*, *E elongation*, *I integration*, *D disassembly*. Insoluble keratin particles appear mainly around focal adhesions from nucleation of its soluble form. While being transported towards the nucleus these form elongated filaments which are finally integrated into network through integration or bundling. It is important to note also that thickening of filaments happens through lateral aggregation of soluble particles on already formed filaments or bundles. Soluble keratins originate from disassembly of the keratin network, particularly around the nucleus.

where a more detailed description will be needed for the derivation of a new model in multi-dimensions.

3.1.2 A brief introduction of the mathematical modelling of IFs

In the years, the spatio-temporal organisation of intermediate filament network has been object of several data-driven mathematical models. In (Portet et al., 2003; Beil et al., 2009) the keratin network is built up from soluble pool, whose evolution is governed by a reaction-diffusion equation, and filaments grow according to stochastic laws in the presence of enough soluble. Keratin filaments organisation has also been modelled with Brownian motion in (Kim et al., 2010). In order to investigate the assembly kinetics of intermediate filaments, a common approach has been the proposal of different model scenarios: for *in vitro* experiments, ordinary differential equations (ODEs) have been used in support of the biological analysis of the kinetics of vimentin (Kirmse et al., 2007; Portet et al., 2009) and keratin filaments assembly (Portet, 2013; Martin et al., 2015) and, in (Mücke et al., 2016), Monte Carlo simulations are used in studying the kinetics of different intermediate filaments families, including keratins. Portet and Arino (2009) studied the *in vivo* assembly of IFs by proposing different ODE models. ODEs have also been used in describing the assembly-disassembly cycle of keratin (Sun et al., 2014, 2017).

A partial differential equations (PDEs) model describing keratin spatio-temporal evolution was proposed in the paper by Portet et al. (2015). In the following section we will present the main ideas and results of this latter reference, since this will be a necessary introduction for a complete understanding of the work presented in this thesis.

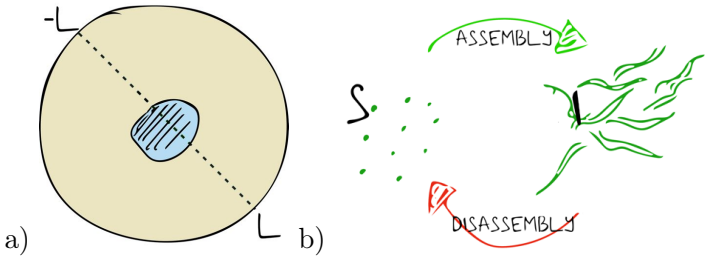

Figure 3.3: The basis of the model by Portet et al. (2015): (a) A cross section of the two-dimensional cell is the one-dimensional domain of the model. Data over the line of $[-L, L]$ are shown in Figure 3.4a; (b) Keratin cycles between a soluble (S) and insoluble (I) form. In terms of the biological model presented in Figure 3.2, assembly involves nucleation, filament elongation and lateral aggregation.

3.1.3 The model by Portet et al. (2015)

While migration requires cells to break their internal symmetry leading to an anisotropic shape, with a well defined front and rear, resting cells have generally a roundish shape and the nucleus is placed around their centre. Indeed, when cells are non-polarised, a reasonable assumption for many protein families is that their internal distribution is circularly symmetric. Therefore the analysis of the two-dimensional spatio-temporal evolution of the keratin network can be reduced to a one-dimensional analysis over a cell line. Portet et al. (2015) developed a mathematical model for keratin dynamics, based on experimental data from the work of Moch et al. (2013). Fluorescence intensity of fluorescent protein-labelled keratins was measured for 50 cells at 24 hours and for 84 cells at 48 hours after seeding. Actual protein concentration is then assumed proportional to fluorescence intensity. In their work, in order to compare data over the different cells, Moch et al. (2013) mapped each cell shape to a unit disc, as described in (Mohl et al., 2012). Therefore, one of the fundamental assumptions in the work by Portet et al. is that the spatio-temporal distribution of keratin essentially follows a radial evolution, so that a one-dimensional model was considered enough to describe the spatial assembly-disassembly dynamics of the keratin material (see also Figure 3.3). In that paper, keratin was classified in soluble (S) and insoluble (I) form, and the respective spatio-temporal concentrations are modelled by the following system of partial differential equations

$$\frac{\partial I}{\partial t} = \frac{\partial}{\partial x}\left(D_I \frac{\partial I}{\partial x} + s(x)v(x)I\right) + a(S) - d(I), \qquad t > 24\text{h}, \quad x \in [-L, L], \tag{3.1}$$

$$\frac{\partial S}{\partial t} = D_S \frac{\partial^2 S}{\partial x^2} - a(S) + d(I), \qquad t > 24\text{h}, \quad x \in [-L, L], \tag{3.2}$$

coupled with zero-flux boundary conditions:

$$D_I \frac{\partial I}{\partial x} + s(x)v(x)I = 0, \qquad t > 24\text{h}, \quad x = -L, \text{ and } x = L, \tag{3.3}$$

$$D_S \frac{\partial S}{\partial x} = 0, \qquad t > 24\text{h}, \quad x = -L, \text{ and } x = L, \tag{3.4}$$

and initial conditions:

$$I(x, 24\text{h}) = I_{24}(x), \qquad x \in [-L, L], \tag{3.5}$$

$$S(x, 24\text{h}) = S_{24}(x), \qquad x \in [-L, L]. \tag{3.6}$$

Equation (3.1) models the evolution of insoluble keratin I, subject to a convective term svI, which describes the tendency of filamentous keratin to move always towards the centre of the cell. A small amount of diffusion $D_I \frac{\partial^2 I}{\partial x^2}$ was also assumed as a regularisation process. The function $v(x)$ represents the magnitude of the speed, while $s(x)$ is a smooth approximation of the sign function such that the material is always transported towards the point $x = 0$ and it is so defined:

$$s(x) = \frac{2}{1 + e^{-x}} - 1. \tag{3.7}$$

The kinetics between insoluble and soluble keratin are described by the functions $a(S)$ and $d(I)$, representing, respectively, assembly and disassembly. In turn, the evolution of the soluble S is described by the reaction-diffusion equation (3.2), where $D_S \gg D_I$.

The boundary conditions (3.3)-(3.4) describe impermeability of the plasma membrane for the keratin material. In equation (3.5) the initial condition $I_{24}(x)$ is the smooth approximation of the biological measurements at the initial time 24h, as shown in Figure 3.6a, while $S_{24}(x)$ is a proportion of $I_{24}(x)$, given that the quantity of soluble keratin in epithelial cells is estimated to be the 5% of the total keratin material, *i.e.*

$$S_{24}(x) = (0.05/0.95)I_{24}(x). \tag{3.8}$$

The cell radius L is 22.5 μm.

Since little is known about the assembly and disassembly dynamics of keratin in cells, Portet et al. proposed a collection of biologically and biochemically relevant hypotheses on the shape of the reaction functions, as well as for the speed profile for insoluble keratin. Data on keratin speed, reported in Figure 3.4b, were calculated in Moch et al. (2013)

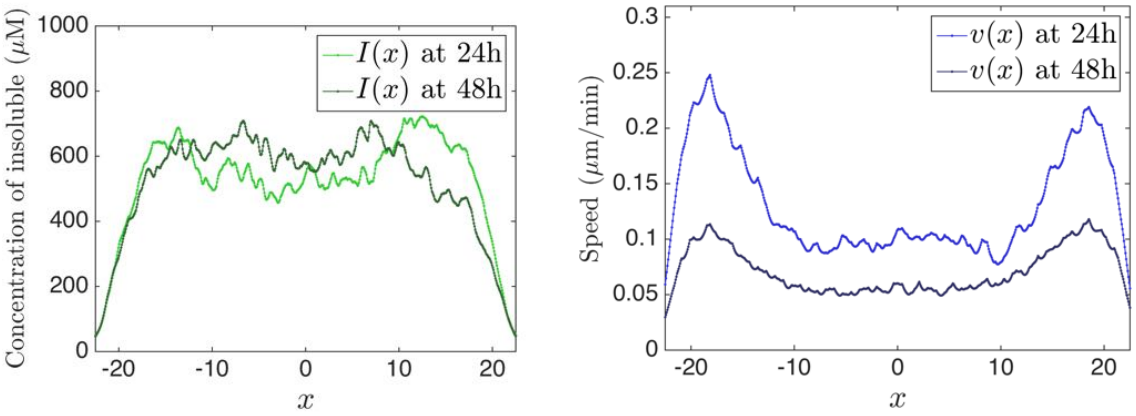

(a) Concentration of insoluble keratin **(b)** Speed of insoluble keratin

Figure 3.4: Experimental data of keratin concentration and speed at the initial and final time over a cross section of the cell. The speed was calculated from data in Moch et al. (2013).

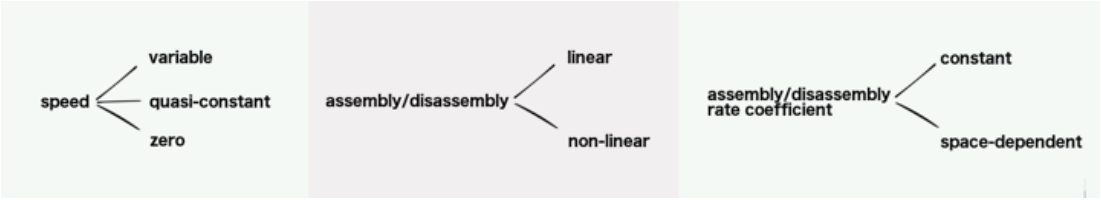

Figure 3.5: The collection of different possibilities in the mathematical modelling by Portet et al. (2015): the function v of (3.1) can be variable in space (based on estimations by Moch et al. (2013)), with the same magnitude in the whole cytosol (and dropping to zero at the nucleus) or zero everywhere ($v \equiv 0$); the kinetics can be of linear (mass action) type or of nonlinear (Michaelis Menten) type; the kinetic rate coefficients can be constant or variable in space. In the latter case the profile shapes are over-imposed (two different profiles for the disassembly, one for the assembly). In the biological model presented by Windoffer et al. (2011), nucleation is observed at the cell peripheries and disassembly around the nucleus, so spatial dependency of keratin cycle was suggested.

with a computational algorithm based on the variation, between consecutive frames, of the fluorescence at each image pixel. As a result, a combination of all the hypothesis (see Figure 3.5), led to 36 different mathematical models. Using an optimisation algorithm, later described in Section 3.3, for each model two to four kinetic parameters were estimated by comparing the solutions of each model to a smooth approximation of the data at the final time 48h, see Figure 3.6. A comparison of all the 36 scenarios was done using the Aikake information criterium, which is a model selection algorithm that takes into account distance from data and number of parameters (Johnson and Omland, 2004). Hence, the resulting best model reads:

$$\frac{\partial I}{\partial t} = \frac{\partial}{\partial x}\left(D_I \frac{\partial I}{\partial x} + svI\right) + \frac{k_{ass} S}{K_S + S} - \frac{k_{dis}(x) I}{K_I + I}, \qquad t > 24\text{h}, \quad x \in (-L, L), \tag{3.9}$$

$$\frac{\partial S}{\partial t} = D_S \frac{\partial^2 S}{\partial x^2} - \frac{k_{ass} S}{K_S + S} + \frac{k_{dis}(x) I}{K_I + I}, \qquad t > 24\text{h}, \quad x \in (-L, L), \tag{3.10}$$

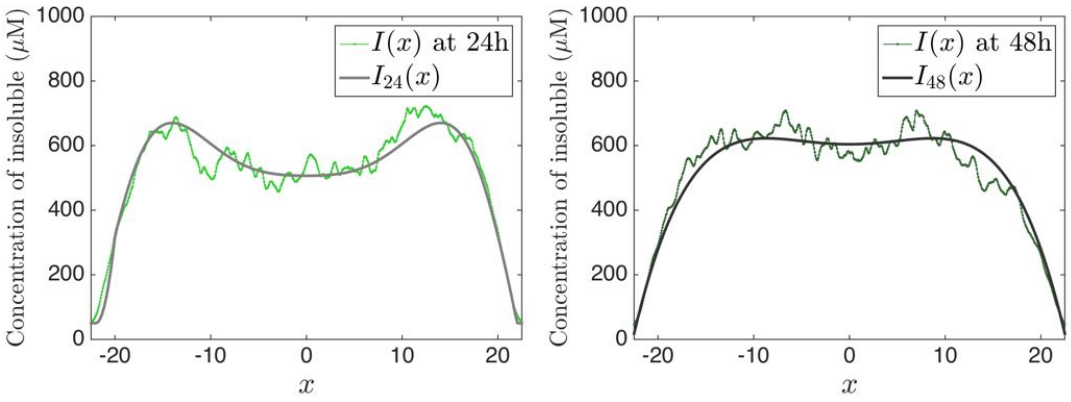

(a) $I_{24}(x)$ as in (3.5) **(b)** $I_{48}(x)$

Figure 3.6: Smoothing the raw data. Explicit definition of the functions is given in Appendix B.1.

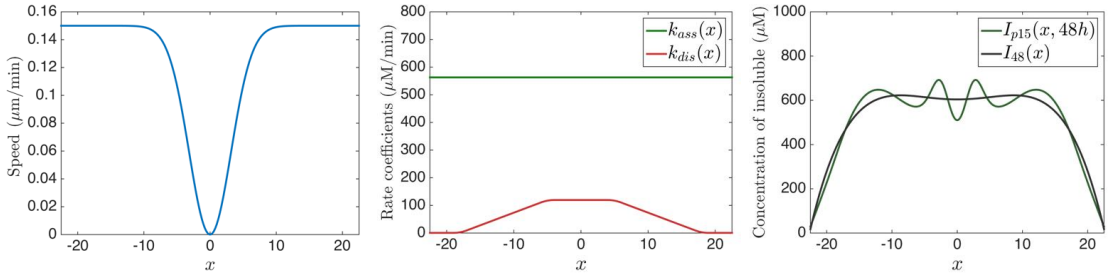

(a) Speed v **(b)** Kinetic rate coefficients **(c)** Solution of the best model

Figure 3.7: The functions from the best model selected among 36 different scenarios in (Portet et al., 2015). The magnitude of the function v is the average of the values reported in Figure 3.4. For an explicit expression of these functions see equations (B.1) and (B.2) in Appendix B.1

coupled with the boundary and initial conditions (3.3)-(3.6). The constants k_{ass}, K_S and K_I have been optimised to fit the solution to the data. In turn k_{dis}, shown in Figure 3.7b, resulted to be space-dependent with an imposed shape, but where its maximal value $k_{dis}^{max} := \max_x\{k_{dis}(x)\}$ was optimised. The magnitude of the speed, v, is shown in Figure 3.7a. The solution I of this model, named $I_{p15}(x,t)$ for convenience, is represented in Figure 3.7c.

3.2 Extending the model by Portet et al.

In Portet et al. (2015) different plausible model scenarios for keratin evolution were proposed and, after a comparison with data, a best one was selected, which is described by (3.9)-(3.10) with boundary conditions (3.3)-(3.4). This model is able to describe the keratin cycle, where the spatial dependency of the kinetics is convincing at the biological level: the disassembly rate coefficient appears to be localised around the nucleus, while

homogeneity in the assembly coefficient rate is also realistic, since this does not cover only nucleation at the cell peripheries but also lateral aggregation of soluble in the filaments, as observed in Miller et al. (1991) and Kölsch et al. (2010). However, in their final discussion an interesting point was made on the reason why scenarios which mostly relied on data were not ranked among the first positions. They proposed a potential explanation for this, which is related to the possibility that noise present in the measurements might negatively influence the parameter estimation. This question is also the starting point of our work, leading to a sequence of new questions:

- For which reasons are data affected by the noise?
- How does the noise influence the data?
- Can we bypass the problems caused by the noise using biological assumptions?
- How well can we estimate the data?

In the following sections we will address all of these questions, which will take us towards a process of "data remodelling", basing our approach on experimental observations.

3.2.1 A comment about the experimental data

Circular symmetry is first of all a biological assumption for resting cells, as their shape is mostly isotropic and many classes of proteins spread radially among the whole cytosol due to motor protein transport along microtubules. In cases of particular events such as migration, or more specifically with polarisation, the internal symmetry is broken and the cell finds its own front-rear (or left-right) directionality, as we discuss for the GTPase proteins in Chapter 2. However, in practice, when dealing with real biological measurements, it is clearly impossible to expect equal values among all the cell radii or a perfect circularity of the resting cell shape. The data presented in Figure 3.4 are an average, among the same radius, between all the cells analysed in the work by Moch et al. (2013). In the absence of polarity, with circular symmetry, all diameters should be more or less equivalent, therefore random rotations of the cells in the averaging process should not have a big impact on the protein distribution profile. However, observing the cells reported in Moch et al. (2013), it is clear that there exist particular configurations such that the data on the interval $[-L, 0)$ might be very different from the $(0, L]$ interval, for certain cross-sections. Indeed, the data for the speed and as well for the concentrations of keratin shown in Figure 3.4 are only "qualitatively symmetric". We bypass this issue by symmetrising the raw data, i.e. all the

data are transformed as follows

$$symmetrised\_data(x) = \frac{data(x) + data(-x)}{2}. \tag{3.11}$$

As a consequence, the function I_{24h} describing the initial condition for the distribution of insoluble keratin is adapted such that

$$I(x, t_0) = \frac{I_{24}(x) + I_{24}(-x)}{2}, \qquad x \in [-L, L] \tag{3.12}$$

where $I_{24}(x)$, originally from the paper by Portet et al. (2015), is described in equation (B.1). The same is done for the final profile at 48 hours. In the same way, the soluble distribution is also symmetrised according to the following expression:

$$S(x, t_0) = \frac{0.05}{0.95}\left(\frac{I_{24}(x) + I_{24}(-x)}{2}\right), \qquad x \in [-L, L]. \tag{3.13}$$

3.2.2 Remodelling the data for the keratin speed

Space dependency. In Figure 3.4b, representing the data for the speed, it is clear the presence of two peaks: apparently the inward movement of keratin initially increases its speed from the cell peripheries towards the interior, until a distance at which it changes its behaviour and starts decreasing. The second part is supported by biological motivations, as crowding effects in the area surrounding the nucleus might play a role in slowing down the transport. Also, radial decreasing in keratin speed was observed in other works, see for example measurements by Wöll et al. (2005). However, the existence of the two peaks, and especially the reason of the initial increase in the speed from the cell boundary, is not very clear. Following a research visit to the Institute of Molecular and Cellular Anatomy of the RWTH Aachen University and a discussion with Prof. Reinhard Windoffer and Prof. Rudolf Leube, we understood that this behaviour might be related to a limitation in the image analyses. Indeed, the small thickness of the cell peripheries can result in difficulties in tracking the weak keratin fluorescence, resulting in underestimation of the speed in the most peripheral regions of the cytoplasm. Therefore we make a conjecture on the speed, proposing a monotonicity in the velocity trend, over the whole cytosol.

The speed is now "remodelled" to match the new conjecture as follows. We ignore the data around the boundaries of the domain and we change theses values, keeping the trend of the more reliable data after the peak. For simplicity, let us consider only the half-left interval $[-L, 0]$ and let M be the maximum value of the speed v on the half-interval,

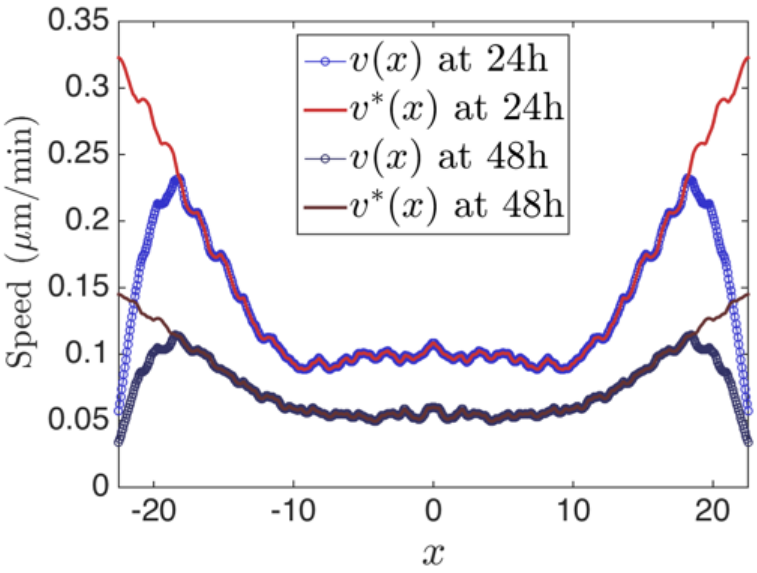

Figure 3.8: The remodelled speed: the original data from figure 3.4b are first symmetrised as in (3.11) (blue colour) and then transformed according to equation (3.14) (red colour).

corresponding to the measurement at the N-th point. Then, the first $N-1$ values of the new speed v^* are calculated as follows:

$$v^*(N-i) = M + (M - v(N+i)), \quad i = 1, \ldots, N-1. \tag{3.14}$$

Symmetrically, the last $N-1$ values of the half-right interval $[0, L]$ are similarly modified. The "remodelling" process is applied to the symmetrised speed profiles at 24 and 48 hours as shown in Figure 3.8.

Another difficulty in experimental measurements is correlated to the presence of the nucleus. Around this area, which corresponds approximately to the interval $[-7.5\mu\text{m}, 7.5\mu\text{m}]$ contained in $[-L, L]$ ($L = 22.5\mu\text{m}$), it is a challenge to control the noise in the data. The presence of the nucleus is a strong obstacle to the keratin movement. At least at $x = 0$, circular symmetry assumption requires that the speed is zero and that its magnitude has an even profile. We propose a smooth approximation of the "re-modelled" data with 4th degree polynomials such that, as a consequence of the circular symmetry, only two coefficients are non-zero, as follows:

$$v_{24h}(x) = a_4^{24} x^4 + a_2^{24} x^2, \tag{3.15}$$

$$v_{48h}(x) = a_4^{48} x^4 + a_2^{48} x^2. \tag{3.16}$$

The speed profiles v_{24h} and v_{48h} are plotted in Figure 3.9 and their coefficients reported

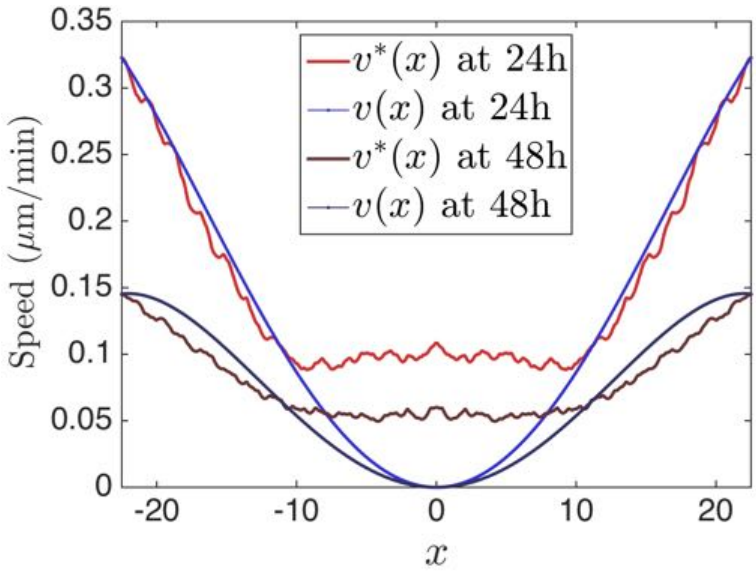

Figure 3.9: The remodelled smooth speed: v_{24h} and v_{48h} as in (3.15)-(3.16) with coefficients $a_4^{24} = -3.36 \times 10^{-5}$, $a_2^{24} = 5.527 \times 10^{-2}$, $a_4^{48} = -3.71 \times 10^{-5}$ and $a_2^{48} = 3.6 \times 10^{-2}$. These values have been found heuristically, imposing the polynomials to pass through two representative data points. The red lines indicate the "remodelled" speed as in (3.14).

in the corresponding caption.

Time dependency. The difference in data at 24 and 48 hours highlights the fact that the speed of keratin changes over time. In particular, the speed at 48 hours appears to have substantially decreased from its initial values. In the absence of further data, it is reasonable to define the speed at any intermediate time as a linear interpolation of $v_{24h}(x)$ and $v_{48h}(x)$, as defined in equations (3.15)-(3.16). Therefore we have:

$$v(x,t) = v_{24h}(x) + \frac{v_{48h}(x) - v_{24h}(x)}{t_0}(t - t_0), \qquad t \in [24h, 48h] \tag{3.17}$$

for all $x \in [-L, L]$.

3.2.3 Reaction kinetics for assembly and disassembly

According to Michaelis Menten's theory, the maximal speed of transformation of a substrate into a product, due to enzymatic activity, is related to the initial concentration of the enzyme, from which it depends linearly. In particular, the maximal speed of reaction, achievable at saturation, is given by the product between the initial concentration of the enzyme and formation rate of the product (for more details see Appendix A.3). Therefore, assuming spatial dependent Michaelis Menten kinetics for the keratin turnover entails the assumption that these processes are coordinated by some particular enzymatic proteins, whose distribution or efficiency can vary radially in the cell. The functions $k_{ass}(x)$ and

$k_{dis}(x)$ represent the maximal rates potentially achievable by the assembly and disassembly processes. A possible interpretation for them is to represent the quantity, at each point, of these unknown enzymes responsible for the turnover. Alternatively, another possibility is to assume the enzymes are uniformly distributed in the cell, but their efficiency to be strictly dependent on their spatial location. In all cases, it is important to understand that since the maximal rates are the asymptotical values of the reactions only when there is saturation of the substrate (which is the soluble pool for the assembly process and insoluble for disassembly), in the non saturation case, the reactions depend also on the substrate, which has a heterogeneous distribution over $[-L, L]$. Therefore, for example, a high value of $k_{ass}(x)$ might not necessarily imply a strong formation of insoluble pool, which can be the case if the soluble concentration is very low at that point.

In the work by Portet et al. (2015), k_{ass} and k_{dis} were constrained over imposed shapes based on biological motivations. The benefit of this choice is that only few parameters were subject to the optimisation process. However, it would be interesting to estimate the spatial efficiency of the kinetics with less constraints. Keeping the Michalis Menten assumption for the assembly and disassembly, in the following we will present a new idea for representing these coefficients.

Space dependency. We chose to describe the space dependency of these rates by continuous piecewise linear functions. These will be determined in order for the solution of our model system to best fit experimental data within an optimal control framework. The basic idea of our approach is to give enough freedom to the model, optimising, with a minimum number of parameters, functions that are now able to show a "non-trivial" shape. Here, the specific structure of the piecewise functions are only detailed for the assembly rate $\overline{k_{ass}}(x)$. A similar derivation suffices for the disassembly rate $\overline{k_{dis}}(x)$. We use the overline to indicate the purely spatial dependent kinetic functions at time $t = 24h$. The spatial domain $[-L, L]$ is partitioned into 6 main sub-intervals such that $\overline{k_{ass}}(x)$ is a linear function on each of them. The partitions occur at the points x_i^{ass} with $i = 0, \ldots, 6$ such as $x_i^{ass} \leq x_{i+1}^{ass}$, where we set $x_5^{ass} = -x_1^{ass}$, $x_4^{ass} = -x_2^{ass}$ and $x_3^{ass} = 0$ in order to have a symmetric profile. Extremity points are $x_0^{ass} = -L$ and $x_6^{ass} = L$.

To have a smooth profile, at each transition x_i^{ass} with $i = 1, \ldots, 5$, a cubic polynomial defined on $[x_i^{ass} - \varepsilon_i, x_i^{ass} + \varepsilon_i)$ is employed as a mollifier. In the numerical resolution of the model the value ε_i is chosen as

$$\varepsilon_i = \min\left\{\frac{x_i^{ass} - x_{i-1}^{ass}}{3}, \frac{x_{i+1}^{ass} - x_i^{ass}}{3}, 0.5\right\}.$$

Hence, $\overline{k_{ass}}(x)$ takes the form:

$$\overline{k_{ass}}(x) = \begin{cases} y_0^{ass} + \frac{y_1^{ass}-y_0^{ass}}{x_1^{ass}+L}(x+L), & \text{if } x \in [-L, x_1^{ass} - \varepsilon_1), \\ \sum_{j=0}^{3} p_j^{ass,l} x^j, & \text{if } x \in [x_l^{ass} - \varepsilon_l, x_l^{ass} + \varepsilon_l), \\ y_l^{ass} + \frac{y_{l+1}^{ass}-y_l^{ass}}{x_{l+1}^{ass}-x_l^{ass}}(x - x_l^{ass}), & \text{if } x \in [x_l^{ass} + \varepsilon_l, x_{l+1}^{ass} - \varepsilon_{l+1}), \text{ for } l = 1, \dots, 4, \\ \sum_{j=0}^{3} p_j^{ass,l+1} x^j, & \text{if } x \in [x_{l+1}^{ass} - \varepsilon_{l+1}, x_{l+1}^{ass} + \varepsilon_{l+1}), \\ y_5^{ass} + \frac{y_6^{ass}-y_5^{ass}}{L-x_5^{ass}}(x - x_5^{ass}), & \text{if } x \in [x_5^{ass} + \varepsilon_5, L], \end{cases} \tag{3.18}$$

where the values of the coefficients $p_j^{ass,i}$, with $j = 0, \dots, 3$, of the polynomial defined on $[x_i^{ass} - \varepsilon_i, x_i^{ass} + \varepsilon_i)$, are determined in order that $\overline{k_{ass}}(x)$ is a C^1-continuous function on $[-L, L]$. Hence, the values of the coefficients $p_j^{ass,i}$, for $j = 0, \dots, 3$, are the solutions of the following linear system:

$$\begin{aligned} \sum_{l=0}^{3} p_l^{ass,i}(x_i^{ass} - \varepsilon_i)^l &= y_{i-1}^{ass} + \frac{y_i^{ass} - y_{i-1}^{ass}}{x_i^{ass} - x_{i-1}^{ass}}(x_i^{ass} - \varepsilon_i - x_{i-1}^{ass}), \\ \sum_{l=0}^{3} p_l^{ass,i}(x_i^{ass} + \varepsilon_i)^l &= y_{i+1}^{ass} + \frac{y_i^{ass} - y_{i+1}^{ass}}{x_i^{ass} - x_{i+1}^{ass}}(x_i^{ass} + \varepsilon_i - x_{i+1}^{ass}), \\ \sum_{l=0}^{3} l p_l^{ass,i}(x_i^{ass} - \varepsilon_i)^{l-1} &= \frac{y_i^{ass} - y_{i-1}^{ass}}{x_i^{ass} - x_{i-1}^{ass}}, \\ \sum_{l=0}^{3} l p_l^{ass,i}(x_i^{ass} + \varepsilon_i)^{l-1} &= \frac{y_i^{ass} - y_{i+1}^{ass}}{x_i^{ass} - x_{i+1}^{ass}}. \end{aligned}$$

Furthermore, to have a symmetric profile, the following requirements have to be satisfied:

$$y_6^{ass} = y_0^{ass}, \quad y_5^{ass} = y_1^{ass} \quad \text{and} \quad y_4^{ass} = y_2^{ass}.$$

To explicitly determine $\overline{k_{ass}}(x)$, the position of 7 points needs to be characterised (see Figure 3.10), hence $\overline{k_{ass}}(x)$ depends on the 6 parameters:

$$y_0^{ass}, \quad x_1^{ass}, \quad y_1^{ass}, \quad x_2^{ass}, \quad y_2^{ass}, \quad y_3^{ass}.$$

Similarly, $\overline{k_{dis}}(x)$ is determined by 6 other parameters

$$y_0^{dis}, \quad x_1^{dis}, \quad y_1^{dis}, \quad x_2^{dis}, \quad y_2^{dis}, \quad y_3^{dis}.$$

used in (3.18).

Our approach follows a relaxation of the original hypothesis by Portet et al. (2015),

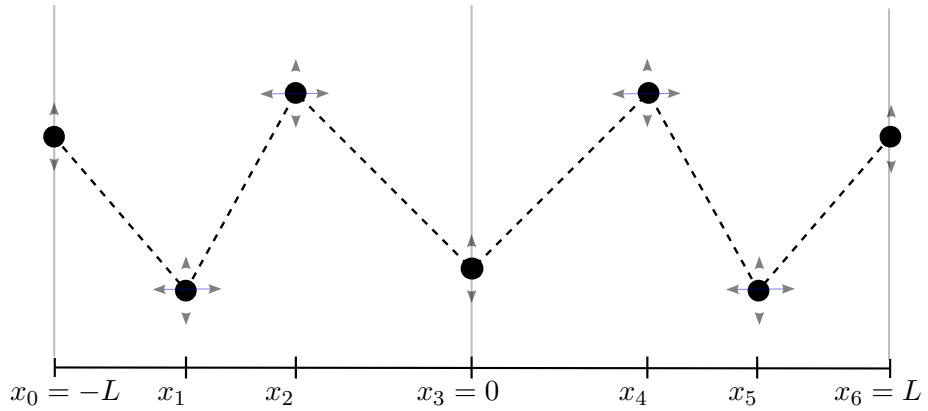

Figure 3.10: Optimisation process of the linear piecewise assembly and disassembly rate coefficients, $k_{ass}(x)$ and $k_{dis}(x)$, respectively. Every point is free to move up and down, while the points with abscissa x_1 and x_2 and those with abscissa x_4 and x_5 are also free to move in the left and/or right directions, constrained by their existence domains given by $[-L, 0]$ and $[0, L]$, respectively.

as the continuous piecewise linear choice for the reaction rate coefficients is one of the simplest generalisation of the ones used by Portet et al. Indeed the optimised functions of Figure 3.7b are a particular case of our more general case, see also Figure 3.10. Now, the values of these 12 parameters, plus the Michaelis Menten constants K_S and K_I have to be estimated using an optimisation algorithm to obtain the solution of the system that best represents experimental observations.

Time dependency. In contrast to the case of the speed, for which we have data at 24 and 48 hours, we do not have any information about the temporal evolution of the assembly and disassembly coefficients k_{ass} and k_{dis}. A deceleration of the entire keratin cycle was observed by Moch et al. (2013). It might be reasonable to assume the cell being able to regulate transport and turnover in a balanced way, meaning that the decreasing of the directed transport speed over time might be related to a decreasing of cellular activities responsible of the keratin turnover and vice versa. Therefore, in order to get some insights about the time dependency of the keratin turnover, we focus our attention on the available data regarding the speed. In particular, it is interesting to note how speed profiles at 24 and 48 hours are qualitatively equivalent. Indeed, it is possible to find an approximate constant of proportionality between the early and late profiles satisfying

$$Data_{48h}(x) \approx C_s Data_{24h}(x), \qquad x \in [-L, L], \tag{3.19}$$

where a good approximation for C_s appears to be 0.5 (see Figure 3.11). Assuming a similar relationship holds for the turnover processes, we can therefore define the following

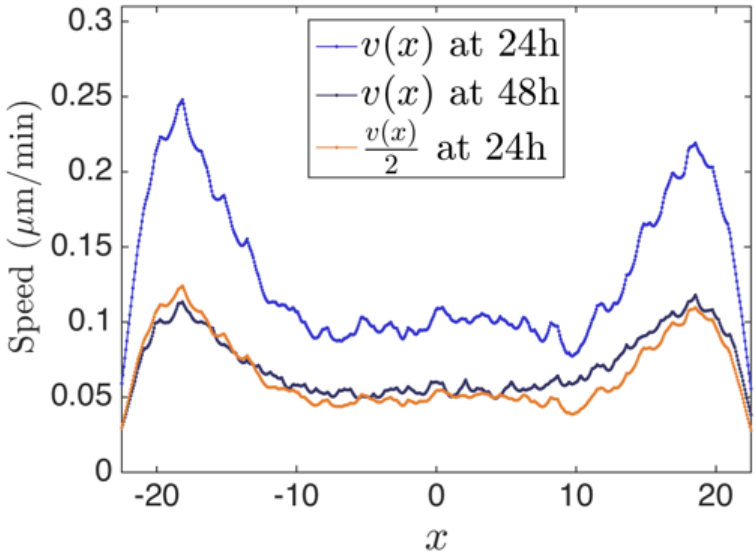

Figure 3.11: The profile of the speed at 48 hours is approximatively half of the profile calculated at 24 hours, equation (3.19) hence $C_s = 0.5$.

time-dependent function

$$\alpha(t) := \left(1 - \frac{t-24}{48}\right), \qquad t \in [24\text{h}, 48\text{h}], \tag{3.20}$$

for which we have the spatio-temporal kinetic coefficients given by

$$k_{ass}(x,t) = \alpha(t)\overline{k_{ass}}(x), \qquad x \in [-L, L], t \in [24\text{h}, 48\text{h}], \tag{3.21}$$

$$k_{dis}(x,t) = \alpha(t)\overline{k_{dis}}(x), \qquad x \in [-L, L], t \in [24\text{h}, 48\text{h}], \tag{3.22}$$

where we recall $\overline{k_{ass}}(x)$ and $\overline{k_{dis}}(x)$ are the kinetic coefficient rates at time $t = 24h$.

3.2.4 Conservation of keratin mass

Summarising all the above modelling assumptions, the new model now reads as follows:

$$\frac{\partial I}{\partial t} = \frac{\partial}{\partial x}\left(D_I \frac{\partial I}{\partial x} + sv(x,t)I\right) + \frac{k_{ass}(x,t)S}{K_S + S} - \frac{k_{dis}(x,t)I}{K_I + I}, \tag{3.23}$$

$$\frac{\partial S}{\partial t} = D_S \frac{\partial^2 S}{\partial x^2} - \frac{k_{ass}(x,t)S}{K_S + S} + \frac{k_{dis}(x,t)I}{K_I + I}, \tag{3.24}$$

for $t > 24\text{h}$ and $x \in [-L, L]$, with boundary conditions

$$D_I \frac{\partial I}{\partial x} + sv(x,t)I = 0, \qquad t > 24\text{h}, \quad x = -L, \text{ and } x = L, \tag{3.25}$$

$$D_S \frac{\partial S}{\partial x} = 0, \qquad t > 24\text{h}, \quad x = -L, \text{ and } x = L, \tag{3.26}$$

and initial conditions (3.12)-(3.13), where $v(x,t)$ is given in (3.17) and $k_{ass}(x,t)$ and $k_{dis}(x,t)$ as in (3.21)-(3.22). We make use of (x,t) to empathise the spatio-temporal dependency of directed transport and kinetics. The model conserves the initial concentration of keratin in both soluble and insoluble form, as stated by the following proposition.

Proposition 3.2.1. Let I and S be solution of (3.23)-(3.26) with initial conditions defined in (3.5)-(3.6). Then

$$K_{TOT}(t) := \int_{-L}^{L} (I(x,t) + S(x,t)) \, \mathrm{d}x = K_{24}, \quad \forall t > 24\text{h}, \tag{3.27}$$

where $K_{24} > 0$ is defined by the initial conditions (3.5)-(3.6) as follows

$$K_{24} := \int_{-L}^{L} (I_{24}(x) + S_{24}(x)) \, \mathrm{d}x.$$

Proof. We show that $K'_{TOT}(t) = 0$. Differentiating (3.27) we have

$$K'_{TOT}(t) = \int_{-L}^{L} \frac{\partial}{\partial t} (I(x,t) + S(x,t)) \, \mathrm{d}x,$$

from which, using (3.23)-(3.24) we get

$$K'_{TOT}(t) = \int_{-L}^{L} \left(\frac{\partial}{\partial x} \left(D_I \frac{\partial I}{\partial x} + sv(x,t)I \right) + D_S \frac{\partial^2 S}{\partial x^2} \right) \mathrm{d}x$$

and integrating we finally get:

$$\begin{aligned} K'_{TOT}(t) = {} & D_I \frac{\partial I}{\partial x}(L,t) + s(L)v(L,t)I(L,t) + D_S \frac{\partial S}{\partial x}(L,t) \\ & - D_I \frac{\partial I}{\partial x}(-L,t) - s(L)v(-L,t)I(-L,t) - D_S \frac{\partial S}{\partial x}(-L,t). \end{aligned}$$

The conclusion follows from the boundary conditions (3.25)-(3.26). □

A fundamental property used in the proof of the above proposition is that the sum of the two reaction functions is zero. Indeed, one could go beyond the particular expression of the reactions, as indicated by the following result.

Theorem 3.2.1. Let us consider the following reaction-diffusion system

$$\frac{\partial u_i}{\partial t} = \frac{\partial}{\partial x}\left(D_i \frac{\partial u_i}{\partial x} + c_i u_i\right) + f_i(u_1, \dots, u_n), \qquad t \geq 0, \quad x \in (a,b), \tag{3.28}$$

$$u_i = u_i^0, \qquad t = 0, \quad x = [a,b], \tag{3.29}$$

$$D_i \frac{\partial u_i}{\partial x} + c_i u_i = 0, \qquad t \geq 0, \quad x = a, b, \tag{3.30}$$

where $a, b \in \mathbb{R}$ (and $a < b$), $n \in \mathbb{N}$, $T > 0$ and $c_i \in C^{1,0}([a,b] \times [0,T])$, $u_i^0 \in L^1([a,b])$ are given for $i = 1, \dots, n$. If the following condition on the reaction functions f_i holds

$$\int_a^b \sum_{i=1}^n f_i \, \mathrm{d}x = 0, \tag{3.31}$$

then the solution $(u_1, \dots, u_n)$ of the above system satisfies

$$K(t) := \int_a^b \sum_{i=1}^n u_i(x,t) \, \mathrm{d}x = \int_a^b \sum_{i=1}^n u_i^0(x) \, \mathrm{d}x, \qquad \forall t \in [0,T].$$

Proof. It is a straightforward extension of the proof of Proposition 3.2.1. □

3.3 Parameters estimation

The solution (I, S) of (3.23)-(3.26) with initial conditions (3.12)-(3.13) depends on $\mathbf{p}$, which is the vector of the unknown parameters:

$$\mathbf{p} = \left[y_0^{ass}, x_1^{ass}, y_1^{ass}, x_2^{ass}, y_2^{ass}, y_3^{ass}, K_S, y_0^{dis}, x_1^{dis}, y_1^{dis}, x_2^{dis}, y_2^{dis}, y_3^{dis}, K_I\right]. \tag{3.32}$$

Note that $\mathbf{p}$ belongs to a particular sample space $\mathcal{P} \subset \mathbb{R}^{14}$ defined by

$$\begin{aligned} \mathcal{P} := \Big\{ \mathbf{p} \in \mathbb{R}^{14} \ : \ & 0 \leq y_i^{ass}, y_i^{dis} \leq M_k, \ -L < x_1^{ass} < x_2^{ass} < 0, \\ & -L < x_1^{dis} < x_2^{dis} < 0, \ 0 \leq K_S, K_I \leq M_K \Big\} \end{aligned} \tag{3.33}$$

for some fixed values M_k and $M_K > 0$, set in order to impose boundedness of all the parameters. The idea of the optimisation method is to first solve the model (3.23)-(3.26) for some initial values of the parameters $\mathbf{p}$ and to calculate the objective function

$$\mathcal{E}(\mathbf{p}) = \sum_{i=0}^{N_x} \left[I(x_i, 48\mathrm{h}, \mathbf{p}) - I_{48}(x_i)\right]^2, \tag{3.34}$$

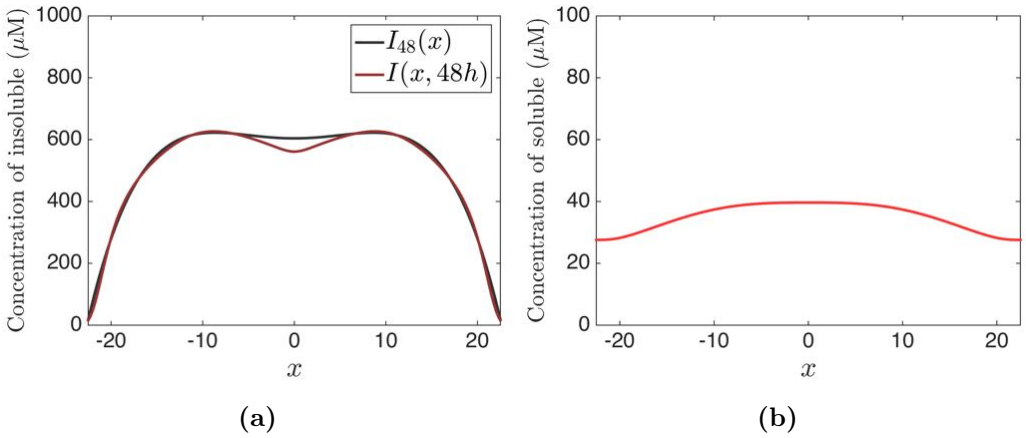

(a) **(b)**

Figure 3.12: The solutions $I(x,t)$ and $S(x,t)$ of the model (3.23)-(3.26) with initial conditions (3.12)-(3.13) at time 48 hours. **(a)** The insoluble distribution $I(x,48h)$ (red colour) and the data $I_{48}(x)$ (dark grey); **(b)** The soluble distribution $S(x,48h)$.

where $x_0, \ldots, x_{N_x}$ are the sampling points discretising the interval $[-L, L]$ and, we recall, $I_{48}(\cdot)$ is a smooth approximation of the data. The final goal is to find a vector $\hat{\mathbf{p}}$ of optimal parameters such that

$$\mathcal{E}(\hat{\mathbf{p}}) = \min_{\mathbf{p}\in\mathcal{P}} \mathcal{E}(\mathbf{p}).$$

For this purpose a genetic algorithm is applied. For more details on this method, see Appendix B.2. As in Portet et al. (2015), we use the Matlab solver `pdepe` to calculate the solution of (3.23)-(3.26), setting $N_x = 200$. The model is then solved iteratively in parallel for different families of vectors of parameters. The process ends either when a vector $\hat{\mathbf{p}}$ such that

$$\mathcal{E}(\hat{\mathbf{p}}) < \varepsilon, \quad \text{with } \varepsilon > 0 \tag{3.35}$$

is found or when no improvements occur after a certain maximal number of iterations.

3.4 Numerical results

The results of the optimisation process are presented in four subsections. First we will present the profile of soluble and insoluble keratin at 48 hours; in the following subsection we show the optimal k_{ass} and k_{dis} and the kinetics are discussed; the temporal evolution of the solutions is presented in the third subsection, while in the final one we will compare our solution to the previous one by Portet et al.

3.4.1 Optimal solution: the keratin distribution at late time

The solution to the new proposed model (3.23)-(3.26) with the new optimised spatio-temporal profiles for speed and kinetics is shown in Figure 3.12a. The solution $I(x,t)$ appears to fit quite well the representation of the data $I_{48}(x)$ over the whole section of the interval representing the cytosol, while it detaches around the nucleus, which is located approximately in $[-7.5\mu\text{m}, 7.5\mu\text{m}]$. However, as already discussed in Section 3.2.2, the presence of the nucleus prevents accurate imaging of keratin concentration and relative measurements in this region. Therefore, around this area, data might not be completely reliable. The cell peripheries, for $|x| > 20\mu\text{m}$, are denoted by the second strongest maximal error. This will be clearer from Figure 3.17b, later presented in Section 3.4.4. It is important to remark also that these regions are the most critical areas with more accurate biological imaging data. Indeed this was one of the reasons for re-modelling the data of the speed of the keratin.

The concentration $S(x,t)$ at the final time 48 hours is shown in Figure 3.12b. As we would expect, since disassembly is mainly observed around the nuclear cage, soluble keratin is maximal at zero and it decays smoothly moving away from the centre of the domain. The difference between central and peripheral concentration is not very strong: at the cell boundary the concentration of soluble is around 70% of the concentration at the cell centre. It is also interesting to note that the initial ratio between soluble and insoluble pool (see equation (3.8)) is approximately maintained. A biological hypothesis is that the total soluble keratin constitutes a percentage of approximately the 5% of the total intracellular keratin (Chou et al., 1993; Portet et al., 2015). Indeed, approximating integrals with the well known trapezoidal rule as

$$S_{TOT}(t) = \int_{-L}^{L} S(x,t)dx \approx \sum_{i=1}^{N_x} \frac{S(x_i,t) + S(x_{i-1},t)}{2} h,$$
$$I_{TOT}(t) = \int_{-L}^{L} I(x,t)dx \approx \sum_{i=1}^{N_x} \frac{I(x_i,t) + I(x_{i-1},t)}{2} h,$$

where h is the spatial step, i.e. $h = x_i - x_{i-1}$ for $i = 1, \ldots, N_x$, we have

$$\frac{S_{TOT}(48h)}{I_{TOT}(48h)} \approx \frac{1571.05}{22908.73} \approx 0.0686 \tag{3.36}$$

while the initial proportion is $0.05/0.95 = 0.0526$ (see equation (3.13)).

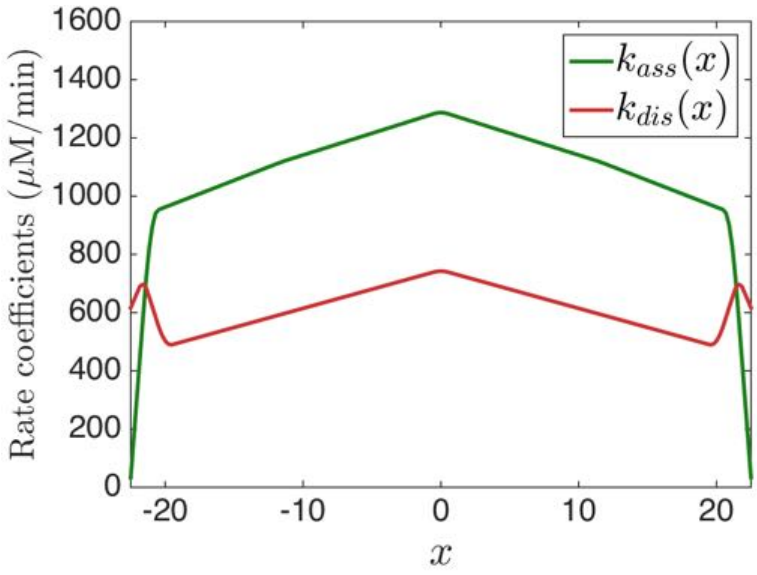

Figure 3.13: The optimal functions $k_{ass}(x,t)$ and $k_{dis}(x,t)$ for assembly and disassembly at time 24 hours. We have $y_0^{ass} = 33.6481$ μM/min, $x_1^{ass} = -21.0220$ μm, $y_1^{ass} = 943.5277$ μM/min, $x_2^{ass} = -11.4869$ μm, $y_2^{ass} = 1118.9$ μM/min, $y_3^{ass} = 1290.6$ μM/min, $y_0^{dis} = 616.7243$ μM/min, $x_1^{dis} = -21.5918$ μm, $y_1^{dis} = 717.5766$ μM/min, $x_2^{dis} = -20.0086$ μm, $y_2^{dis} = 483.3821$ μM/min, $y_3^{dis} = 745.8448$ μM/min. The saturation constants for the assembly and disassembly are $K_S = 227.4028$ μM and $K_I = 976.07$ μM.

3.4.2 Optimal assembly and disassembly rates

The optimal kinetic rates for the assembly and disassembly of keratin are shown in Figure 3.13. We recall that these have been obtained among the class of continuous piecewise linear functions using a genetic algorithm as described in Section 3.3 and Appendix B.2. The shapes of $k_{ass}(x,t)$ and $k_{dis}(x,t)$ share common features. In both cases the maximal value is achieved at zero and the rates decrease approximately linearly as $|x|$ increases. Only around the boundaries the linearity is broken with a huge drop of the assembly rate and an oscillation for the disassembly. The rates decrease linearly over time, halving at 48 hours their initial value (as shown in Figure 3.13).

The optimal Michaelis Menten constants $K_S = 227.4028$ μM and $K_I = 976.07$ μM define the concentration of proteins, respectively S and I, needed to reach half of the maximal reaction rate, respectively for assembly and disassembly. It is interesting to note that at any point of the interval these values are reached. This happens at all the times, as it can be checked in the Figure 3.15 of the following section. Therefore our model never reaches saturation effects in the turnover.

Since there is an inward movement of material but no accumulation happening at the cell centre, we expect the central region to have predominance of disassembled material with assembly characterising the cell peripheries. It is therefore interesting to check how the

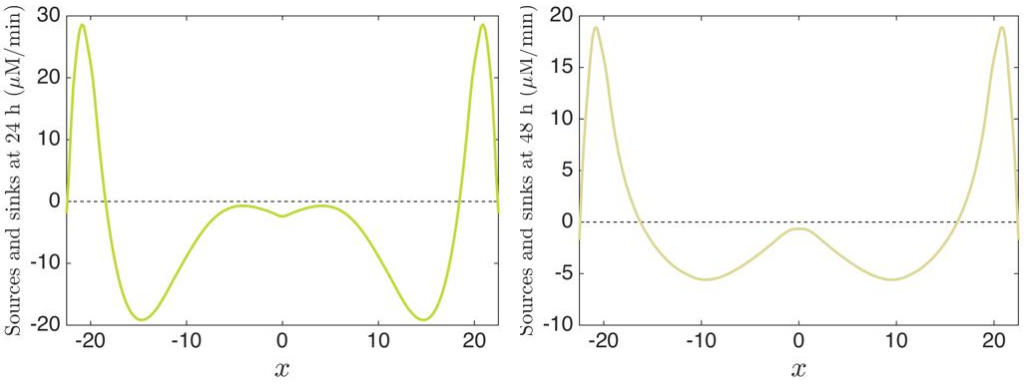

(a) 24 hours **(b)** 48 hours

Figure 3.14: Source and sink regions of keratin insoluble material calculated from the optimised model. The function, representing the net assembled material, is given in equation (3.37).

turnover changes from being mainly assembly to disassembly. Knowing the concentration of S soluble and I insoluble keratin, the rates $k_{ass}(x,t)$, $k_{dis}(x,t)$ and the Michaelis Menten constants K_S and K_I, it is possible to calculate the net assembled material at each point. Let us consider the function

$$SS(x,t) = \frac{k_{ass}(x,t)S(x,t)}{K_S + S(x,t)} - \frac{k_{dis}(x,t)I(x,t)}{K_I + I(x,t)}, \tag{3.37}$$

which is positive when $\frac{k_{ass}(x,t)S(x,t)}{K_S+S(x,t)} > \frac{k_{dis}(x,t)I(x,t)}{K_I+I(x,t)}$, i.e. when more insoluble pool is produced than depleted. The plots of the function (3.37) are shown in Figure 3.14 at 24 and 48 hours. These graphs are very close to the sources and sinks data reported in Moch et al. (2013) and in Portet et al. (2015), confirming the location of the assembly-disassembly regions. The insoluble material is predominantly assembled at the cell peripheries, transported towards the nucleus, which we recall is approximately represented by the interval $[-7.5, 7.5]$, and disassembled in the surrounding areas, where the network is more predominant. This is in a total agreement with the biological model by Windoffer et al. (2011). As well, it is interesting to note that at the cell centre the net assembled material is approximately zero.

What can we say about the biology of the kinetic coefficients k_{ass} and k_{dis}? We have shown that assembly areas might not necessarily coincide with higher values of k_{ass}, and the same is valid for k_{dis}. However, in order to entirely clarify the role of k_{ass} and k_{dis} is necessary, first of all, their biological identification. This step requires a good understanding of the cellular mechanisms, currently widely unknown, behind the assembly and disassembly processes and cannot probably be achieved by solely mathematical tools.

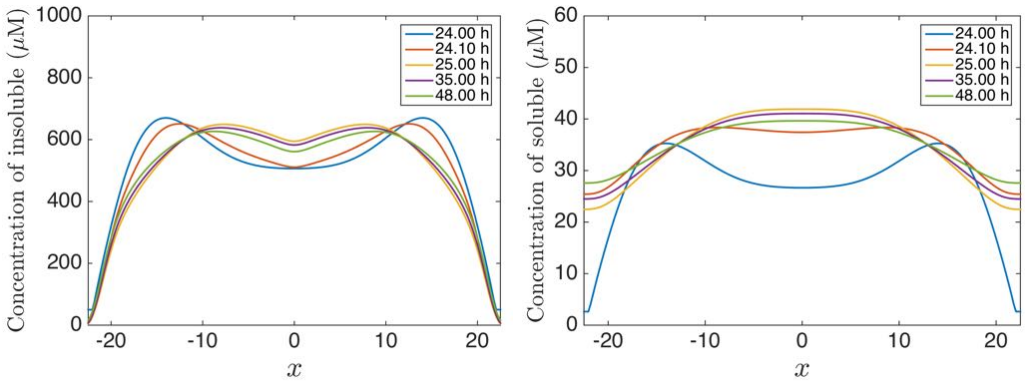

Figure 3.15: The spatio-temporal evolution of the solutions $I(x,t)$ (left) and $S(x,t)$ (right). We have selected 5 different non-equidistant time-steps.

3.4.3 Temporal behaviour of the solutions

We observe that both solutions I and S vary very quickly in the first hour, tending to an apparent profile shape stabilisation. In Figure 3.15 the spatio-temporal evolution of I and S is shown at different times: the transition from the initial condition occurs very quickly and in less than one hour the solutions have reached a profile, which remains qualitatively equivalent for all the remaining time steps. In order to have a quantitative idea of this behaviour, we have calculated the L^2-norm, over $[-L,L]$, of the difference between solutions at consecutive time steps, i.e. the functions

$$\tau_I(t^{n+1}) := \|I(x,t^{n+1}) - I(x,t^n)\|_{L^2([-L,L])},$$
$$\tau_S(t^{n+1}) := \|S(x,t^{n+1}) - S(x,t^n)\|_{L^2([-L,L])},$$

which are numerically approximated by

$$\tau_{I,h}(t^{n+1}) = \sqrt{\sum_{i=1}^{N_x} \frac{\left(I(x_i,t^{n+1}) - I(x_i,t^n)\right)^2 + \left(I(x_{i-1},t^{n+1}) - I(x_{i-1},t^n)\right)^2}{2} h}, \tag{3.38}$$

$$\tau_{S,h}(t^{n+1}) = \sqrt{\sum_{i=1}^{N_x} \frac{\left(S(x_i,t^{n+1}) - S(x_i,t^n)\right)^2 + \left(S(x_{i-1},t^{n+1}) - S(x_{i-1},t^n)\right)^2}{2} h}, \tag{3.39}$$

and are plotted in Figure 3.16. In the absence of other restrictions, such as fitting at intermediate time steps, the model is able to immediately find optimal concentration distributions able to balance transport and turnover of keratin in an almost stable way. The successive transition towards the data profile then occurs very slowly.

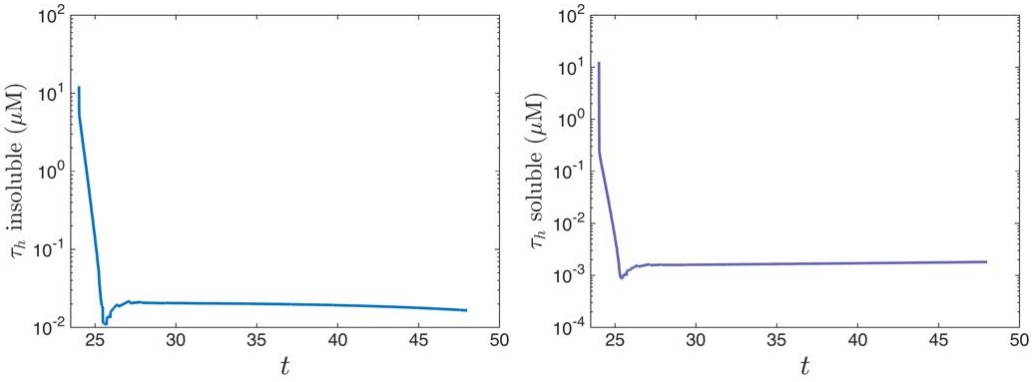

Figure 3.16: The functions defined in (3.38)-(3.39) are plotted in a logarithmic scale which best shows the model behaviour. After a strong jump in the initial times, the variation occurs very slowly.

3.4.4 Comparison with the work by Portet et al.

In order to understand if the new model (3.23)-(3.26) provides a closer approximation of the data with respect to the previous work by Portet et al. (2015) we compare the two solutions by quantifying the error with respect to the data profile $I_{48}(x)$ at 48 hours. For convenience, let $I_{p15}(x,t)$ be the solution of the model (3.9)-(3.10) with boundary conditions (3.5)-(3.6) and optimal parameters as in Portet et al. (2015). Let $I_{new}(x,t)$ be the solution of (3.24)-(3.25) with optimal parameters as in Figure 3.13. In Figure 3.17a the two solutions are plotted together with the data. It is possible to observe how the new model produces a more accurate solution especially in the intervals representing the cytosolic areas, where it almost overlaps the data. As well, the behaviour of the model changes and the oscillations from the previous model by Portet et al. (2015) have disappeared.

In Figure 3.17b a graph indicating the error at each point x is plotted, represented by a vertical line. The regions in which the error of the new model is greater than the one by Portet et al. are minimal and indeed it mainly relies below the previous error. The maximal value is achieved at the point $x = 0$ and in its neighbourhood the error has a maximal area.

To quantify the improvement of the results we can compare the values of the objective functions:

$$\mathcal{E}_{p15} := \sum_{i=0}^{N_x} \left[I_{p15}(x_i, 48\text{h}) - I_{48}(x_i)\right]^2 = 348549.6071, \tag{3.40}$$

$$\mathcal{E}_{new} := \sum_{i=0}^{N_x} \left[I_{new}(x_i, 48\text{h}) - I_{48}(x_i)\right]^2 = 53322.7994. \tag{3.41}$$

This confirms that the new model has strongly improved the fitting to the data, reducing

the error to more than half of its original by Portet et al. (2015).

The Akaike information criterion (Burnham and Anderson, 2002) was a method used in Portet et al. (2015) to compare the different 36 scenarios and to select the best one. This criterion puts in relation the error as in (3.40)-(3.41), the number N_x of compared points and the number N_p of estimated parameters as follows:

$$AIC = N_x \ln\left(\frac{\mathcal{E}}{N_x}\right) + 2N_p.$$

When the number of estimated parameters is bigger than about $N_x/40$, then it is convenient to introduce the corrected Aikake number (Sugiura, 1978; Hurvich and Tsai, 1989; Burnham and Anderson, 2002), defined as

$$AIC_c = N_x \ln\left(\frac{\mathcal{E}}{N_x}\right) + 2N_p\left(\frac{N_x}{N_x - N_p - 1}\right).$$

AIC_c includes a further penalisation to models with many parameters to fit. Indeed it can also be written as

$$AIC_c = AIC + 2N_p\left(\frac{N_p + 1}{N_x - N_p - 1}\right).$$

Two models with different errors and number of estimated parameters are then compared by their AIC numbers and the one having a lower value is selected as the best one. For the two models we have

$$AIC_{p15} = 200 \ln\left(\frac{348549.6071}{200}\right) + 2 \cdot 4 \approx 1500.64, \tag{3.42}$$

$$AIC_{new} = 200 \ln\left(\frac{53322.7994}{200}\right) + 2 \cdot 14 + 2 \cdot 14\left(\frac{14 + 1}{200 - 14 - 1}\right) \approx 1147.43, \tag{3.43}$$

where the corrected Aikake number is used for the new model (since $N_p > N_x/40$). Since $AIC_{new} < AIC_{p15}$, also the Aikake criterion selects the new model as the best one, in spite the fact that the new model has more parameters to fit (14 versus the original 4 by Portet et al.).

3.5 Conclusion

In this chapter we have presented an extension to a pre-existing model for keratin spatio-temporal dynamics previously developed by Portet et al. (2015). Four main questions regarding the data were posed in the introduction to our work. From the understanding of the first three, regarding methods used and difficulties faced in data collection, we were

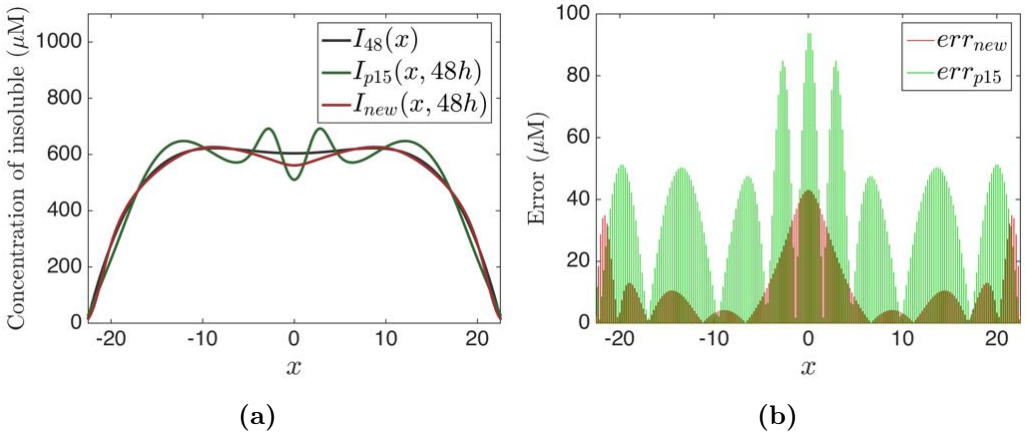

(a) **(b)**

Figure 3.17: Comparison with the model by Portet et al. (2015). Red colour is used to represent the solution and error of the new model, while green colour is used for the model by Portet et al. (2015). **(a)** The solutions of the two models compared to the data; **(b)** Errors with respect to the data. Each vertical line represents the distance between the solution and the data in the point x, i.e. the function $E(x) = \left|I_{48}(x) - I(x, 48h)\right|$, where $I_{48}(x)$ represents the data and $I(x, 48h)$ is the solution of the model.

able to introduce new features in the model. These were derived directly from biological observations and measurements, in collaboration with the biology group directed by Prof. Rudolf Leube, during a research visit at the Institute of Molecular and Cellular Anatomy of the RWTH Aachen University. We were able to substantially modify the pre-existing model. First, the measurements of the speed were reshaped in the most noisy regions, which appear to be the cell peripheries and the nucleus. We have also taken into account the temporal dependency of the keratin transport and turnover. As well, since important protagonists in the keratin cycle in cells are the (unknown) turnover kinetics, we proposed a new way to identify and estimate their spatial profile. Finally we could address the last question posed in the introduction of this work, regarding errors in the approximation of the data, by applying the same genetic algorithm used by Portet et al. in fitting the model to the experimental measurements. We were able to find an optimal solution which well describes the data, especially in the cytosolic area. We have also analysed the kinetics and we were able to confirm the biological keratin cycle proposed by Windoffer et al. (2011): cell peripheries are source regions for filamentous keratin, while sinks of material occurs in the regions surrounding the nucleus. Lastly, we have compared our model to the one developed by Portet et al. (2015). In our case, the error with respect to the data is less than half of the previous one. This confirms that the whole set of assumptions, combined with a less constrained spatial shape of the reaction coefficients, provide a better biological description of the phenomenon.

Now that all the parameters are estimated, it would be very interesting to test other

cases of keratin distribution in other cell lines and check whether our model is able to predict their final configuration. This might be a starting point for a possible future work. As well, we could possibly apply this approach to other intermediate filaments to test possible common properties in their spatio-temporal dynamics.

It is also important to remark that the derivation of this model was driven by data recorded at two different time points. The first one is used as the initial condition, the second one for the parameters estimation. Data taken at another time would more probably prevent our model to evolve very quickly towards a more stable configuration, similar to the final one. Indeed, it would be interesting to see what really happens at an intermediate time and how the model would react to new data and if it could predict the new data profile. As well, with more data, the temporal dependency of the transport and turnover might not result in a linear evolution law.

In the next chapter we will present a new model for keratin dynamics in which radial symmetry is no longer an applicable assumption. This will require an extension to a more appropriate two-dimensional spatial setting.

Chapter 4

A multidimensional model for the spatio-temporal dynamics of the keratin network

4.1 Introduction

In the previous chapter we have introduced the main ideas of the biological model of keratin network remodelling (Kölsch et al., 2010; Windoffer et al., 2011) which was represented in Figure 3.2. These ideas were the base for the development of a one-dimensional mathematical model by Portet et al. (2015), for which we have proposed an extension. The cellular symmetry assumption, leading to the model derivation in a one-dimensional spatial domain, is generally valid for resting cells. However, in general, cells are subject to many different stimuli which cause internal reorganisation and changes in shape. This is observed, for example, in processes such as cell migration: see network distribution in the migrating cell in Figure 4.1 and compare with the resting cell in Figure 3.1 of Chapter 3. Therefore, if we want to model the keratin distribution in general cases, a two- or three-dimensional spatial domain is necessary. In doing so, we decided simply not extend the one-dimensional mathematical model from the previous chapter, but to derive a more detailed one, first by extending the keratin classification to three different components: soluble, precursors and network, whereas in the previous chapter precursors and network were both considered as insoluble. In this way it is possible to distinguish different kinetics such as the nucleation and the network formation, which were previously considered together. Another novelty of this new work is that processes occurring close to the cell and nucleus membrane are included into the model through the boundary conditions.

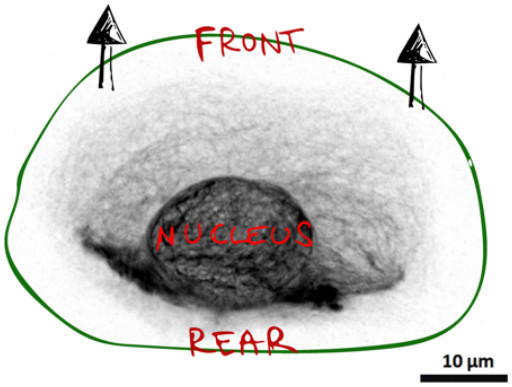

Figure 4.1: The keratin network organisation in a migrating cell. The green curve approximately indicates the cell boundary the two arrows the direction of migration. Migrating human foreskin keratinocyte synthesising fluorescent human keratin 5. Primary keratinocytes were obtained from CELLSYSTEMS (Troisdorf, Germany) and were transfected with an expression construct encoding a human keratin 5-enhanced yellow fluorescent protein chimera (Moch et al., 2013). Fluorescence was recorded with a confocal laser scanning microscope (LSM 710, Zeiss, Jena, Germany) two days after transfection. Picture taken by Nadieh Kuijpers at the Institute of Molecular and Cellular Anatomy (MOCA), RWTH Aachen University.

The chapter is therefore organised as follows: the derivation of the model is presented in Section 4.2. The biology of the keratin proteins accompanies and drives the derivation process. First we derive a purely kinetic model, in which we take into account relevant reactions between the three considered forms of keratins. In a successive subsection, the keratin spatial flow is introduced and, using mass conservation laws, three spatio-temporal reaction-advection-diffusion equations are derived. Boundary conditions are imposed at the cell membrane and at the nucleus membrane, and describe the process of nucleation of precursors, network formation and network disassembly. In Section 4.3 conservation of total mass and non-negativity of the solutions is proved for the model. Section 4.4 is entirely dedicated to the numerical method used to solve the model. The Streamline Upwind Petrov Galerkin (SUPG) finite element method is applied to discretise the equations in space, while discretion in time uses the IMEX finite differences scheme. Finally in Section 4.5 we present the results of a simulation over a simple geometry, which are consistent with the biological model by Windoffer et al. (2011). Since our mathematical model describes a general modelling framework, which can be modified by including further biological aspects of the keratin network remodelling, in the conclusive Section 4.6 we present several possible extensions and indicate future directions which can be taken from this project.

4.2 Derivation of the model driven by biological assumptions

4.2.1 Spatial domain: the cell

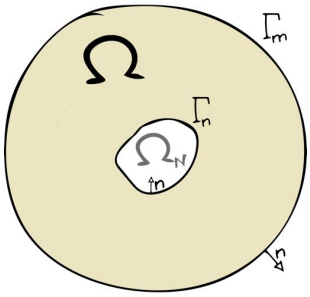

Figure 4.2: The cytosolic space is represented by the domain Ω, whose boundaries are the cell membrane Γ_m and the nucleus envelope Γ_n. The nucleus Ω_N is excluded from the domain.

Let Ω_N be an open, bounded subset of $\mathbb{R}^d$ $(d = 2, 3)$, representing the nucleus of the cell. Its boundary denoted by $\Gamma_n := \partial\Omega_N$ represents the nuclear envelope, which is a membrane composed of phospholipid bilayers (Karp, 2010). Let Ω be another open, bounded subset of $\mathbb{R}^d$ $(d = 2, 3)$, representing the cytosolic volume of the cell, such that $\Omega \cap \Omega_N = \emptyset$ and $\overline{\Omega} \cap \overline{\Omega_N} = \Gamma_n$. Its boundary $\partial\Omega$ is the union of two disjoint closed curves ($d = 2$, surfaces for $d = 3$): the nuclear envelope Γ_n and $\Gamma_m := \partial\Omega \setminus \Gamma_n$, representing the cell membrane. We will always refer to Γ_m as the cell membrane and to Γ_n as the nucleus membrane. A graphical description is represented in Figure 4.2.

4.2.2 Model variables: the keratin forms

Keratin material is found in cells in three different forms: the most predominant constitutes the **network**; a second form is constituted by the **soluble** pool, as we discussed in the previous chapter; the last one, which we will refer to as **precursors**, is the less present form and it is constituted by insoluble keratin in the form of small particles, squiggles, small filaments (Kölsch et al., 2010; Windoffer et al., 2011). The concentration of these three forms is indicated by the functions $N, S, P : \Omega \to \mathbb{R}$.

As a result of discussions with the biologists Anne Pora, Nadieh Kuijpers, Prof. Rudolf Leube and Prof. Reinhard Windoffer from the Institute of Molecular and Cellular Anatomy of RWTH Aachen University, a biological characterisation of these three forms is proposed, based on their biochemical and morphological properties. This is illustrated in Table 4.1. With respect to the one-dimensional model of the previous chapter, the insoluble keratin I is now considered in two forms (P and N).

Categorisation of keratins in these three forms for the *in vivo* analysis was firstly pro-

posed in Portet et al. (2004). Later, this has been the base for the ODE models analysed by Sun et al. (2014, 2017). While these works were purely focused on the kinetics, in the following we aim to describe the evolution of the keratin concentrations subject to both transport and kinetic effects.

	biochemical features	morphological features	modes of assembly
S	soluble	diameter $<$ ULF diameter	lateral growth
P	insoluble	filaments with two free ends	longitudinal and lateral growth
N	insoluble	no free hands	lateral growth

Table 4.1: Categorisation of keratin material in cells. ULF is acronym for unit length filament, which is the filament basic building block (obtained by purely lateral assembly of tetramers), the starting point for longitudinal elongation (Hémonnot et al., 2015; Martin et al., 2015; Deek et al., 2016)

Figure 4.3: Intermediate filaments subunits: the filaments are composed by a longitudinal annihilation of polymers, which are constituted of laterally associated non-polar tetramers made of two dimers associated in a anti-parallel fashion (Etienne-Manneville, 2018).

.

4.2.3 Temporal variation: kinetics between the three forms

In this section we will describe in detail how we model keratin changes between its three forms S, P and N. In order to give a clearer picture of the intermediate filament (IF) family, which include keratins (see Section 3.1.1), in the following lines we briefly introduce the main concepts of the IF structure (Robert et al., 2016; Etienne-Manneville, 2018). As introduced in Chapter 3 and shown in Figure 4.3, the IF subunit structure is composed of a central α-helical rod domain that is flanked by two non α-helical N-terminal and C-terminal end domains. The lateral association of two monomers defines a polar coiled-coil dimer. Among the soluble keratin molecules are the tetramers, which are constituted of two dimers associated laterally in an anti-parallel fashion, thus tetramers are non-polar IF subunits. Lateral association of tetramers constitutes a mini-filament which, in the case of keratin, has a length of about 60 nm (Kayser et al., 2012). The anti-parallel lateral association of dimers is the reason why intermediate filaments have no polarity, and this is one of the main differences with respect to the other cytoskeletal proteins. The principal assembly subunits for keratin IFs are non-polar heteropolymers composed of keratins of type I (acidic) and type II (basic) (Lichtenstern et al., 2012; Kayser et al., 2012; Bray

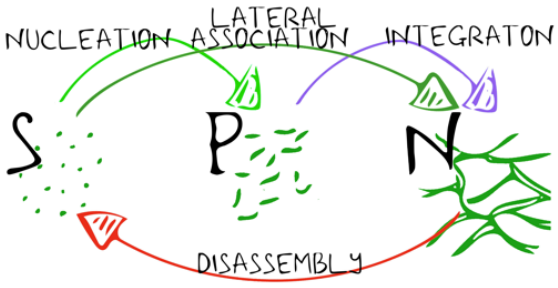

Figure 4.4: Interactions between soluble keratin, precursors and network.

et al., 2015). An important step in the assembly process is the longitudinal association of these "mini-filament" structures in order to create elongated filaments (Köster et al., 2015; Robert et al., 2016).

In vitro studies have been able to characterise the assembly dynamics of different intermediate filament proteins (Herrmann et al., 2007; Chernyatina et al., 2015; Robert et al., 2016), often with the help of mathematical models (Kirmse et al., 2007; Portet et al., 2009; Portet, 2013; Mücke et al., 2016). However, in cells the IF assembly process is not so clear (Jacob et al., 2018). Indeed, the *in vitro* assembly is independent from other proteins or cofactors, i.e. the IF proteins are able to self-assemble, but in cells this process is most probably regulated by some cofactors (Chernyatina et al., 2015). Moreover, disassembly of filaments is a process coordinated by the cell, but this does not occur in *in vitro* experiments where the filaments, once they are assembled, reach a very stable configuration. Indeed, the IF network is a highly dynamic structure in cells (Windoffer et al., 2004, 2011; Leube et al., 2011). Its remodelling is regulated according to specific needs and cell activities, such as adhesion or migration (Leduc and Etienne-Manneville, 2015; Etienne-Manneville, 2018; Robert et al., 2016). In the following, based on the works by Kölsch et al. (2010) and Windoffer et al. (2011), we model each one of the interactions between the three forms of keratin, which are schematically reported in Figure 4.4.

Nucleation With this term we mean one of the ways in which keratin assemblies from its soluble form. In particular we assume nucleation is a process mainly conducted by lateral association of keratin subunits. Following the above introduction, nucleation is modelled as an enzymatic reaction which transforms S into P. It constitutes a part of the assembly process described for the one-dimensional model (3.23)-(3.26) in Chapter 3. Consistently, nucleation is therefore modelled with the Michaelis Menten law. The interconversion of S

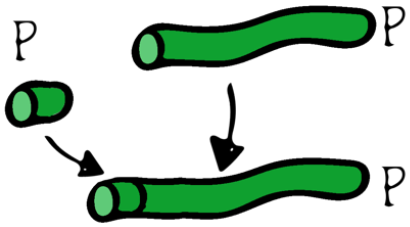

Figure 4.5: We assume keratin filament elongation occurs through end-to-end longitudinal attachment of precursors.

into P is described by the function

$$f_{SP}(S) := \frac{k_{SP}S}{K_{SP} + S} \tag{4.1}$$

such that the temporal variation of S and P purely due to nucleation is described by the system

$$\begin{aligned} \frac{\partial S}{\partial t}(\mathbf{x}, t) &= -f_{SP}(S(\mathbf{x}, t)), \\ \frac{\partial P}{\partial t}(\mathbf{x}, t) &= f_{SP}(S(\mathbf{x}, t)). \end{aligned}$$

Elongation and bundling. Elongation is the longitudinal association of keratin units which increases the length of a filament (Windoffer et al., 2011). We simplify the model by assuming this process occurs only between different forms of precursors, as shown in Figure 4.5. Hence, a precursor can elongate only by the attachment at one end of new keratin particles, previously formed by lateral association of soluble keratins. This means that we are considering elongation as an internal process to precursors, which has no impact in terms of concentrations. Indeed, the total concentration of two neighbour precursors does not change whether they longitudinally attach together or not. Therefore, elongation will be neglected in the model.

Bundling is the lateral association of two filaments of the network resulting in a single bundle (Windoffer et al., 2011). Using similar motivations as for elongation, we can neglect bundling, as it does not change the keratin concentration of the merging filaments.

Integration. Keratin free filaments are continuously transported towards the cell nucleus, getting integrated into the keratin network. Clearly a necessary condition for this to occur is the presence of the network at the integration points. Therefore we choose one of the

simplest description of such kinetics using the *law of mass action* (see Appendix A.3), which states that the reaction rate is proportional to the concentration of the reagents. We obtain the following function

$$f_{PN}(P, N) := k_{PN} PN \tag{4.2}$$

such that, the temporal variation of P and N purely due to integration is given by

$$\begin{aligned} \frac{\partial P}{\partial t}(\mathbf{x}, t) &= -f_{PN}(P(\mathbf{x}, t), N(\mathbf{x}, t)), \\ \frac{\partial N}{\partial t}(\mathbf{x}, t) &= f_{PN}(P(\mathbf{x}, t), N(\mathbf{x}, t)). \end{aligned}$$

Disassembly. As discussed in the previous chapter of this thesis, in cells a soluble pool of keratin is always present, due to the balance between assembly (nucleation and lateral association) and disassembly of filaments and bundles. To model this process we keep the same assumptions from the unidimensional model of Chapter 3, treating the disassembly of the network as a Michaelis Menten reaction with the function

$$f_{NS}(N) := \frac{k_{NS} N}{K_{NS} + N} \tag{4.3}$$

such that, the temporal variation of S and N purely due to integration is described by

$$\begin{aligned} \frac{\partial S}{\partial t}(\mathbf{x}, t) &= f_{NS}(N(\mathbf{x}, t)), \\ \frac{\partial N}{\partial t}(\mathbf{x}, t) &= -f_{NS}(N(\mathbf{x}, t)). \end{aligned}$$

Lateral association. A big part of the keratin network remodelling is constituted by lateral exchange of subunits (Miller et al., 1991). This is predominant in the keratin cycle and represents soluble keratin S getting integrated into the network N, without passing through the nucleation-elongation-integration steps. As for the integration function, S can be transformed into N only in the presence of network, therefore we model this phenomenon again using the Law of Mass Action, with the function

$$f_{SN}(S, N) := k_{SN} SN \tag{4.4}$$

such that, the temporal variation of S and N purely due to lateral association is

$$\frac{\partial S}{\partial t}(\mathbf{x},t) = -f_{SN}(S(\mathbf{x},t),N(\mathbf{x},t)),$$
$$\frac{\partial N}{\partial t}(\mathbf{x},t) = f_{SN}(S(\mathbf{x},t),N(\mathbf{x},t)).$$

The full kinetic model

Finally, the spatial-independent (or well-mixed) model is described by the following system of ordinary differential equations:

$$\frac{dS}{dt} = f_{NS}(N) - f_{SP}(S) - f_{SN}(S,N), \tag{4.5}$$
$$\frac{dP}{dt} = f_{SP}(S) - f_{PN}(P,N), \tag{4.6}$$
$$\frac{dN}{dt} = f_{PN}(P,N) + f_{SN}(S,N) - f_{NS}(N), \tag{4.7}$$

with the reaction functions defined by equations (4.1)-(4.24). It is easy to verify the following proposition.

Proposition 4.2.1. The model (4.5)-(4.7) coupled with the initial conditions

$$S(0) = S_0 > 0$$
$$P(0) = P_0 \geq 0$$
$$N(0) = N_0 > 0$$

satisfies

$$S(t) + P(t) + N(t) = S_0 + P_0 + N_0. \tag{4.8}$$

Proof. It is sufficient to show that

$$\frac{d}{dt}(S + P + N) = 0, \quad \forall t > 0.$$

This is straightforward, by summing the three ODEs (4.5)-(4.7). □

In particular it follows that one variable can be expressed in terms of the other two and the initial given quantity $S_0 + P_0 + N_0$, i.e. the ODE system (4.5)-(4.7) can be reduced to a system of two differential and one algebraic equation.

4.2.4 Spatial variation: transport and movement of keratin

Soluble. The keratin soluble pool is subject to diffusion, probably due to its small size and solubility in the cytoplasm (Windoffer et al., 2011). In this way material obtained from network disassembly reaches the cell periphery where it can be assembled again. Measurements for diffusivity have been published in Kölsch et al. (2010), with the diffusion coefficient estimated to be around 52.8 ± 4.8 μm^2 per minute. Therefore, in our model, we assume the soluble moves subject to Fick's law (see also Section 2.2.1), i.e. its flux is given by

$$\mathbf{J}_S(\mathbf{x}, t, S) := D_S \nabla S, \tag{4.9}$$

where D_S is the constant diffusion coefficient.

Precursors and network. Insoluble keratin appears to be mainly subject to a directed transport towards the cell nucleus. Continuous transport of keratin appears to be predominantly linked to the actin cytoskeleton (Kölsch et al., 2009, 2010; Windoffer et al., 2011; Leduc and Etienne-Manneville, 2015), however a small percentage of microtubule-related transport has also been observed. In the latter case, this seems to be mainly characterised by fast granular particles which move peripherally in a discontinuous manner (Liovic et al., 2003; Windoffer et al., 2011; Kim et al., 2015).

Despite all this, the biological mechanisms behind keratin transport are still largely unknown and are currently subject of research studies. Therefore we suggest to model the speed of transport from data as done in the previous chapter for the one-dimensional case. It is important to note that the available data, obtained through methods for measuring keratin flow based on fluorescence intensity, are currently unable to make an automatic distinction between insoluble keratin in the form of precursors and insoluble keratin in the form of network. New image analysis methods are producing satisfactory results in tracking single keratin filaments (Kotsur et al., 2017), so in the future it might be possible to have distinct data for precursors and network.

In terms of the model we assume a small amount of diffusion is also involved in the insoluble keratin transport. This accounts for the tendency of the network to expand over the whole cytoskeleton. This choice has also a mathematical regularisation consequence. The precursors and network fluxes are therefore given by

$$\mathbf{J}_P(\mathbf{x}, t, P) := D_P \nabla P - \mathbf{v}_P(\mathbf{x}, t) P, \tag{4.10}$$

$$\mathbf{J}_N(\mathbf{x}, t, N) := D_N \nabla N - \mathbf{v}_N(\mathbf{x}, t) N, \tag{4.11}$$

where D_P and D_N are constants representing diffusion coefficients and are such that $D_P, D_N \ll D_S$. The vector functions $\mathbf{v}_P$, $\mathbf{v}_N$ are the velocity fields for precursors and network respectively, which we expect to vary in space and time, as discussed in Chapter 3. In particular we have $\nabla \cdot \mathbf{v}_P \neq 0$ and $\nabla \cdot \mathbf{v}_N, \neq 0$. As done for the one-dimensional model, when comparing to the experimental data, we expect to use a smooth approximation, therefore in general we will consider continuous fields $\mathbf{v}_P$, $\mathbf{v}_N \in C^1(\Omega)$.

4.2.5 Anchorages for the keratin network

Hemidesmosomes are transmembrane multiprotein complexes responsible of the epithelial cell adhesions at the extracellular matrix (Jones et al., 1998; Walko et al., 2015). *Desmosomes*, in turn, are different multiprotein complexes responsible for cell to cell adhesions (Garrod and Chidgey, 2008; Delva et al., 2009). For our work it is important to highlight the fact that both structures are known to create a complex with the intermediate filaments, so these can be seen as anchoring points for the keratin cytoskeletal filaments at the cell membrane (Windoffer et al., 2011; Osmani and Labouesse, 2015).

4.2.6 A remark on the time-space dependency of the kinetic parameters

In Chapter 3 a spatio-temporal dependency for the kinetic coefficients for assembly and disassembly was hypothesised and those spatial profiles approximated by continuous linear piecewise functions. We achieved a good matching between model solution and experimental data as well as consistency in the assembly and disassembly regions comparing with the biological model proposed in literature. Therefore it is natural to ask whether the coefficients k_{SP}, k_{PN}, k_{NS} and k_{SN} of the new proposed reaction functions (4.1)-(4.4) should vary in time and space.

In the last 10-15 years a possible link between keratin nucleation and *focal adhesions*, which are protein complexes responsible of cell-substrate adhesions, has been proposed. This hypothesis follows from several experimental observations in which nucleation and focal adhesions seem to colocalise (Windoffer et al., 2006, 2011; Moch et al., 2016), but this still needs to be entirely understood from a biological and biochemical point of view (Leube et al., 2015). Therefore one would expect k_{SP} (4.1) to change its value in the cell, with a maximum achieved around the focal adhesions. Inspired by this, as a added-value project of this work on keratin, in Appendix C a simple model for the shape of the focal adhesions is presented. Also the disassembly coefficient k_{NS} (4.3), as we have seen in Chapter 3 is expected to vary in space, while spatial dependency in k_{PN} (integration,

(4.2)) and k_{SN} (lateral association, (4.4)), is potentially implicitly included in the functions as they both depend on the local concentration of the network N.

For simplicity, the modelling of the spatio-temporal dependency of the coefficients k_{SP}, k_{PN}, k_{NS} and k_{SN} is not included in this thesis and will be left such extensions for future work. For the moment we will only assume k_{SP}, k_{PN}, k_{NS} and k_{SN} are generic positive functions depending on space and time. The same holds for the modelling of the insoluble keratin transport flow, which is only assumed to be compressible (non divergence-free).

4.2.7 The equations of the model in the cytosol

Let $\mathcal{K} = \mathcal{K}(\mathbf{x}, t) \in C(\overline{\Omega} \times [0, T]) \cap C^{2,1}(\Omega \times (0, T]) \cap C^{1,0}(\overline{\Omega} \times (0, T])$ be the concentration of keratin in one of its three forms (S, P or N) and $\mathcal{K}^c = \mathcal{K}^c(\mathbf{x}, t)$ the concentration of any other of the remaining forms. Since all the three forms are moving in the cytosol, $\mathcal{K}$ is subject to a flux $\mathbf{J}(\mathbf{x}, t, \mathcal{K})$, which we assume to be continuously differentiable. As well, due to its kinetics, $\mathcal{K}$ is both produced and depleted, depending on its concentration and the interactions with the other components $\mathcal{K}^c$. Let $\mathcal{P}_{\mathcal{K}}(\mathbf{x}, t, \mathcal{K}, \mathcal{K}^c)$ and $\mathcal{D}_{\mathcal{K}}(\mathbf{x}, t, \mathcal{K}, \mathcal{K}^c)$ be the functions quantifying the local amount of $\mathcal{K}$ respectively produced and depleted in $\mathbf{x}$ at time t. Hence, by conservation laws (see Section 1.2.1 in Chapter 1 and Section 2.2.1 in Chapter 2), the evolution of $\mathcal{K}$ is described by the following equation:

$$\frac{\partial \mathcal{K}}{\partial t}(\mathbf{x}, t) = -\nabla \cdot \mathbf{J}_{\mathcal{K}}(\mathbf{x}, t, \mathcal{K}) + \mathcal{P}_{\mathcal{K}}(\mathbf{x}, t, \mathcal{K}, \mathcal{K}^c) - \mathcal{D}_{\mathcal{K}}(\mathbf{x}, t, \mathcal{K}, \mathcal{K}^c), \quad \forall \mathbf{x} \in \Omega,\ t \in [t_0, t_f],$$

with $\mathcal{K} \in \{S, P, N\}$ and $\mathcal{K}^c \in \{S, P, N\} \setminus \mathcal{K}$.

The above equation represents a general expression describing the spatio-temporal evolution of each one of the three forms S, P and N. The fluxes $\mathbf{J}_S(\mathbf{x}, t, S)$, $\mathbf{J}_P(\mathbf{x}, t, P)$, $\mathbf{J}_N(\mathbf{x}, t, N)$ have been described in equations (4.9)-(4.11), while the difference between production $\mathcal{P}_{\mathcal{K}}$ and depletion $\mathcal{D}_{\mathcal{K}}$ is described for S, P and N in system (4.5)-(4.7) with the reaction functions given in (4.1)-(4.4). Finally we propose the following full model for

the cytosolic spatio-temporal dynamics of keratin in cells:

$$\underbrace{\frac{\partial S}{\partial t}}_{\substack{\text{soluble}\\ \text{temporal}\\ \text{variation}}} = \underbrace{\nabla\cdot(D_S\nabla S)}_{\text{diffusion}} + \underbrace{f_{NS}(N)}_{\text{disassembly}} - \underbrace{f_{SP}(S)}_{\text{nucleation}} - \underbrace{f_{SN}(S,N)}_{\text{lateral association}}, \tag{4.12}$$

$$\underbrace{\frac{\partial P}{\partial t}}_{\substack{\text{soluble}\\ \text{temporal}\\ \text{variation}}} = \underbrace{\nabla\cdot\big(D_P\nabla P - P\mathbf{v}_P(\mathbf{x},t)\big)}_{\text{transport of } P} + \underbrace{f_{SP}(S)}_{\text{nucleation}} - \underbrace{f_{PN}(P,N)}_{\text{integration}}, \tag{4.13}$$

$$\underbrace{\frac{\partial N}{\partial t}}_{\substack{\text{network}\\ \text{temporal}\\ \text{variation}}} = \underbrace{\nabla\cdot\big(D_N\nabla N - N\mathbf{v}_N(\mathbf{x},t)\big)}_{\text{transport of } N} + \underbrace{f_{PN}(P,N)}_{\text{integration}} + \underbrace{f_{SN}(S,N)}_{\text{lateral association}} - \underbrace{f_{NS}(N)}_{\text{disassembly}}, \tag{4.14}$$

for $\mathbf{x}\in\Omega$ and $t\in(0,T]$. The initial conditions for the model are given by

$$S(\mathbf{x},0) = S_0(\mathbf{x}), \qquad \mathbf{x}\in\Omega, \tag{4.15}$$

$$P(\mathbf{x},0) = P_0(\mathbf{x}), \qquad \mathbf{x}\in\Omega, \tag{4.16}$$

$$N(\mathbf{x},0) = N_0(\mathbf{x}), \qquad \mathbf{x}\in\Omega, \tag{4.17}$$

where S_0, P_0, N_0 are smooth functions representing the spatial distribution of the keratin material at the first experimental observation. Hence, these functions should be modelled from biological data.

4.2.8 Boundary conditions at the cell membrane and nucleus surface

In order to close the system it is necessary to describe the behaviour of S, P and N both at the cell membrane and nucleus envelope. Inspired by modelling ideas for the GTPases in Chapter 2, we couple the protein kinetics to the boundary conditions. Therefore at the membranes the interconversion between the three forms of keratin is described as a flux of each one of the three components. At the cell membrane, we impose the following flux conditions:

$$D_S\nabla S\cdot\mathbf{n} = -f_{SP}(S) - g_{SN}(S), \qquad \mathbf{x}\in\Gamma_m, \tag{4.18}$$

$$(D_P\nabla P - P\mathbf{v}_P)\cdot\mathbf{n} = f_{SP}(S), \qquad \mathbf{x}\in\Gamma_m, \tag{4.19}$$

$$(D_N\nabla N - N\mathbf{v}_N)\cdot\mathbf{n} = g_{SN}(S), \qquad \mathbf{x}\in\Gamma_m, \tag{4.20}$$

while at the nucleus surface we impose

$$D_S \nabla S \cdot \mathbf{n} = f_{NS}(N), \qquad \mathbf{x} \in \Gamma_n, \tag{4.21}$$

$$(D_P \nabla P - P\mathbf{v}_P) \cdot \mathbf{n} = 0, \qquad \mathbf{x} \in \Gamma_n, \tag{4.22}$$

$$(D_N \nabla N - N\mathbf{v}_N) \cdot \mathbf{n} = -f_{NS}(N), \qquad \mathbf{x} \in \Gamma_n. \tag{4.23}$$

The boundary condition (4.19) describes nucleation occurring at the cell membrane. For example, as previously stated, since focal adhesions were hypothesised to be involved in the keratin nucleation, this boundary condition could be potentially used to test this hypothesis. The boundary condition (4.20) describes formation of the network at the cell membrane, which can be related to the presence of hemidesmosomes and desmosomes. This last reaction is modelled, like nucleation, by the Michaelis Menten function of the soluble pool, as follows:

$$g_{SN}(S) := \frac{k_{SN,\Gamma} S}{K_{SN,\Gamma} + S}. \tag{4.24}$$

As a consequence of discussions in Section 4.2.5, a spatial dependency of $k_{S,N,\Gamma}$ is expected. Moreover, it is important to highlight the fact that, unlike f_{SN} (4.4), the function g_{SN} does not depend on the concentration of N. Equation (4.18) provides the source of material for nucleation and network formation.

At the nucleus surface we impose zero flux of keratin precursors, as we assume these are all integrated before reaching the nucleus, while the boundary conditions (4.21) and (4.23) represent disassembly of the keratin network.

Table 4.2 summarises all the variables and parameters used in our model, indicating their dimensional units.

4.3 Basic properties of the model

4.3.1 Conservation of the total mass

The purely kinetic model (4.5)-(4.7) had the property to conserve the total initial keratin concentration (Proposition 4.2.1). This property is conserved in the spatial extension, as stated in the following:

Proposition 4.3.1. Let S, P and N be solutions of (4.12)-(4.23). Then

$$M(t) := \int_\Omega \left(S(\mathbf{x},t) + P(\mathbf{x},t) + N(\mathbf{x},t)\right)\, \mathrm{d}\mathbf{x} = M_0, \quad \forall t \geq 0 \tag{4.25}$$

Param.	Unit	Description
Ω	μm^d $(d = 2, 3)$	cell interior
Γ_m	μm^{d-1}	cell membrane
Γ_n	μm^{d-1}	nucleus envelope
S, P, N	μM	keratin soluble, precursors, network
k_{SP}	$\mu\text{M min}^{-1}$	nucleation coefficient (eq. (4.1))
K_{SP}	μM	saturation parameter for nucleation (eq. (4.1))
k_{PN}	$\mu\text{M}^{-1}\text{ min}^{-1}$	integration coefficient (eq. (4.2))
k_{NS}	$\mu\text{M min}^{-1}$	disassembly coefficient (eq. (4.3))
K_{NS}	μM	saturation parameter for disassembly (eq. (4.3))
k_{SN}	$\mu\text{M}^{-1}\text{ min}^{-1}$	lateral association coefficient (eq. (4.4))
$k_{NS,\Gamma}$	$\mu\text{M}^{-1}\text{ min}^{-1}$	network formation coefficient at Γ_m (eq. (4.24))
$K_{NS,\Gamma}$	μM	saturation parameter for network formation at Γ_m (eq. (4.24))
D_S	$\mu\text{m}^2\text{ min}^{-1}$	soluble diffusion coefficient
D_P	$\mu\text{m}^2\text{ min}^{-1}$	precursors diffusion coefficient
D_N	$\mu\text{m}^2\text{ min}^{-1}$	network diffusion coefficient
$\mathbf{v}_P$	$\mu\text{m min}^{-1}$	precursors velocity field
$\mathbf{v}_N$	$\mu\text{m min}^{-1}$	network velocity field

Table 4.2: Coefficients and parameters of the keratin model (4.12)-(4.23).

where $M_0 \in \mathbb{R}$ is defined by the initial conditions (4.15)-(4.17)

$$M_0 := \int_\Omega \left(S_0(\mathbf{x}) + P_0(\mathbf{x}) + N_0(\mathbf{x})\right)\ \mathrm{d}\mathbf{x}. \tag{4.26}$$

Proof. We show that $M'(t) = 0$ for any t. We have

$$\begin{aligned} M'(t) &= \frac{d}{dt}\int_\Omega \left(S(\mathbf{x},t) + P(\mathbf{x},t) + N(\mathbf{x},t)\right)\ \mathrm{d}\mathbf{x} \\ &= \int_\Omega \frac{\partial S}{\partial t}(\mathbf{x},t)\ \mathrm{d}\mathbf{x} + \int_\Omega \frac{\partial P}{\partial t}(\mathbf{x},t)\ \mathrm{d}\mathbf{x} + \int_\Omega \frac{\partial N}{\partial t}(\mathbf{x},t)\ \mathrm{d}\mathbf{x}, \end{aligned}$$

and using equations (4.12)-(4.14),

$$\begin{aligned} M'(t) = &\int_\Omega \left(\nabla\cdot(D_S\nabla S) + f_{NS}(N) - f_{SP}(S) - f_{SN}(S,N)\right)\ \mathrm{d}\mathbf{x} \\ &+ \int_\Omega \left(\nabla\cdot\left(D_P\nabla P - P\mathbf{v}_P(\mathbf{x},t)\right) + f_{SP}(S) - f_{PN}(P,N)\right)\ \mathrm{d}\mathbf{x} \\ &+ \int_\Omega \left(\nabla\cdot\left(D_N\nabla N - N\mathbf{v}_N(\mathbf{x},t)\right) + f_{PN}(P,N) + f_{SN}(S,N) - f_{NS}(N)\right)\ \mathrm{d}\mathbf{x} \\ = &\int_\Omega \nabla\cdot(D_S\nabla S)\ \mathrm{d}\mathbf{x} + \int_\Omega \nabla\cdot\left(D_P\nabla P - P\mathbf{v}_P(\mathbf{x},t)\right)\ \mathrm{d}\mathbf{x} \\ &+ \int_\Omega \nabla\cdot\left(D_N\nabla N - N\mathbf{v}_N(\mathbf{x},t)\right)\ \mathrm{d}\mathbf{x} \end{aligned}$$

$$
\begin{aligned}
&= \int_{\Gamma_m} \mathbf{n} \cdot (D_S \nabla S)\ \mathrm{d}s + \int_{\Gamma_m} \mathbf{n} \cdot \big(D_P \nabla P - P\mathbf{v}_P(\mathbf{x},t)\big)\ \mathrm{d}s \\
&\quad + \int_{\Gamma_m} \mathbf{n} \cdot \big(D_N \nabla N - N\mathbf{v}_N(\mathbf{x},t)\big)\ \mathrm{d}s + \int_{\Gamma_n} \mathbf{n} \cdot (D_S \nabla S)\ \mathrm{d}s \\
&\quad + \int_{\Gamma_n} \mathbf{n} \cdot \big(D_P \nabla P - P\mathbf{v}_P(\mathbf{x},t)\big)\ \mathrm{d}s + \int_{\Gamma_n} \mathbf{n} \cdot \big(D_N \nabla N - N\mathbf{v}_N(\mathbf{x},t)\big)\ \mathrm{d}s
\end{aligned}
$$

where in the last equality we have used the divergence theorem. Finally, applying the boundary conditions (4.18)-(4.23) the proposition is proved. □

As done in the previous chapters, also in this case the conservation of total mass can be extended to more general systems, as indicated by the following result.

Theorem 4.3.1. Let us consider the following system composed of $N_\Omega \geq 1$ reaction-advection-diffusion equations

$$
\frac{\partial u_i}{\partial t} = \nabla \cdot (D_i \nabla u_i + u_i \mathbf{c_i}) + f_i(u_1, \ldots, u_{N_\Omega}), \qquad \mathbf{x} \in \Omega, t \in (0,T], \tag{4.27}
$$

$$
u_i = u_i^0, \qquad \mathbf{x} \in \Omega, t = 0, \tag{4.28}
$$

$$
(D_i \nabla u_i + u_i \mathbf{c_i}) \cdot \mathbf{n} = g_i(u_1, \ldots, u_{N_\Omega}), \qquad \mathbf{x} \in \Gamma_m, t \in (0,T], \tag{4.29}
$$

$$
(D_i \nabla u_i + u_i \mathbf{c_i}) \cdot \mathbf{n} = h_i(u_1, \ldots, u_{N_\Omega}), \qquad \mathbf{x} \in \Gamma_n, t \in (0,T], \tag{4.30}
$$

for $i = 1, \ldots, N_\Omega$, and $\mathbf{c_i} \in C^{1,0}(\Omega \times [0,T])$, $u_i^0 \in L^1(\Omega)$ are given. If the following condition holds

$$
\sum_{i=1}^{N_\Omega} \left(\int_\Omega f_i\ \mathrm{d}\mathbf{x} + \int_{\Gamma_m} g_i\ \mathrm{d}s + \int_{\Gamma_n} h_i\ \mathrm{d}s \right) = 0, \tag{4.31}
$$

then the solution $(u_1, \ldots, u_n)$ of the above system satisfies

$$
K(t) := \sum_{i=1}^{N_\Omega} \int_\Omega u_i\ \mathrm{d}\mathbf{x} = K_0, \quad \forall t \geq 0, \tag{4.32}
$$

where

$$
K_0 := \sum_{i=1}^{N_\Omega} \int_\Omega u_i^0\ \mathrm{d}\mathbf{x}
$$

is defined by the initial conditions.

Proof. Following the same steps of the proof of Proposition 4.3.1, we show that $K(t)$ is

constant for all $t \in [0,T]$. Differentiating (4.32) we get

$$\begin{aligned} K'(t) &= \sum_{i=1}^{N_\Omega} \int_\Omega \frac{\partial u_i}{\partial t} \, \mathrm{d}\mathbf{x} \\ &= \sum_{i=1}^{N_\Omega} \int_\Omega (\nabla \cdot (D_i \nabla u_i + u_i \mathbf{c_i}) + f_i(u_1, \ldots, u_n)) \, \mathrm{d}\mathbf{x} \\ &= \sum_{i=1}^{N_\Omega} \int_{\Gamma_m} (D_i \nabla u_i + u_i \mathbf{c_i}) \cdot \mathbf{n} \, \mathrm{d}s + \sum_{i=1}^{N_\Omega} \int_{\Gamma_n} (D_i \nabla u_i + u_i \mathbf{c_i}) \cdot \mathbf{n} \, \mathrm{d}s \\ &+ \sum_{i=1}^{N_\Omega} \int_\Omega f_i(u_1, \ldots, u_n) \, \mathrm{d}\mathbf{x}. \end{aligned}$$

Applying the boundary conditions (4.29)-(4.30) we finally get

$$M'(t) = \sum_{i=1}^{N_\Omega} \int_{\Gamma_m} g_i \, \mathrm{d}s + \sum_{i=1}^{N_\Omega} \int_{\Gamma_n} h_i \, \mathrm{d}s + \sum_{i=1}^{N_\Omega} \int_\Omega f_i \, \mathrm{d}\mathbf{x}, \tag{4.33}$$

which is zero due to condition (4.31). □

Remark 4.3.1. The model (4.12)-(4.23) represents a particular case of Theorem 4.3.1, in which

$$\sum_{i=1}^{N_\Omega} f_i = \sum_{i=1}^{N_\Omega} g_i = \sum_{i=1}^{N_\Omega} h_i = 0.$$

4.3.2 Non-negativity of the solutions

Let us rewrite system (4.12)-(4.14) in compact form as follow

$$\mathbf{u}_t = \mathrm{D}\Delta\mathbf{u} - J_\mathbf{v}(\mathbf{u}) + \mathbf{f}(\mathbf{u}) \qquad \mathbf{x} \in \Omega \text{ and } t \in (0,T], \tag{4.34}$$

where $\mathbf{u} = (S,P,N)^T$, $\mathrm{D} = \mathrm{diag}(D_S, D_P, D_N)$, $\Delta\mathbf{u} := (\Delta S, \Delta P, \Delta N)^T$, $J_\mathbf{v}(\mathbf{u}) := (0, \nabla \cdot P\mathbf{v}_P, \nabla \cdot N\mathbf{v}_N)^T$, and

$$\mathbf{f}(\mathbf{u}) = \begin{pmatrix} f_{NS}(N) - f_{SP}(S) - f_{SN}(S,N) \\ f_{SP}(S) - f_P N(P,N) \\ f_{PN}(P,N) + f_{SN}(S,N) - f_{NS}(N) \end{pmatrix}.$$

Definition 4.3.1. Let $\Sigma = \{(u_1,u_2,u_3) \ : \ u_1,u_2,u_3 \geq 0\}$ be the positive octant in the three dimensional space. If for any $\mathbf{u}_0 = (S_0,P_0,N_0) \in \Sigma$ the solution $\mathbf{u}(\mathbf{x},t)$ of (4.34) remains in Σ for any time t, then we say Σ is *invariant* under the system (4.34).

The following holds:

Theorem 4.3.2. The set

$$\Sigma = \{(u_1, u_2, u_3) \ : \ u_1, u_2, u_3 \geq 0\} \tag{4.35}$$

is invariant for the system (4.34).

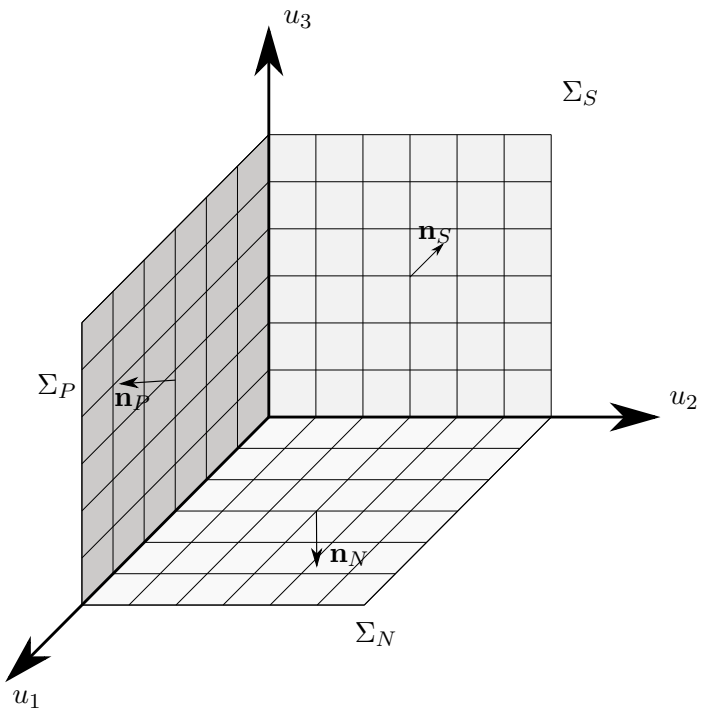

Figure 4.6: The set Σ as defined in (4.35).

Proof. Let us denote with Σ_S, Σ_P and Σ_N the three faces of Σ, i.e.

$$\begin{aligned}
\Sigma_S &= \{(0, u_2, u_3) \ : \ u_2, u_3 \geq 0\}, \\
\Sigma_P &= \{(u_1, 0, u_3) \ : \ u_1, u_3 \geq 0\}, \\
\Sigma_N &= \{(u_1, u_2, 0) \ : \ u_1, u_2 \geq 0\},
\end{aligned}$$

as in Figure 4.6. We will study the behaviour of the system at each one of them showing that, starting from initial conditions within Σ, the solutions of the system (4.34) cannot cross any of these faces.

Following standard techniques (see for example Chapter 6 of Logan (2007)), we will proceed by contradiction assuming Σ is not invariant.

(Σ_S) We assume the existence of an isolated point $(\mathbf{x}_0, t_0) \in \Omega \times (0, T]$ such that $S(\mathbf{x}_0, t_0) = 0$ and $S(\mathbf{x}, t) > 0$, $\forall \mathbf{x} \in \Omega$ and $t < t_0$. This means that t_0 is the first time at which $S = 0$ at a point $\mathbf{x}_0 \in \Omega$.

Since the region Σ is (by assumption) not invariant, we can assume that

$$\frac{\partial S(\mathbf{x}_0, t_0)}{\partial t} < 0. \tag{4.36}$$

We note that the function $s(\mathbf{x}) := S(\mathbf{x}, t_0)$ has a minimum in $\mathbf{x}_0$, which implies $\nabla s(\mathbf{x}_0) = \mathbf{0}$ and that the matrix

$$H_S(\mathbf{x}_0, t_0) = \begin{pmatrix} \frac{\partial^2 S}{\partial x^2}(\mathbf{x}_0, t_0) & \frac{\partial^2 S}{\partial x \partial y}(\mathbf{x}_0, t_0) \\ \frac{\partial^2 S}{\partial y \partial x}(\mathbf{x}_0, t_0) & \frac{\partial^2 S}{\partial y^2}(\mathbf{x}_0, t_0) \end{pmatrix}$$

is symmetric positive semi-definite. If we now multiply system (4.34) at the point $(\mathbf{x}_0, t_0)$ by $\mathbf{n}_S = (-1, 0, 0)$, which is the outward orthogonal unit vector to Σ_S (see Figure 4.6), we get:

$$\frac{\partial S}{\partial t}(\mathbf{x}_0, t_0) = D_S \Delta S(\mathbf{x}_0, t_0) + f_{NS}(N(\mathbf{x}_0, t_0)) - f_{SP}(S(\mathbf{x}_0, t_0)) - f_{SN}(S(\mathbf{x}_0, t_0)) \tag{4.37}$$

which hides a contradiction. Indeed, the right-hand side is non negative as it is the sum of non negative terms: $D_S \Delta S(\mathbf{x}_0, t_0) = D_S \left(\frac{\partial^2 S}{\partial x^2}(\mathbf{x}_0, t_0) + \frac{\partial^2 S}{\partial y^2}(\mathbf{x}_0, t_0) \right) \geq 0$ for the minimum properties (D_S is also positive), and

$$\begin{aligned} &f_{NS}(N(\mathbf{x}_0, t_0)) - f_{SP}(S(\mathbf{x}_0, t_0)) - f_{SN}(S(\mathbf{x}_0, t_0), N(\mathbf{x}_0, t_0)) \\ &= f_{NS}(N(\mathbf{x}_0, t_0)) - f_{SP}(0) - f_{SN}(0, N(\mathbf{x}_0, t_0)) = \frac{k_{NS} N}{K_{NS} + N} \geq 0. \end{aligned}$$

On the other hand the left-hand side of (4.37) is negative by inequality (4.36). Hence, at least at the face Σ_S, the non invariance assumption led to a contradiction: as long as N remains on the positive side of Σ_N, the solution S never gets negative values at any point of Ω.

(Σ_P) Following the previous analysis from step Σ_S, let $(\mathbf{x}_1, t_1) \in \Omega$ be an isolated point such that $P(\mathbf{x}_1, t_1) = 0$ and

$$P(\mathbf{x}, t) > 0, \quad \forall \mathbf{x} \in \Omega \text{ and } t < t_1. \tag{4.38}$$

By assumption the region Σ is (by assumption) non-invariant,

$$\frac{\partial P(\mathbf{x}_1, t_1)}{\partial t} < 0. \tag{4.39}$$

For the same reasons as before it is now trivial to see that $\nabla P(\mathbf{x}_1, t_1) = \mathbf{0}$.

If we now multiply the system (4.34) at the point $(\mathbf{x}_1, t_1)$ by $\mathbf{n}_P = (0, -1, 0)$, which is the outward orthogonal unit vector to Σ_P, we get:

$$\begin{aligned}\frac{\partial P}{\partial t}(\mathbf{x}_1, t_1) = D_P \Delta P(\mathbf{x}_1, t_1) - \nabla \cdot (P\mathbf{v}_P)(\mathbf{x}_1, t_1) \\ + f_{SP}(S(\mathbf{x}_1, t_1)) - f_{PN}(P(\mathbf{x}_1, t_1), N(\mathbf{x}_1, t_1)).\end{aligned}$$

Again we encounter a contradiction: $D_P \Delta P(\mathbf{x}_1, t_1) \geq 0$ for the minimum properties (and $D_P \geq 0$), $P(\mathbf{x}_1, t_1)\nabla \cdot \mathbf{v}_P = 0$ as $P(\mathbf{x}_1, t_1) = 0$ by hypothesis, $\mathbf{v}_P \cdot \nabla P(\mathbf{x}_1, t_1) = 0$ as $\mathbf{x}_1$ is a minimum for $p(\mathbf{x}) = P(\mathbf{x}, t_1)$ and

$$\begin{aligned}f_{SP}(S(\mathbf{x}_1, t_1)) - f_{PN}(P(\mathbf{x}_1, t_1), N(\mathbf{x}_1, t_1)) = f_{SP}(S(\mathbf{x}_1, t_1)) - f_{PN}(0, N(\mathbf{x}_1, t_1)) \\ = \frac{k_{SP} S(\mathbf{x}_1, t_1)}{K_{SP} + S(\mathbf{x}_1, t_1)} \geq 0.\end{aligned}$$

As the right-hand side is non-negative and the left-hand side negative, also at Σ_P we obtain a contradiction. It remains to check if non invariance is true at the face Σ_N.

(Σ_N) This case can be studied in a similar fashion to the previous ones, except for the fact that we need to check the non-negativity of the net reaction for N at an isolated point $(\mathbf{x}_2, t_2) \in \Omega$ such that $N(\mathbf{x}_2, t_2) = 0$ and satisfying the equivalent conditions to (4.38)-(4.39). We have:

$$\begin{aligned}f_{PN}(P(\mathbf{x}_2, t_2), N(\mathbf{x}_2, t_2)) + f_{SN}(S(\mathbf{x}_2, t_2), N(\mathbf{x}_2, t_2)) - f_{NS}(N(\mathbf{x}_2, t_2)) \\ = f_{PN}(P(\mathbf{x}_2, t_2), 0) + f_{SN}(S(\mathbf{x}_2, t_2), 0) - f_{NS}(0) = 0.\end{aligned}$$

This would lead to another contradiction following the same steps as those of the system at Σ_P.

This shows that the solutions of system (4.34) corresponding to initial conditions in Σ cannot pass through any of the three faces of Σ, proving Σ to be an invariant set for the system. □

4.4 The numerical method

We propose to solve the model system (4.12)-(4.23) numerically by using a combination of finite differences and finite element method. In order to do so, we first present the

weak formulation of system (4.12)-(4.23). This formulation will be discretised in space by using the finite element method and in time by using a finite difference scheme. Since the dominance of the directed transport over the diffusion for the network and precursors might create some unphysical oscillations when applying the standard finite element method, a variation of the form, known as the *Streamline Upwind Petrov Galerkin* (SUPG) method, will be adopted (Brooks and Hughes, 1982). The finite difference scheme used for the discretisation in time is an implicit-explicit (IMEX) scheme which considers the transport terms implicitly in time and the reaction terms explicitly (Ruuth, 1995). As it will be clearer in Section 4.4.4, IMEX solves the problem of the nonlinearities in the reaction functions. However, nonlinearities remain from the boundary conditions. Hence, at the end of this section we will discuss on how to solve this last step before having a completely linear problem.

4.4.1 The weak formulation of the model

Let φ_S, φ_P, φ_N be functions of $H^1(\Omega)$. The weak formulation of model system (4.12)-(4.23) is obtained by testing the equations (4.12)-(4.14) respectively with φ_S, φ_P, φ_N as follows:

$$\begin{aligned}
\int_\Omega \frac{\partial S}{\partial t}\varphi_S \,\mathrm{d}\mathbf{x} &= \int_\Omega \nabla\cdot(D_S\nabla S)\varphi_S \,\mathrm{d}\mathbf{x} + \int_\Omega f_{NS}(N)\varphi_S \,\mathrm{d}\mathbf{x} - \int_\Omega f_{SP}(S)\varphi_S \,\mathrm{d}\mathbf{x} \\
&\quad - \int_\Omega f_{SN}(S,N)\varphi_S \,\mathrm{d}\mathbf{x}, \\
\int_\Omega \frac{\partial P}{\partial t}\varphi_P \,\mathrm{d}\mathbf{x} &= \int_\Omega \nabla\cdot\big(D_P\nabla P - P\mathbf{v}_P\big)\varphi_P \,\mathrm{d}\mathbf{x} + \int_\Omega f_{SP}(S)\varphi_P \,\mathrm{d}\mathbf{x} - \int_\Omega f_{PN}(P,N)\varphi_P \,\mathrm{d}\mathbf{x}, \\
\int_\Omega \frac{\partial N}{\partial t}\varphi_N \,\mathrm{d}\mathbf{x} &= \int_\Omega \nabla\cdot\big(D_N\nabla N - N\mathbf{v}_N\big)\varphi_N \,\mathrm{d}\mathbf{x} + \int_\Omega f_{PN}(P,N)\varphi_N \,\mathrm{d}\mathbf{x} \\
&\quad + \int_\Omega f_{SN}(S,N)\varphi_N \,\mathrm{d}\mathbf{x} - \int_\Omega f_{NS}(N)\varphi_N \,\mathrm{d}\mathbf{x}.
\end{aligned}$$

Applying the divergence theorem these are equivalent to:

$$\begin{aligned}
\int_\Omega \frac{\partial S}{\partial t}\varphi_S \,\mathrm{d}\mathbf{x} + \int_\Omega D_S\nabla S\cdot\nabla\varphi_S \,\mathrm{d}\mathbf{x} &= \int_{\Gamma_m} \mathbf{n}\cdot(D_S\nabla S)\varphi_S \,\mathrm{d}s + \int_{\Gamma_n} \mathbf{n}\cdot(D_S\nabla S)\varphi_S \,\mathrm{d}s \\
&\quad + \int_\Omega f_{NS}(N)\varphi_S \,\mathrm{d}\mathbf{x} - \int_\Omega f_{SP}(S)\varphi_S \,\mathrm{d}\mathbf{x} - \int_\Omega f_{SN}(S,N)\varphi_S \,\mathrm{d}\mathbf{x},
\end{aligned}$$

$$\int_\Omega \frac{\partial P}{\partial t}\varphi_P \,\mathrm{d}\mathbf{x} + \int_\Omega \big(D_P\nabla P - P\mathbf{v}_P\big)\cdot\nabla\varphi_P \,\mathrm{d}\mathbf{x} = \int_{\Gamma_m} \mathbf{n}\cdot\big(D_P\nabla P - P\mathbf{v}_P\big)\varphi_P \,\mathrm{d}s + \int_{\Gamma_n} \mathbf{n}\cdot\big(D_P\nabla P - P\mathbf{v}_P\big)\varphi_P \,\mathrm{d}s + \int_\Omega f_{SP}(S)\varphi_P \,\mathrm{d}\mathbf{x} - \int_\Omega f_{PN}(P,N)\varphi_P \,\mathrm{d}\mathbf{x},$$

$$\int_\Omega \frac{\partial N}{\partial t}\varphi_N \,\mathrm{d}\mathbf{x} + \int_\Omega \big(D_N\nabla N - N\mathbf{v}_N\big)\cdot\nabla\varphi_N \,\mathrm{d}\mathbf{x} = \int_{\Gamma_m} \mathbf{n}\cdot\big(D_N\nabla N - N\mathbf{v}_N\big)\varphi_N \,\mathrm{d}s + \int_{\Gamma_n} \mathbf{n}\cdot\big(D_N\nabla N - N\mathbf{v}_N\big)\varphi_N \,\mathrm{d}s + \int_\Omega f_{PN}(P,N)\varphi_N \,\mathrm{d}\mathbf{x} + \int_\Omega f_{SN}(S,N)\varphi_N \,\mathrm{d}\mathbf{x} - \int_\Omega f_{NS}(N)\varphi_N \,\mathrm{d}\mathbf{x}.$$

Finally, applying the boundary conditions (4.18)-(4.23) and using the dot notation to indicate the temporal derivative, the weak formulation of the model reads: find

$$S, P, N \in L^2([0,T]; H^1(\Omega)) \cap L^\infty([0,T]\times\Omega) \text{ with } \dot{S}, \dot{P}, \dot{N} \in L^2([0,T]; H^{-1}(\Omega))$$

such that

$$\int_\Omega \dot{S}\varphi_S \,\mathrm{d}\mathbf{x} + \int_\Omega D_S\nabla S\cdot\nabla\varphi_S \,\mathrm{d}\mathbf{x} + \int_{\Gamma_m} (f_{SP}(S) + g_{SN}(S))\varphi_S \,\mathrm{d}s - \int_{\Gamma_n} f_{NS}(N)\varphi_S \,\mathrm{d}s = \int_\Omega f_{NS}(N)\varphi_S \,\mathrm{d}\mathbf{x} - \int_\Omega f_{SP}(S)\varphi_S \,\mathrm{d}\mathbf{x} - \int_\Omega f_{SN}(S,N)\varphi_S \,\mathrm{d}\mathbf{x},$$

$$\int_\Omega \dot{P}\varphi_P \,\mathrm{d}\mathbf{x} + \int_\Omega \big(D_P\nabla P - P\mathbf{v}_P\big)\cdot\nabla\varphi_P \,\mathrm{d}\mathbf{x} - \int_{\Gamma_m} f_{SP}(S)\varphi_P \,\mathrm{d}s = \int_\Omega f_{SP}(S)\varphi_P \,\mathrm{d}\mathbf{x} - \int_\Omega f_{PN}(P,N)\varphi_P \,\mathrm{d}\mathbf{x},$$

$$\int_\Omega \dot{N}\varphi_N \,\mathrm{d}\mathbf{x} + \int_\Omega \big(D_N\nabla N - N\mathbf{v}_N\big)\cdot\nabla\varphi_N \,\mathrm{d}\mathbf{x} - \int_{\Gamma_m} g_{SN}(S)\varphi_N \,\mathrm{d}s + \int_{\Gamma_n} f_{NS}(N)\varphi_N \,\mathrm{d}s = \int_\Omega f_{PN}(P,N)\varphi_N \,\mathrm{d}\mathbf{x} + \int_\Omega f_{SN}(S,N)\varphi_N \,\mathrm{d}\mathbf{x} - \int_\Omega f_{NS}(N)\varphi_N \,\mathrm{d}\mathbf{x},$$

$\forall\varphi_S$, φ_P, $\varphi_N \in H^1(\Omega)$, $t \in (0,T]$ and such that (4.15)-(4.17) are satisfied. We remind that the spaces H^1 and $L^2([0,T]; H^1)$ are defined in Section 1.5.1, while H^{-1} is the dual space of H^1 (for definition and theory see for example the textbook Evans (2010)).

4.4.2 Spatial discretisation

We solve the keratin model on an approximation Ω_h of the cell domain Ω. Here, we consider Ω in $\mathbb{R}^2$. For the extension to three-dimensional domains see Section 2.9.2 of Chapter 2.

We approximate the boundaries Γ_m and Γ_n with two interpolant closed polygonal curves $\Gamma_{m,h}$ and $\Gamma_{n,h}$. Then we further discretise Ω_h into the union of $N_{\mathcal{T}}$ triangles, i.e. given a set $\mathcal{T}_h = \{T_1, \ldots, T_{N_{\mathcal{T}}}\}$ we have $\overline{\Omega_h} = \bigcup_{i=1}^{N_{\mathcal{T}}} T_i$. The triangles share the following properties: $\overset{\circ}{T}_i \cap \overset{\circ}{T}_j = \emptyset$ for any couple $T_i \neq T_j$ and if $T_i \cap T_j \neq \emptyset$ then the intersection is either a common vertex or a common edge. We consider the function space

$$V_h(\Omega_h) := \left\{ v_h : \Omega_h \to \mathbb{R} \ : \ v_h \in C^0(\Omega_h), v_h\big|_T \in \mathbb{P}_1(T), \ \forall T \in \mathcal{T}_h \right\} \subset H^1(\Omega_h) \cap L^\infty(\Omega_h),$$

composed of all the continuous functions which are linear over every element T of the mesh $\mathcal{T}_h$. We use the subscript h to denote functions in $V_h(\Omega_h)$. Let $S_{0,h}(\mathbf{x}), P_{0,h}(\mathbf{x}), N_{0,h}(\mathbf{x})$ be functions in $V_h(\Omega_h)$ representing the initial conditions (4.15)-(4.17). We keep for later the description on how we select these functions. As well with $\mathbf{v}_{P,h}$ and $\mathbf{v}_{N,h}$ we represent approximations of $\mathbf{v}_P$ and $\mathbf{v}_N$ in $V_h(\Omega_h) \times V_h(\Omega_h)$. Hence the semi-discrete weak formulation reads: find

$$S_h, P_h, N_h \in L^2([0,T]; V_h(\Omega_h)) \text{ with } \dot{S}_h, \dot{P}_h, \dot{N}_h \in L^2([0,T]; V_h(\Omega_h))$$

such that

$$\begin{aligned} &\int_{\Omega_h} \dot{S}_h \varphi_{S,h} \, \mathrm{d}\mathbf{x} + \int_{\Omega_h} D_S \nabla S_h \cdot \nabla \varphi_{S,h} \, \mathrm{d}\mathbf{x} + \int_{\Gamma_{m,h}} (f_{SP}(S_h) + g_{SN}(S_h)) \varphi_{S,h} \, \mathrm{d}s \\ &\quad - \int_{\Gamma_{n,h}} f_{NS}(N_h) \varphi_{S,h} \, \mathrm{d}s = \int_{\Omega} f_{NS}(N_h) \varphi_{S,h} \, \mathrm{d}\mathbf{x} - \int_{\Omega_h} f_{SP}(S_h) \varphi_{S,h} \, \mathrm{d}\mathbf{x} \\ &\quad - \int_{\Omega_h} f_{SN}(S_h, N_h) \varphi_{S,h} \, \mathrm{d}\mathbf{x}, \end{aligned} \tag{4.40}$$

$$\begin{aligned} &\int_{\Omega_h} \dot{P}_h \varphi_{P,h} \, \mathrm{d}\mathbf{x} + \int_{\Omega_h} \left(D_P \nabla P_h - P_h \mathbf{v}_{P,h} \right) \cdot \nabla \varphi_{P,h} \, \mathrm{d}\mathbf{x} - \int_{\Gamma_{m,h}} f_{SP}(S_h) \varphi_{P,h} \, \mathrm{d}s \\ &\quad = \int_{\Omega_h} f_{SP}(S_h) \varphi_{P,h} \, \mathrm{d}\mathbf{x} - \int_{\Omega_h} f_{PN}(P_h, N_h) \varphi_{P,h} \, \mathrm{d}\mathbf{x}, \end{aligned} \tag{4.41}$$

$$\begin{aligned} &\int_{\Omega_h} \dot{N}_h \varphi_{N,h} \, \mathrm{d}\mathbf{x} + \int_{\Omega_h} \left(D_N \nabla N_h - N_h \mathbf{v}_{N,h} \right) \cdot \nabla \varphi_{N,h} \, \mathrm{d}\mathbf{x} - \int_{\Gamma_{m,h}} g_{SN}(S_h) \varphi_{N,h} \, \mathrm{d}s \\ &\quad + \int_{\Gamma_{n,h}} f_{NS}(N_h) \varphi_{N,h} \, \mathrm{d}s = \int_{\Omega_h} f_{PN}(P_h, N_h) \varphi_{N,h} \, \mathrm{d}\mathbf{x} + \int_{\Omega_h} f_{SN}(S_h, N_h) \varphi_{N,h} \, \mathrm{d}\mathbf{x} \\ &\quad - \int_{\Omega_h} f_{NS}(N_h) \varphi_{N,h} \, \mathrm{d}\mathbf{x}, \end{aligned} \tag{4.42}$$

$\forall\ \varphi_{S,h},\ \varphi_{P,h},\ \varphi_{N,h} \in V_h(\Omega_h),\ t \in (0,T]$, and

$$S_h(\mathbf{x},0) = S_{0,h}, \tag{4.43}$$

$$P_h(\mathbf{x},0) = P_{0,h}, \tag{4.44}$$

$$N_h(\mathbf{x},0) = N_{0,h}. \tag{4.45}$$

The set of continuous piecewise linear hat functions $\varphi_1, \ldots, \varphi_{N_h}$ such that

$$\varphi_i(\mathbf{x}_j) = \delta_{i,j}, \qquad 1 \le i,j \le N_x,$$

where $\delta_{i,j}$ is the Kronecker delta ($= 1$ for $i = j$, zero otherwise), constitutes a basis for the function space $V_h(\Omega_h)$. Hence, since every element of $V_h(\Omega_h)$ can be written as a linear combination of $\varphi_1, \ldots, \varphi_{N_h}$, solving equations (4.40)-(4.42) is equivalent to find the $3N_h$ time dependent coefficients $S_1(t), \ldots, S_{N_h}(t)$, $P_1(t), \ldots, P_{N_h}(t)$, $N_1(t), \ldots, N_{N_h}(t)$ of the unknown solutions $S_h(\mathbf{x},t)$, $P_h(\mathbf{x},t)$, $N_h(\mathbf{x},t)$.

In particular, since the initial conditions $S_{0,h}(\mathbf{x}), P_{0,h}(\mathbf{x}), N_{0,h}(\mathbf{x}) \in V_h(\Omega_h)$ are also linear combinations of the hat functions, one way of defining their coefficients is to take the nodal values of the original functions $S_0(\mathbf{x}), P_0(\mathbf{x}), N_0(\mathbf{x})$ defined in (4.15)-(4.17), i.e.

$$S_{0,h}(\mathbf{x}) = \sum_{j=1}^{N_h} S_0(\mathbf{x}_j)\varphi_j(\mathbf{x}), \quad P_{0,h}(\mathbf{x}) = \sum_{j=1}^{N_h} P_0(\mathbf{x}_j)\varphi_j(\mathbf{x}), \quad N_{0,h}(\mathbf{x}) = \sum_{j=1}^{N_h} N_0(\mathbf{x}_j)\varphi_j(\mathbf{x}). \tag{4.46}$$

Therefore the problem (4.40)-(4.45) can be restated as follows: we aim to find $S_1(t), \ldots, S_{N_h}(t)$, $P_1(t), \ldots, P_{N_h}(t)$, $N_1(t), \ldots, N_{N_h}(t)$ such that

$$\begin{aligned}
&\sum_{j=1}^{N_h} \dot{S}_j \int_{\Omega_h} \varphi_j\varphi_i \,\mathrm{d}\mathbf{x} + \sum_{j=1}^{N_h} S_j \int_{\Omega_h} D_S \nabla\varphi_j \cdot \nabla\varphi_i \,\mathrm{d}\mathbf{x} + \int_{\Gamma_{m,h}} (f_{SP}(S_h) + g_{SN}(S_h))\varphi_i \,\mathrm{d}s \\
&\quad - \int_{\Gamma_{n,h}} f_{NS}(N_h)\varphi_i \,\mathrm{d}s = \int_{\Omega} f_{NS}(N_h)\varphi_i \,\mathrm{d}\mathbf{x} - \int_{\Omega_h} f_{SP}(S_h)\varphi_i \,\mathrm{d}\mathbf{x} \\
&\quad - \int_{\Omega_h} f_{SN}(S_h,N_h)\varphi_i \,\mathrm{d}\mathbf{x}, \qquad\qquad i = 1, \ldots, N_h,
\end{aligned} \tag{4.47}$$

$$\sum_{j=1}^{N_h} \dot{P}_j \int_{\Omega_h} \varphi_j \varphi_i \, \mathrm{d}\mathbf{x} + \sum_{j=1}^{N_h} P_j \int_{\Omega_h} \left(D_P \nabla \varphi_j - \varphi_j \mathbf{v}_{P,h} \right) \cdot \nabla \varphi_i \, \mathrm{d}\mathbf{x} - \int_{\Gamma_{m,h}} f_{SP}(S_h) \varphi_i \, \mathrm{d}s$$
$$= \int_{\Omega_h} f_{SP}(S_h) \varphi_i \, \mathrm{d}\mathbf{x} - \int_{\Omega_h} f_{PN}(P_h, N_h) \varphi_i \, \mathrm{d}\mathbf{x}, \qquad i = 1, \dots, N_h, \tag{4.48}$$

$$\sum_{j=1}^{N_h} \dot{N}_j \int_{\Omega_h} \varphi_j \varphi_i \, \mathrm{d}\mathbf{x} + \sum_{j=1}^{N_h} N_j \int_{\Omega_h} \left(D_N \nabla \varphi_j - \varphi_j \mathbf{v}_{N,h} \right) \cdot \nabla \varphi_i \, \mathrm{d}\mathbf{x} - \int_{\Gamma_{m,h}} g_{SN}(S_h) \varphi_i \, \mathrm{d}s$$
$$+ \int_{\Gamma_{n,h}} f_{NS}(N_h) \varphi_i \, \mathrm{d}s = \int_{\Omega_h} f_{PN}(P_h, N_h) \varphi_i \, \mathrm{d}\mathbf{x} + \int_{\Omega_h} f_{SN}(S_h, N_h) \varphi_i \, \mathrm{d}\mathbf{x}$$
$$- \int_{\Omega_h} f_{NS}(N_h) \varphi_i \, \mathrm{d}\mathbf{x}, \qquad i = 1, \dots, N_h, \tag{4.49}$$

for $t \in (0, T]$ and such that $S_j(0) = S_0(\mathbf{x}_j)$, $P_j(0) = P_0(\mathbf{x}_j)$, $N_j(0) = N_0(\mathbf{x}_j)$ for $j = 1, \dots, N_h$.

Before proceeding into discretising in time and solving nonlinearities we introduce a variation of our method in the next section.

4.4.3 The Streamline Upwind Petrov Galerkin method

The standard Galerkin finite element method might fail in accuracy when solving a reaction-advection-diffusion equation. Indeed, when advection dominates over diffusion, the numerical solution can exhibit large oscillations around the exact solution. This is particularly evident when the real solution presents boundary layers. A typical example of a steady state one-dimensional advection-diffusion equation is generally used to show the equivalence between the standard Galerkin finite element method and the central finite difference scheme $\frac{u(x_{i+1}) - u(x_{i-1})}{x_{i+1} - x_{i-1}}$ in the approximation of the convective term $u'(x_i)$, which is generally not the best choice for transport problems (for the example and discussion see Brooks and Hughes (1982), Johnson (1987) (Chapter 9) or Quarteroni and Valli (2008) (Chapter 8)). Indeed, since information propagate in one direction, for example in the direction of the increasing x, $u(x_{i-1})$ might contain more relevant information for the point x_i than $u(x_{i+1})$. The finite element discretisation of the diffusion term $u''(x_i)$ is, in turn, equivalent to the second order centered finite difference scheme $\frac{u(x_{i+1}) - 2u(x_i) + u(x_{i-1})}{h^2}$, where $h = x_i - x_{i-1}$ is the homogeneous spatial discretisation step.

One possible way to prevent numerical oscillations is to perturb the system by adding further diffusion in order to counterbalance the convective term and solve the model still us-

ing the standard finite element method. Indeed, the upwind finite difference discretisation, more suitable than the centered scheme, can be written as

$$\frac{u(x_i) - u(x_{i-1})}{h} = \frac{u(x_{i+1}) - u(x_{i-1})}{2h} - \frac{h}{2}\frac{u(x_{i+1}) - 2u(x_i) + u(x_{i-1})}{h^2},$$

which shows that, in order to obtain the equivalent of the upwind finite difference scheme when applying the standard Galerkin method, it is sufficient to add a diffusion term of coefficient $-h/2$, generally called artificial diffusion. This choice results in a perturbation of the original system and introduces unnecessary crosswind diffusion.

The *Streamline Upwind Petrov Galerkin* (SUPG) is a method, firstly proposed by Brooks and Hughes (1982), which is able to add diffusion without changing the nature of the equation. In particular, in two or three dimensions, the artificial diffusion is added only in the flow direction defined by the convective term, hence this method is less over-diffusive compared to simply adding diffusion in all directions. The method is based on a variation of the weak formulation of the problem, achieved by using new test functions. The idea is to replace $\varphi_{P,h}$ in (4.41) with

$$\widehat{\varphi_{P,h}} = \varphi_{P,h} + \tau_{P,h}\mathbf{v}_{P,h} \cdot \nabla\varphi_{P,h}$$

and $\varphi_{N,h}$ in (4.42) with

$$\widetilde{\varphi_{N,h}} = \varphi_{N,h} + \tau_{N,h}\mathbf{v}_{N,h} \cdot \nabla\varphi_{N,h},$$

where $\varphi_{P,h}$ and $\varphi_{N,h}$ still belong to $V_h(\Omega_h)$. The gradients need to be understood in the distributional sense, therefore $\nabla\varphi_{P,h}$ and $\nabla\varphi_{N,h}$ exist over Ω_h and are discontinuous functions, piecewise constants over the mesh elements. The coefficients $\tau_{P,h} = \tau_{P,h}(\mathbf{v}_{P,h}, D_P, h_T)$ and $\tau_{N,h} = \tau_{P,h}(\mathbf{v}_{N,h}, D_N, h_T)$ might also be spatial dependent over Ω and we consider these to be discontinuous, elementwise constant, whose expression is a function of the speed, diffusion and element size h_T. Later in this section we will give an explicit expression for these coefficients.

The equation for S_h remains the same as (4.40). For a clearer exposition we introduce the following notation:

$$\begin{aligned}
&\mathcal{L}_S(S) := -\nabla \cdot (D_S \nabla S), && \mathcal{F}_S(S,N) := f_{NS}(N) - f_{SP}(S) - f_{SN}(S,N),\\
&\mathcal{L}_P(P) := -\nabla \cdot \big(D_P \nabla P - P\mathbf{v}_P\big), && \mathcal{F}_P(S,P,N) := f_{SP}(S) - f_{PN}(P,N),\\
&\mathcal{L}_N(N) := -\nabla \cdot \big(D_N \nabla N - N\mathbf{v}_N\big), && \mathcal{F}_N(S,P,N) := f_{PN}(P,N) + f_{SN}(S,N) - f_{NS}(N),
\end{aligned}$$

so that the classical formulation (4.12)-(4.14) of our model can be written as:

$$\dot{S} + \mathcal{L}_S(S) = \mathcal{F}_S(S, N), \tag{4.50}$$

$$\dot{P} + \mathcal{L}_P(P) = \mathcal{F}_P(S, P, N), \tag{4.51}$$

$$\dot{N} + \mathcal{L}_N(N) = \mathcal{F}_N(S, P, N). \tag{4.52}$$

Finally, the SUPG semi-discrete weak formulation reads: find

$$S_h, P_h, N_h \in L^2([0,T]; V_h(\Omega_h)) \text{ with } \dot{S}_h, \dot{P}_h, \dot{N}_h \in L^2([0,T]; V_h(\Omega_h))$$

such that

$$\begin{aligned}
&\int_{\Omega_h} \dot{S}_h \varphi_{S,h} \, \mathrm{d}\mathbf{x} + \int_{\Omega_h} D_S \nabla S_h \cdot \nabla \varphi_{S,h} \, \mathrm{d}\mathbf{x} + \int_{\Gamma_{m,h}} (f_{SP}(S_h) + g_{SN}(S_h)) \varphi_{S,h} \, \mathrm{d}s \\
&\quad - \int_{\Gamma_{n,h}} f_{NS}(N_h) \varphi_{S,h} \, \mathrm{d}s = \int_{\Omega} f_{NS}(N_h) \varphi_{S,h} \, \mathrm{d}\mathbf{x} - \int_{\Omega_h} f_{SP}(S_h) \varphi_{S,h} \, \mathrm{d}\mathbf{x} \\
&\quad - \int_{\Omega_h} f_{SN}(S_h, N_h) \varphi_{S,h} \, \mathrm{d}\mathbf{x},
\end{aligned} \tag{4.53}$$

$$\begin{aligned}
&\int_{\Omega_h} \dot{P}_h \varphi_{P,h} \, \mathrm{d}\mathbf{x} + \int_{\Omega_h} \left(D_P \nabla P_h - P_h \mathbf{v}_{P,h} \right) \cdot \nabla \varphi_{P,h} \, \mathrm{d}\mathbf{x} - \int_{\Gamma_{m,h}} f_{SP}(S_h) \varphi_{P,h} \, \mathrm{d}s \\
&\quad + \sum_{T_k \in \mathcal{T}_h} \int_{T_k} \left(\dot{P}_h + \mathcal{L}_P(P_h) \right) \left(\tau_{P,h} \mathbf{v}_{P,h} \cdot \nabla \varphi_{P,h} \right) \, \mathrm{d}\mathbf{x} = \int_{\Omega_h} f_{SP}(S_h) \varphi_{P,h} \, \mathrm{d}\mathbf{x} \\
&\quad - \int_{\Omega_h} f_{PN}(P_h, N_h) \varphi_{P,h} \, \mathrm{d}\mathbf{x} + \sum_{T_k \in \mathcal{T}_h} \int_{T_k} \mathcal{F}_P(S_h, P_h, N_h) \left(\tau_{P,h} \mathbf{v}_{P,h} \cdot \nabla \varphi_{P,h} \right) \, \mathrm{d}\mathbf{x},
\end{aligned} \tag{4.54}$$

$$\begin{aligned}
&\int_{\Omega_h} \dot{N}_h \varphi_{N,h} \, \mathrm{d}\mathbf{x} + \int_{\Omega_h} \left(D_N \nabla N_h - N_h \mathbf{v}_{N,h} \right) \cdot \nabla \varphi_{N,h} \, \mathrm{d}\mathbf{x} - \int_{\Gamma_{m,h}} g_{SN}(S_h) \varphi_{N,h} \, \mathrm{d}s \\
&\quad + \int_{\Gamma_{n,h}} f_{NS}(N_h) \varphi_{N,h} \, \mathrm{d}s + \sum_{T_k \in \mathcal{T}_h} \int_{T_k} \left(\dot{N}_h + \mathcal{L}_N(N_h) \right) \left(\tau_{N,h} \mathbf{v}_{N,h} \cdot \nabla \varphi_{N,h} \right) \, \mathrm{d}\mathbf{x} \\
&\quad = \int_{\Omega_h} f_{PN}(P_h, N_h) \varphi_{N,h} \, \mathrm{d}\mathbf{x} + \int_{\Omega_h} f_{SN}(S_h, N_h) \varphi_{N,h} \, \mathrm{d}\mathbf{x} \\
&\quad - \int_{\Omega_h} f_{NS}(N_h) \varphi_{N,h} \, \mathrm{d}\mathbf{x} + \sum_{T_k \in \mathcal{T}_h} \int_{T_k} \mathcal{F}_N(S, P, N) \left(\tau_{N,h} \mathbf{v}_{N,h} \cdot \nabla \varphi_{N,h} \right) \, \mathrm{d}\mathbf{x},
\end{aligned} \tag{4.55}$$

for all $\varphi_{S,h}$, $\varphi_{P,h}$, $\varphi_{N,h} \in V_h(\Omega_h)$.

We note that if S_h, P_h, N_h are solutions for the standard semi-discrete problem (4.40)-(4.42) then they are also solutions for the SUPG semi-discrete problem (4.53)-(4.55). The

equation for S_h (4.53) remains the same as (4.40). The equation for P_h (4.54) has now more terms than (4.41), and it can be seen as the composition of two parts: the first one is the standard Galerkin part (4.41), which is clearly satisfied; the second part is the summation of elementwise integrals. The test functions $\tau_{P,h}\mathbf{v}_{P,h} \cdot \nabla\varphi_{P,h}$ are discontinuous over Ω_h, however they are linear over every element of the mesh. Therefore this second part can be seen as a "elementwise weak formulation", which still holds if P satisfies (4.51). The same considerations are valid for equation (4.55) for the variable N.

We also remark that the diffusion terms $\nabla \cdot D_P \nabla P_h$ and $\nabla \cdot D_N \nabla N_h$, present in $\mathcal{L}_P$ and $\mathcal{L}_N$, disappear in (4.54) and (4.55), since functions of $V_h(\Omega_h)$ are continuous and piecewise linear polynomials, hence have zero second derivatives (in weak sense).

The choice of the stabilisation parameter τ is considered to be the major drawback for the SUPG method, since many choices have been proposed but an optimal expression is still unknown (Codina, 1998; Russo, 2006). However we will make use of a common expression, for which we first need to introduce the following quantities. For every $T \in \mathcal{T}_h$ we define:

$$v_{P,T}(t) := \max_{\mathbf{x}\in T} ||\mathbf{v}_{P,h}(t)||_2, \qquad v_{N,T}(t) := \max_{\mathbf{x}\in T} ||\mathbf{v}_{N,h}(t)||_2, \tag{4.56}$$

and the local *Péclet numbers*:

$$\mathrm{Pe}_{P,T}(t) := \frac{v_{P,T}(t)h_T}{2D_P} \quad \text{and} \quad \mathrm{Pe}_{N,T}(t) := \frac{v_{N,T}(t)h_T}{2D_N}, \tag{4.57}$$

where h_T is the size of the element T, for example its major edge. Better results are achieved by considering h_T to be the element length in the convective flow direction (John and Knobloch, 2007). In the end, we will use the following expression for the stabilisation parameter (Codina, 1998):

$$\tau_{P,h}(\mathbf{x},t)\Big|_{\mathbf{x}\in T} = \frac{\alpha\big(\mathrm{Pe}_{P,T}(t)\big)h_T}{2v_{P,T}(t)} \quad \text{and} \quad \tau_{N,h}(\mathbf{x},t)\Big|_{\mathbf{x}\in T} = \frac{\alpha\big(\mathrm{Pe}_{N,T}(t)\big)h_T}{2v_{N,T}(t)}, \tag{4.58}$$

where

$$\alpha(x) = \coth(x) - \frac{1}{x}.$$

This choice is nodally exact at least in some particular steady-state one-dimensional cases (John and Knobloch, 2007).

To conclude, we report for convenience's sake the semi-discrete model in terms of the basis functions, which reads: find $S_1(t), \ldots, S_{N_h}(t)$, $P_1(t), \ldots, P_{N_h}(t)$, $N_1(t), \ldots, N_{N_h}(t)$

such that

$$\begin{aligned}
&\sum_{j=1}^{N_h} \dot{S}_j \int_{\Omega_h} \varphi_j \varphi_i \, \mathrm{d}\mathbf{x} + \sum_{j=1}^{N_h} S_j \int_{\Omega_h} D_S \nabla\varphi_j \cdot \nabla\varphi_i \, \mathrm{d}\mathbf{x} \\
&+ \int_{\Gamma_{m,h}} (f_{SP}(S_h) + g_{SN}(S_h))\varphi_i \, \mathrm{d}s - \int_{\Gamma_{n,h}} f_{NS}(N_h)\varphi_i \, \mathrm{d}s \\
&= \int_{\Omega} f_{NS}(N_h)\varphi_i \, \mathrm{d}\mathbf{x} - \int_{\Omega_h} f_{SP}(S_h)\varphi_i \, \mathrm{d}\mathbf{x} \\
&- \int_{\Omega_h} f_{SN}(S_h, N_h)\varphi_i \, \mathrm{d}\mathbf{x}, \qquad\qquad i = 1, \ldots, N_h,
\end{aligned} \tag{4.59}$$

$$\begin{aligned}
&\sum_{j=1}^{N_h} \dot{P}_j \left(\int_{\Omega_h} \varphi_j \varphi_i \, \mathrm{d}\mathbf{x} + \sum_{T_k \in \mathcal{T}_h} \int_{T_k} \tau_{P,h} \varphi_j \mathbf{v}_{P,h} \cdot \nabla\varphi_i \, \mathrm{d}\mathbf{x} \right) \\
&+ \sum_{j=1}^{N_h} P_j \int_{\Omega_h} \left(D_P \nabla\varphi_j - \varphi_j \mathbf{v}_{P,h} \right) \cdot \nabla\varphi_i \, \mathrm{d}\mathbf{x} \\
&+ \sum_{j=1}^{N_h} P_j \sum_{T_k \in \mathcal{T}_h} \int_{T_k} \tau_{P,h} \nabla \cdot (\varphi_j \mathbf{v}_{P,h}) \left(\mathbf{v}_{P,h} \cdot \nabla\varphi_i \right) \, \mathrm{d}\mathbf{x} \\
&- \int_{\Gamma_{m,h}} f_{SP}(S_h)\varphi_i \, \mathrm{d}s = \int_{\Omega_h} f_{SP}(S_h)\varphi_i \, \mathrm{d}\mathbf{x} - \int_{\Omega_h} f_{PN}(P_h, N_h)\varphi_i \, \mathrm{d}\mathbf{x} \\
&+ \sum_{T_k \in \mathcal{T}_h} \int_{T_k} \tau_{P,h} f_{SP}(S_h) \mathbf{v}_{P,h} \cdot \nabla\varphi_i \, \mathrm{d}\mathbf{x} \\
&- \sum_{T_k \in \mathcal{T}_h} \int_{T_k} \tau_{P,h} f_{PN}(P_h, N_h) \mathbf{v}_{P,h} \cdot \nabla\varphi_i \, \mathrm{d}\mathbf{x}, \qquad\qquad i = 1, \ldots, N_h,
\end{aligned} \tag{4.60}$$

$$
\begin{aligned}
&\sum_{j=1}^{N_h} \dot{N}_j \left(\int_{\Omega_h} \varphi_j \varphi_i \, \mathrm{d}\mathbf{x} + \sum_{T_k \in \mathcal{T}_h} \int_{T_k} \tau_{N,h} \varphi_j \mathbf{v}_{N,h} \cdot \nabla \varphi_i \, \mathrm{d}\mathbf{x} \right) \\
&+ \sum_{j=1}^{N_h} N_j \int_{\Omega_h} \left(D_N \nabla \varphi_j - \varphi_j \mathbf{v}_{N,h} \right) \cdot \nabla \varphi_i \, \mathrm{d}\mathbf{x} \\
&+ \sum_{j=1}^{N_h} N_j \sum_{T_k \in \mathcal{T}_h} \int_{T_k} \tau_{N,h} \nabla \cdot \left(\varphi_j \mathbf{v}_{N,h} \right) \left(\mathbf{v}_{N,h} \cdot \nabla \varphi_i \right) \, \mathrm{d}\mathbf{x} \\
&- \int_{\Gamma_{m,h}} g_{SN}(S_h) \varphi_i \, \mathrm{d}s + \int_{\Gamma_{n,h}} f_{NS}(N_h) \varphi_i \, \mathrm{d}s \\
&= \int_{\Omega_h} f_{PN}(P_h, N_h) \varphi_i \, \mathrm{d}\mathbf{x} + \int_{\Omega_h} f_{SN}(S_h, N_h) \varphi_i \, \mathrm{d}\mathbf{x} \\
&- \int_{\Omega_h} f_{NS}(N_h) \varphi_i \, \mathrm{d}\mathbf{x} + \sum_{T_k \in \mathcal{T}_h} \int_{T_k} \tau_{N,h} f_{PN}(P_h, N_h) \mathbf{v}_{N,h} \cdot \nabla \varphi_i \, \mathrm{d}\mathbf{x} \\
&+ \sum_{T_k \in \mathcal{T}_h} \int_{T_k} \tau_{N,h} f_{SN}(S_h, N_h) \mathbf{v}_{N,h} \cdot \nabla \varphi_i \, \mathrm{d}\mathbf{x} \\
&- \sum_{T_k \in \mathcal{T}_h} \int_{T_k} \tau_{N,h} f_{NS}(N_h) \mathbf{v}_{N,h} \cdot \nabla \varphi_i \, \mathrm{d}\mathbf{x}, \qquad\qquad i = 1, \ldots, N_h.
\end{aligned}
\tag{4.61}
$$

for $t \in (0, T]$ and such that $S_j(0) = S_0(\mathbf{x}_j)$, $P_j(0) = P_0(\mathbf{x}_j)$, $N_j(0) = N_0(\mathbf{x}_j)$ for $j = 1, \ldots, N_h$.

In these last two sections, through spatial discretisation, we have approximated the continuous model (4.12)-(4.23) with three ODE systems (one for each component). Before proceeding in the temporal discretisation, we first show a result of the semi-discrete system.

Theorem 4.4.1. Let S_h, P_h, N_h be solutions of the semi-discrete SUPG problem (4.59)-(4.61). Therefore, the following equality holds:

$$
\begin{aligned}
&\int_{\Omega_h} S_h(\mathbf{x}, t) \, \mathrm{d}\mathbf{x} + \int_{\Omega_h} P_h(\mathbf{x}, t) \, \mathrm{d}\mathbf{x} + \int_{\Omega_h} N_h(\mathbf{x}, t) \, \mathrm{d}\mathbf{x} \\
&= \int_{\Omega_h} S_{0,h}(\mathbf{x}) \, \mathrm{d}\mathbf{x} + \int_{\Omega_h} P_{0,h}(\mathbf{x}) \, \mathrm{d}\mathbf{x} + \int_{\Omega_h} N_{0,h}(\mathbf{x}) \, \mathrm{d}\mathbf{x},
\end{aligned}
\tag{4.62}
$$

$\forall t \in [0, T]$.

Proof. As in Chapter 2, we again take advantage of the fact that $\sum_{i=1}^{N_h} \varphi_i(\mathbf{x}) = 1$ and consequently $\sum_{i=1}^{N_h} \nabla \varphi_i(\mathbf{x}) = \mathbf{0}$. Summing equation (4.59) over the index $i = 1, \ldots, N_h$, we get:

$$
\begin{aligned}
&\sum_{j=1}^{N_h} \dot{S}_j \int_{\Omega_h} \varphi_j \, \mathrm{d}\mathbf{x} + \int_{\Gamma_{m,h}} \left(f_{SP}(S_h) + g_{SN}(S_h) \right) \mathrm{d}s - \int_{\Gamma_{n,h}} f_{NS}(N_h) \, \mathrm{d}s \\
&\qquad = \int_{\Omega} f_{NS}(N_h) \, \mathrm{d}\mathbf{x} - \int_{\Omega_h} f_{SP}(S_h) \, \mathrm{d}\mathbf{x} - \int_{\Omega_h} f_{SN}(S_h, N_h) \, \mathrm{d}\mathbf{x}.
\end{aligned}
\tag{4.63}
$$

Applying the same operation for the equations (4.60) and (4.61), all the terms added by the SUPG method disappear and we get:

$$\begin{aligned}\sum_{j=1}^{N_h} \dot{P}_j \int_{\Omega_h} \varphi_j \, \mathrm{d}\mathbf{x} - \int_{\Gamma_{m,h}} f_{SP}(S_h) \, \mathrm{d}s \\ = \int_{\Omega_h} f_{SP}(S_h) \, \mathrm{d}\mathbf{x} - \int_{\Omega_h} f_{PN}(P_h, N_h) \, \mathrm{d}\mathbf{x},\end{aligned} \tag{4.64}$$

and similarly,

$$\begin{aligned}\sum_{j=1}^{N_h} \dot{N}_j \int_{\Omega_h} \varphi_j \, \mathrm{d}\mathbf{x} - \int_{\Gamma_{m,h}} g_{SN}(S_h) \, \mathrm{d}s + \int_{\Gamma_{n,h}} f_{NS}(N_h) \, \mathrm{d}s \\ = \int_{\Omega_h} f_{PN}(P_h, N_h) \, \mathrm{d}\mathbf{x} + \int_{\Omega_h} f_{SN}(S_h, N_h) \, \mathrm{d}\mathbf{x} - \int_{\Omega_h} f_{NS}(N_h) \, \mathrm{d}\mathbf{x}.\end{aligned} \tag{4.65}$$

If we now sum the three equations (4.63)-(4.65) we get:

$$\sum_{j=1}^{N_h} \dot{S}_j \int_{\Omega_h} \varphi_j \, \mathrm{d}\mathbf{x} + \sum_{j=1}^{N_h} \dot{P}_j \int_{\Omega_h} \varphi_j \, \mathrm{d}\mathbf{x} + \sum_{j=1}^{N_h} \dot{N}_j \int_{\Omega_h} \varphi_j \, \mathrm{d}\mathbf{x} = 0,$$

and, by (4.46), this is equivalent to

$$\frac{\mathrm{d}}{\mathrm{d}t} \left(\int_{\Omega_h} S_h \, \mathrm{d}\mathbf{x} + \int_{\Omega_h} P_h \, \mathrm{d}\mathbf{x} + \int_{\Omega_h} N_h \, \mathrm{d}\mathbf{x} \right) = 0,$$

which implies (4.62). □

4.4.4 Temporal discretisation

In order to fully discretise our problem we set a number N_t of time points with the corresponding time step $\tau_h = \frac{T}{N_t}$. Let $t^0 = 0$ and consider the sequence

$$t^n = t^{n-1} + \tau_h, \qquad n = 1, \ldots, N_t.$$

The aim is to find the solutions at every time point t^n, defined at t^0 by the initial conditions (4.46). We will use the superscript n to indicate a function at the time $t = t^n$, for example $S_h^n = S_h(\mathbf{x}, t^n)$ or, in vectorial notation, $\mathbf{S}^n = [S_1(t^n), \ldots, S_{N_h}(t^n)]$.

For the computation of the solution at the different time steps, the time derivatives are first approximated by difference quotients. Then the IMEX method is applied, which considers the spatial variations (4.9)-(4.11) implicitly and the reactions (4.5)-(4.7) explicitly in time (Ruuth, 1995). Hence the fully discrete problem reads: given $S_1^0, \ldots, S_{N_h}^0$,

$P_1^0, \dots, P_{N_h}^0$, $N_1^0, \dots, N_{N_h}^0$, for every $n = 1, \dots, N_t$ find $S_1^n, \dots, S_{N_h}^n$, $P_1^n, \dots, P_{N_h}^n$, $N_1^n, \dots, N_{N_h}^n$ such that:

$$\begin{aligned}
&\frac{1}{\tau_h}\sum_{j=1}^{N_h} S_j^n \int_{\Omega_h} \varphi_j\varphi_i \,\mathrm{d}\mathbf{x} + \sum_{j=1}^{N_h} S_j^n \int_{\Omega_h} D_S \nabla\varphi_j \cdot \nabla\varphi_i \,\mathrm{d}\mathbf{x} + \int_{\Gamma_{m,h}} (f_{SP}(S_h^n) + g_{SN}(S_h^n))\varphi_i \,\mathrm{d}s \\
&\quad - \int_{\Gamma_{n,h}} f_{NS}(N_h^n)\varphi_i \,\mathrm{d}s = \frac{1}{\tau_h}\sum_{j=1}^{N_h} S_j^{n-1} \int_{\Omega_h} \varphi_j\varphi_i \,\mathrm{d}\mathbf{x} + \int_{\Omega} f_{NS}(N_h^{n-1})\varphi_i \,\mathrm{d}\mathbf{x} \\
&\quad - \int_{\Omega_h} f_{SP}(S_h^{n-1})\varphi_i \,\mathrm{d}\mathbf{x} - \int_{\Omega_h} f_{SN}(S_h^{n-1}, N_h^{n-1})\varphi_i \,\mathrm{d}\mathbf{x}, \qquad i = 1, \dots, N_h,
\end{aligned} \tag{4.66}$$

$$\begin{aligned}
&\frac{1}{\tau_h}\sum_{j=1}^{N_h} P_j^n \left(\int_{\Omega_h} \varphi_j\varphi_i \,\mathrm{d}\mathbf{x} + \sum_{T_k\in\mathcal{T}_h} \int_{T_k} \tau_{P,h}^n \varphi_j \mathbf{v}_{P,h}^n \cdot \nabla\varphi_i \,\mathrm{d}\mathbf{x} \right) \\
&\qquad + \sum_{j=1}^{N_h} P_j^n \int_{\Omega_h} \left(D_P \nabla\varphi_j - \varphi_j \mathbf{v}_{P,h}^n\right) \cdot \nabla\varphi_i \,\mathrm{d}\mathbf{x} \\
&\qquad + \sum_{j=1}^{N_h} P_j^n \sum_{T_k\in\mathcal{T}_h} \int_{T_k} \tau_{P,h}^n \nabla\cdot(\varphi_j \mathbf{v}_{P,h}^n) \left(\mathbf{v}_{P,h}^n \cdot \nabla\varphi_i\right) \,\mathrm{d}\mathbf{x} - \int_{\Gamma_{m,h}} f_{SP}(S_h^n)\varphi_i \,\mathrm{d}s \\
&= \frac{1}{\tau_h}\sum_{j=1}^{N_h} P_j^{n-1} \left(\int_{\Omega_h} \varphi_j\varphi_i \,\mathrm{d}\mathbf{x} + \sum_{T_k\in\mathcal{T}_h} \int_{T_k} \tau_{P,h}^n \varphi_j \mathbf{v}_{P,h}^n \cdot \nabla\varphi_i \,\mathrm{d}\mathbf{x} \right) \\
&+ \int_{\Omega_h} f_{SP}(S_h^{n-1})\varphi_i \,\mathrm{d}\mathbf{x} - \int_{\Omega_h} f_{PN}(P_h^{n-1}, N_h^{n-1})\varphi_i \,\mathrm{d}\mathbf{x} \\
&+ \sum_{T_k\in\mathcal{T}_h} \int_{T_k} \tau_{P,h}^{n-1} f_{SP}(S_h^{n-1}) \mathbf{v}_{P,h}^{n-1} \cdot \nabla\varphi_i \,\mathrm{d}\mathbf{x} \\
&- \sum_{T_k\in\mathcal{T}_h} \int_{T_k} \tau_{P,h}^{n-1} f_{PN}(P_h^{n-1}, N_h^{n-1}) \mathbf{v}_{P,h}^{n-1} \cdot \nabla\varphi_i \,\mathrm{d}\mathbf{x}, \qquad i = 1, \dots, N_h,
\end{aligned} \tag{4.67}$$

$$
\begin{aligned}
&\frac{1}{\tau_h}\sum_{j=1}^{N_h} N_j^n \left(\int_{\Omega_h} \varphi_j\varphi_i \,\mathrm{d}\mathbf{x} + \sum_{T_k\in\mathcal{T}_h} \int_{T_k} \tau_{N,h}^n \varphi_j \mathbf{v}_{N,h}^n \cdot \nabla\varphi_i \,\mathrm{d}\mathbf{x} \right) \\
&\quad + \sum_{j=1}^{N_h} N_j^n \int_{\Omega_h} \left(D_N \nabla\varphi_j - \varphi_j \mathbf{v}_{N,h}^n\right)\cdot\nabla\varphi_i \,\mathrm{d}\mathbf{x} \\
&\quad + \sum_{j=1}^{N_h} N_j^n \sum_{T_k\in\mathcal{T}_h} \int_{T_k} \tau_{N,h}^n \nabla\cdot(\varphi_j \mathbf{v}_{N,h}^n)\left(\mathbf{v}_{N,h}^n\cdot\nabla\varphi_i\right) \,\mathrm{d}\mathbf{x} \\
&\quad - \int_{\Gamma_{m,h}} g_{SN}(S_h^n)\varphi_i \,\mathrm{d}s + \int_{\Gamma_{n,h}} f_{NS}(N_h^n)\varphi_i \,\mathrm{d}s \\
&= \frac{1}{\tau_h}\sum_{j=1}^{N_h} N_j^{n-1} \left(\int_{\Omega_h} \varphi_j\varphi_i \,\mathrm{d}\mathbf{x} + \sum_{T_k\in\mathcal{T}_h} \int_{T_k} \tau_{N,h}^n \varphi_j \mathbf{v}_{N,h}^n \cdot \nabla\varphi_i \,\mathrm{d}\mathbf{x} \right) \\
&+ \int_{\Omega_h} f_{PN}(P_h^{n-1}, N_h^{n-1})\varphi_i \,\mathrm{d}\mathbf{x} + \int_{\Omega_h} f_{SN}(S_h^{n-1}, N_h^{n-1})\varphi_i \,\mathrm{d}\mathbf{x} \\
&- \int_{\Omega_h} f_{NS}(N_h^{n-1})\varphi_i \,\mathrm{d}\mathbf{x} + \sum_{T_k\in\mathcal{T}_h} \int_{T_k} \tau_{N,h}^{n-1} f_{PN}(P_h^{n-1}, N_h^{n-1}) \mathbf{v}_{N,h}^{n-1}\cdot\nabla\varphi_i \,\mathrm{d}\mathbf{x} \\
&+ \sum_{T_k\in\mathcal{T}_h} \int_{T_k} \tau_{N,h}^{n-1} f_{SN}(S_h^{n-1}, N_h^{n-1}) \mathbf{v}_{N,h}^{n-1}\cdot\nabla\varphi_i \,\mathrm{d}\mathbf{x} \\
&- \sum_{T_k\in\mathcal{T}_h} \int_{T_k} \tau_{N,h}^{n-1} f_{NS}(N_h^{n-1}) \mathbf{v}_{N,h}^{n-1}\cdot\nabla\varphi_i \,\mathrm{d}\mathbf{x}, \qquad i = 1,\ldots,N_h.
\end{aligned}
\tag{4.68}
$$

One property of the numerical method is that it inherits the conservation of total mass from the continuous model (Proposition 4.3.1), as follows:

Proposition 4.4.1. Let S_h^n, P_h^n, N_h^n be solutions of the fully discrete SUPG problem (4.66)-(4.68) at the $n-$th time step t^n. Therefore, for any $n = 1,\ldots,N_t$, the following equality holds:

$$
\begin{aligned}
&\int_{\Omega_h} S_h^n(\mathbf{x}) \,\mathrm{d}\mathbf{x} + \int_{\Omega_h} P_h^n(\mathbf{x}) \,\mathrm{d}\mathbf{x} + \int_{\Omega_h} N_h^n(\mathbf{x}) \,\mathrm{d}\mathbf{x} \\
&= \int_{\Omega_h} S_h^0(\mathbf{x}) \,\mathrm{d}\mathbf{x} + \int_{\Omega_h} P_h^0(\mathbf{x}) \,\mathrm{d}\mathbf{x} + \int_{\Omega_h} N_h^0(\mathbf{x}) \,\mathrm{d}\mathbf{x}.
\end{aligned}
\tag{4.69}
$$

Proof. We follow the steps of the proof of Theorem 4.4.1. Hence, summing equation (4.66) over the index $i = 1,\ldots,N_h$, we get:

$$
\begin{aligned}
&\frac{1}{\tau_h}\sum_{j=1}^{N_h} S_j^n \int_{\Omega_h} \varphi_j \,\mathrm{d}\mathbf{x} + \int_{\Gamma_{m,h}} \left(f_{SP}(S_h^n) + g_{SN}(S_h^n)\right) \mathrm{d}s - \int_{\Gamma_{n,h}} f_{NS}(N_h^n) \,\mathrm{d}s \\
&\quad = \frac{1}{\tau_h}\sum_{j=1}^{N_h} S_j^{n-1} \int_{\Omega_h} \varphi_j \,\mathrm{d}\mathbf{x} + \int_{\Omega} f_{NS}(N_h^{n-1}) \,\mathrm{d}\mathbf{x} - \int_{\Omega_h} f_{SP}(S_h^{n-1}) \,\mathrm{d}\mathbf{x} \\
&\quad - \int_{\Omega_h} f_{SN}(S_h^{n-1}, N_h^{n-1}) \,\mathrm{d}\mathbf{x}.
\end{aligned}
\tag{4.70}
$$

Applying the same operation for the equations (4.67) and (4.68) all the terms added by the SUPG method disappear and we get:

$$\begin{aligned}&\frac{1}{\tau_h}\sum_{j=1}^{N_h} P_j^n \int_{\Omega_h} \varphi_j \, \mathrm{d}\mathbf{x} - \int_{\Gamma_{m,h}} f_{SP}(S_h^n) \, \mathrm{d}s \\ &\quad = \frac{1}{\tau_h}\sum_{j=1}^{N_h} P_j^{n-1} \int_{\Omega_h} \varphi_j \, \mathrm{d}\mathbf{x} + \int_{\Omega_h} f_{SP}(S_h^{n-1}) \, \mathrm{d}\mathbf{x} - \int_{\Omega_h} f_{PN}(P_h^{n-1}, N_h^{n-1}) \, \mathrm{d}\mathbf{x},\end{aligned} \tag{4.71}$$

and similarly,

$$\begin{aligned}&\frac{1}{\tau_h}\sum_{j=1}^{N_h} N_j^n \int_{\Omega_h} \varphi_j \, \mathrm{d}\mathbf{x} - \int_{\Gamma_{m,h}} g_{SN}(S_h^n) \, \mathrm{d}s + \int_{\Gamma_{n,h}} f_{NS}(N_h^n) \, \mathrm{d}s \\ &\quad = \frac{1}{\tau_h}\sum_{j=1}^{N_h} N_j^{n-1} \int_{\Omega_h} \varphi_j \, \mathrm{d}\mathbf{x} + \int_{\Omega_h} f_{PN}(P_h^{n-1}, N_h^{n-1}) \, \mathrm{d}\mathbf{x} + \int_{\Omega_h} f_{SN}(S_h^{n-1}, N_h^{n-1}) \, \mathrm{d}\mathbf{x} \\ &\quad - \int_{\Omega_h} f_{NS}(N_h^{n-1}) \, \mathrm{d}\mathbf{x}.\end{aligned} \tag{4.72}$$

If we now sum the three equations (4.70)-(4.72) we get:

$$\frac{1}{\tau_h}\sum_{j=1}^{N_h} S_j^n \int_{\Omega_h} \varphi_j \, \mathrm{d}\mathbf{x} + \frac{1}{\tau_h}\sum_{j=1}^{N_h} P_j^n \int_{\Omega_h} \varphi_j \, \mathrm{d}\mathbf{x} + \frac{1}{\tau_h}\sum_{j=1}^{N_h} N_j^n \int_{\Omega_h} \varphi_j \, \mathrm{d}\mathbf{x}$$

$$= \frac{1}{\tau_h}\sum_{j=1}^{N_h} S_j^{n-1} \int_{\Omega_h} \varphi_j \, \mathrm{d}\mathbf{x} + \frac{1}{\tau_h}\sum_{j=1}^{N_h} P_j^{n-1} \int_{\Omega_h} \varphi_j \, \mathrm{d}\mathbf{x} + \frac{1}{\tau_h}\sum_{j=1}^{N_h} N_j^{n-1} \int_{\Omega_h} \varphi_j \, \mathrm{d}\mathbf{x},$$

and applying an iterative procedure over the index n

$$\begin{aligned}&\int_{\Omega_h} \sum_{j=1}^{N_h} S_j^n \varphi_j(\mathbf{x}) \, \mathrm{d}\mathbf{x} + \int_{\Omega_h} \sum_{j=1}^{N_h} P_j^n \varphi_j(\mathbf{x}) \, \mathrm{d}\mathbf{x} + \int_{\Omega_h} \sum_{j=1}^{N_h} N_j^n \varphi_j(\mathbf{x}) \, \mathrm{d}\mathbf{x} \\ &\quad = \int_{\Omega_h} \sum_{j=1}^{N_h} S_j^0 \varphi_j(\mathbf{x}) \, \mathrm{d}\mathbf{x} + \int_{\Omega_h} \sum_{j=1}^{N_h} P_j^0 \varphi_j(\mathbf{x}) \, \mathrm{d}\mathbf{x} + \int_{\Omega_h} \sum_{j=1}^{N_h} N_j^0 \varphi_j(\mathbf{x}) \, \mathrm{d}\mathbf{x},\end{aligned}$$

which is (4.69). □

Applying the numerical method presented in this chapter to the more general reaction-advection-diffusion system (4.27)-(4.30), the fully discrete problem reads as follows: for every $n = 1, \ldots, N_t$, given $U_{k,1}^0, \ldots, U_{k,N_h}^0$, we aim to find the coefficients $U_{k,1}^n, \ldots, U_{k,N_h}^n$

of the linear combinations

$$u^n_{k,h}(\mathbf{x}) = \sum_{j=1}^{N_h} U^n_{k,j}\varphi_j(\mathbf{x}) \tag{4.73}$$

which approximate $u_k(\mathbf{x}, t^n)$. These coefficients are solutions the following systems

$$\begin{aligned}
&\frac{1}{\tau_h}\sum_{j=1}^{N_h} U^n_{k,j}\left(\int_{\Omega_h}\varphi_j\varphi_i\,\mathrm{d}\mathbf{x} + \sum_{T\in\mathcal{T}_h}\int_T \tau^n_{k,h}\varphi_j\mathbf{v}^n_{k,h}\cdot\nabla\varphi_i\,\mathrm{d}\mathbf{x}\right)\\
&+\sum_{j=1}^{N_h} U^n_{k,j}\int_{\Omega_h}\left(D_k\nabla\varphi_j - \varphi_j\mathbf{v}^n_{k,h}\right)\cdot\nabla\varphi_i\,\mathrm{d}\mathbf{x}\\
&+\sum_{j=1}^{N_h} U^n_{k,j}\sum_{T\in\mathcal{T}_h}\int_T \tau^n_{k,h}\nabla\cdot(\varphi_j\mathbf{v}^n_{k,h})\left(\mathbf{v}^n_{k,h}\cdot\nabla\varphi_i\right)\,\mathrm{d}\mathbf{x}\\
&-\int_{\Gamma_{m,h}} g_k(u^n_{1,h},\dots,u^n_{N_\Omega,h})\varphi_i\,\mathrm{d}s - \int_{\Gamma_{n,h}} h_k(u^n_{1,h},\dots,u^n_{N_\Omega,h})\varphi_i\,\mathrm{d}s\\
&=\frac{1}{\tau_h}\sum_{j=1}^{N_h} U^{n-1}_{k,j}\left(\int_{\Omega_h}\varphi_j\varphi_i\,\mathrm{d}\mathbf{x} + \sum_{T\in\mathcal{T}_h}\int_T \tau^n_{k,h}\varphi_j\mathbf{v}^n_{k,h}\cdot\nabla\varphi_i\,\mathrm{d}\mathbf{x}\right)\\
&+\int_{\Omega_h} f_k(u^{n-1}_{1,h},\dots,u^{n-1}_{N_\Omega,h})\varphi_i\,\mathrm{d}\mathbf{x}\\
&+\sum_{T\in\mathcal{T}_h}\int_T \tau^{n-1}_{k,h} f_k(u^{n-1}_{1,h},\dots,u^{n-1}_{N_\Omega,h})\mathbf{v}^{n-1}_{k,h}\cdot\nabla\varphi_i\,\mathrm{d}\mathbf{x},\\
&\qquad\qquad\qquad\qquad\text{for } i=1,\dots,N_h,\ \text{and } k=1,\dots,N_\Omega,
\end{aligned} \tag{4.74}$$

where k is the index of the k-th component of system (4.27)-(4.30).

Hence, a generalisation of Proposition 4.4.1 is represented by the following result.

Theorem 4.4.2. Let us consider the fully discrete problem (4.74) and assume

$$\sum_{k=1}^{N_\Omega}\int_{\Omega_h} f_k\,\mathrm{d}\mathbf{x} = 0 \tag{4.75}$$

and

$$\sum_{k=1}^{N_\Omega}\left(\int_{\Gamma_{m,h}} g_k\,\mathrm{d}s + \int_{\Gamma_{n,h}} h_k\,\mathrm{d}s\right) = 0. \tag{4.76}$$

Therefore, the solution $(U^n_{1,1},\dots,U^n_{1,N_h},\dots,U^n_{N_\Omega,1},\dots,U^n_{N_\Omega,N_h})$ of (4.74) satisfies

$$K(t^n) := \sum_{k=1}^{N_\Omega}\int_{\Omega_h} u^n_{k,h}(\mathbf{x})\,\mathrm{d}\mathbf{x} = K_0, \quad \forall t\geq 0, \tag{4.77}$$

where $u^n_{k,h}(\mathbf{x})$ is defined in (4.73) and K_0 by the initial condition, defined as follows

$$K_0 := \sum_{k=1}^{N_\Omega} \int_{\Omega_h} \sum_{j=1}^{N_h} U^0_{k,j} \varphi_j(\mathbf{x}) \, \mathrm{d}\mathbf{x}.$$

Proof. Following the same ideas of the proof of Theorem 4.4.1 and Proposition 4.4.1, we sum (4.74) over the index $i = 1, \ldots, N_h$, to obtain

$$\begin{aligned} &\frac{1}{\tau_h} \sum_{j=1}^{N_h} U^n_{k,j} \int_{\Omega_h} \varphi_j \, \mathrm{d}\mathbf{x} - \int_{\Gamma_{m,h}} g_k(u^n_{1,h}, \ldots, u^n_{N_\Omega,h}) \, \mathrm{d}s - \int_{\Gamma_{n,h}} h_k(u^n_{1,h}, \ldots, u^n_{N_\Omega,h}) \, \mathrm{d}s \\ &= \frac{1}{\tau_h} \sum_{j=1}^{N_h} U^{n-1}_{k,j} \int_{\Omega_h} \varphi_j \, \mathrm{d}\mathbf{x} + \int_{\Omega_h} f_k(u^{n-1}_{1,h}, \ldots, u^{n-1}_{N_\Omega,h}) \, \mathrm{d}\mathbf{x}. \end{aligned}$$

Using (4.73) and the superscript n to mean the dependency on $(u^n_{1,h}, \ldots, u^n_{N_\Omega,h})$, we rewrite the last equation as

$$\frac{1}{\tau_h} \int_{\Omega_h} u^n_{k,h} \, \mathrm{d}\mathbf{x} - \int_{\Gamma_{m,h}} g^n_k \, \mathrm{d}s - \int_{\Gamma_{n,h}} h^n_k \, \mathrm{d}s = \frac{1}{\tau_h} \int_{\Omega_h} u^{n-1}_{k,h} \, \mathrm{d}\mathbf{x} + \int_{\Omega_h} f^{n-1}_k \, \mathrm{d}\mathbf{x}.$$

Summing over the index $k = 1, \ldots, N_\Omega$, we get

$$\begin{aligned} &\frac{1}{\tau_h} \sum_{k=1}^{N_\Omega} \int_{\Omega_h} u^n_{k,h} \, \mathrm{d}\mathbf{x} - \sum_{k=1}^{N_\Omega} \left(\int_{\Gamma_{m,h}} g^n_k \, \mathrm{d}s + \int_{\Gamma_{n,h}} h^n_k \, \mathrm{d}s \right) \\ &= \frac{1}{\tau_h} \sum_{k=1}^{N_\Omega} \int_{\Omega_h} u^{n-1}_{k,h} \, \mathrm{d}\mathbf{x} + \sum_{k=1}^{N_\Omega} \int_{\Omega_h} f^{n-1}_k \, \mathrm{d}\mathbf{x}, \end{aligned}$$

from which, applying (4.75) and (4.76), we obtain

$$\sum_{k=1}^{N_\Omega} \int_{\Omega_h} u^n_{k,h} \, \mathrm{d}\mathbf{x} = \sum_{k=1}^{N_\Omega} \int_{\Omega_h} u^{n-1}_{k,h} \, \mathrm{d}\mathbf{x}$$

and iterating over n we get (4.77), which concludes the proof. □

4.4.5 Matrix form

Equations (4.66)-(4.68) can be written in a more compact matrix-vector form. First, we introduce the functions

$$h_{SP}(S) := \frac{k_{SP}}{K_{SP} + S}, \tag{4.78}$$

$$h_{NS}(N) := \frac{k_{NS}}{K_{NS} + N}, \tag{4.79}$$

$$h_{SN}(S) = \frac{k_{SN,\Gamma}}{K_{SN,\Gamma} + S}, \tag{4.80}$$

so that, in reference to (4.1), (4.3) and (4.24), $f_{SP}(S) = h_{SP}(S)S$, $f_{NS}(N) = h_{NS}(N)N$ and $g_{SN}(S) = h_{SN}(S)S$.

Let $\mathbf{S}^n = [S_1^n, \ldots, S_{N_h}^n]$, $\mathbf{P}^n = [P_1^n, \ldots, P_{N_h}^n]$, $\mathbf{N}^n = [N_1^n, \ldots, N_{N_h}^n]$. Then equation (4.66) can be written in the matrix-vector form as

$$\left(\frac{1}{\tau_h}M + D_S K + H_{SP}(\mathbf{S}^{n-1}) + H_{SN}(\mathbf{S}^{n-1})\right)\mathbf{S}^n - H_{NS}(\mathbf{N}^{n-1})\mathbf{N}^n$$
$$= \frac{1}{\tau_h}M\mathbf{S}^{n-1} + \mathbf{F}_{NS}(\mathbf{N}^{n-1}) - \mathbf{F}_{SP}(\mathbf{S}^{n-1}) - \mathbf{F}_{SN}(\mathbf{S}^{n-1}, \mathbf{N}^{n-1}).$$

Equation (4.67) is equivalent to

$$\left(\frac{1}{\tau_h}(M + \widehat{M}^n) + D_P K - J_P^n + \widehat{J_P}^n\right)\mathbf{P}^n - H_{SN}(\mathbf{S}^n)\mathbf{S}^n$$
$$= \frac{1}{\tau_h}(M + \widehat{M}^n)\mathbf{P}^{n-1} + \mathbf{F}_{SP}(\mathbf{S}^{n-1}) - \mathbf{F}_{PN}(\mathbf{P}^{n-1}, \mathbf{N}^{n-1}) + \widehat{\mathbf{F}_{SP}}(\mathbf{S}^{n-1})$$
$$-\widehat{\mathbf{F}_{PN}}(\mathbf{P}^{n-1}, \mathbf{N}^{n-1}).$$

Similarly, equation (4.68) is equivalent to

$$\left(\frac{1}{\tau_h}(M + \widetilde{M}^n) + D_N K - J_N^n + \widetilde{J_N}^n + H_{NS}(\mathbf{N}^n)\right)\mathbf{N}^n - H_{SN}(\mathbf{S}^n)\mathbf{S}^n$$

$$= \frac{1}{\tau_h}(M + \widetilde{M}^n)\mathbf{N}^n + \mathbf{F}_{PN}(\mathbf{P}^{n-1}\mathbf{N}^{n-1}) + \mathbf{F}_{SN}(\mathbf{S}^{n-1}, \mathbf{N}^{n-1}) - \mathbf{F}_{NS}(\mathbf{N}^{n-1})$$
$$+\widetilde{\mathbf{F}_{PN}}(\mathbf{P}^{n-1}, \mathbf{N}^{n-1}) + \widetilde{\mathbf{F}_{SN}}(\mathbf{S}^{n-1}, \mathbf{N}^{n-1}) - \widetilde{\mathbf{F}_{NS}}(\mathbf{N}^{n-1}),$$

where

$$
\begin{aligned}
M &= \left(\int_\Omega \varphi_j \varphi_i \ \mathrm{d}\mathbf{x} \right)_{i,j=1,\dots,N_h}, \\
\widehat{M}^n &= \left(\sum_{T_k \in \mathcal{T}_h} \int_{T_k} \tau_{P,h}^n \varphi_j \mathbf{v}_{P,h}^n \cdot \nabla \varphi_i \ \mathrm{d}\mathbf{x} \right)_{i,j=1,\dots,N_h}, \\
\widetilde{M}^n &= \left(\sum_{T_k \in \mathcal{T}_h} \int_{T_k} \tau_{N,h}^n \varphi_j \mathbf{v}_{N,h}^n \cdot \nabla \varphi_i \ \mathrm{d}\mathbf{x} \right)_{i,j=1,\dots,N_h}, \\
K &= \left(\int_\Omega \nabla \varphi_j \cdot \nabla \varphi_i \ \mathrm{d}\mathbf{x} \right)_{i,j=1,\dots,N_h},
\end{aligned}
$$

$$
\begin{aligned}
J_P^n &= \left(\int_{\Omega_h} \varphi_j \mathbf{v}_{P,h}^n \cdot \nabla \varphi_i \ \mathrm{d}\mathbf{x} \right)_{i,j=1,\dots,N_h}, \\
J_N^n &= \left(\int_{\Omega_h} \varphi_j \mathbf{v}_{N,h}^n \cdot \nabla \varphi_i \ \mathrm{d}\mathbf{x} \right)_{i,j=1,\dots,N_h}, \\
\widehat{J_P}^n &= \left(\sum_{T_k \in \mathcal{T}_h} \int_{T_k} \tau_{P,h}^n \nabla \cdot (\varphi_j \mathbf{v}_{P,h}^n) \left(\mathbf{v}_{P,h}^n \cdot \nabla \varphi_i \right) \ \mathrm{d}\mathbf{x} \right)_{i,j=1,\dots,N_h}, \\
\widetilde{J_N}^n &= \left(\sum_{T_k \in \mathcal{T}_h} \int_{T_k} \tau_{N,h}^n \nabla \cdot (\varphi_j \mathbf{v}_{N,h}^n) \left(\mathbf{v}_{N,h}^n \cdot \nabla \varphi_i \right) \ \mathrm{d}\mathbf{x} \right)_{i,j=1,\dots,N_h},
\end{aligned}
$$

$$
\begin{aligned}
H_{SP}(\mathbf{S}^n) &= \left(\int_{\Gamma_{m,h}} h_{SP}(S_h^n) \varphi_j \varphi_i \ \mathrm{d}s \right)_{i,j=1,\dots,N_h}, \\
H_{SN}(\mathbf{S}^n) &= \left(\int_{\Gamma_{m,h}} h_{SN}(S_h^n) \varphi_j \varphi_i \ \mathrm{d}s \right)_{i,j=1,\dots,N_h}, \\
H_{NS}(\mathbf{N}^n) &= \left(\int_{\Gamma_{N,h}} h_{NS}(N_h^n) \varphi_j \varphi_i \ \mathrm{d}s \right)_{i,j=1,\dots,N_h},
\end{aligned}
$$

$$
\begin{aligned}
\mathbf{F}_{NS}(\mathbf{N}^{n-1}) &= \left(\int_\Omega f_{NS}(N_h^{n-1}) \varphi_i \ \mathrm{d}\mathbf{x} \right)_{i=1,\dots,N_h}, \\
\mathbf{F}_{SP}(\mathbf{P}^{n-1}, \mathbf{N}^{n-1}) &= \left(\int_\Omega f_{SP}(S_h^{n-1}) \varphi_i \ \mathrm{d}\mathbf{x} \right)_{i=1,\dots,N_h}, \\
\mathbf{F}_{SN}(\mathbf{S}^{n-1}, \mathbf{N}^{n-1}) &= \left(\int_\Omega f_{SN}(S_h^{n-1}, N_h^{n-1}) \varphi_i \ \mathrm{d}\mathbf{x} \right)_{i=1,\dots,N_h}, \\
\mathbf{F}_{PN}(\mathbf{P}^{n-1}, \mathbf{N}^{n-1}) &= \left(\int_\Omega f_{PN}(P_h^{n-1}, N_h^{n-1}) \varphi_i \ \mathrm{d}\mathbf{x} \right)_{i=1,\dots,N_h},
\end{aligned}
$$

$$\widehat{\mathbf{F}_{SP}}(\mathbf{S}^{n-1}) = \left(\sum_{T_k \in \mathcal{T}_h} \int_{T_k} \tau_{P,h}^{n-1} f_{SP}(S_h^{n-1}) \mathbf{v}_{P,h}^{n-1} \cdot \nabla \varphi_i \, \mathrm{d}\mathbf{x} \right)_{i=1,\dots,N_h},$$

$$\widehat{\mathbf{F}_{PN}}(\mathbf{P}^{n-1}, \mathbf{N}^{n-1}) = \left(\sum_{T_k \in \mathcal{T}_h} \int_{T_k} \tau_{P,h}^{n-1} f_{PN}(P_h^{n-1}, N_h^{n-1}) \mathbf{v}_{P,h}^{n-1} \cdot \nabla \varphi_i \, \mathrm{d}\mathbf{x} \right)_{i=1,\dots,N_h},$$

$$\widetilde{\mathbf{F}_{PN}}(\mathbf{P}^{n-1}, \mathbf{N}^{n-1}) = \left(\sum_{T_k \in \mathcal{T}_h} \int_{T_k} \tau_{N,h}^{n-1} f_{PN}(P_h^{n-1}, N_h^{n-1}) \mathbf{v}_{N,h}^{n-1} \cdot \nabla \varphi_i \, \mathrm{d}\mathbf{x} \right)_{i=1,\dots,N_h},$$

$$\widetilde{\mathbf{F}_{SN}}(\mathbf{S}^{n-1}, \mathbf{N}^{n-1}) = \left(\sum_{T_k \in \mathcal{T}_h} \int_{T_k} \tau_{N,h}^{n-1} f_{SN}(S_h^{n-1}, N_h^{n-1}) \mathbf{v}_{N,h}^{n-1} \cdot \nabla \varphi_i \, \mathrm{d}\mathbf{x} \right)_{i=1,\dots,N_h},$$

$$\widetilde{\mathbf{F}_{NS}}(\mathbf{N}^{n-1}) = \left(\sum_{T_k \in \mathcal{T}_h} \int_{T_k} \tau_{N,h}^{n-1} f_{NS}(N_h^{n-1}) \mathbf{v}_{N,h}^{n-1} \cdot \nabla \varphi_i \, \mathrm{d}\mathbf{x} \right)_{i=1,\dots,N_h}.$$

More compactly in block matrix form, defining

$$\mathbf{U}^n = [S_1^n, \dots, S_{N_h}^n, P_1^n, \dots, P_{N_h}^n, N_1^n, \dots, N_{N_h}^n],$$

we aim to solve the following system

$$\left(\frac{1}{\tau_h} \mathrm{M}_0^n + \mathrm{A}_0^n + \mathrm{A}_t\left(\mathbf{U}^n\right) \right) \mathbf{U}^n = \frac{1}{\tau_h} \mathrm{M}_0^n \mathbf{U}^{n-1} + \mathbf{F}\left(\mathbf{U}^{n-1}\right), \qquad n = 1, \dots, N_t \tag{4.81}$$

where

$$\mathrm{M}_0^n := \begin{bmatrix} M & 0 & 0 \\ 0 & M + \widehat{M}^n & 0 \\ 0 & 0 & M + \widetilde{M}^n \end{bmatrix}, \tag{4.82}$$

$$\mathrm{A}_0^n := \begin{bmatrix} D_S K & 0 & 0 \\ 0 & D_P K - J_P^n + \widehat{J_P}^n & 0 \\ 0 & 0 & D_N K - J_N^n + \widehat{J_N}^n \end{bmatrix}, \tag{4.83}$$

$$\mathrm{A}_t(\mathbf{U}^n) := \begin{bmatrix} H_{SP}(\mathbf{S}^n) + H_{SN}(\mathbf{S}^n) & 0 & -H_{NS}(\mathbf{N}^n) \\ -H_{SN}(\mathbf{S}^n) & 0 & 0 \\ H_{SN}(\mathbf{S}^n) & 0 & H_{NS}(\mathbf{N}^n) \end{bmatrix}, \tag{4.84}$$

$$\mathbf{F}(\mathbf{U}^{n-1}) := \begin{bmatrix} \mathbf{F}_{NS}(\mathbf{N}^{n-1}) - \mathbf{F}_{SP}(\mathbf{S}^{n-1}) - \mathbf{F}_{SN}(\mathbf{S}^{n-1}, \mathbf{N}^{n-1}) \\ \hline \mathbf{F}_{SP}(\mathbf{S}^{n-1}) - \mathbf{F}_{PN}(\mathbf{P}^{n-1}, \mathbf{N}^{n-1}) + \widehat{\mathbf{F}_{SP}}(\mathbf{S}^{n-1}) - \widehat{\mathbf{F}_{PN}}(\mathbf{P}^{n-1}, \mathbf{N}^{n-1}) \\ \hline \mathbf{F}_{PN}(\mathbf{P}^{n-1}\mathbf{N}^{n-1}) + \mathbf{F}_{SN}(\mathbf{S}^{n-1}, \mathbf{N}^{n-1}) - \mathbf{F}_{NS}(\mathbf{N}^{n-1}) \\ + \widetilde{\mathbf{F}_{PN}}(\mathbf{P}^{n-1}, \mathbf{N}^{n-1}) + \widetilde{\mathbf{F}_{SN}}(\mathbf{S}^{n-1}, \mathbf{N}^{n-1}) - \widetilde{\mathbf{F}_{NS}}(\mathbf{N}^{n-1}) \end{bmatrix}, \tag{4.85}$$

and $\mathbf{U}^0 = \left[S_1^0, \ldots, S_{N_h}^0, P_1^0, \ldots, P_{N_h}^0, N_1^0, \ldots, N_{N_h}^0\right]^T$ is given by the initial conditions.

4.4.6 Numerical treatment of the non-linearities

The usage of the IMEX scheme (Ruuth, 1995) implies the implicit evaluation of the non-linear boundary conditions (4.18)-(4.23). This causes the discrete system (4.81) to be nonlinear. In particular, its nonlinearity is represented by the block matrix $A_t(\mathbf{U}^n)$. To bypass this issue, at every time point the system is iteratively solved in a linearised form by applying a technique known as Picard's method or fixed point iteration (Quarteroni et al., 2010; Burden and Faires, 2011). The algorithmic approach is described as follows.

We first set a fixed tolerance $\varepsilon > 0$ and a maximum number of iterations $N_{\max} \in \mathbb{N}$. Knowing the solution $\mathbf{U}^{n-1}$ at the $(n-1)$-th time step, we initialise the calculation of $\mathbf{U}^n$ with

$$\mathbf{Y}_0 = \mathbf{U}^{n-1}. \tag{4.86}$$

Then for $k = 1, \ldots, N_{\max}$ we solve the following system in the unknown $\mathbf{Y}_k$:

$$\left(\frac{1}{\tau_h}\mathrm{M}_0 + \mathrm{A}_0 + \mathrm{A}_t\left(\mathbf{Y}_{k-1}\right)\right)\mathbf{Y}_k = \frac{1}{\tau_h}\mathrm{M}_0\mathbf{U}^{n-1} + \mathbf{F}\left(\mathbf{U}^{n-1}\right). \tag{4.87}$$

If the solution $\mathbf{Y}_k$ satisfies

$$||\mathbf{Y}_k - \mathbf{Y}_{k-1}||_\infty < \varepsilon$$

then we stop the iteration and set

$$\mathbf{U}^n = \mathbf{Y}_k, \tag{4.88}$$

which represents the solution at the n-th time step.

Following the same steps of the proof of Proposition 4.4.1, one can show that at the n-th time step, for every iteration k, the solutions of the system (4.87) still conserve the total mass of the solutions at time t^{n-1}. Hence, iterating over n, the total initial mass is conserved by the linearised numerical method.

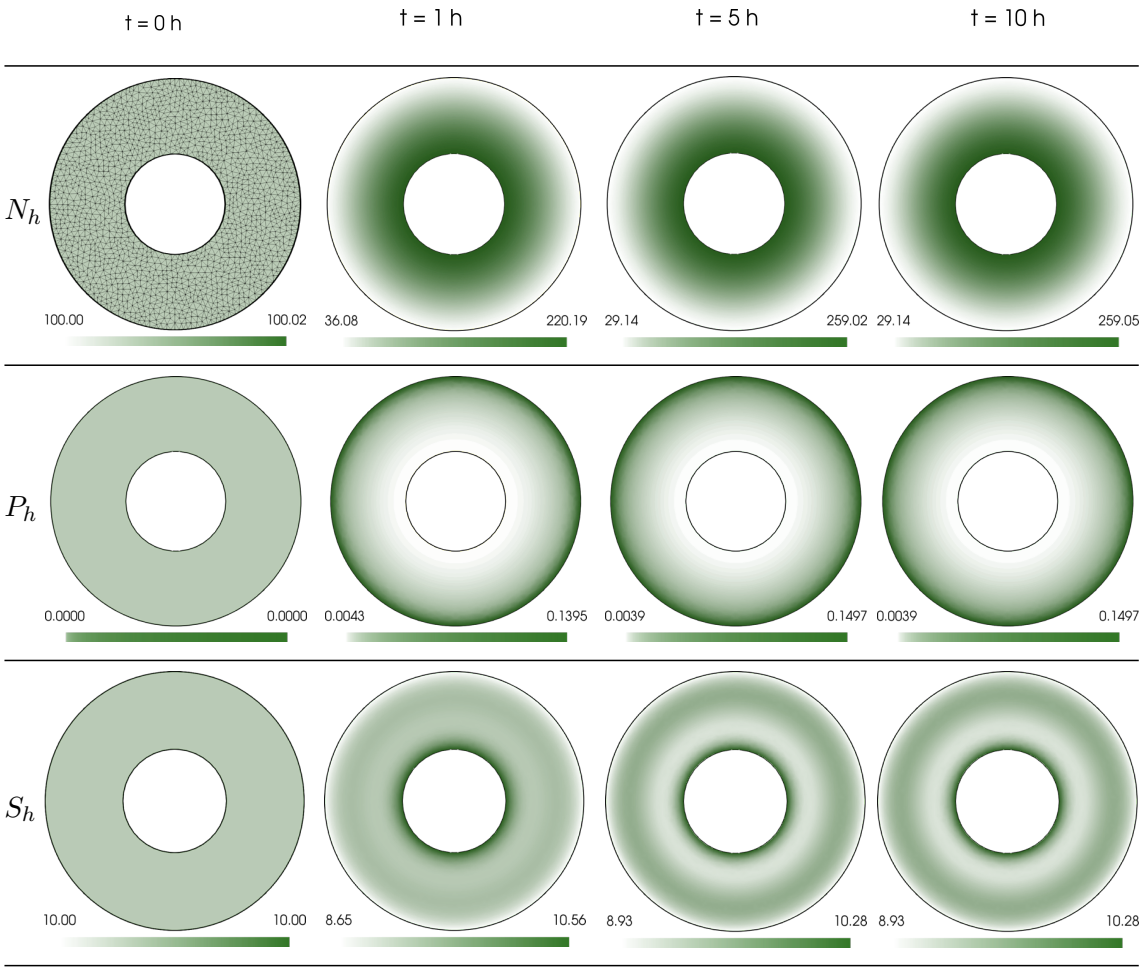

Figure 4.7: The results of a simulation of the model (4.12)-(4.23) on a ring domain with outer radius $R_m = 5$ and inner radius $R_n = 2$. The model was simulated for $t \in [0, 10]$ with time step $\tau_h = 0.5 \times 10^{-2}$. On each line is reported a solution: N on the first one, P on the middle one and S on the last line. The solutions are shown at four different time steps $t = 0$, $t = 1$, $t = 5$, $t = 10$. The mesh used for the simulation is well refined and it is shown in the initial condition for N. The initial conditions (4.15)-(4.17) are $S_0 = 10$, $P_0 = 0.0$, $N_0 = 100$. The diffusion coefficients are $D_S = 30$, $D_P = 1.1$, $D_N = 1.8$. The speed is so defined $\mathbf{v}_P = \mathbf{v}_N = -\frac{v_{max}}{R_m}\mathbf{x}$ where $v_{max} = 2.1$. The kinetic parameters are $k_{SP} = 1$, $K_{SP} = 1$, $k_{SN,\Gamma} = 50$, $K_{SN,\Gamma} = 1$, $k_{SN} = 0.1$, $K_{SN} = 1$, $k_{NS} = 100$, $K_{NS} = 1$, $k_{PN} = 1$, $K_{PN} = 1$. It is important to remark that these values do not have any biological relevance, since they have been heuristically set in order to balance the different phenomena described by the model.

4.5 Numerical simulations of the keratin model in a two-dimensional domain

All the coefficients and parameters of the model (4.12)-(4.23) are summarised in Table 4.2. It is clear that each one of them needs to be fine tuned with respect to all the others, but the high number of parameters makes this process not easy (for example, assuming the kinetic coefficients to be constant, we have 8 parameters only for the kinetics). The kinetic parameters need to balance the transport phenomena, for example strong accumulation of the keratin variable N at the outflow boundary Γ_n needs to be prevented by the disassembly process. In general, one expects all the parameters to work together in a harmonious way, simulating the "dynamical equilibrium" of the keratin cycle. The question is then how to obtain an optimal set of all these parameters. We know some of them from experiments, like the transport-related ones (speed and soluble diffusion), but for the kinetics there are not much information. Therefore a biologically relevant simulation cannot disregard a parameter estimation or identification process, necessary to have everything working in a reasonable way. However this part is not included in the thesis and is left for future work. We refer the interested reader to works by Portet et al. (2015) and Campillo-Funollet et al. (2019), where parameter estimation through Bayesian methods or optimal control methods has been carried out.

In order to show a reasonable behaviour of the model we have heuristically set some values for the parameters and the results of the corresponding simulation is shown in Figure 4.7. The parameters are able to keep a balance in the keratin cycle, eventually reaching a steady state, however it is important to note that they do not have a real biological meaning. As well, in the simulation, we use constant values for the kinetic coefficients, but future work must be done in order to identify their spatio-temporal dependency, which is suggested by the biology (Windoffer et al., 2011) and supported by the modelling work presented in Chapter 3. Consistently with the constant kinetics, also the speeds $\mathbf{v}_P$ and $\mathbf{v}_N$ are set constant in time. The speed fields are directed towards the point $(0, 0)$, the centre of the nucleus, and their magnitude increases linearly in space. More details are reported in the caption of Figure 4.7. We can appreciate that after time $t = 5$ the model reaches a stable configuration. This is clear from the L^2-norms of the increments, i.e. the L^2-norms of the difference between consecutive solutions, reported in Figure 4.8, but also from the temporal evolution of the mass of the three components in Figure 4.9. The network, shown in the first line of plots, tends to distribute around the cell nucleus and excessive accumulation of material at Γ_n is prevented by the disassembly process. On

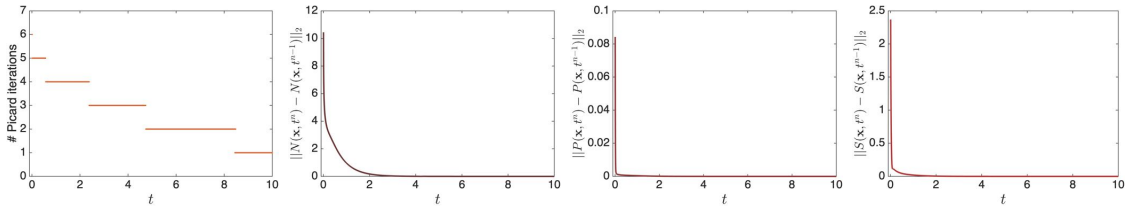

Figure 4.8: In (a) is reported the number of Picard iterations at each time point (in the simulation we set $N_{max} = 50$). In the other three images is reported the L^2-norm of the difference between consecutive solutions: (a) $\left(\int_\Omega \left(N(\mathbf{x}, t^n) - N(\mathbf{x}, t^{n-1})\right)^2 \, \mathrm{d}\mathbf{x}\right)^{1/2}$ (network); (b) $\left(\int_\Omega \left(P(\mathbf{x}, t^n) - P(\mathbf{x}, t^{n-1})\right)^2 \, \mathrm{d}\mathbf{x}\right)^{1/2}$ (precursors); (c) $\left(\int_\Omega \left(S(\mathbf{x}, t^n) - S(\mathbf{x}, t^{n-1})\right)^2 \, \mathrm{d}\mathbf{x}\right)^{1/2}$ (soluble). These results refer to the simulation shown in Figure 4.7.

the other side, the amount of network is continuously replenished by the integration of precursors, lateral aggregation of soluble units and network formation at the boundary Γ_m. In turn the highest concentration of precursors is located in the vicinity of the cell membrane, where they nucleate thanks to the boundary condition (4.19). The presence of the network enhances the integration, resulting in lower concentrations of precursors far away from Γ_m. Lastly, the soluble pool, supported by the disassembly of the network, is mainly formed at the nucleus membrane Γ_n. It is consumed predominantly around Γ_m by nucleation of precursors and in the perinuclear region (the internal area close to Γ_n), where the strong presence of the network enhances lateral association, causing a drop in soluble concentration. The number of Picard iterations at every time point is shown in Figure 4.8a. It decreases in time, from a number of 6 iterations at the initial time to a single iteration when the system is at the steady state. Indeed, only 1 Picard iteration indicates that the system (4.87) was solved only once, i.e. the solution immediately satisfies $||\mathbf{U}^n - \mathbf{U}^{n-1}||_\infty < \varepsilon$.

This simulation shows the behaviour of the model on a two-dimensional geometry. We have not included three-dimensional simulations, but these are possible. Indeed, we make clear that the work presented in this chapter is valid for both cases.

4.6 Conclusion

In this chapter we have presented a mathematical model for simulating keratin spatio-temporal dynamics in cells. The model is derived on two- and three-dimensional geometries, based on the recent literature regarding keratin filaments assembly and keratin network remodelling. An interesting aspect of the model are the boundary conditions, which have

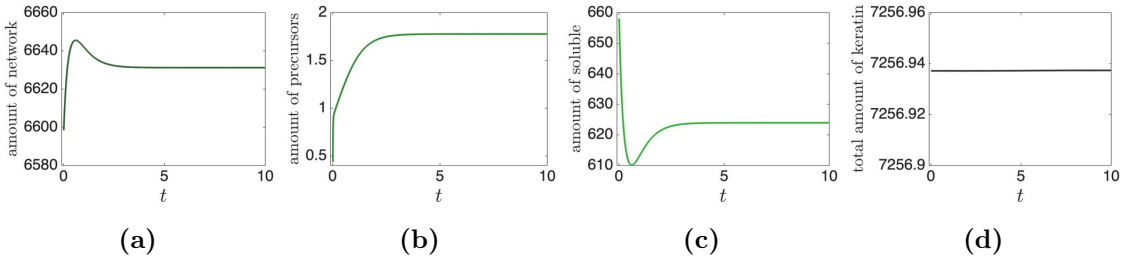

Figure 4.9: The temporal evolution of the keratin masses: (a) the integral $\int_\Omega N(\mathbf{x},t)\,\mathrm{d}\mathbf{x}$; (b) $\int_\Omega P(\mathbf{x},t)\,\mathrm{d}\mathbf{x}$; (c) $\int_\Omega S(\mathbf{x},t)\,\mathrm{d}\mathbf{x}$; (d) the total amount of keratin $\int_\Omega \left(N(\mathbf{x},t)+P(\mathbf{x},t)+S(\mathbf{x},t)\right)\,\mathrm{d}\mathbf{x}$. These results refer to the simulation shown in Figure 4.7.

been imposed to satisfy specific keratin kinetics, i.e. nucleation, network formation and disassembly. This is one of the main differences with respect to the one-dimensional model presented in the previous chapter. Another difference is that in this new model three forms of keratin are considered, which represent the three main steps of the biological cycle of keratin in cells: a soluble pool S, precursors P and the network N. In Chapter 3 these three were grouped into two components: the same soluble pool S and the insoluble keratin I. The categorisation used in this chapter results in a more interesting modelling framework, as this allows to consider nucleation and lateral association independently, while in Chapter 3 these two phenomena were grouped into the more general assembly process. In order to solve the model we use the SUPG finite element method, which is able to stabilise the numerical solution through a regularisation process with respect to possible spurious oscillations due to the advection-dominated flows. Finally a simulation on a two-dimensional spatial domain with "artificial" (non biologically relevant) parameters is presented. Starting from uniform initial conditions, the model is able to show a relevant behaviour, reaching a stable configuration in which the keratin network covers the whole cell interior, surrounds the nucleus and is mainly concentrated in the nuclear peripheral areas.

Given the high number of parameters playing a role in the model, a crucial step is their estimation. For this it is necessary to optimise the parameters by comparing the solutions of the model to the experimental data. Therefore for a future work we propose to use either a genetic algorithm (see Appendix B.2), as done for the model in Chapter 3, or a Bayesian approach, which is able to provide credible regions for the parameters (Campillo-Funollet et al., 2019; Juma, 2019).

It is important to remark that the keratin model describes a general framework which can be easily modified. For instance, one future goal is to understand the spatio-temporal dependency of the nucleation process. As stated in the section dedicated to the derivation

of the model, in the last years nucleation has been thought to be linked to special transmembrane protein complexes called focal adhesions. An interesting idea for future work is to derive a profile for the time and space dependent nucleation coefficients depending on the evolving focal adhesions. Inspired by this, in the Appendix C we present a first model for shaping focal adhesions.

Along the same lines, another variation of the model could be done by modelling the kinetic coefficient $k_{SN,\Gamma}$ of equation (4.24) as a function of the network anchorage points such as hemidesmosomes and desmosomes. In particular, it would be interesting to do these variations in a three-dimensional domain, where the base of the cell has many focal adhesions and hemidesmosomes.

Once the parameters are estimated, it would also be interesting to understand how these are affected by changes in cell shape. Indeed, a future goal is the investigation of the model on non isotropic spatial domains. As well, another important extension to be done is to test the model on evolving domains, for example during cell migration. Using the conservation of mass on evolving domains (see for example DiBenedetto (2010)) the equations for a migrating cell are:

$$\begin{aligned}
\frac{\partial S}{\partial t} + \underbrace{\nabla \cdot (S\mathbf{v}_C)}_{\text{cell velocity}} &= \nabla \cdot (D_S \nabla S) + f_{NS}(N) - f_{SP}(S) - f_{SN}(S,N),\\
\frac{\partial P}{\partial t} + \underbrace{\nabla \cdot (P\mathbf{v}_C)}_{\text{cell velocity}} &= \nabla \cdot \big(D_P \nabla P - P\mathbf{v}_P(\mathbf{x},t)\big) + f_{SP}(S) - f_{PN}(P,N),\\
\frac{\partial N}{\partial t} + \underbrace{\nabla \cdot (N\mathbf{v}_C)}_{\text{cell velocity}} &= \nabla \cdot \big(D_N \nabla N - N\mathbf{v}_N(\mathbf{x},t)\big) + f_{PN}(P,N) + f_{SN}(S,N) - f_{NS}(N),\\
\mathbf{x} \in \Omega(t), \qquad & t \in (0,T],
\end{aligned}$$

where each point of the closure of the domain is subject to the equation $\frac{\partial}{\partial t}\mathbf{x}(t) = \mathbf{v}_C$, $\mathbf{v}_C$ being the velocity field of the cell. The vector field $\mathbf{v}_C$ describes the motion of every point of the cell domain, see for example the cell in Figure 4.1. More generally this model can also be studied for shape changing cells, even for the case without directed migration.

Finally, a very important advance in the modelling part would be to find dependencies between optimal parameters and functions of the stationary cell model (4.12)-(4.23) and the cell velocity $\mathbf{v}_C$, revealing therefore the coupling between biochemical and biomechanical properties of the keratin network in cell migration.

Chapter 5

Conclusion

In this thesis we have presented different mathematical approaches for modelling cellular processes such as cell polarisation and keratin network remodelling. A qualitative approach was applied in modelling cell polarisation, which resulted in the bulk-surface wave pinning model presented in Chapter 2. Since cell polarisation is the result of an intricate network of biochemical reactions involving a large number of biological entities, a detailed model would have been mathematically intractable. Therefore, following the work done by Mori et al. (2008), our modelling idea focused on the reduction of the biological assumptions to a minimal level of complexity and a phenomenological representation of the processes. This resulted in a model derivation based on only few fundamental features of the Rho GTPases, which were common to all the members of this protein family. In particular, by considering spatial compartmentalisation and bistable biochemical reactions, we obtain a bulk-surface model describing a membrane-bound active and a cytosolic inactive GTPase, which interact at the cell membrane and generate polarisation patterns.

On the other side, Chapter 3 is devoted to the description of a quantitative modelling approach for investigating the dynamics of keratin filaments in resting cells. The model is based on the experimental measurements by Moch et al. (2013) and aims at quantifying the keratin assembly/disassembly cycle, by extending a previous mathematical model by Portet et al. (2015). Our approach is strictly dependent on a new interpretation of the experimental data, which are remodelled in order to overcome the technical difficulties in getting the data from real cells. Complementing this with new modelling ideas, we developed a model whose solutions accurately match experimental measurements. Furthermore, our model is able to estimate the spatial location of the kinetic processes which are involved in the cycle, showing consistency with the well-known biological model proposed by Windoffer et al. (2011).

Lastly, in Chapter 4 we set new basis for a more detailed understanding of the processes involved in the keratin network remodelling. In order to do so, we consider three different forms of keratin in cells and five type of interactions between them. The model is developed in a perforated d-dimensional domain Ω with $d = 2$ or 3, where the nucleus of the cell, excluded from the computational domain, constitutes an internal hole in Ω. Through a fabricated example, obtained by testing the model with "artificial" parameters, we showed that our mathematical formulation is able to describe the qualitative behaviour of the keratin cycle. However, since the model aims at quantifying the dynamics, in the future, we expect to work on the parameter estimation by comparing the model solutions to experimental data.

In this thesis we have tackled research questions of different nature, in the context of cell migration, with appropriate mathematical tools and approaches. In Chapter 2 the aim was to provide theoreticians with an easy tool for polarisation pattern formation and the biologists with some hints for the understanding of fundamental reactions within the complex GTPase biochemical network. Hence a qualitative approach was the most convenient modelling strategy to adopt. The active GTPases, that in cell polarisation tend to concentrate only in some specific areas of the cell membrane, are modelled by a reaction-diffusion equation. The model builds on the fact that the action of GEFs, which are factors responsible of GTPase activation, is stimulated by the same active GTPases. This is a central aspect as it introduces nonlinarities in the reaction function: describing it through a Hill function with exponent $n = 2$, the final equation for the evolution of the active GTPase is of a bistable reaction-diffusion type. The positive feedback of the active GTPase is crucial for the polarisation response in the previous works by Mori et al. (2008) and Giese et al. (2015). Our work confirms that this property is maintained also on three-dimensional geometries, where proteins are compartmentalised between cell membrane and cytosol. The model was solved in several three-dimensional geometries and some of the results inspired us to further investigate on the long-time behaviour of the solutions. In particular, we set some starting points for studying the effects of geometry on the evolution of the solutions. We will come back on this point in Section 5.1.

Of a different nature are, instead, the works on keratin dynamics, in which the primary interest was the quantification of the kinetics involved in the filament and network formation. Therefore a quantitative approach was needed, which in Chapter 3 was based on the available experimental data. Moreover, this work was complemented by a reinterpretation of the data agreed with the experimentalists. This allowed us a more consistent

use of their measurements, with a consequent improvement in the modelling results. The predictive potential of the model is its ability to localise in space and time the kinetic coefficients, which allows the identification of the assembly and disassembly regions in the keratin network cycle. Similar, but more detailed conclusions are expected also for the model proposed in Chapter 4. Discussions about this point are postponed to future work, which is presented in the following section.

5.1 Future work

Across this thesis are posed many new research questions, which we would like to summarise in this conclusion.

5.1.1 A coupled bulk-surface model for cell polarisation

- The simulation shown in Figure 2.10 of Chapter 2 is well representative of the fact that the polarisation pattern resulting from the BSWP model (2.15)-(2.18) is only apparently stable. In the long time indeed, the active patch moves towards specific regions of the domain very slowly. Several new numerical investigations are proposed in Section 2.11, confirming this behaviour. Despite the fact that this occurs for times which are beyond the biological relevance, an interesting extension of this work regards the mathematical understanding of this behaviour: how does the surface geometry affect the membrane-bound component?

- Future research should be devoted to the extension of the BSWP model (2.15)-(2.18) to migrating cells. This has been introduced in Section 2.12, but needs further investigation, especially in modelling the role of the Rho GTPases in the evolution of the cell shape remodelling and migration. This would link the biochemistry to a mechanical model for cell migration, where research challenges also include the mathematical formulation for the evolution law of the migrating cells.

- It would be of interest to extend the BSWP model (2.15)-(2.18) to three components, by including a membrane-bound inactive GTPase. Hence, which kind of binding functions can generate a similar behaviour to the initial two components model? Can we identify some parameter set?

5.1.2 Spatio-temporal dynamics of the keratin network in one dimension

- The model proposed in Chapter 3 is based on experimental data taken at 24 hours and 48 hours after the cells are seeded. What happens in the between, for example at 36 hours? This is a question which can be easily addressed by using the mathematical model (3.23)-(3.26). However it would be very interesting to test with data how close our predictions are to experimental observations.

- Seeing from a different point of view the previous question, a useful and interesting study would be to calibrate the model with respect to experimental data taken at different time points. How are the optimised kinetic parameters affected by the introduction of new data?

- The last question that we leave open with respect to Chapter 3 still relates to the testing of the model with new experimental data. Indeed, it would be interesting to check if other intermediate filaments proteins (such as vimentin for instance) can be modelled within the same setting. If this is the case, how are the parameters of the model affected by the change of the intermediate filament proteins?

5.1.3 A multidimensional model for the spatio-temporal dynamics of the keratin network

- The study presented in Chapter 4 needs to be finalised by finding reasonable values for the parameters. This can be done by comparing the model (4.12)-(4.23) to experimental data. In the literature, many methods have been presented for this scope, and the review paper by Ashyraliyev et al. (2009) highlights the most common ones. In Chapter 3 we have used a genetic algorithm (Holland, 1992; Mitchell, 1998; Portet et al., 2015) which is also briefly described in Appendix B.2. In this case, at the end of the algorithm, each parameters finds a single best value. On the other hand, Bayesian methods (Wilkinson, 2007; Stuart, 2010; Campillo-Funollet et al., 2019) are able to estimate the probability distributions for the parameters, providing a set of different possible values. As well, these methods are suitable when dealing with data characterised by uncertainty, as they can generally counterbalance the experimental noise in the measurements. However, a drawback of the Bayesian methods is the computation cost, which is generally quite expensive. Hence, robust, stable and efficient solvers must be developed if one is to exploit the powerful nature of the Bayesian methods for partial differential equations.

- A second point which needs to be addressed is related to the efficiency of the numerical method, which requires highly detailed meshes. Indeed, it would be convenient to refine the method in order to speed-up the simulations. This is particularly an important step which needs to be done for a quicker parameter estimation over two- or even three-dimensional domains.

- The model (4.12)-(4.23) provides a mathematical tool for studying the effects of cell shape on keratin dynamics. This can be done by estimating the parameters for different spatial domains, comparing the solutions of the model to experimental data. From the other side, this goal can be experimentally supported by using micropatterns of predefined shape, which are well-known biological tools employed to constrict the cell to acquire a given configuration (Théry et al., 2006). Hence, by coupling experiments and simulations, we expect to obtain new quantitative results able to explain the relationship between cell shape and keratin dynamics.

5.1.4 Investigating the connections

Following the discussion in the Introduction, and especially in Section 1.4, it would be very interesting to work on the relationships between keratin intermediate filaments, Rho GTPases and cell adhesions in the context of cell migration. In particular possible research projects could be:

- Once the parameters for the keratin model (4.12)-(4.23) are estimated, it would be of interest to check how these are affected by cell migration. A starting point can be the study of the model proposed in the conclusion of Chapter 4 (Section 4.6). One of the questions to be answered would be: can we provide a quantitative study of the keratin dynamics in the different cases?

- The keratin model (4.12)-(4.23) provides a framework for testing biological hypotheses. It would be interesting to test the effect of the focal adhesions in the nucleation process, or include the presence of the hemidesmosomes. For testing the effects of the focal adhesions we propose to use the simple FAs model presented in Appendix C.

- In Section 1.4 we highlighted the role of keratin intermediate filaments in regulating the RhoA activity. Hence it would be interesting to study a possible connection between the BSWP model (2.15)-(2.18) and the keratin model (4.12)-(4.23). Consistently with the work by Bordeleau et al. (2012), keratin effects could be included

in the parameters k_0 and γ of the BSWP function (2.18).

In conclusion, we have presented some research ideas which could be addressed as a continuation or extension to the work done in this thesis. However this list could be much longer, confirming the fact that cell biology provides an incredible number of research questions. In addressing many of them, a close collaboration between mathematicians and experimentalists, supported by a continuous feedback between these two worlds, can potentially be the key for many new interesting results.

Appendix A

Enzymatic reactions

A.1 Law of mass action

Let us consider two chemical species A and B, called *reagents*, which interact together to form a third specie C, called *product*. The reaction is described by the following diagram:

$$A + B \xrightarrow{k} P,$$

where k is a proportionality constant associated to the reaction. One is generally interested in studying the speed of this reaction. The *law of mass action* helps in this, as it states that the product is formed at a rate proportional to the product of the reagent concentrations. Hence the reaction can be easily translated into mathematics by the following system of ordinary differential equations:

$$\begin{aligned}
\frac{d[C]}{dt} &= k[A][B], \\
\frac{d[A]}{dt} &= -k[A][B], \\
\frac{d[B]}{dt} &= -k[A][B],
\end{aligned}$$

where, if X is a chemical specie, $[X]$ indicates its concentration.

A.2 Michaelis Menten kinetics

In cells, most of the biochemical reactions are governed and catalysed by particular proteins called *enzymes*, which act on other proteins called *substrates*. These kind of kinetic reactions are called *enzymatic reactions* and the most famous type was proposed by Leonor Michaelis and Maud Menten in 1913. The *Michalis Menten kinetic theory* describes

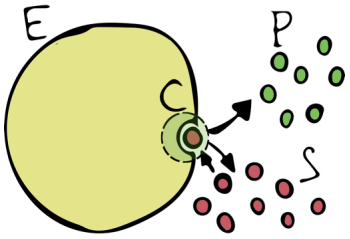

Figure A.1: A graphical representation of an enzymatic reaction: an enzyme E (in yellow colour) forms a compound C (in transparent green) with a substrate protein S (in red). The bounded substrate is transformed in a new protein P called product (in green) which is then released from the binding site which becomes again available for other substrates.

the conversion of a substrate S into a product P, after its binding to an enzyme E. The reaction is described by the following diagram

$$S + E \underset{k_{-1}}{\overset{k_1}{\rightleftarrows}} C \overset{k_2}{\rightarrow} E + P,$$

where C indicates the enzyme-substrate compound. At the end of the reaction the product P is released and the enzyme E is again available for other substrates. The Michaelis and Menten theory is based on the *quasi-steady state assumption* which describes the fact that the compound C gets to the equilibrium very fast. Applying this assumption to the system of ODEs derived by applying the law of mass action, one gets the following expression for the product formation rate:

$$V := \frac{d[P]}{dt} = \frac{V_{max}[S]}{K_m + [S]}. \tag{A.1}$$

K_m is the *Michaelis Menten constant* and represents the affinity of the substrate towards the enzyme E and $V_{max} = k_2 E_0$ is a constant, where $E_0 = [E(0)]$ is the initial concentration of enzymes. The plot of the function $V = V([S])$, shown Figure A.2 for $n = 1$ (orange colour), has a hyperbolic shape.

A.3 Cooperative kinetics

Not all the enzymes obey to the Michaelis Menten theory and many cases have been noted whereby the plot of the reaction rate as a function of the substrate is sigmoidal. This happens because many enzymes and substrates have a *cooperative* behaviour. In 1910 Archibald Hill showed that the binding of a substrate to one site of the enzyme can affect the binding properties of another site on the same enzyme (Hill (1910); Nelson et al. (2008); Smith (1983) (in the Michaelis Menten theory only one binding site per enzyme

is assumed). This happens because, after the binding of a substrate, proteins can change their shape, becoming more or less attractive for the same substrate. A protein showing this behaviour is called *allosteric* protein. In particular Hill showed that haemoglobin presents this feature in binding to oxygen and from his studies he came out with a general approach for cooperative ligand[1] binding to multisubunits proteins. For an enzyme E with n binding sites we have the following sequence of reactions:

$$E + nS \underset{k_{-1}}{\overset{k_1}{\rightleftarrows}} ES_1 + (n-1)S \underset{k_{-2}}{\overset{k_2}{\rightleftarrows}} ES_2 + (n-2)S \underset{k_{-3}}{\overset{k_3}{\rightleftarrows}} ... \underset{k_{-n}}{\overset{k_n}{\rightleftarrows}} ES_n \overset{k'_n}{\rightarrow} ES_{n-1} + P,$$

where the product can be released also at an intermediate step:

$$ES_i \underset{k'_{-i}}{\overset{k'_i}{\rightleftarrows}} ES_{i-1} + P, \quad \text{for } i = 1, ..., n-1, \quad \text{with } ES_0 = E.$$

We simplify the sequence of reactions with the following:

$$E + nS \underset{k_{-1}}{\overset{k_1}{\rightleftarrows}} ES_n \overset{k'_1}{\rightarrow} E + P,$$

i.e. in the compound, the substrates occupy simultaneously n binding sites of the enzyme and we assume no product is released at intermediate states. The associated ordinary differential equations are:

$$\frac{d[E]}{dt} = -k_1[E][S]^n + (k_{-1} + k'_1)[ES_n], \tag{A.2}$$

$$\frac{d[nS]}{dt} = -k_1[E][S]^n + k_{-1}[ES_n], \tag{A.3}$$

$$\frac{d[ES_n]}{dt} = k_1[E][S]^n - (k_{-1} + k'_1)[ES_n], \tag{A.4}$$

$$\frac{d[P]}{dt} = k_2[ES_n]. \tag{A.5}$$

From the equations (A.2) and (A.4) follows the conservation equation

$$[E] + [ES_n] = E_{tot} = E_0, \tag{A.6}$$

that means there is conservation of the total binding sites. If, as in Michaelis Menten theory, we assume that

$$\frac{d[ES_n]}{dt} = 0,$$

[1] a ligand is any kind of molecule, including proteins, that binds reversibly to another protein.

then by using (A.6) in (A.4) to obtain $[ES_n]$, from (A.5) we have

$$V = \frac{d[P]}{dt} = \frac{V_{max}[S]^n}{K^n + [S]^n} \tag{A.7}$$

where $V_{max} = k_1' E_0$ and $K = \frac{k_{-1}+k_1'}{k_1}$. From experiments it has been shown that n does not represent the number of binding sites, but the degree of interactions between them, and the number of binding sites is the upper limit for n. The Hill coefficient determines the cooperative behaviour in the reaction. It is important to note that in general n is not necessarily an integer, but a positive real number. In Figure A.2 three cases are represented: there is positive cooperative behaviour if $n > 1$, non cooperative if $n = 1$, negative if $n < 1$. It is easy now to notice that Michaelis Menten equation (A.1) is just a special case of (A.7), where the reaction is non cooperative ($n = 1$).

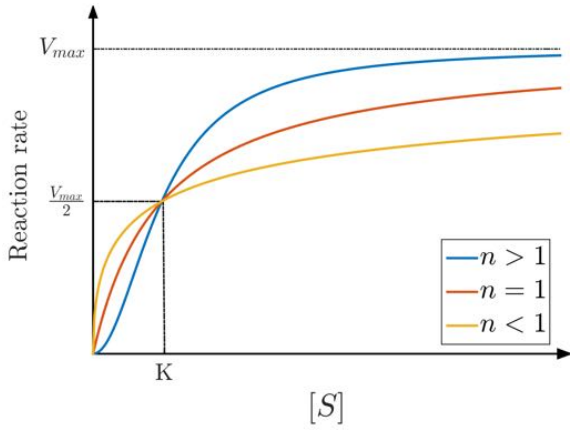

Figure A.2: The velocity V of enzymatic reactions as a function of the substrate concentration. The image shows the function V as defined in eq. (A.7). Cooperative behaviour is defined by the parameter n: $n > 1$ indicates positive cooperative behaviour, $n = 1$ non cooperative, $n < 1$ negative cooperative behaviour. All the three functions asymptotically tend to the value V_{max}. The constant K represents the concentration of substrate necessary for the reaction to reach half of its speed.

For more details on the biochemistry we refer to the textbook of Nelson (2003) and for the mathematical approach to the textbooks by Edelstein-Keshet (2005); Murray (2002).

Appendix B

Spatio-temporal dynamics of keratin in one dimension

B.1 The explicit functions for the one-dimensional model of keratin

The initial condition $I_{24}(x)$ is defined from the experimental profile of the assembled keratin material measured at 24 hours (Moch et al., 2013). The polynomial $P(x) = \sum_{i=0}^{8} p_i x^i$ for which $p_8 = 5.441\times10^{-8}\frac{\mu M}{\mu m^8}$, $p_7 = 3.397\times10^{-21}\frac{\mu M}{\mu m^7}$, $p_6 = -5.379\times10^{-5}\frac{\mu M}{\mu m^6}$, $p_5 = -2.077\times10^{-18}\frac{\mu M}{\mu m^5}$, $p_4 = 0.01062\frac{\mu M}{\mu m^4}$, $p_3 = 2.801\times10^{-16}\frac{\mu M}{\mu m^3}$, $p_2 = 0.4104\frac{\mu M}{\mu m^2}$, $p_1 = 1.4\times10^{-14}\frac{\mu M}{\mu m}$ and $p_0 = 506.5\mu M$ is a good approximation of the data. In order to satisfy the boundary conditions defined in (3.3) the function is modified close to the boundaries as follows:

$$I_{24}(x) = \begin{cases} c, & x < a_1 - \epsilon, \\ \frac{P(a_1+\epsilon)-c}{4\epsilon^2}x^2 + \frac{(\epsilon-a_1)(P(a_1+\epsilon)-c)}{2\epsilon^2}x & \\ \quad + \frac{(\epsilon-a_1)^2P(a_1+\epsilon)+(3\epsilon^2+2a_1\epsilon-a_1^2)c}{4\epsilon^2}, & a_1-\epsilon \le x < a_1+\epsilon, \\ P(x), & a_1+\epsilon \le x < a_2-\epsilon, \\ -\frac{P(a_2-\epsilon)-c+2\epsilon D(a_2-\epsilon)}{4\epsilon^2}x^2 & \\ -\frac{(\epsilon-a_2)(P(a_2-\epsilon)-c)-2\epsilon a_2 D(a_2-\epsilon)}{2\epsilon^2}x & \\ \quad + \frac{(3\epsilon^2+2a_2\epsilon-a_2^2)P(a_2-\epsilon)}{4\epsilon^2} & \\ \quad + \frac{2\epsilon(\epsilon^2-a_2^2)D(a_2-\epsilon)+(\epsilon-a_2)^2c}{4\epsilon^2}, & a_2-\epsilon \le x < a_2+\epsilon, \\ c, & a_2+\epsilon \le x, \end{cases} \tag{B.1}$$

with $a_1 = -21\mu m$, $a_2 = -a_1$, $\epsilon = 1\mu m$, $c = 50\mu M$ and $D(x) = \sum_{i=1}^{8}(9-i)p_i x^{8-i}$.

The approximation of the data after 48 hours of seeding Moch et al. (2013) is repres-

ented by:

$$I_{48}(x) = p_1 x^4 + p_2 x^3 + p_3 x^2 + p_4 x + p_5, \tag{B.2}$$

where $p_1 = -0.003255 \frac{\mu M}{\mu m^4}$, $p_2 = 2.61 \times 10^{-17} \frac{\mu M}{\mu m^3}$, $p_3 = 0.4899 \frac{\mu M}{\mu m^2}$, $p_4 = 1.558 \times 10^{-15} \frac{\mu M}{\mu m}$ and $p_5 = 604.1 \mu M$.

Both I_{24} and I_{48} are reported in Figure 3.6 and were proposed in Portet et al. (2015). Note that both I_{24} and I_{48} are very close to a even function.

B.1.1 The optimal speed and kinetic coefficients from Portet et al. (2015)

The functions reported in Figures 3.7a-3.7b for the speed and kinetics of the model in Portet et al. (2015) are:

$$v(x) = u(1 - e^{-ax^2}), \tag{B.3}$$

with $u = 0.15 \mu m/\text{min}$ and $a = 0.05$. The disassembly rate coefficient is described as follows

$$k_{dis}(x) = \begin{cases} k_{baseline} + k_{max} & 0 \leq |x| < a_3 - \varepsilon \\ I_{a_3}(x) & a_3 - \varepsilon \leq |x| < a_3 + \varepsilon \\ k_{baseline} + k_{max} - k_{max} \frac{x - a_3}{a_4 - a_3} & a_3 + \varepsilon \leq |x| < a_4 - \varepsilon \\ I_{a_4}(x) & a_4 - \varepsilon \leq |x| < a_4 + \varepsilon \\ k_{baseline} & a_4 + \varepsilon \leq |x| \leq L \end{cases} \tag{B.4}$$

where $k_{baseline} = 0.59988 \mu M/\text{min}$, $k_{max} = 118.77524 \mu M/\text{min}$, $a_3 = 5 \mu m$, $a_4 = 18 \mu m$ and $I_{a_3}(x)$ and $I_{a_4}(x)$ are second degree polynomials whose coefficients are determined in order to have $k_{dis} \in C^1([-L, L])$. The assembly rate coefficient k_{ass} is spatially uniform with value $562.914 \mu M/\text{min}$.

B.2 The Genetic Algorithm

The genetic algorithm is a well-known method (Holland, 1992; Mitchell, 1998), whose ideas are based on the Darwinian evolution theory of natural selection and genetics. When applying this algorithm to parameter estimation, a sequence of different generations of parameters is created based on the "survival of the fittest" principle. In this appendix we will briefly describe the basic ideas.

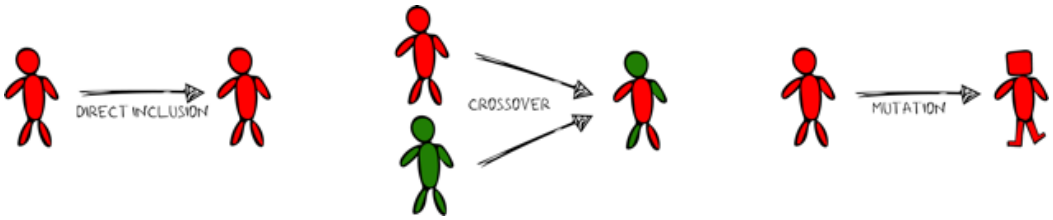

Figure B.1: Genetic algorithm: creation of a new generation.

Starting from an initial *population* G^0 of candidate parameters over a specified search space X, the genetic algorithm iterates towards an optimal solution producing, at each iteration $k+1$, a new *generation* G^{k+1} of *individuals* (parameter values) from the fittest ones of the current generation G^k. By *fittest* we refer to the suitability of the parameters with respect to the specified problem. The new generation G^{k+1} inherits the best traits from G^k as it is created in three possible ways: direct inclusion, crossover and mutation. The first one represents the possibility of an individual to survive for more than one generation, if fit enough; the second one is the creation of an individual by combination of the traits of two parents from G^k; in the third one an individual from G^k is included in the successive generation G^{k+1} after a mutation of at least one trait.

We now describe the steps of the algorithm: assume we need to estimate d real values $\hat{p}_1, \ldots, \hat{p}_d$ and let X be the d-dimensional search space, which we can imagine as the Cartesian product of real intervals $X = [a_1, b_1] \times [a_2, b_2] \times \ldots \times [a_d, b_d]$, with a_i and b_i determined by *a priori* knowledge (for example non-negativity requires $a_i > 0$). Let $f(\mathbf{p}) = f(p_1, \ldots, p_d)$ be the objective function which we want to minimise, for example as in equation (3.34) of Chapter 3.

1. Let G^0 be an initial population composed of m (even integer) candidate vectors (individuals) $\mathbf{p_1}^0, \ldots, \mathbf{p_m}^0 \in X$, each one composed of the d parameters we want to estimate. This initialisation step can be a result of some *a priori* knowledge on the behaviour of the objective function f or some random selection.

2. At the $(k+1)$-th iteration of the algorithm, the objective function is evaluated for every individual of the generation G^k. With this step a certain number of individuals will be included in the next generation G^{k+1}. A possible method for the selection is to introduce a probability function, such as (Dorsey and Mayer, 1995):

$$p_i = \frac{T(f(\mathbf{p_i}^k))}{\sum_{j=1}^{m} T(f(\mathbf{p_j}^k))}, \qquad i = 1, \ldots, m, \tag{B.5}$$

where T is a non-negative and strictly increasing function, which guarantees that

each p_i is well defined. Each individual $\mathbf{p_i}^k$ will be directly included in G^{k+1} with probability $1 - p_i^m$. Therefore the less fit individuals will have a smaller probability of survival to the new generation while better fit individuals will go through the selection process with better chances.

3. This step regards the generation of a provisional m-dimensional set H^k. Each individual $\tilde{\mathbf{p}}_\mathbf{i}^k \in H^k$ is selected from G^k with probability (B.5) (it is possible to select the same element multiple times).

4. Randomly select two individuals $\tilde{\mathbf{p}}_\mathbf{i}^k$ and $\tilde{\mathbf{p}}_\mathbf{j}^k$ from H^k and an integer $i_c \leq d$. Set $\eta \in [0, 1]$ (*crossover rate*). With probability $1 - \eta$ (*direct inclusion*) we include $\tilde{\mathbf{p}}_\mathbf{i}^k$ and $\tilde{\mathbf{p}}_\mathbf{j}^k$ in G^{k+1}, while with probability η both $\tilde{\mathbf{p}}_\mathbf{i}^k$ and $\tilde{\mathbf{p}}_\mathbf{j}^k$ are included in G^{k+1} only after their c_i-components are swapped. The individuals $\tilde{\mathbf{p}}_\mathbf{i}^k$ and $\tilde{\mathbf{p}}_\mathbf{j}^k$ are then removed from H^k.

5. The previous step is repeated until G^{k+1} has m individuals.

6. For each j-th component of $\mathbf{p_i}^{k+1}$ a scalar value α_{ij}^{k+1} is selected randomly in $[a_j, b_j]$. Set $\gamma \in (0, 1)$ (*mutation rate*). Therefore with probability γ the j-th component of $\mathbf{p_i}^{k+1}$ is replaced by α_{ij}^{k+1}, while with probability $1 - \gamma$ nothing occurs. This step is repeated over all components of each vector of G^{k+1}.

7. The whole process (steps 2-6) is repeated until a certain number of generations have been created without any improvement.

Appendix C

A simple model for shaping focal adhesion

C.1 The biological assumptions

Focal adhesions (FAs) are protein complexes used by the cell to anchor itself to the substrate. Through attachment to actin stress fibres, the cell uses the FAs to apply traction forces during migration. In particular, the evolution of focal adhesions is not only the result of biochemical reactions, but it is also characterised by a clear mechanical dependency. Using fluorescence labelling techniques to target FA characteristic proteins such as paxillin or vinculin, it is possible to visualize their shape. Mainly they appear as long and thin ellipses. Focal adhesions are not stable but highly dynamic: in Figure C.1 we schematise their life phases. In this section, we present a simple model for the evolution of a focal adhesion shape, inspired by the works of Berginski et al. (2011) and Mohl et al. (2012), to which we refer for more biological details. We simplify the FA life in the two following steps:

1. FA forms at a certain point P_1 and it starts elongating in only one direction, until

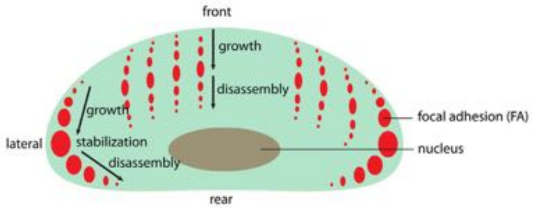

Figure C.1: Evolution of a focal adhesion: after appearing it starts elongating until maturation. Then it starts disassembling from the other end, until final disappearing. Picture from Mohl et al. (2012), *reproduced with permission of COMPANY OF BIOLOGISTS LTD., Journal of Cell Science.*

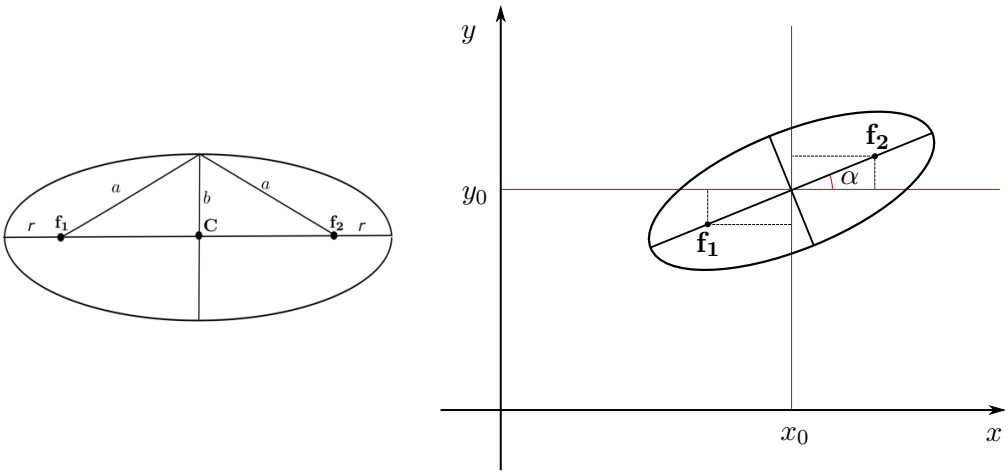

Figure C.2: On the left, an ellipse with focal points $\mathbf{f_1}, \mathbf{f_2}$, centre $\mathbf{C} = (\mathbf{f_2} + \mathbf{f_1})/2$ and semi minor axis $b > 0$ and semi major axes $a = \sqrt{||\mathbf{f_1} - \mathbf{C}||^2 + b^2} = \sqrt{\left(\frac{||\mathbf{f_2} - \mathbf{f_1}||}{2}\right)^2 + b^2}$. On the right, ellipse with centre $\mathbf{C} = (x_0, y_0)$ and orientation α.

reaching the point P_2. At the end of this step the length and size of the FA is maximal;

2. FA starts the disassembly process in only one direction, from point P_1 until disappearing at the point P_2.

During all their life time, FAs are characterised by a sliding speed. However, in order to simplify the exposition, let us ignore for the moment this aspect. As well, we will assume that a focal adhesion keeps always the same orientation α during its whole lifetime. However, it is important to remark the fact that these last two assumptions are not restrictive and, as it will be clearer at the end, the model will easily support extensions to sliding FAs and orientation changes.

C.2 The model

An ellipse $\mathcal{E}$ is a set of all points $\mathbf{P}$, such that the sum of the distances $|\mathbf{PF}_1|, |\mathbf{PF}_2|$ to two fixed points $\mathbf{F}_1, \mathbf{F}_2$, known as *foci*, is a constant value c. Let us denote with $a = \frac{c}{2}$ the major semi-axis, such that the ellipse is given by

$$\mathcal{E}(\mathbf{F}_1, \mathbf{F}_2, c) := \{\mathbf{P} \text{ such that } ||\mathbf{P} - \mathbf{F}_1|| + ||\mathbf{P} - \mathbf{F}_2|| = 2a\},$$

where $||\cdot||$ is the Euclidean norm. The minor semi-axis will be indicated with b. See Figure C.2 for a graphical description.

It could be technically easier, in terms of comparison to real data, to avoid a description

of the focal adhesion involving the foci, which might be hard to calculate. Thus, every ellipse can be identified by the following parameters:

1. Centre $\mathbf{C} = (x_0, y_0)$;

2. Major semiaxis a and minor semi-axis b;

3. Orientation α, with indicates the anticlockwise angle between the horizontal line $y = y_0$ and the major semi-axis of the ellipse, see Figure C.2.

The distances $||\mathbf{F_1} - \mathbf{C}||$ and $||\mathbf{F_2} - \mathbf{C}||$ of the foci $\mathbf{F_1}, \mathbf{F_2}$ from the centre $\mathbf{C}$ are $||\mathbf{F_1} - \mathbf{C}|| = ||\mathbf{F_2} - \mathbf{C}|| = \sqrt{a^2 - b^2}$. Hence the foci are:

$$\mathbf{F_1} = \begin{pmatrix} x_0 + \sqrt{a^2 - b^2}\cos\alpha \\ y_0 + \sqrt{a^2 - b^2}\sin\alpha \end{pmatrix} \quad \text{and} \quad \mathbf{F_2} = \begin{pmatrix} x_0 - \sqrt{a^2 - b^2}\cos\alpha \\ y_0 - \sqrt{a^2 - b^2}\sin\alpha \end{pmatrix}.$$

Let now t_a be the appearing time and t_f the disappearing time of the FA such that

$$0 \leq t_a < t_f \leq T,$$

where $t = 0$ is the initial time and $t = T$ is the final time imposed for the model. The cell is represented as a two-dimensional domain Ω on the xy plane. In the following we define:

$$\mathbf{F}_1 : [0, T] \to \Omega, \qquad \mathbf{F}_2 : [0, T] \to \Omega, \qquad a : [0, T] \to \mathbb{R}^+,$$

which represent, respectively, the position of the two evolving foci and the length of major semi-axis of the ellipse. Furthermore, we define a function $r : [0, T] \to \mathbb{R}^+$, such that:

$$r := a - ||\mathbf{F}_1 - \mathbf{C}|| = a - ||\mathbf{F}_2 - \mathbf{C}||,$$

as shown in Figure C.2. A focal adhesion is represented by a time evolving ellipse on the xy plane:

$$FA(t) := \{\mathbf{P} \text{ such that } ||\mathbf{P} - \mathbf{F}_1(t)|| + ||\mathbf{P} - \mathbf{F}_2(t)|| = 2a(t)\}.$$

As well, it is necessary to impose that $FA(t) \subset \overline{\Omega}$ at any time $t \in [0, T]$.

Let now $t_m \in (t_a, t_f)$ be the time of the maximal expansion of the FA, which corresponds to the instant separating the step 1 and 2 described in Section C.1. At this time the focal points are

$$\mathbf{F}_{1,M} := \mathbf{F}_1(t_m), \quad \text{and} \quad \mathbf{F}_{2,M} := \mathbf{F}_2(t_m),$$

and the semi-axis are

$$a_M := a(t_m), \quad \text{and} \quad b_M := b(t_m).$$

We also define $r_M := r(t_m)$. A snapshot of the focal adhesion at this time is given by the ellipse

$$FA_M := \{\mathbf{P} \text{ such that } ||\mathbf{P} - \mathbf{F}_{1,M}|| + ||\mathbf{P} - \mathbf{F}_{2,M}|| = 2a_M\}.$$

For the model we will assume that the configuration at the maximal expansion is known and given in input.

Before the focal adhesion is formed, i.e. for $t \leq t_a$, we set:

$$\mathbf{F}_1(t) = \mathbf{F}_2(t) = \mathbf{F}_{1,M}, \text{ and } r(t) = 0,$$

so the focal adhesion does not exist.

Immediately after $t = t_a$, the focal point $\mathbf{F}_2(t)$ starts moving from $\mathbf{F}_{1,M}$ until it reaches the point $\mathbf{F}_{2,M}$ at the time $t = t_m$. The point $\mathbf{F}_1(t)$, instead, does not move from $\mathbf{F}_{1,M}$. During this interval of time, $r(t)$ (and consequently also $a(t)$) increases until the maximal value $r(t_m) = r_M$ is reached, accordingly with the speed of $\mathbf{F}_2(t)$. At $t = t_m$ the FA is mature, $\mathbf{F}_2$ stops moving and the FA has reached its maximal size.

Immediately after, i.e. for $t > t_m$, the disassembly process starts: the focal point $\mathbf{F}_1(t)$ moves away from $\mathbf{F}_{1,M}$ on the same line and direction as previously done by $\mathbf{F}_2(t)$ over the time interval $(t_a, t_m]$. On the other hand, the second focal point remains fixed, i.e. $\mathbf{F}_2(t) = \mathbf{F}_{2,M}$ for $t > t_m$. The value $r(t)$ (and consequently also $a(t)$) decreases, accordingly with the speed of the focal point $\mathbf{F}_1(t)$. At the end of this interval of time, when $t = t_f$, $\mathbf{F}_1(t)$ has reached the point $\mathbf{F}_{2,M}$ and collapsed on $\mathbf{F}_2(t)$, $r(t)$ is finally zero and the FA has been completely disassembled. The following equations translate this in mathematical terms:

$$\mathbf{F}_1(t) = \mathbf{F}_{1,M} + g_1(t)\Big(\mathbf{F}_{2,M} - \mathbf{F}_{1,M}\Big), \tag{C.1}$$

$$\mathbf{F}_2(t) = \mathbf{F}_{1,M} + g_2(t)\Big(\mathbf{F}_{2,M} - \mathbf{F}_{1,M}\Big), \tag{C.2}$$

$$r(t) = g(t)r_M, \tag{C.3}$$

$$a(t) = \frac{||\mathbf{F}_2(t) - \mathbf{F}_1(t)||}{2} + r(t) \tag{C.4}$$

for some suitable functions $g_1(t), g_2(t), g(t)$. In a first approach, inspired by the experimental measurements by Berginski et al. (2011) and Mohl et al. (2012), we propose para-

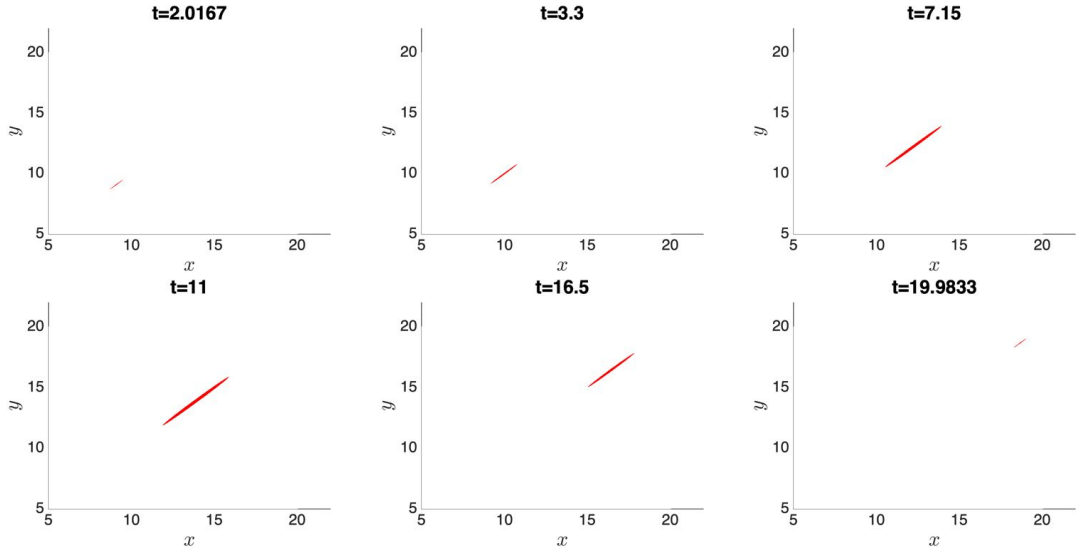

Figure C.3: Life of a focal adhesion, from formation at time $t_a = 1$ until disappearing at time $t_f = 21$. It reaches the maximal size at time $t = 11$. In this example, we set $\mathbf{C} = (10, 10)$, $a_M = 2.82$, $b_M = 0.113$, $\alpha = \pi/4$. In this simulation we take into account also the sliding of the FA (see Section C.3): a speed of 0.5 over the direction indicated by the vector $(\cos\phi, \sin\phi)$ with $\phi = \alpha$ is imposed. With this particular choice of ϕ the FA is sliding on the same direction of the growth. The area of this focal adhesion is represented by the green line in Figure C.4 (left image).

bolic time-dependent functions

$$g(t) := \begin{cases} -4\frac{(t-t_a)(t_f-t)}{(t_f-t_a)^2}, & \text{if } t \in [t_a, t_f], \\ 0, & \text{otherwise,} \end{cases} \tag{C.5}$$

$$g_1(t) := \begin{cases} 0, & t < \frac{t_a+t_f}{2}, \\ 1-g(t), & t \in \left[\frac{t_a+t_f}{2}, t_f\right], \\ 1, & t > t_f, \end{cases} \qquad g_2(t) := \begin{cases} 0, & t < t_a, \\ g(t), & t \in \left[t_a, \frac{t_a+t_f}{2}\right], \\ 1, & t > \frac{t_a+t_f}{2}. \end{cases} \tag{C.6}$$

The maximal expansion time is then $t_m = (t_a + t_f)/2$, so step 1 and step 2 of Section C.1 have exactly the same duration. The functions $g(t)$, $g_1(t)$, $g_2(t)$ assume values between 0 and 1. In Figure C.3 is shown a simulation of the FA model is presented in Figure C.3 and in Figure C.4 we show the areas of different focal adhesions generated using different parameters. A visual qualitative comparison is done by using data from Mohl et al. (2012).

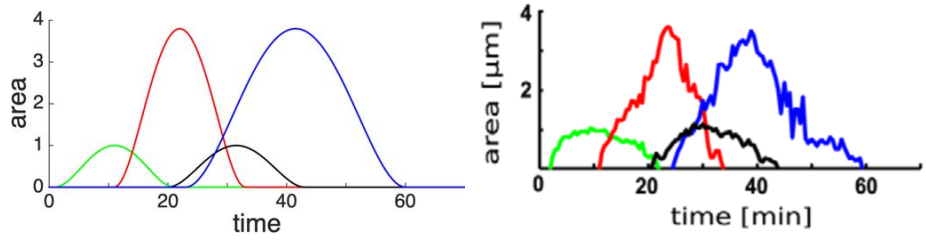

Figure C.4: Left image: areas of 4 simulated focal adhesions, with $t_{a,1} = 1$, $t_{f,1} = 21$, $a_{M,1} = 2.82$, $b_{M,1} = 0.113$, (corresponding to the focal adhesion in Figure C.3); $t_{a,2} = 11$, $t_{f,2} = 33$, $a_{M,2} = 9.837$, $b_{M,2} = 0.123$; $t_{a,3} = 20$, $t_{f,3} = 43$, $a_{M,3} = 1.38$, $b_{M,3} = 0.23$; $t_{a,4} = 23, t_{f,4} = 60, a_{M,4} = 6.02, b_{M,4} = 0.20$. Right image: experimental data from Mohl et al. (2012), *reproduced with permission of COMPANY OF BIOLOGISTS LTD., Journal of Cell Science.*

C.3 Sliding of a focal adhesion

The sliding speed of a focal adhesion can be easily included in the model. If a sliding speed $\mathbf{v}$ is known, the equations (C.1)-(C.2) can be modified as follows:

$$\mathbf{F}_1(t) = \mathbf{F}_{1,M} + g_1(t)\Big(\mathbf{F}_{2,M} - \mathbf{F}_{1,M}\Big) + \mathbf{v}t, \tag{C.7}$$

$$\mathbf{F}_2(t) = \mathbf{F}_{1,M} + g_2(t)\Big(\mathbf{F}_{2,M} - \mathbf{F}_{1,M}\Big) + \mathbf{v}t. \tag{C.8}$$

The speed can also be described in terms of an angle ϕ, a direction + or -, and a magnitude $v > 0$:

$$\mathbf{v} = \pm v \begin{pmatrix} \cos\phi \\ \sin\phi \end{pmatrix}.$$

Bibliography

Alnæs, M., Blechta, J., Hake, J., Johansson, A., Kehlet, B., Logg, A., Richardson, C., Ring, J., Rognes, M. E., and Wells, G. N. (2015). The FEniCS project version 1.5. *Archive of Numerical Software*, 3(100):9–23. 20

Altschuler, S. J., Angenent, S. B., Wang, Y., and Wu, L. F. (2008). On the spontaneous emergence of cell polarity. *Nature*, 454(7206):886. 22, 23

Andrew, N. and Insall, R. H. (2007). Chemotaxis in shallow gradients is mediated independently of PtdIns 3-kinase by biased choices between random protrusions. *Nature cell biology*, 9(2):193. 21

Ashyraliyev, M., Fomekong-Nanfack, Y., Kaandorp, J. A., and Blom, J. G. (2009). Systems biology: Parameter estimation for biochemical models. *FEBS Journal*, 276(4):886–902. 159

Beil, M., Lück, S., Fleischer, F., Portet, S., Arendt, W., and Schmidt, V. (2009). Simulating the formation of keratin filament networks by a piecewise-deterministic Markov process. *Journal of Theoretical Biology*, 256(4):518–532. 88

Berginski, M. E., Vitriol, E. A., Hahn, K. M., and Gomez, S. M. (2011). High-resolution quantification of focal adhesion spatiotemporal dynamics in living cells. *PLoS ONE*, 6(7):e22025. 170, 173

Bonetti, E., Cavaterra, C., Freddi, F., Grasselli, M., and Natalini, R. (2019). A nonlinear model for marble sulphation including surface rugosity: Theoretical and numerical results. *Communications on Pure and Applied Analysis*, 18(2):977–998. 11

Bordeleau, F., Lapierre, M. E., Sheng, Y., and Marceau, N. (2012). Keratin 8/18 regulation of cell stiffness-extracellular matrix interplay through modulation of rho-mediated actin cytoskeleton dynamics. *PLoS ONE*, 7(6):1–10. 15, 160

Boulter, E. and Garcia-Mata, R. (2010). RhoGDI. *Small GTPases*, 1(1):65–68. 7

Bray, D. J., Walsh, T. R., Noro, M. G., and Notman, R. (2015). Complete structure of an epithelial keratin dimer: Implications for intermediate filament assembly. *PLoS ONE*, 10(7). 115

Brezis, H. (2010). *Functional Analysis, Sobolev Spaces and Partial Differential Equations*. 16

Brooks, A. N. and Hughes, T. J. R. (1982). Streamline upwind/Petrov-Galerkin formulations for convection dominated flows with particular emphasis on the incompressible Navier-Stokes equations. *Computer Methods in Applied Mechanics and Engineering*, 32(1-3):199–259. 13, 131, 135, 136

Burden, R. L. and Faires, J. D. (2011). *Numerical Analysis*. Brooks/Cole, 9th edition. 150

Burnham, K. P. and Anderson, D. R. (2002). *Model Selection Multimodel Inference*. 109

Camley, B. A., Zhao, Y., Li, B., Levine, H., and Rappel, W.-J. (2017). Crawling and turning in a minimal reaction-diffusion cell motility model: coupling cell shape and biochemistry. *Physical Review E*, 95(1):012401. 68, 82, 83

Campillo-Funollet, E., Venkataraman, C., and Madzvamuse, A. (2019). Bayesian Parameter Identification for Turing Systems on Stationary and Evolving Domains. *Bulletin of Mathematical Biology*, 81(1):81–104. 152, 154, 159

Chang, Y.-C., Nalbant, P., Birkenfeld, J., Chang, Z.-F., and Bokoch, G. M. (2008). GEF-H1 couples nocodazole-induced microtubule disassembly to cell contractility via RhoA. *Molecular Biology of the Cell*, 19(5):2147–2153. 14, 22

Chernyatina, A. A., Guzenko, D., and Strelkov, S. V. (2015). Intermediate filament structure: The bottom-up approach. *Current Opinion in Cell Biology*, 32:65–72. 116

Chiou, J.-G., Ramirez, S. A., Elston, T. C., Witelski, T. P., Schaeffer, D. G., and Lew, D. J. (2018). Principles that govern competition or co-existence in Rho-GTPase driven polarization. *PLoS Computational Biology*, 14(4):e1006095. 25, 69, 70, 83

Chou, C. F., Riopel, C. L., Rott, L. S., and Omary, M. B. (1993). A significant soluble keratin fraction in 'simple' epithelial cells. Lack of an apparent phosphorylation and glycosylation role in keratin solubility. *Journal of Cell Science*, pages 433–44. 104

Codina, R. (1998). Comparison of some finite element methods for solving the diffusion-convection-reaction equation. *Computer Methods in Applied Mechanics and Engineering*. 138

Coulombe, P. A., Kerns, M. L., and Fuchs, E. (2009). Epidermolysis bullosa simplex: A paradigm for disorders of tissue fragility. *Journal of Clinical Investigation*, 119(7):1784–1793. 5

Cusseddu, D., Edelstein-Keshet, L., Mackenzie, J. A., Portet, S., and Madzvamuse, A. (2018). A coupled bulk-surface model for cell polarisation. *Journal of Theoretical Biology*. 12, 25, 69, 71

Davies, J. (2013). Mechanisms of Morphogenesis. In *Mechanisms of Morphogenesis*, volume 2, chapter 7, pages 77–84. Academic Press, 2nd edition. 3

De Pascalis, C. and Etienne-Manneville, S. (2017). Single and collective cell migration: the mechanics of adhesions. *Molecular Biology of the Cell*, 28(14):1833–1846. 3

Deek, J., Hecht, F., Rossetti, L., Wißmiller, K., and Bausch, A. R. (2016). Mechanics of soft epithelial keratin networks depend on modular filament assembly kinetics. *Acta Biomaterialia*, 43:218–229. 115

Delva, E., Tucker, D. K., and Kowalczyk, A. P. (2009). The Desmosome. *Cold Spring Harbor Perspectives in Biology*, 1(2):1–17. 121

DerMardirossian, C. and Bokoch, G. M. (2005). GDIs: central regulatory molecules in Rho GTPase activation. *Trends in Cell Biology*, 15(7):356–363. 7, 21

DeSimone, D. W. and Horwitz, A. R. (2014). Many modes of motility. *Science*, 345(6200):1002–1003. 3

DiBenedetto, E. (2010). *Partial Differential Equations*. Birkhäuser Basel, 2nd edition. 80, 155

Diegmiller, R., Montanelli, H., Muratov, C. B., and Shvartsman, S. Y. (2018). Spherical Caps in Cell Polarization. *Biophysical Journal*, 115:26–30. 24, 25, 31, 84

Do Carmo, M. P. (1976). *Differential Geometry of Curves and Surfaces*. Prentice-Hall, 1st edition. 17

Dorsey, R. E. and Mayer, W. J. (1995). Genetic algorithms for estimation problems with multiple optima, nondifferentiabiiity, and other irregular features. *Journal of Business and Economic Statistics*. 168

Drubin, D. G. and Nelson, W. J. (1996). Origins of cell polarity. *Cell*, 84(3):335–344. 21

Dziuk, G. and Elliott, C. M. (2007). Finite elements on evolving surfaces. *IMA Journal of Numerical Analysis*, 27(2):262–292. 80

Dziuk, G. and Elliott, C. M. (2013). Finite element methods for surface PDEs. *Acta Numerica*, 22:289–396. 17, 25, 81

Edelstein-Keshet, L. (2005). *Mathematical Models in Biology*. SIAM: Society for Industrial and Applied Mathematics. 8, 165

Edelstein-Keshet, L., Holmes, W. R., Zajac, M., and Dutot, M. (2013). From simple to detailed models for cell polarization. *Philosophical Transactions of the Royal Society of London B: Biological Sciences*, 368(1629):20130003. 22, 23

Elliott, C. M. and Ranner, T. (2013). Finite element analysis for a coupled bulk–surface partial differential equation. *IMA Journal of Numerical Analysis*, 33(2):377–402. 25

Elliott, C. M., Stinner, B., and Venkataraman, C. (2012). Modelling cell motility and chemotaxis with evolving surface finite elements. *Journal of The Royal Society Interface*, (June):rsif20120276. 82

Etienne-Manneville, S. (2008). Polarity proteins in migration and invasion. *Oncogene*, 27(55):6970. 21

Etienne-Manneville, S. (2013). Microtubules in cell migration. *Annual review of cell and developmental biology*, 29:471–99. 5

Etienne-Manneville, S. (2018). Cytoplasmic Intermediate Filaments in Cell Biology. *Annual Review of Cell and Developmental Biology*, 34(1):1–28. 5, 6, 115, 116

Evans, L. C. (2010). *Partial differential equations*. American Mathematical Society. 16, 59, 132

Fernández, J. R., Kalita, P., Migórski, S., Muñiz, M. C., and Núñez, C. (2016). Existence and Uniqueness Results for a Kinetic Model in Bulk-Surface Surfactant Dynamics. *SIAM Journal on Mathematical Analysis*, 48(5):3065–3089. 10

Fife, P. C. and McLeod, J. B. (1977). The approach of solutions of nonlinear diffusion equations to travelling front solutions. *Archive for Rational Mechanics and Analysis*, 65(4):335–361. 23, 46

Fletcher, D. A. and Mullins, R. D. (2010). Cell mechanics and the cytoskeleton. *Nature*, 463(7280):485–492. 4, 86

Frankel, J. (2018). Preface: Defining polarity. In Conn, P. M., editor, *Cell Polarity in Development and Disease*, Perspectives in Translational Cell Biology, pages xiii – xviii. Academic Press, Boston. 21

Fritz, R. D. and Pertz, O. (2016). The dynamics of spatio-temporal Rho GTPase signaling: formation of signaling patterns. *F1000Research*, 5:749. 7

Fujiwara, S., Ohashi, K., Mashiko, T., Kondo, H., and Mizuno, K. (2016). Interplay between Solo and keratin filaments is crucial for mechanical force–induced stress fiber reinforcement. *Molecular Biology of the Cell*, 27(6):954–966. 15, 16, 22

Garcia-Mata, R., Boulter, E., and Burridge, K. (2011). The 'invisible hand': Regulation of RHO GTPases by RHOGDIs. *Nature Reviews Molecular Cell Biology*, 12(8):493–504. 7

Garrod, D. and Chidgey, M. (2008). Desmosome structure, composition and function. *Biochimica et Biophysica Acta - Biomembranes*, 1778(3):572–587. 121

Geiger, B., Spatz, J. P., and Bershadsky, A. D. (2009). Environmental sensing through focal adhesions. *Nature reviews. Molecular cell biology*, 10(1):21–33. 6

Geuzaine, C. and Remacle, J.-F. (2009). Gmsh: A 3-D finite element mesh generator with built-in pre-and post-processing facilities. *International Journal for Numerical Methods in Engineering*, 79(11):1309–1331. 20

Giese, W., Eigel, M., Westerheide, S., Engwer, C., and Klipp, E. (2015). Influence of cell shape, inhomogeneities and diffusion barriers in cell polarization models. *Physical Biology*, 12(6):066014. 24, 25, 26, 71, 83, 157

Goryachev, A. B. and Leda, M. (2017). Many roads to symmetry breaking: molecular mechanisms and theoretical models of yeast cell polarity. *Molecular Biology of the Cell*, 28(3):370–380. 22

Goryachev, A. B. and Pokhilko, A. V. (2008). Dynamics of Cdc42 network embodies a Turing-type mechanism of yeast cell polarity. *FEBS Letters*, 582(10):1437–1443. 23

Graessl, M., Koch, J., Calderon, A., Kamps, D., Banerjee, S., Mazel, T., Schulze, N., Jungkurth, J. K., Patwardhan, R., Solouk, D., Hampe, N., Hoffmann, B., Leif, D., and Nalbant, P. (2017). An excitable Rho GTPase signaling network generates dynamic subcellular contraction patterns. *Journal of Cell Biology*. 21, 83

Guilluy, C., Garcia-Mata, R., and Burridge, K. (2011). Rho protein crosstalk: another social network? *Trends in Cell Biology*, 21(12):718–726. 11, 21

Hanna, S. and El-Sibai, M. (2013). Signaling networks of Rho GTPases in cell motility. *Cellular Signalling*, 25(10):1955–1961. 7

Harburger, D. S. and Calderwood, D. A. (2009). Integrin signalling at a glance. *Journal of Cell Science*, 122(Pt 2):159–63. 6

Hémonnot, C. Y., Mauermann, M., Herrmann, H., and Köster, S. (2015). Assembly of Simple Epithelial Keratin Filaments: Deciphering the Ion Dependence in Filament Organization. *Biomacromolecules*, 16(10):3313–3321. 115

Herrmann, H., Bär, H., Kreplak, L., Strelkov, S. V., and Aebi, U. (2007). Intermediate filaments: from cell architecture to nanomechanics. *Molecular Cell Biology*, 8(7):562–73. 86, 116

Hill, A. V. (1910). The possible effects of the aggregation of the molecule of hemoglobin on its dissociation curves. *Journal of Physiology*, 40:iv–vii. 163

Hodge, R. G. and Ridley, A. J. (2016). Regulating Rho GTPases and their regulators. *Nature Reviews Molecular Cell Biology*, 17(8):496. 7, 21, 27

Hodgkin, A. L. and Huxley, A. F. (1952). A quantitative description of membrane current and its application to conduction and excitation in nerve. *The Journal of Physiology*, 117(4):500–544. 1

Holland, J. H. (1992). *Adaptation in Natural and Artificial Systems: An Introductory Analysis with Applications to Biology, Control and Artificial Intelligence*. MIT press. 159, 167

Holmes, W. R. (2014). An efficient, nonlinear stability analysis for detecting pattern formation in reaction diffusion systems. *Bulletin of Mathematical Biology*, 76(1):157–183. 26, 56

Holmes, W. R. and Edelstein-Keshet, L. (2016). Analysis of a minimal Rho-GTPase circuit regulating cell shape. *Physical Biology*, 13(4):046001. 31, 56, 57

Holmes, W. R., Mata, M. A., and Edelstein-Keshet, L. (2015). Local perturbation analysis: A computational tool for biophysical reaction-diffusion models. *Biophysical Journal*, 108(2):230–236. 26, 56

Hurvich, C. M. and Tsai, C. L. (1989). Regression and time series model selection in small samples. *Biometrika*, 76(2):297–307. 109

Iden, S. and Collard, J. G. (2008). Crosstalk between small GTPases and polarity proteins in cell polarization. *Nature Reviews Molecular Cell Biology*, 9(11):846–859. 7

Irvine, A. D. and McLean, W. H. I. (1999). Human keratin diseases: The increasing spectrum of disease and subtlety of the phenotype-genotype correlation. *British Journal of Dermatology*, 140(5):815–828. 5

Irving, R. S. (2004). *Integers, Polynomials, and Rings*. Undergraduate Texts in Mathematics. Springer-Verlag, New York. 38

Iwasa, J. and Marshall, W. (2016). *Karp's Cell and Molecular Biology: Concepts and Experiments, 8th Edition*. John Wiley & Sons, 8th edition. 4, 10

Jacob, J. T., Coulombe, P. A., Kwan, R., and Omary, M. B. (2018). Types I and II keratin intermediate filaments. *Cold Spring Harbor Perspectives in Biology*, 10(4). 5, 116

Jilkine, A. and Edelstein-Keshet, L. (2011). A comparison of mathematical models for polarization of single eukaryotic cells in response to guided cues. *PLoS Computational Biology*, 7(4):e1001121. 23

Jiu, Y., Peränen, J., Schaible, N., Cheng, F., Eriksson, J. E., Krishnan, R., and Lappalainen, P. (2017). Vimentin intermediate filaments control actin stress fiber assembly through GEF-H1 and RhoA. *Journal of Cell Science*, 130(5):892–902. 16

John, V. and Knobloch, P. (2007). On spurious oscillations at layers diminishing (SOLD) methods for convection-diffusion equations: Part I - A review. *Computer Methods in Applied Mechanics and Engineering*, 196(17-20):2197–2215. 138

Johnson, C. (1987). *Numerical Solution of Partial Differential Equations by the Finite Element Method*. Cambridge University Press. 135

Johnson, J. B. and Omland, K. S. (2004). Model selection in ecology and evolution. *Trends in Ecology and Evolution*, 19(2):101–108. 91

Jones, J. C. R., Hopkinson, S. B., and Goldfinger, L. E. (1998). Structure and assembly of hemidesmosomes. *BioEssays*, 20(6):488–494. 121

Juma, V. O. (2019). *Data-driven mathematical modelling and simulation of Rho-Myosin temporal dynamics*. PhD thesis, University of Sussex. 154

Karp, G. (2010). *Cell and molecular biology : concepts and experiments*. John Wiley. 114

Kayser, J., Grabmayr, H., Harasim, M., Herrmann, H., and Bausch, A. R. (2012). Assembly kinetics determine the structure of keratin networks. *Soft Matter*, 8(34):8873–8879. 115

Kim, H. J., Choi, W. J., and Lee, C. H. (2015). Phosphorylation and reorganization of keratin networks: Implications for carcinogenesis and epithelial mesenchymal transition. *Biomolecules and Therapeutics*, 23(4):301–312. 120

Kim, J. S., Lee, C. H., and Coulombe, P. A. (2010). Modeling the self-organization property of keratin intermediate filaments. *Biophysical Journal*, 99(9):2748–2756. 88

Kirfel, G. and Herzog, V. (2004). Migration of epidermal keratinocytes: Mechanisms, regulation, and biological significance. *Protoplasma*, 223(2-4):67–78. 13

Kirmse, R., Portet, S., Mücke, N., Aebi, U., Herrmann, H., and Langowski, J. (2007). A quantitative kinetic model for the in vitro assembly of intermediate filaments from tetrameric vimentin. *Journal of Biological Chemistry*, 282(25):18563–18572. 88, 116

Kölsch, A., Windoffer, R., and Leube, R. E. (2009). Actin-Dependent Dynamics of Keratin Filament Precursors. *Cell Motility and the Cytoskeleton*, 66(11):76–985. 15, 120

Kölsch, A., Windoffer, R., Würflinger, T., Aach, T., Leube, R. E., and Wurflinger, T. (2010). The keratin-filament cycle of assembly and disassembly. *Journal of Cell Science*, 123(13):2266–2272. 93, 112, 114, 116, 120

Köster, S., Weitz, D. A., Goldman, R. D., Aebi, U., and Herrmann, H. (2015). Intermediate filament mechanics in vitro and in the cell: From coiled coils to filaments, fibers and networks. *Current Opinion in Cell Biology*, 32:82–91. 116

Kotsur, D., Leube, R. E., Windoffer, R., and Mattes, J. (2017). Active contour models for individual keratin filament. In *Proceedings of the OAGM&ARW Joint Workshop. Vision, Automation and Robotics*, pages 99–100, Vienna. Verlag der Technischen Universität Graz. 120

Kozlov, M. M. and Mogilner, A. (2007). Model of polarization and bistability of cell fragments. *Biophysical Journal*, 93(11):3811–3819. 31

Kwon, Y. I. and Derby, J. J. (2001). Modeling the coupled effects of interfacial and bulk phenomena during solution crystal growth. *Journal of Crystal Growth*, 230(1-2):328–335. 10

Ladoux, B., Mège, R.-M., and Trepat, X. (2016). Front–rear polarization by mechanical cues: From single cells to tissues. *Trends in Cell Biology*, 26(6):420–433. 7, 21

Leduc, C. and Etienne-Manneville, S. (2015). Intermediate filaments in cell migration and invasion: The unusual suspects. *Current Opinion in Cell Biology*, 32:102–112. 5, 86, 87, 116, 120

Leube, R. E., Moch, M., Kölsch, A., and Windoffer, R. (2011). "Panta rhei": Perpetual cycling of the keratin cytoskeleton. *BioArchitecture*, 1(1):39–44. 86, 116

Leube, R. E., Moch, M., and Windoffer, R. (2015). Intermediate filaments and the regulation of focal adhesion. *Current Opinion in Cell Biology*, 32:13–20. 15, 87, 121

Lichtenstern, T., Mücke, N., Aebi, U., Mauermann, M., and Herrmann, H. (2012). Complex formation and kinetics of filament assembly exhibited by the simple epithelial keratins K8 and K18. *Journal of Structural Biology*, 177(1):54–62. 86, 115

Liovic, M., Mogensen, M. M., Prescott, A. R., and Lane, E. B. (2003). Observation of keratin particles showing fast bidirectional movement colocalized with microtubules. *Journal of Cell Science*, 116(Pt 8):1417–27. 15, 120

Logan, J. D. (2007). *An Introduction to Nonlinear Partial Differential Equations: Second Edition*. Wiley-Interscience, 2nd edition. 128

Luria, S. E. and Delbrück, M. (1943). Mutations of Bacteria from Virus Sensitivity to Virus Resistance. *Genetics*, 28(8):491–511. 1

MacDonald, G., Mackenzie, J. A., Nolan, M., and Insall, R. (2016a). A computational method for the coupled solution of reaction–diffusion equations on evolving domains and manifolds: Application to a model of cell migration and chemotaxis. *Journal of Computational Physics*, 309:207–226. 25, 26, 63

MacDonald, G., MacKenzie, J. A., Nolan, M., and Insall, R. H. (2016b). A computational method for the coupled solution of reaction-diffusion equations on evolving domains and manifolds: Application to a model of cell migration and chemotaxis. *Journal of Computational Physics*, 309:207–226. 82

Machacek, M., Hodgson, L., Welch, C., Elliott, H., Pertz, O., Nalbant, P., Abell, A., Johnson, G. L., Hahn, K. M., and Danuser, G. (2009). Coordination of Rho GTPase activities during cell protrusion. *Nature*, 461(7260):99–103. 8

MacKenzie, J. A., Nolan, M., and Insall, R. H. (2016). Local modulation of chemoattractant concentrations by single cells: dissection using a bulk-surface computational model. *Interface Focus*, 6(5). 82

Madzvamuse, A. and Chung, A. (2016a). Analysis and simulations of coupled bulk-surface reaction-diffusion systems on exponentially evolving volumes. *Mathematical Modelling of Natural Phenomena*, 11(5):4–32. 25

Madzvamuse, A. and Chung, A. H. (2016b). The bulk-surface finite element method for reaction–diffusion systems on stationary volumes. *Finite Elements in Analysis and Design*, 108:9–21. 25, 26, 58, 82

Madzvamuse, A., Chung, A. H., and Venkataraman, C. (2015). Stability analysis and simulations of coupled bulk-surface reaction–diffusion systems. *Proceedings of the Royal Society of London A*, 471(2175):20140546. 25

Madzvamuse, A. and Lubkin, S. R. (2016). A note on how to develop interdisciplinary collaborations between experimentalists and theoreticians. *Interface focus*, 6. 1

Marée, A. F., Jilkine, A., Dawes, A., Grieneisen, V. A., and Edelstein-Keshet, L. (2006). Polarization and movement of keratocytes: a multiscale modelling approach. *Bulletin of Mathematical Biology*, 68(5):1169–1211. 22

Martin, I., Leitner, A., Walther, P., Herrmann, H., and Marti, O. (2015). Model-based analysis of keratin intermediate filament assembly. *Journal of Physics D: Applied Physics*, 48(37). 88, 115

Mayor, R. and Carmona-Fontaine, C. (2010). Keeping in touch with contact inhibition of locomotion. *Trends in Cell Biology*, 20(6):319–328. 22

Michaelis, L. and Menten, M. L. (1913). Die Kinetik der Invertinwirkung (The Kinetics of Invertase Action translated). *Biochemistry Zeitung*. 1

Miller, R. K., Vikstrom, K., and Goldman, R. D. (1991). Keratin incorporation into intermediate filament networks is a rapid process. *Journal of Cell Biology*, 113(4):843–855. 93, 118

Milo, R. and Phillips, R. (2015). *Cell biology by the numbers*. 9, 10, 37

Mitchell, M. (1998). *An Introduction to Genetic Algorithms (Complex Adaptive Systems)*. MIT Press. 159, 167

Mitchison, T. J. and Cramer, L. P. (1996). Actin-based cell motility and cell locomotion. *Cell*, 84(3):371–379. 3, 4

Möbius, W. and Laan, L. (2015). Physical and Mathematical Modeling in Experimental Papers. *Cell*, 163(7):1577–1583. 1

Moch, M., Herberich, G., Aach, T., Leube, R. E., and Windoffer, R. (2013). Measuring the regulation of keratin filament network dynamics. *Proceedings of the National Academy of Sciences*, 110(26):10664–10669. 12, 86, 87, 89, 90, 91, 93, 99, 106, 113, 156, 166

Moch, M., Windoffer, R., Schwarz, N., Pohl, R., Omenzetter, A., Schnakenberg, U., Herb, F., Chaisaowong, K., Merhof, D., Ramms, L., Fabris, G., Hoffmann, B., Merkel, R., and Leube, R. E. (2016). Effects of plectin depletion on keratin network dynamics and organization. *PLoS ONE*, 11(3):e0149106. 15, 121

Mohl, C., Kirchgessner, N., Schafer, C., Hoffmann, B., and Merkel, R. (2012). Quantitative mapping of averaged focal adhesion dynamics in migrating cells by shape normalization. *Journal of Cell Science*, 125(1):155–165. 89, 170, 173, 174, 175

Mori, Y., Jilkine, A., and Edelstein-Keshet, L. (2008). Wave-pinning and cell polarity from a bistable reaction-diffusion system. *Biophysical Journal*, 94(9):3684–3697. 11, 22, 23, 31, 32, 58, 67, 70, 82, 156, 157

Mori, Y., Jilkine, A., and Edelstein-Keshet, L. (2011). Asymptotic and bifurcation analysis of wave-pinning in a reaction-diffusion model for cell polarization. *SIAM Journal on Applied Mathematics*, 71(4):1401–1427. 23, 37, 45, 48, 54, 82

Mücke, N., Winheim, S., Merlitz, H., Buchholz, J., Langowski, J., and Herrmann, H. (2016). In vitro assembly kinetics of cytoplasmic intermediate filaments: A correlative Monte Carlo simulation study. *PLoS ONE*, 11(6):e0157451. 88, 116

Murray, J. D. (2002). *Mathematical Biology: I: An Introduction*, volume 17. Springer-Verlag New York, third edition. 165

Murray, J. D. (2003). *Mathematical Biology. II: Spatial Models and Biomedical Applications*. Springer-Verlag New York, third edition. 8

Nahidiazar, L., Kreft, M., van den Broek, B., Secades, P., Manders, E. M. M., Sonnenberg, A., and Jalink, K. (2015). The molecular architecture of hemidesmosomes, as revealed with super-resolution microscopy. *Journal of Cell Science*, 128(20):3714–3719. 6

Nalbant, P., Chang, Y.-C., Birkenfeld, J., Chang, Z.-F., and Bokoch, G. M. (2009). Guanine Nucleotide Exchange Factor-H1 Regulates Cell Migration via Localized Activation of RhoA at the Leading Edge. *Molecular Biology of the Cell*, 20(18):4070–4082. 8

Nelson, D. L., Lehninger, A. L., and Cox, M. M. (2008). *Lehninger principles of biochemistry*. Macmillan. 163

Nelson, W. J. (2003). Adaptation of core mechanisms to generate cell polarity. *Nature*, 422(6933):766. 21, 165

Novak, I. L., Gao, F., Choi, Y.-S., Resasco, D., Schaff, J. C., and Slepchenko, B. M. (2007). Diffusion on a curved surface coupled to diffusion in the volume: Application to cell biology. *Journal of Computational Physics*, 226(2):1271–1290. 24

Ohashi, K., Fujiwara, S., and Mizuno, K. (2017). Roles of the cytoskeleton, cell adhesion and rho signalling in mechanosensing and mechanotransduction. *The Journal of Biochemistry*, 161(3):245–254. 22

Okubo, A. and Levin, S. A. (2001). *Diffusion and Ecological Problems: Modern Perspectives*, volume 14. Springer-Verlag New York, 2nd edition. 9

Omary, M. B., Coulombe, P. A., and McLean, W. H. I. (2004). Intermediate filament proteins and their associated diseases. *New England Journal of Medicine*, 351(20):2087–2100. 5

Osmani, N. and Labouesse, M. (2015). Remodeling of keratin-coupled cell adhesion complexes. *Current Opinion in Cell Biology*, 32:30–38. 121

Otsuji, M., Ishihara, S., Kaibuchi, K., Mochizuki, A., Kuroda, S., et al. (2007). A mass conserved reaction–diffusion system captures properties of cell polarity. *PLoS computational biology*, 3(6):e108. 23

Pan, X., Hobbs, R. P., and Coulombe, P. A. (2013). The expanding significance of keratin intermediate filaments in normal and diseased epithelia. *Current Opinion in Cell Biology*, 25(1):1–10. 5

Pollard, T. D. and Borisy, G. G. (2003). Cellular motility driven by assembly and disassembly of actin filaments. *Cell*, 112(4):453–465. 4

Pollard, T. D. and Cooper, J. A. (2009). Actin, a central player in cell shape and movement. *Science*, 326(5957):1208–1212. 4

Portet, S. (2013). Dynamics of in vitro intermediate filament length distributions. *Journal of Theoretical Biology*, 332:20–29. 88, 116

Portet, S. and Arino, J. (2009). An in vivo intermediate filament assembly model. *Mathematical biosciences and engineering : MBE*, 6(1):117–134. 88

Portet, S., Arino, O., Vassy, J., and Schoëvaërt, D. (2003). Organization of the cytokeratin network in an epithelial cell. *Journal of theoretical biology*, 223(3):313–33. 88

Portet, S., Madzvamuse, A., Chung, A. H. W., Leube, R. E., and Windoffer, R. (2015). Keratin dynamics: Modeling the interplay between turnover and transport. *PLoS ONE*, 10(3). ix, xi, 4, 12, 85, 88, 89, 91, 92, 94, 97, 98, 103, 104, 106, 108, 109, 110, 112, 152, 156, 159, 167

Portet, S., Mücke, N., Kirmse, R., Langowski, J., Beil, M., and Herrmann, H. (2009). Vimentin intermediate filament formation: In vitro measurement and mathematical modeling of the filament length distribution during assembly. *Langmuir*, 25(15):8817–8823. 88, 116

Portet, S., Vassy, J., Hogue, C. W., Arino, J., and Arino, O. (2004). Intermediate filament networks: In vitro and in vivo assembly models. *Comptes Rendus - Biologies*, 327(11):970–976. 115

Postma, M., Bosgraaf, L., Loovers, H. M., and Van Haastert, P. J. (2004). Chemotaxis: signalling modules join hands at front and tail. *EMBO Reports*, 5(1):35–40. 32, 37

Quarteroni, A., Sacco, R., and Saleri, F. (2010). *Numerical mathematics*, volume 37. Springer Science & Business Media. 63, 150

Quarteroni, A. and Valli, A. (2008). *Numerical approximation of partial differential equations*. Springer-Verlag Berlin Heidelberg. 60, 135

Rafiq, N. M., Nishimura, Y., Plotnikov, S. V., Thiagarajan, V., Zhang, Z., Natarajan, M., Shi, S., Viasnoff, V., Jones, G. E., Kanchanawong, P., and Bershadsky, A. D. (2018). The cytoskeleton as a smart composite material: A unified pathway linking microtubules, myosin-II filaments and integrin adhesions. *bioRxiv*, page 195495. 14

Ramirez, S. A., Raghavachari, S., and Lew, D. J. (2015). Dendritic spine geometry can localize GTPase signaling in neurons. *Molecular Biology of the Cell*, 26(22):4171–4181. 24, 25

Ramms, L., Fabris, G., Windoffer, R., Schwarz, N., Springer, R., Zhou, C., Lazar, J., Stiefel, S., Hersch, N., Schnakenberg, U., Magin, T. M., Leube, R. E., Merkel, R., and Hoffmann, B. (2013). Keratins as the main component for the mechanical integrity of keratinocytes. *Proceedings of the National Academy of Sciences*, 110(46):18513–18518. 5

Rappel, W.-J. and Edelstein-Keshet, L. (2017). Mechanisms of cell polarization. *Current Opinion in Systems Biology*, 3:43–53. 22

Rätz, A. and Röger, M. (2012). Turing instabilities in a mathematical model for signaling networks. *Journal of Mathematical Biology*, 65(6-7):1215–1244. 30

Rätz, A. and Röger, M. (2014). Symmetry breaking in a bulk–surface reaction–diffusion model for signalling networks. *Nonlinearity*, 27(8):1805. 24, 84

Reig, G., Pulgar, E., and Concha, M. L. (2014). Cell migration: from tissue culture to embryos. *Development*, 141(10):1999–2013. 57

Ridley, A. J. (2001). Rho GTPases and cell migration. *Journal of Cell Science*, 114:2713–2722. 3, 7

Ridley, A. J. (2015). Rho GTPase signalling in cell migration. *Current Opinion in Cell Biology*, 36:103–112. 3, 7

Ridley, A. J., Schwartz, M. A., Burridge, K., Firtel, R. A., Ginsberg, M. H., Borisy, G., Parsons, J. T., and Horwitz, A. R. (2003). Cell migration: integrating signals from front to back. *Science*, 302(5651):1704–1709. 3, 7, 14, 21

Robert, A., Hookway, C., and Gelfand, V. I. (2016). Intermediate filament dynamics: What we can see now and why it matters. *BioEssays*, 38(3):232–243. 115, 116

Roubíček, T. (2013). *Nonlinear partial differential equations with applications: Second edition*. 17

Rubinstein, J. and Sternberg, P. (1992). Nonlocal reaction—diffusion equations and nucleation. *IMA Journal of Applied Mathematics*, 48(3):249–264. 47

Russo, A. (2006). Streamline-upwind Petrov/Galerkin method (SUPG) vs residual-free bubbles (RFB). *Computer Methods in Applied Mechanics and Engineering*, 195(13-16):1608–1620. 138

Ruuth, S. J. (1995). Implicit-explicit methods for reaction-diffusion problems in pattern formation. *Journal of Mathematical Biology*, 34(2):148–176. 131, 141, 150

Sadok, A. and Marshall, C. J. (2014). Rho GTPases: masters of cell migration. *Small GTPases*, 5(4):e983878. 7, 14, 21

Seltmann, K., Fritsch, A. W., Käs, J. a., and Magin, T. M. (2013). Keratins significantly contribute to cell stiffness and impact invasive behavior. *Proceedings of the National Academy of Sciences of the United States of America*, 110(46):18507–12. 6

Servedio, M. R., Brandvain, Y., Dhole, S., Fitzpatrick, C. L., Goldberg, E. E., Stern, C. A., Van Cleve, J., and Yeh, D. J. (2014). Not Just a Theory—The Utility of Mathematical Models in Evolutionary Biology. *PLoS Biology*, 12(12):e1002017. 1

Sharma, V. and Morgan, J. (2016). Global existence of solutions to reaction-diffusion systems with mass transport type boundary conditions. *SIAM Journal on Mathematical Analysis*, 48(6):4202–4240. 32, 33

Shou, W., Bergstrom, C. T., Chakraborty, A. K., and Skinner, F. K. (2015). Theory, models and biology. *eLife*, 4:1–4. 1

Smith, E. L. (1983). *Principles of biochemistry: general aspects*, volume 1. McGraw-Hill. 163

Snider, N. T. and Omary, M. B. (2014). Post-translational modifications of intermediate filament proteins: mechanisms and functions. *Nature reviews. Molecular cell biology*, 15(3):163–77. 87

Spill, F., Andasari, V., Mak, M., Kamm, R. D., and Zaman, M. H. (2016). Effects of 3D geometries on cellular gradient sensing and polarization. *Physical Biology*, 13(3):036008. 24

St Johnston, D. and Ahringer, J. (2010). Cell polarity in eggs and epithelia: parallels and diversity. *Cell*, 141(5):757–774. 21

Strnad, P., Windoffer, R., and Leube, R. E. (2002). Induction of rapid and reversible cytokeratin filament network remodeling by inhibition of tyrosine phosphatases. *Journal of Cell Science*, 115(Pt 21):4133–4148. 86

Stuart, A. M. (2010). *Inverse problems: A Bayesian perspective*, volume 19. 159

Sugiura, N. (1978). Further Analysis of the Data by Anaike' S Information Criterion and the Finite Corrections. *Communications in Statistics - Theory and Methods*, 7(1):13–26. 109

Sun, C., Arino, J., and Portet, S. (2017). Intermediate filament dynamics: Disassembly regulation. *International Journal of Biomathematics*, 10(01):1750015. 88, 115

Sun, C., Leube, R. E., Windoffer, R., and Portet, S. (2014). A mathematical model for the keratin cycle of assembly and disassembly. *IMA Journal of Applied Mathematics (Institute of Mathematics and Its Applications)*, 80(1):100–114. 88, 115

Tee, Y. H., Shemesh, T., Thiagarajan, V., Hariadi, R. F., Anderson, K. L., Page, C., Volkmann, N., Hanein, D., Sivaramakrishnan, S., Kozlov, M. M., and Bershadsky, A. D. (2015). Cellular chirality arising from the self-organization of the actin cytoskeleton. *Nature Cell Biology*. 87

Temam, R., Miranville, A., and Gremaud, P. (2003). *Mathematical Modeling in Continuum Mechanics*, volume 54. 80

Théry, M., Racine, V., Piel, M., Pépin, A., Dimitrov, A., Chen, Y., Sibarita, J.-B., and Bornens, M. (2006). Anisotropy of cell adhesive microenvironment governs cell internal organization and orientation of polarity. *Proceedings of the National Academy of Sciences*, 103:19771–19776. 160

Thomée, V. (1997). *Galerkin Finite Element Methods for Parabolic Problems*. Springer Berlin Heidelberg, 2nd ed edition. 60

Toivola, D. M., Boor, P., Alam, C., and Strnad, P. (2015). Keratins in health and disease. *Current Opinion in Cell Biology*, 32:73–81. 5

Trepat, X., Chen, Z., and Jacobson, K. (2012). Cell Migration. *Comprehensive Physiology*, 2(4):2369–2392. 4

Tsuruta, D., Hashimoto, T., Hamill, K. J., and Jones, J. C. R. (2011). Hemidesmosomes and focal contact proteins: Functions and cross-talk in keratinocytes, bullous diseases and wound healing. *Journal of Dermatological Science*, 62(1):1–7. 6

Tuncer, N. and Madzvamuse, A. (2017). Projected Finite Elements for Systems of Reaction-Diffusion Equations on Closed Evolving Spheroidal Surfaces. *Communications in Computational Physics*, 21(3):718–747. 82

Turing, A. M. (1952). The chemical basis of morphogenesis. *Philosophical Transactions of the Royal Society of London. Series B, Biological Sciences*, 237(641):37–72. 1

Tyson, J. J., Chen, K. C., and Novak, B. (2003). Sniffers, buzzers, toggles and blinkers: Dynamics of regulatory and signaling pathways in the cell. *Current Opinion in Cell Biology*, 15(2):221–231. 8

Vanderlei, B., Feng, J. J., and Edelstein-Keshet, L. (2011). A computational model of cell polarization and motility coupling mechanics and biochemistry. *Multiscale Modeling & Simulation*, 9(4):1420–1443. 25, 68, 82, 83

Vicente-Manzanares, M. (2005). Cell migration at a glance. *Journal of Cell Science*, 118(21):4917–4919. 3

Walko, G., Castañón, M. J., and Wiche, G. (2015). Molecular architecture and function of the hemidesmosome. *Cell and Tissue Research*, 360(2):363–378. 121

Wang, W., Tao, K., Wang, J., Yang, G., Ouyang, Q., Wang, Y., Zhang, L., and Liu, F. (2017). Exploring the inhibitory effect of membrane tension on cell polarization. *PLoS Computational Biology*, 13(1):e1005354. 83

Watanabe, T., Noritake, J., and Kaibuchi, K. (2005). Regulation of microtubules in cell migration. *Trends in Cell Biology*, 15(2):76–83. 5

Wilkinson, D. J. (2007). Bayesian methods in bioinformatics and computational systems biology. *Briefings in Bioinformatics*, 8(2):109–116. 159

Windoffer, R., Beil, M., Magin, T. M., and Leube, R. E. (2011). Cytoskeleton in motion: The dynamics of keratin intermediate filaments in epithelia. *Journal of Cell Biology*, 194(5):669–678. 5, 12, 13, 15, 85, 86, 87, 88, 91, 106, 110, 112, 113, 114, 116, 117, 120, 121, 152, 156

Windoffer, R., Kölsch, A., Wöll, S., and Leube, R. E. (2006). Focal adhesions are hotspots for keratin filament precursor formation. *Journal of Cell Biology*, 173(3):341–348. 15, 121

Windoffer, R., Wöll, S., Strnad, P., and Leube, R. E. (2004). Identification of Novel Principles of Keratin Filament Network Turnover in Living Cells. *Molecular Biology of the Cell*, 15(5):2436–2448. 86, 87, 116

Wöll, S., Windoffer, R., and Leube, R. E. (2005). Dissection of keratin dynamics: Different contributions of the actin and microtubule systems. *European Journal of Cell Biology*, 84(2-3):311–328. 15, 94

Xu, B. and Jilkine, A. (2018). Modeling the dynamics of Cdc42 oscillation in fission yeast. *Biophysical Journal*, 114(3):711–722. 24

Yam, P. T., Wilson, C. A., Ji, L., Hebert, B., Barnhart, E. L., Dye, N. A., Wiseman, P. W., Danuser, G., and Theriot, J. A. (2007). Actin-myosin network reorganization breaks symmetry at the cell rear to spontaneously initiate polarized cell motility. *Journal of Cell Biology*, 178(7):1207–1221. 7

Zaidel-Bar, R., Ballestrem, C., Kam, Z., and Geiger, B. (2003). Early molecular events in the assembly of matrix adhesions at the leading edge of migrating cells. *Journal of Cell Science*, 116:4605–4613. 6

Zaidel-Bar, R., Cohen, M., Addadi, L., and Geiger, B. (2004). Hierarchical assembly of cell-matrix adhesion complexes. *Biochemical Society Transactions*, 32(Pt3):416–20. 6